

2023 Fall

“Phase Transformation *in* Materials”

12.04.2023

Eun Soo Park

Office: 33-313

Telephone: 880-7221

Email: espark@snu.ac.kr

Office hours: by an appointment

Contents in Phase Transformation

Background
to understand
phase
transformation

(Ch1) Thermodynamics and Phase Diagrams

(Ch2) Diffusion: Kinetics

(Ch3) Crystal Interface and Microstructure

Representative
Phase
transformation

(Ch4) Solidification: Liquid \rightarrow Solid

(Ch5) Diffusional Transformations in Solid: Solid \rightarrow Solid

(Ch6) Diffusionless Transformations: Solid \rightarrow Solid

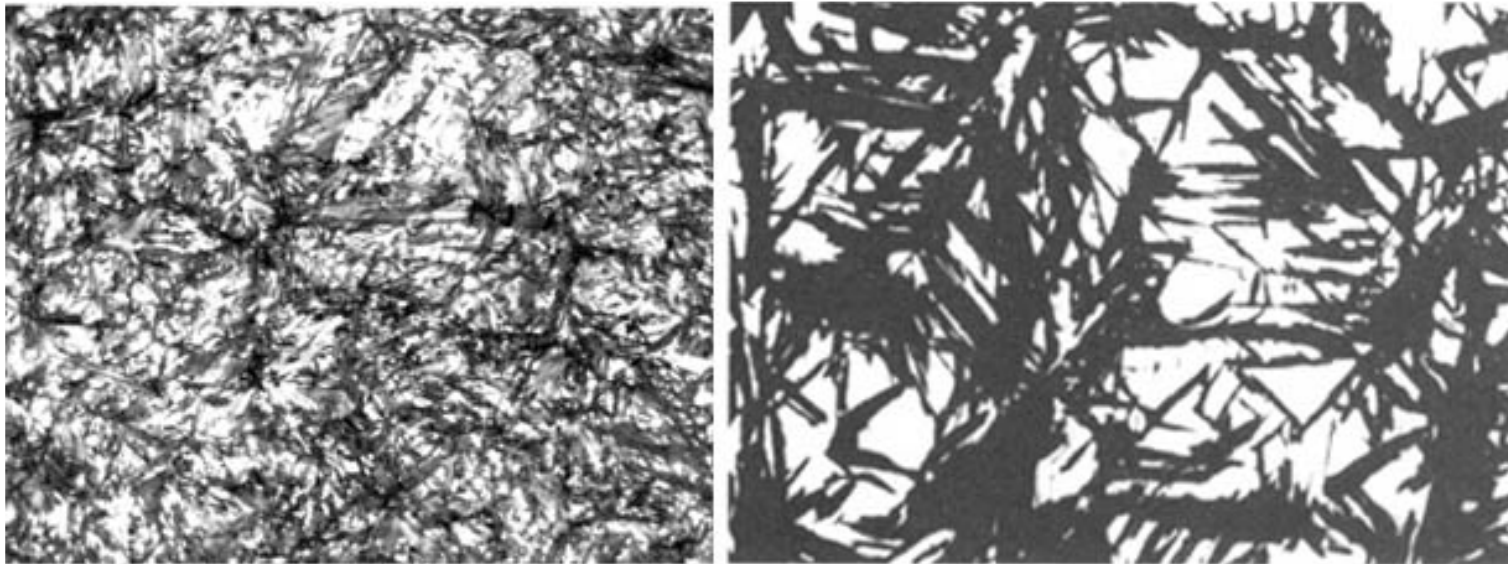
Q: What is a martensitic transformation?

Chapter 6 Diffusionless Transformation

Individual atomic movements are less than one interatomic spacing.

→ Martensite Transformation

핵생성 및 성장에 의해 일어나는 상변태, 조성변화 없이, 전단변형에 의해 정합계면이나 부분정합계면의 이동으로 결정구조가 변하는, 무확산 변태



($\gamma \rightarrow \alpha$)

Martensite with some retained austenite

"Needle like" Structure of martensite

Supersaturated solid solution of carbon in α -Fe

Named for the German metallurgist **Adolph Martens**, Martensite is the hardened phase of steel that is obtained by cooling Austenite fast enough to trap carbon atoms within the cubic iron matrix distorting it into a body centered tetragonal structure. Now,

martensite is used in physical metallurgy to describe any diffusionless trans. product. 3

One of the most important technological processes is the **hardening of steel by quenching.**

6.1 Introduction to M in Ferrous system

M transformation : γ (fcc) \rightarrow α' martensite (bcc or bct M) (e.g. Fe-C-X)

γ (fcc) with low stacking fault E at room temp.
 (cooling or stress) \rightarrow ϵ M (hcp) (e.g. Fe-Cr-Ni, Fe-Mn (high Mn steel))

동소변태 : Ti, Mn, Fe, Co, Zr...

일반적으로 fcc 혹은 hcp (조밀격자)
 \rightarrow 낮은 내부 E & 엔탈피 \rightarrow 낮은 온도
 영역 안정, bcc (낮은 충진율) \rightarrow 높은
 vibrational entropy \rightarrow 높은
 온도영역 안정 : Ti, Mn, Co, Zr

But

Fe의 경우, bcc α 저온 안정 / Fcc γ
 고온안정 \rightarrow γ 상과 α 상의 자기적
 성질에 기인 \rightarrow “복잡한 상변화 거동”

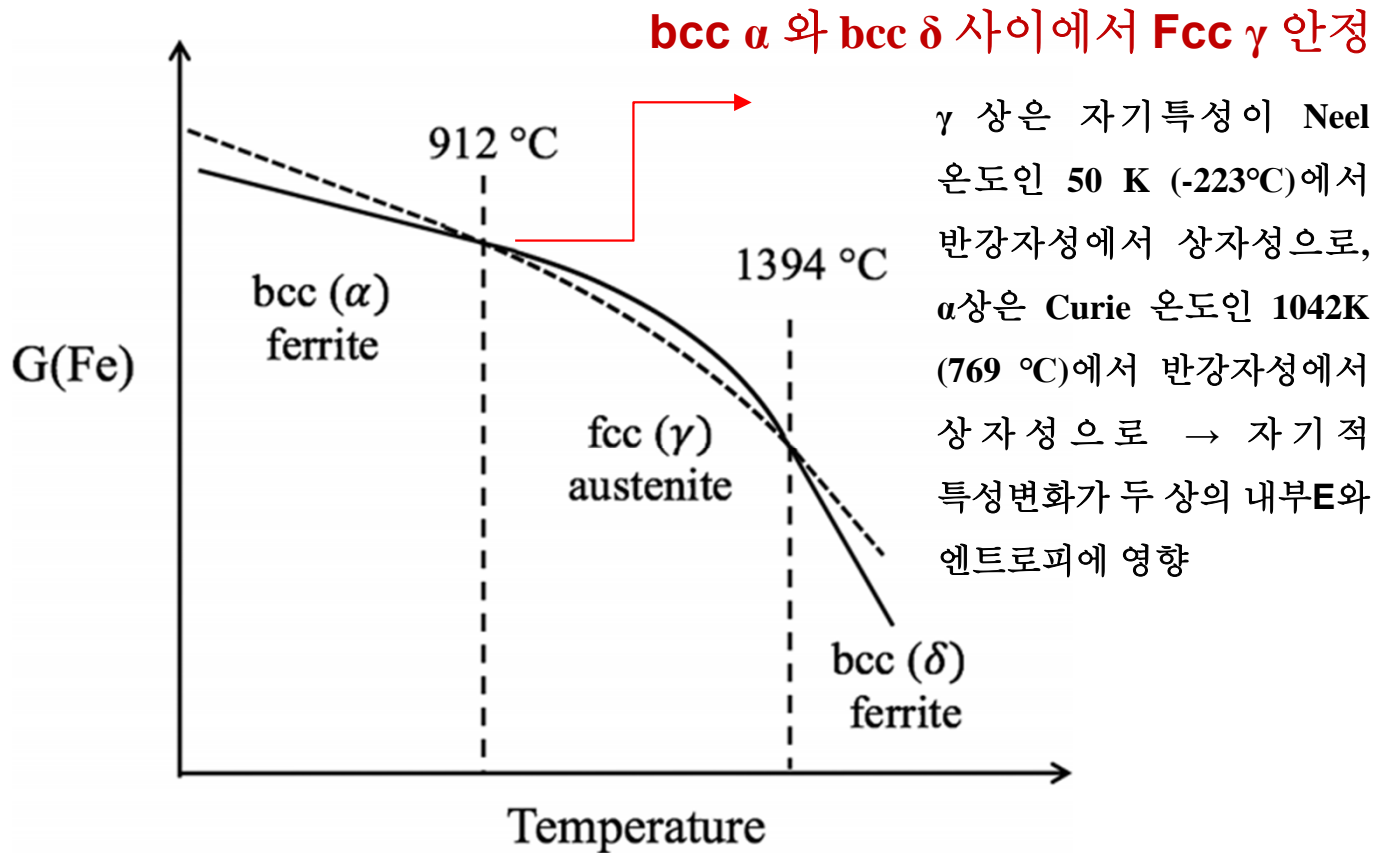
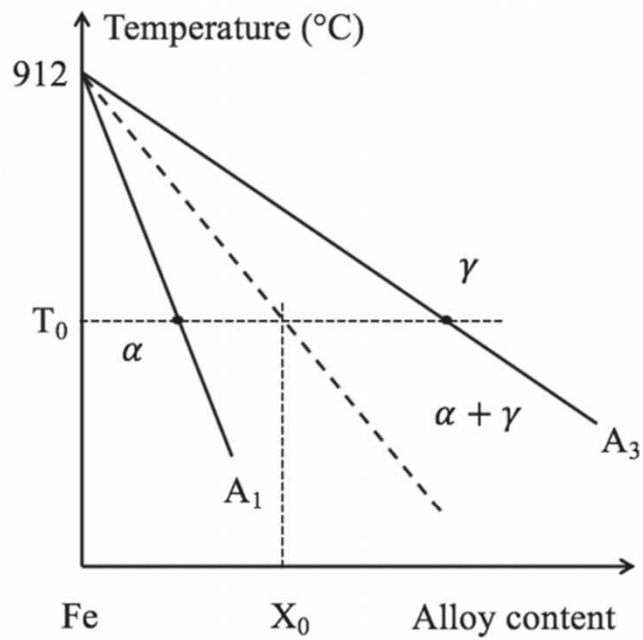
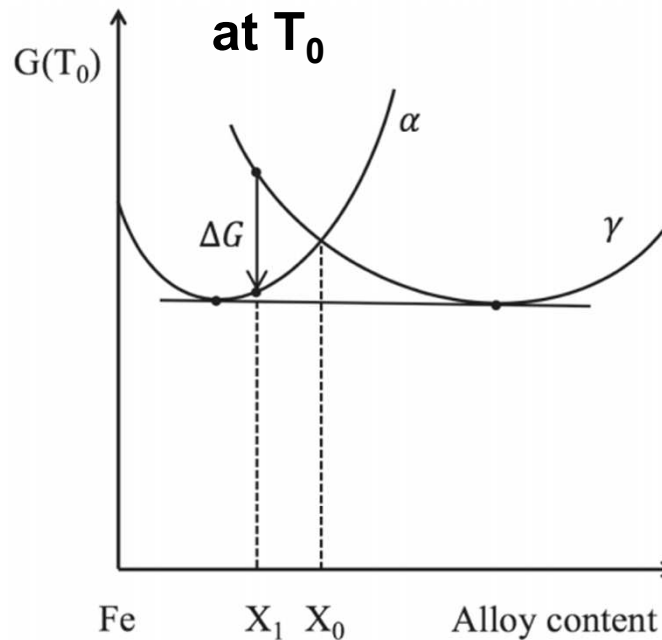


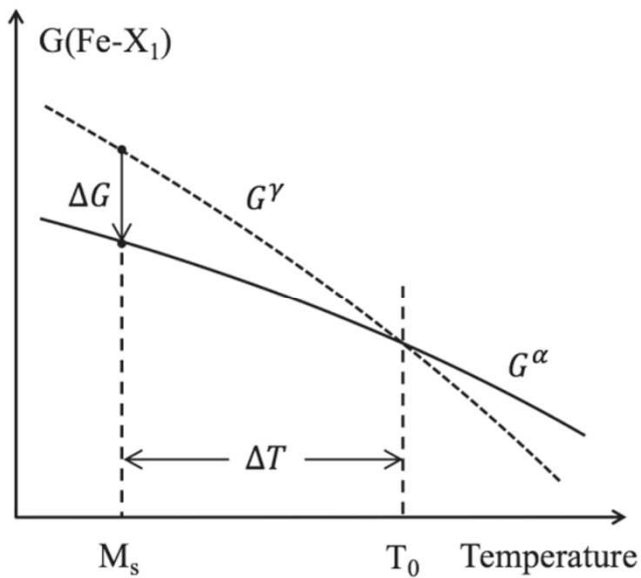
FIGURE 6.1 Schematic representation of the Gibbs free energy of iron as a function of temperature. Full line bcc and dashed line fcc. Ref. CALPHAD: Comput. Coupling Phase Diagrams Thermochem., 33: 3 (2009) 4



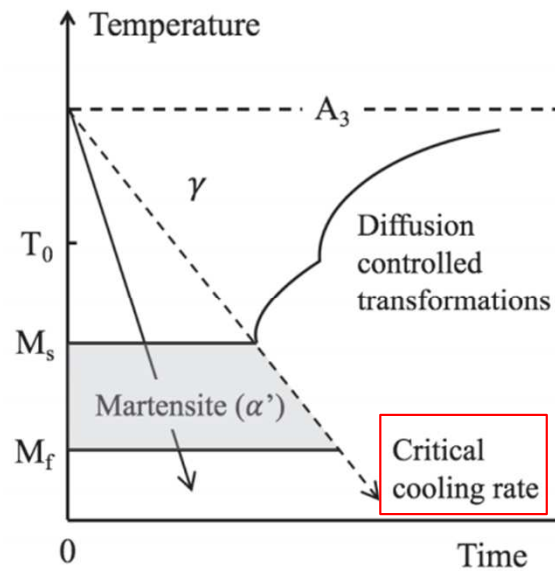
(a)



(b) (C, Mn, Cr, Ni, Cu 등)



(c)



(d)

M_s 온도 : 조성에 민감하게 변화
e.g. Pure Fe의 M_s 540°C(813K),
Fe-31Ni-10Co-3Ti 합금 -190°C (83K)

M_f 온도: 100% M 변태 조건 찾기
어려움/ M_s 보다 불분명

(순금속 $\sim 10^5$ K/s, 고합금강인
18Ni 마레이징 강 $< 10^{-2}$ K/s)

FIGURE 6.2 Conditions for the $\gamma \rightarrow \alpha'$ transformation in ferrous systems on cooling. (a) Schematic binary phase diagram showing the compositions of γ and α in equilibrium and the equilibrium temperatures A_1 and A_3 . (b) Schematic Gibbs free energy vs. composition diagram for the temperature T_0 in (a). (c) Free energy vs. temperature for composition X_1 in (b). (d) CCT diagram for composition X_1 .

6.2 Ferrous Martensite Morphologies and Crystallography

저탄소 혹은 중탄소 범위 저 합금강 M transformation : γ (fcc) \rightarrow bcc 혹은 bct M

bcc 혹은 bct M 3가지 대표 형상 : lath / lenticular plate (렌즈형 판상) / thin plate

6.2.1 (a) Lath Martensite: 저탄소강, 저합금 구조용강, Ni 함량이 28% 이하인 Fe-Ni 합금
고강도 고인성 e.g. 고인성 cryogenic 합금 9%Ni강의 주요 구성상
다른 형상 M 보다 높은 상변화 온도 (상온 이상) e.g. 저합금 탄소강 $M_s \sim 400^\circ\text{C}$, $M_f \sim 200^\circ\text{C}$

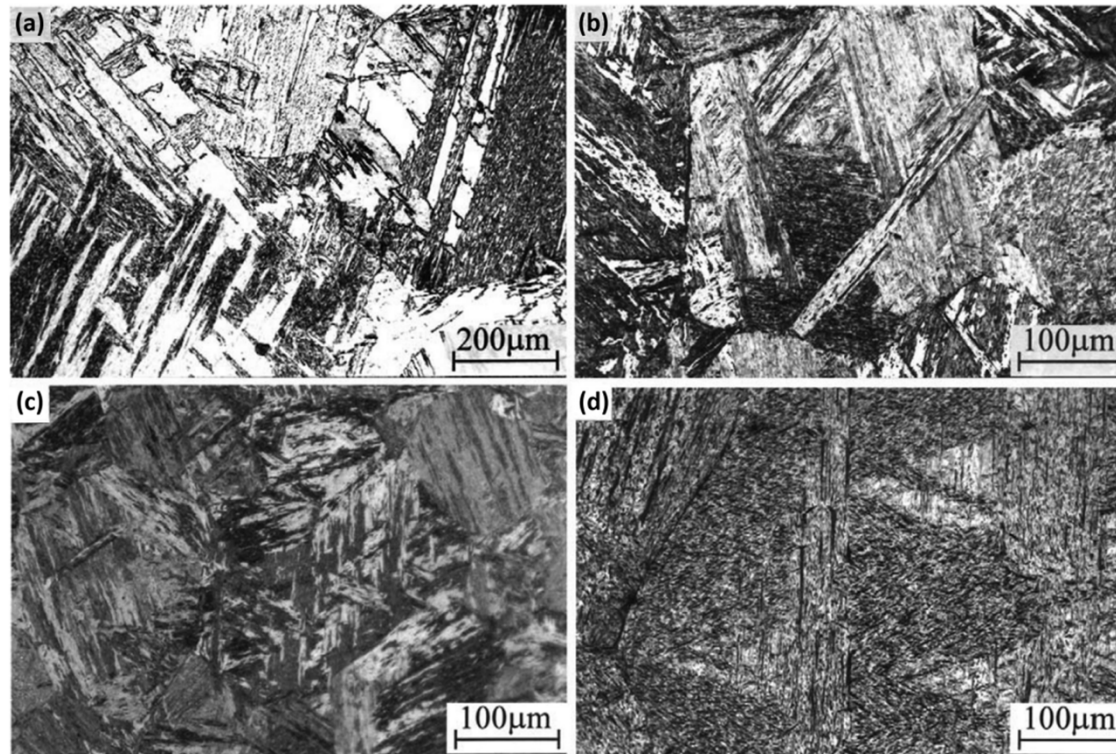


FIGURE 6.3 Light optical micrographs of lath martensite in Fe-C alloys with carbon contents in wt.% (a) 0.0026, (b) 0.18, (c) 0.38 and (d) 0.61. Etched in 3% nital solution. (Reprinted from *Acta Materialia* Vol. 51, S. Morito, H. Tanaka, R. Konishi, T. Furuhashi, T. Maki, The morphology and crystallography of lath martensite in Fe-C alloys, 1789–1799 (2003), with permission from Elsevier.)

* 결정립 - Packet - block - Sub-block - Lath 구조

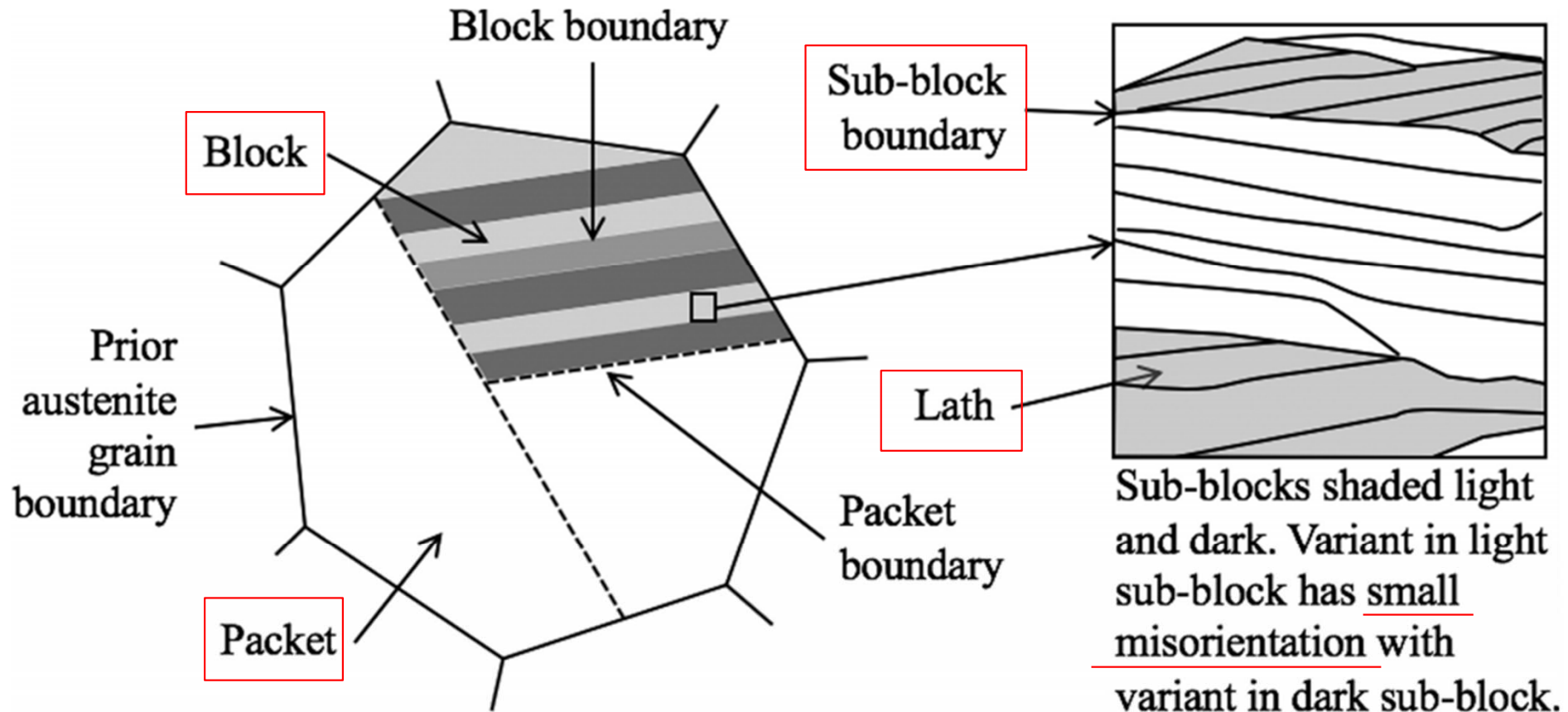
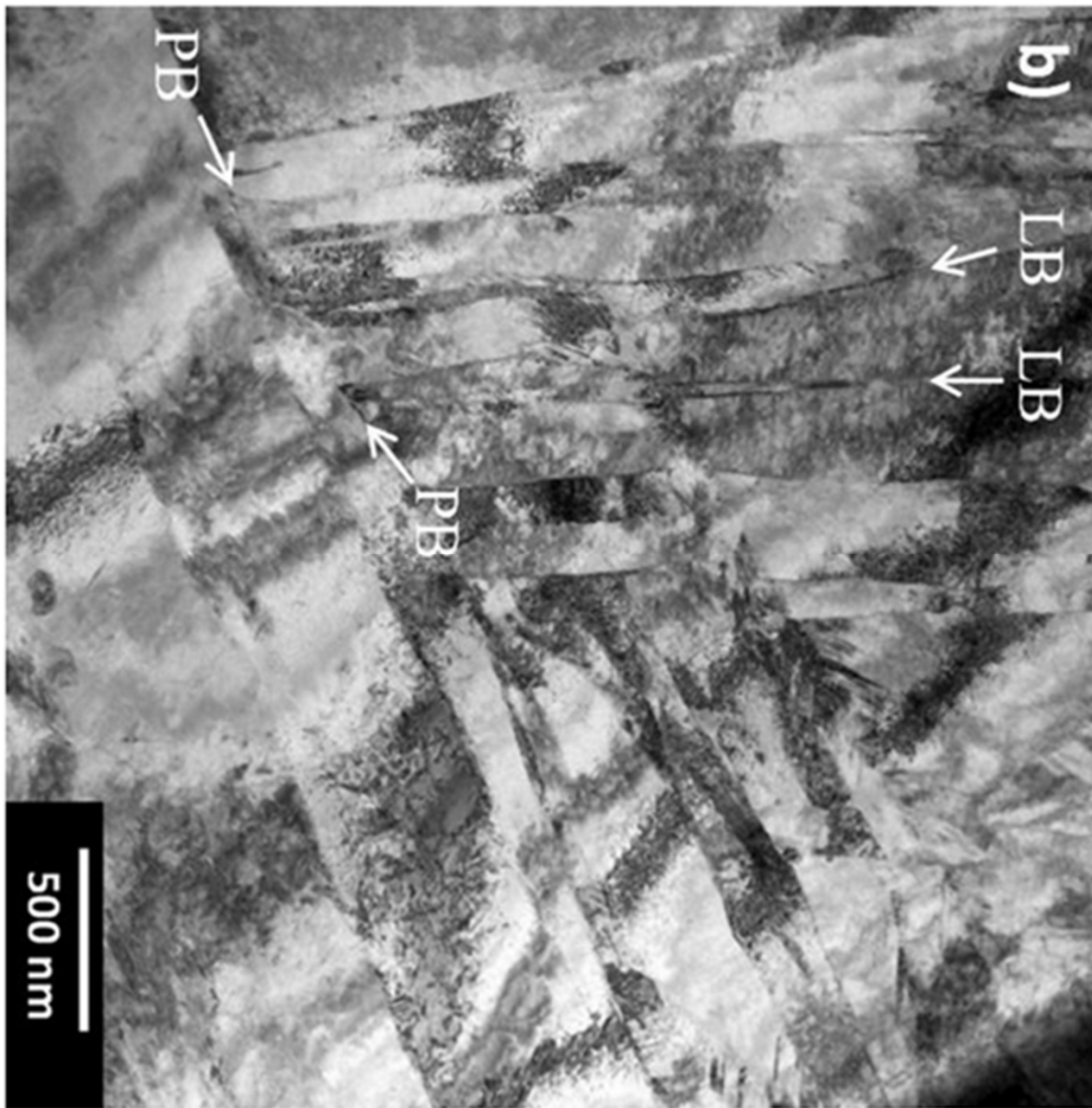


FIGURE 6.4 Schematic representation of lath martensite morphology in low-carbon alloys and steels.



Lath에서 마주보는 면이
완전히 평행하지 않기 때문에
3차원 이미징 기술을 이용해야
lath 폭과 길이 결정 가능

대략적으로 약 0.1~ 1 μm

10^{15} m^{-2} 의 매우 높은 전위 밀도

Lath 결정구조 : bcc (α')

$$\{110\}_{\alpha'} \parallel \{111\}_{\gamma}$$

KS 방위관계/ Greninger-Troiano 방위
관계/ NW 방위관계 (KS 대비 5.26°)

FIGURE 6.5 Bright-field transmission electron microscope image of lath martensite in a thin foil of a low-carbon steel. Two lath boundaries and one packet boundary are marked (LB, PB). The distances between the lath boundaries vary from 50 to 500 nm. The dark–light banding is due to bending of the thin foil causing changes in the diffraction conditions. (Courtesy of Shashank Ramesh Babu.)

* 결정립 - Packet - block - Sub-block - Lath 구조

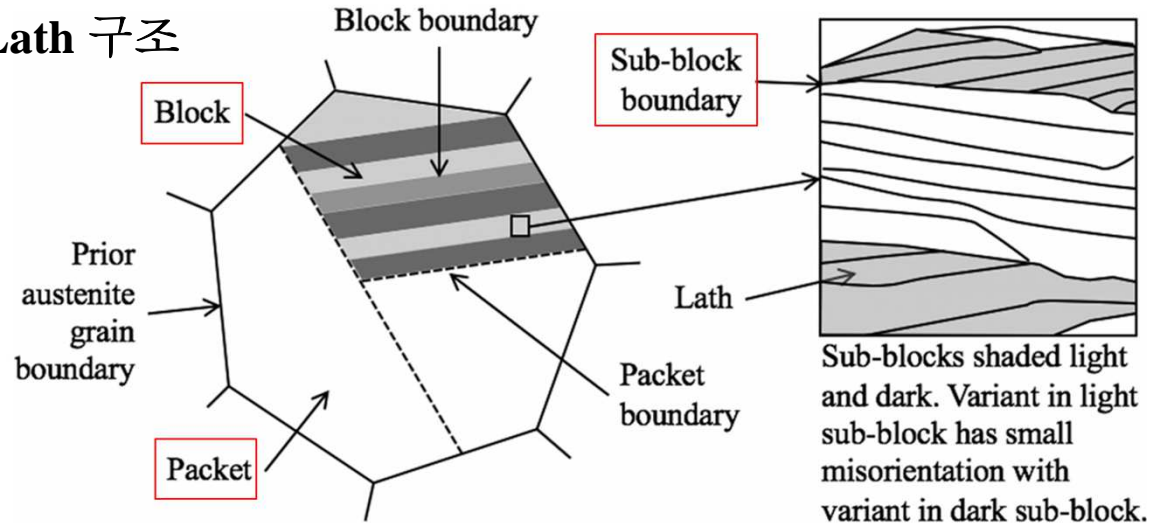


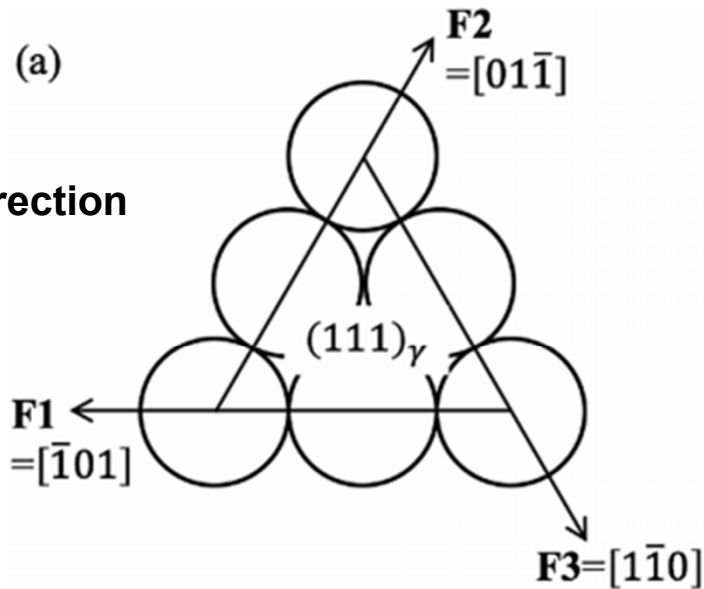
FIGURE 6.4 Schematic representation of lath martensite morphology in low-carbon alloys and steels.

- **변태전 γ 결정립은 Packet으로 분리** - 이 안에 모든 Lath는 $\{111\}$ 면 변형에 의한 K-S 방위관계 따라서, 한 Packet에는 V1-V6 의 6 개의 이형 (Variant)이 존재 (next page)
- 저탄소 합금이나 저탄소강의 경우, 패킷은 블록으로 나뉘지며, 각 블록에 있는 모든 Lath는 V1과 V4 같이 서로 근접한 방위를 갖는 이형들로 구성되어 있으며, **블록 내의 같은 이형 모임을 Sub-block**이라고 함. Lath의 habit plane은 서브블록마다 어느정도는 변할 수 있음.
- **Sub-block 내 Lath**의 방위는 4° 이하에서 변할 수 있으며, 이들 **Lath 사이의 경계는 소경각 입계**가 됨. **블록간의 경계면**은 조밀면에 평행하게 유지하려 하며, 따라서 **$49.5-70.5^\circ$ 범위의 고경각입계**를 이룸

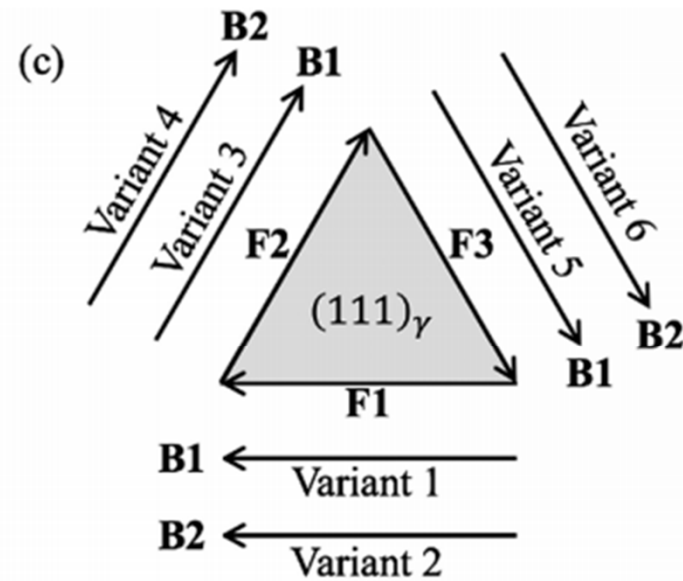
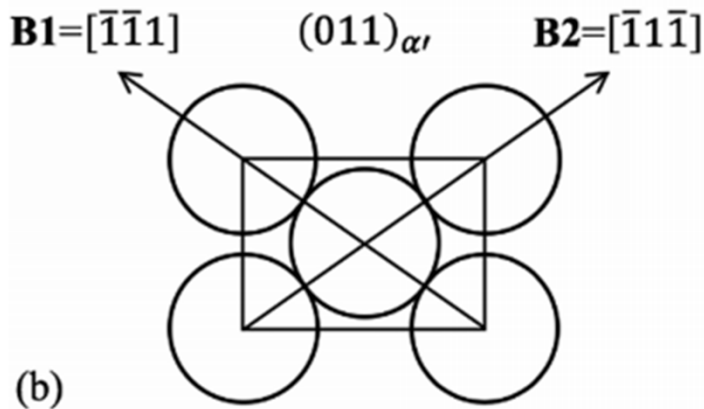
고탄소 합금의 경우, 패킷과 블록의 크기가 감소, 저탄소 합금에 비해 작으며, 각각의 블록은 단 한가지의 방위 이형 (Variant)을 가짐.

모상 γ 의 결정립 크기가 감소하면 패킷과 블록의 크기가 감소.

Close packed direction
fcc 3개



bcc 2개



총 6가지 조합

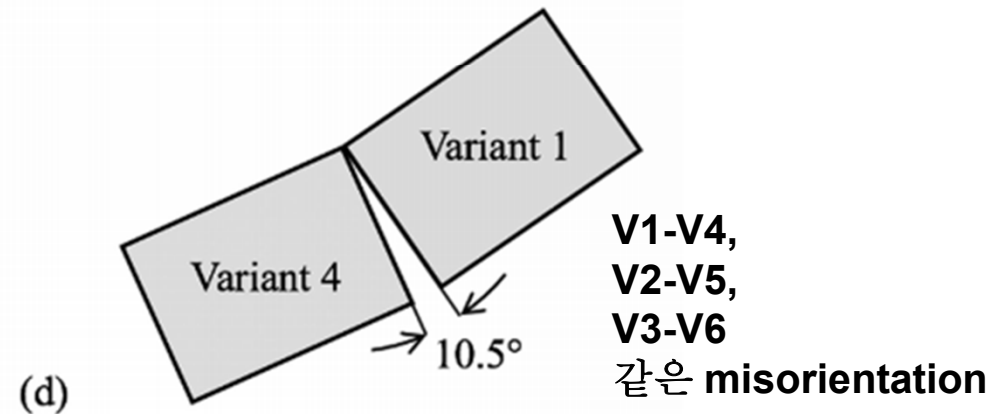


FIGURE 6.6 Variants of the Kurdjumov–Sachs orientation relationship for one close-packed austenite plane $(111)_\gamma$. (a) Atomic arrangement and the three close-packed directions on $(111)_\gamma$. For brevity, the symbols F1, F2 and F3 are used in place of the Miller indices (F meaning fcc). (b) The two close-packed directions in a $(011)_{\alpha'}$ plane abbreviated to B1 and B2 (B meaning bcc). (c) The six ways of aligning the close-packed directions in the two lattices giving six orientation variants. (d) $(011)_{\alpha'}$ sections through the bcc unit cells for variants 1 and 4 showing that there is only a 10.5° rotation about $[011]_{\alpha'}$. The same misorientation exists for the corresponding variant pairs V2-V5 and V3-V6.

EBSD image = 블록간의 경계 (고경각입계)

K-S 방위관계 가정/ Lath 방위데이터 고려시
변태전 γ 결정립계 분석 가능

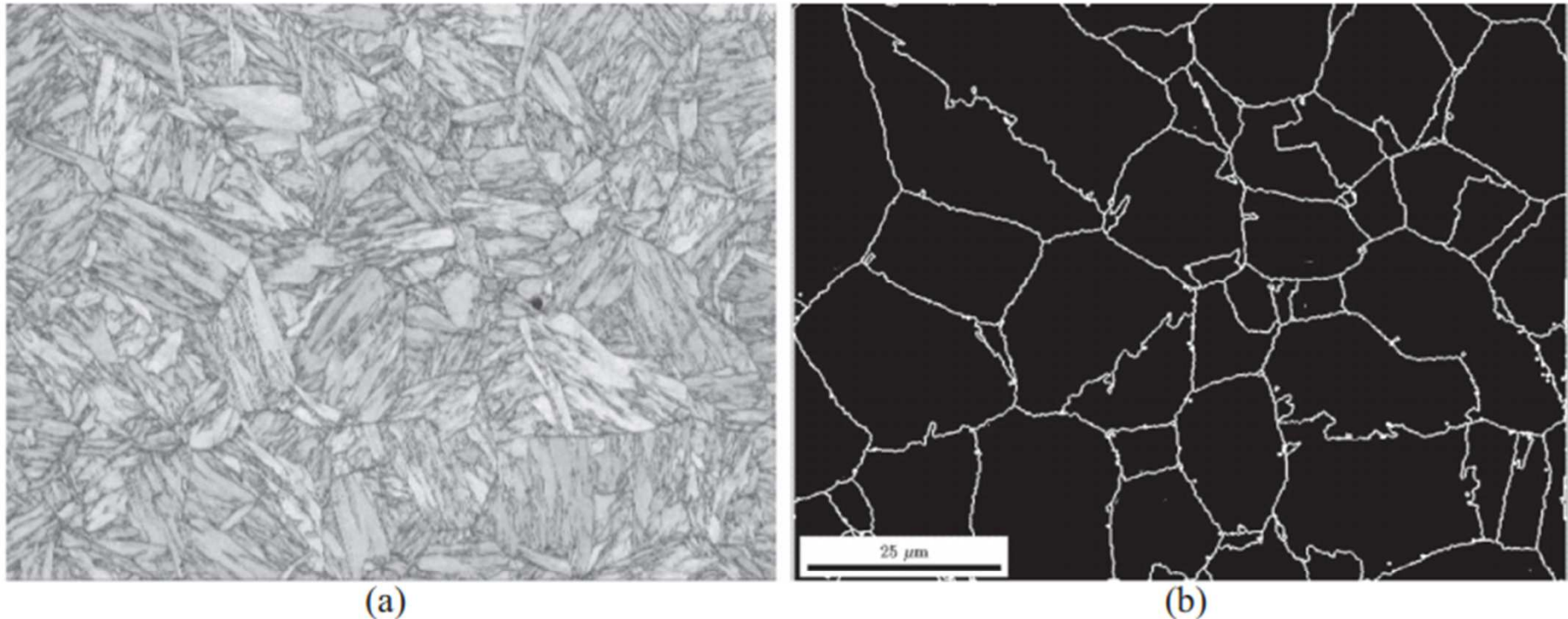


FIGURE 6.7 Lath martensite in a steel containing 0.13C–0.7Si–1.7Mn–0.3Cr. (a) Scanning electron backscattered diffraction band contrast image showing block structure. (b) Prior austenite grain boundaries reconstructed from the pixel orientation data assuming a K–S orientation relationship. Note that the jaggedness of some boundaries is due to misindexing of the diffraction patterns near the boundaries. Courtesy of Shashank Ramesh Babu and Matias Jaskari.

6.2.2 Plate Martensite : Thin plate and Lenticular plate martensite

(c) Thin plate M : 상온 이하 낮은 온도의 M_s 를 가지는 경우, 쌍정으로 이루어진 얇은 판상 형성 $\{259\}_\gamma$ 또는 $\{3\ 10\ 15\}_\gamma$ *habit plane*에 평행하게 배열

M과 γ 의 방위관계는 **K – S**와 **N – W** 관계의 중간에 해당하는 **G – T** 방위관계

M에 접한 γ 는 탄성변형만 받고 있음, 이 탄성변형장의 깊이는 **M** 두께의 **10** 배

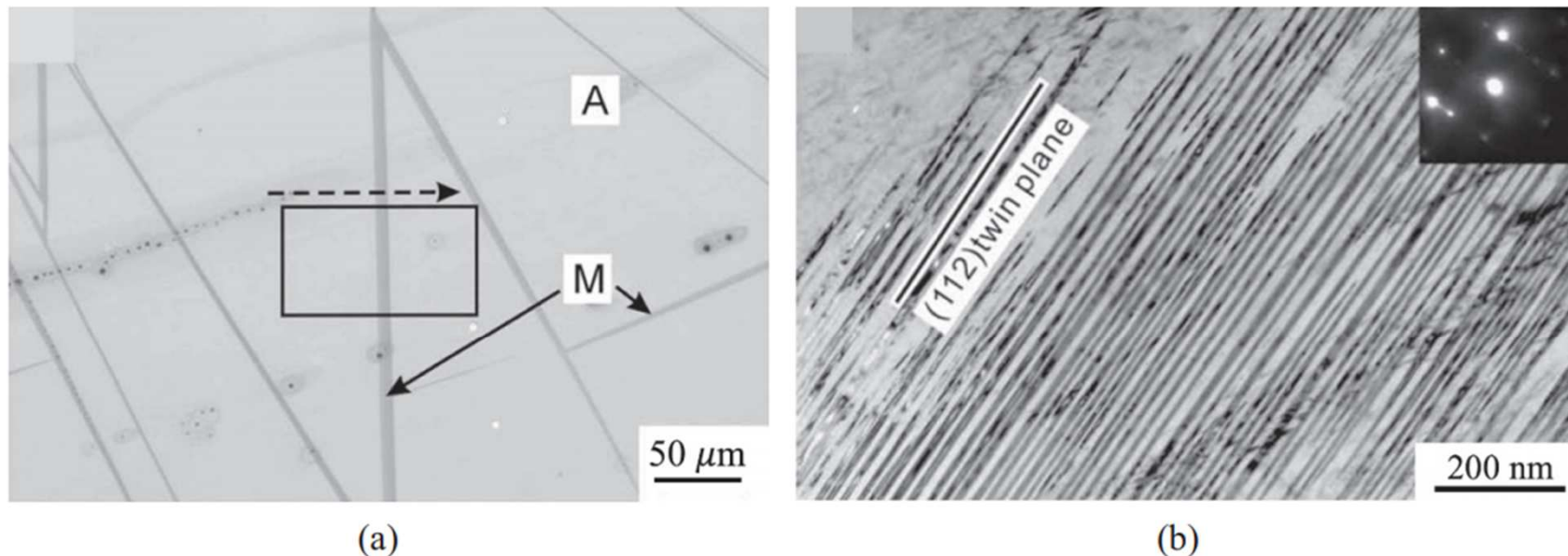


FIGURE 6.8 (a) Thin plate martensite formed by cooling an Fe–30Ni–0.4C alloy (wt.%) to just below its M_s temperature (77 K, -196°C). Scanning electron microscope image. Boxed area used for strain measurements. (Reprinted from *Acta Materialia*, Vol. 57, G. Miyamoto, A. Shibata, T. Maki, T. Furuhashi, Precise measurement of strain accommodation in austenite matrix surrounding martensite in ferrous alloys by electron backscatter diffraction analysis, 1120–1131 (2009),¹¹ with permission from Elsevier.) (b) Transmission electron microscopy image of a thin foil specimen showing fine twins as seen in thin plate martensite and the midrib of lenticular martensite. Twin thickness ~ 10 nm and spacing ~ 20 nm. (Reprinted from *Acta Materialia*, Vol. 57, A. Shibata, S. Morito, T. Furuhashi, T. Maki, Substructures of lenticular martensites with different martensite start temperatures in ferrous alloys, 483–492 (2009), with permission from Elsevier.)

(b) Lenticular plate martensite : $M_{s_thin\ plate\ M} < M_{s_LPM} < M_{s_lath\ M}$

초기엔 쌍정으로 이루어진 얇은 판상 M으로 자라다 변태 잠열에 의한 온도 증가로 렌즈모양으로 두꺼워짐.

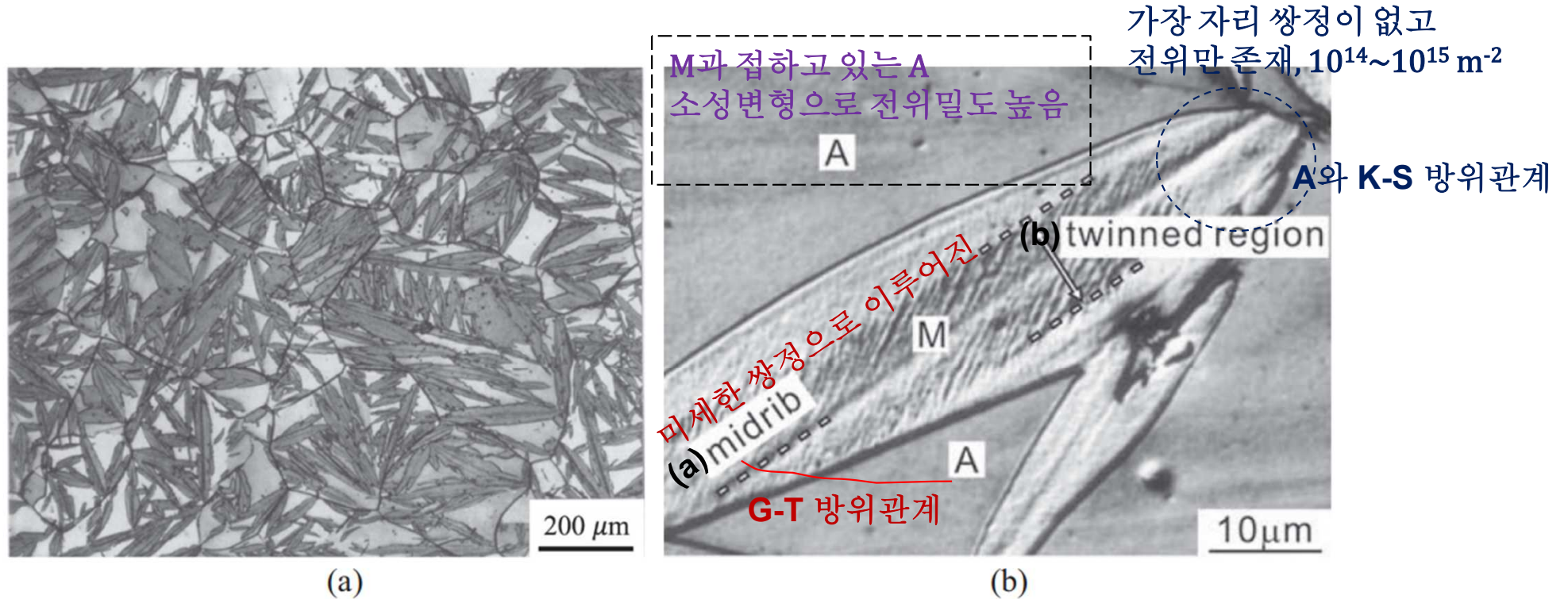


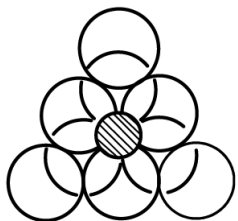
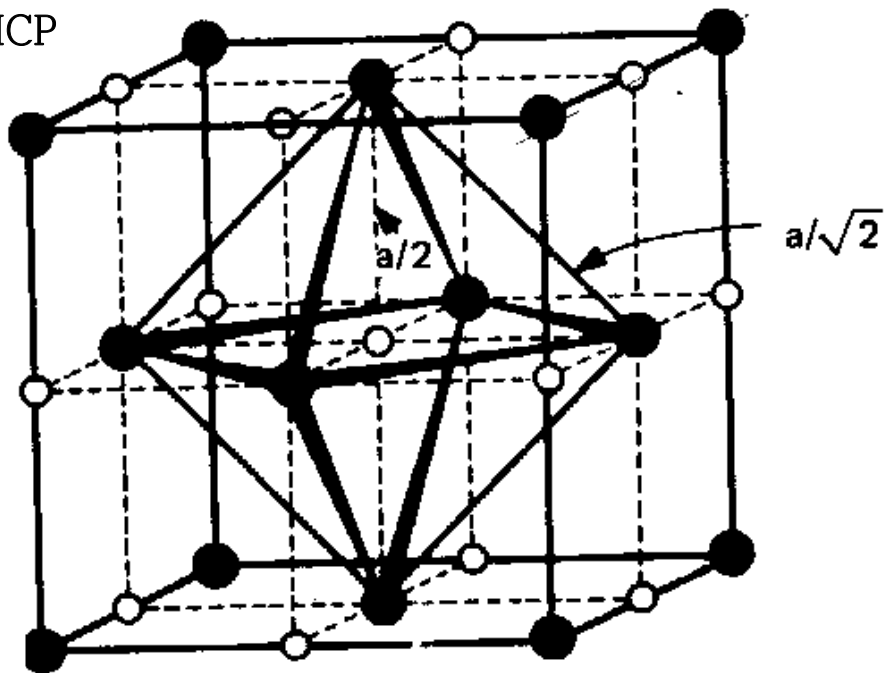
FIGURE 6.9 Examples of lenticular plate martensite. Specimens fully austenitic at room temperature, cooled to below M_s and reheated back to room temperature. Light optical micrographs after polishing and etching. (a) Typical zig-zig pattern. Fe-32.3Ni cooled to 202 K (-71°C) for 150 mins. (Reprinted by permission from Springer Nature Customer Service Centre GmbH: Springer, *Metallurgical and Materials Transactions A*, **23A**:2987–2998, Distributed-activation kinetics of heterogeneous martensitic nucleation, M. Lin, G.B. Olson and M. Cohen (1992).) (b) Detail of the internal structure of a lenticular plate in Fe-33Ni (M_s 171 K, -102°C). A = austenite, M = martensite. (Reprinted from *Acta Materialia*, Vol. 57, A. Shibata, S. Morito, T. Furuhashi, T. Maki, Substructures of lenticular martensites with different martensite start temperatures in ferrous alloys, 483–492 (2009), with permission from Elsevier.)

Q. Crystallography: Why tetragonal Fe-C martensite?

Solid Solution of carbon (or nitrogen) in Iron

Illustrating possible sites for interstitial atoms in the fcc or hcp lattices.

FCC or HCP

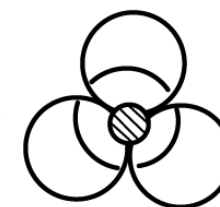
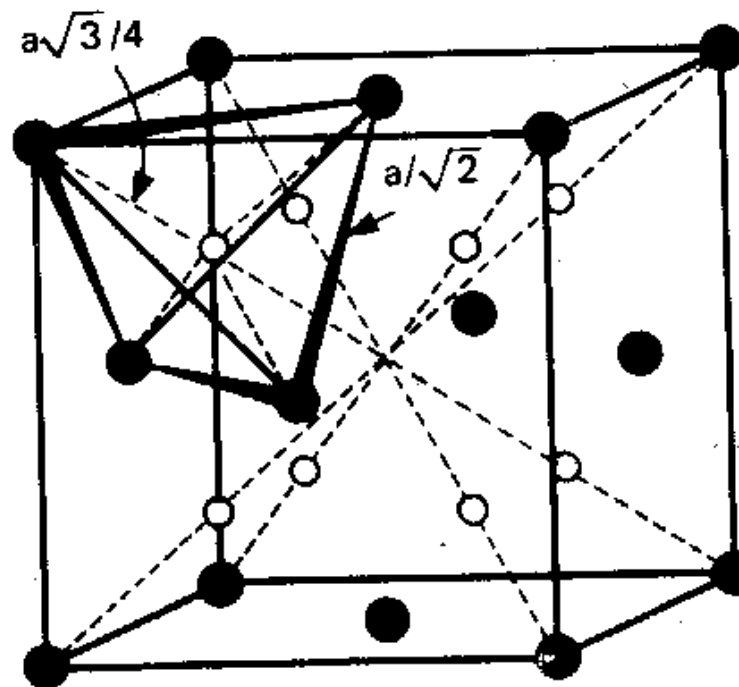


(b) Octahedral

● METAL ATOMS

○ OCTAHEDRAL INTERSTICES

8면체 공극



(a) Tetrahedral

● METAL ATOMS

○ TETRAHEDRAL INTERSTICES

4면체 공극

Six nearest neighbors/ $d_6 = 0.414D = 1.044 \text{ \AA}$ surrounded by four atoms/ $d_4 = 0.225D = 0.568 \text{ \AA}$

D is the diameter of the parent atoms/ d_4 and d_6 are the maximum interstitial diameters

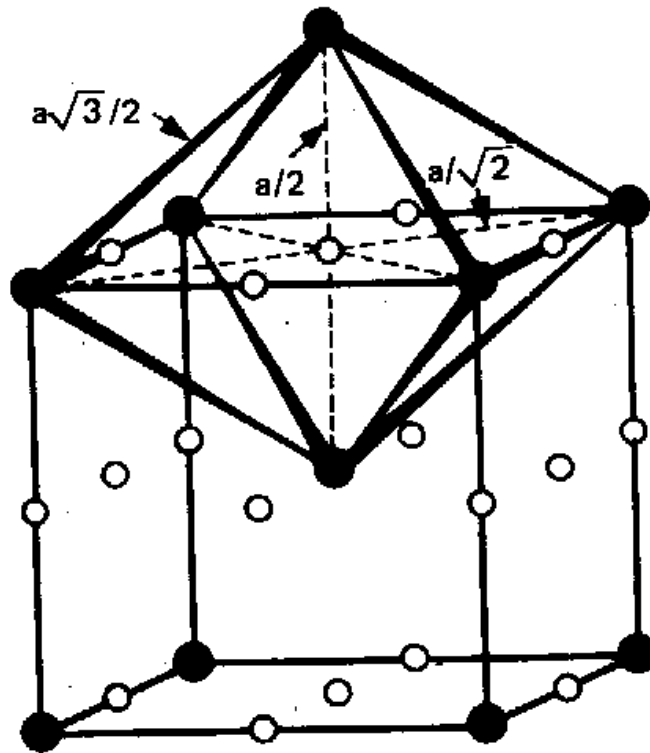
Diameter of a carbon atom: 1.54 \AA

: This means that **considerable distortion** of the γ austenite lattice must occur to contain carbon atoms in solution and that the **octahedral interstices should be the most favorable**.

Solid Solution of carbon (or nitrogen) in Iron

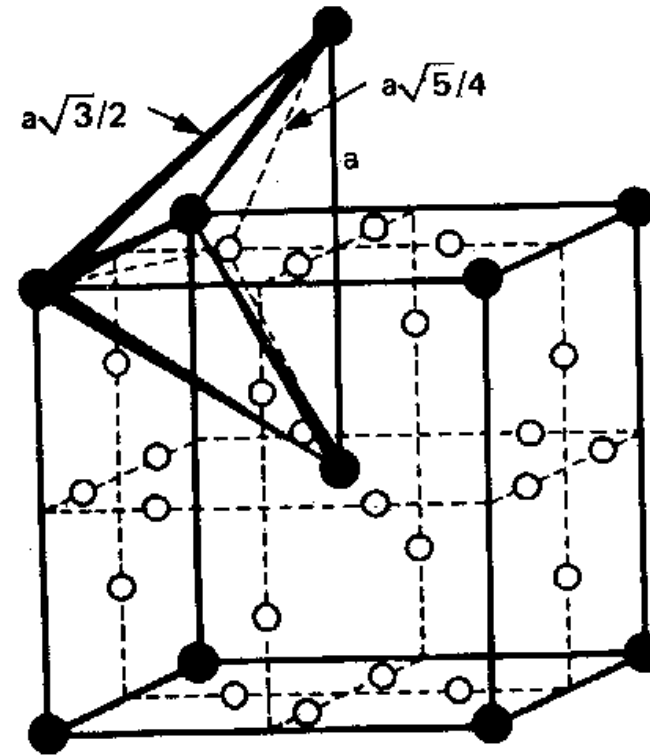
Figure. Illustrating possible sites for interstitial atoms in the bcc lattices.

BCC



● METAL ATOMS
○ OCTAHEDRAL INTERSTICES

Three possible octahedral positions/
 $d_6 = 0.155D = 0.38 \text{ \AA}$



● METAL ATOMS
○ TETRAHEDRAL INTERSTICES

Six possible tetrahedral spaces/
 $d_4 = 0.291D = 0.733 \text{ \AA}$

D is the diameter of the parent atoms/ d_4 and d_6 are the maximum interstitial diameters

Free space: FCC < BCC but space available per interstitial: FCC > BCC

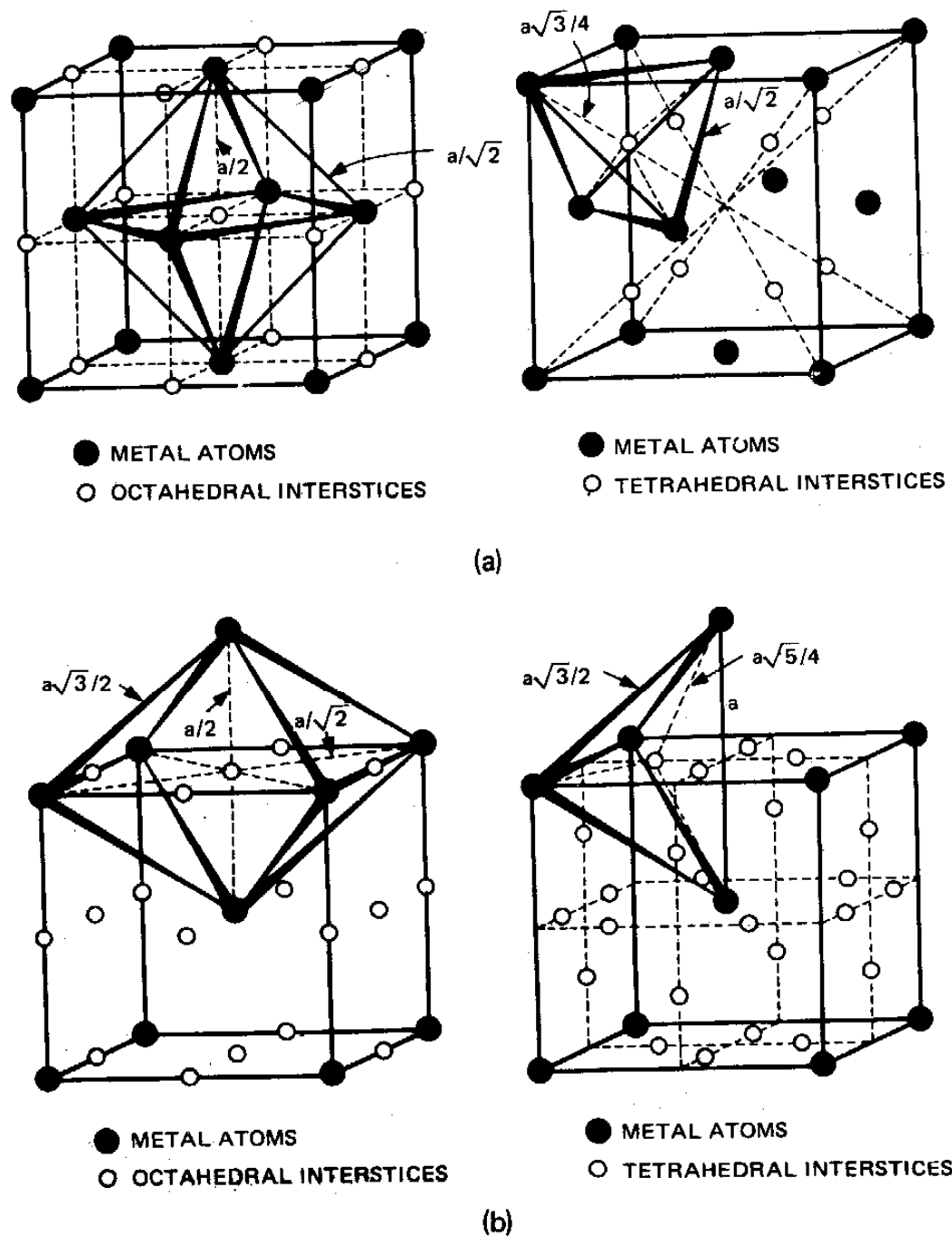
* In spite of $d_6 < d_4$, C & N prefer to occupy the octahedral positions in BCC.

→ required considerable distortion but <100> directions~weaker due to the lower number of near and next nearest neighbors compared to the tetrahedral interstitial position

Interstitial sites for C (or N) in Fe

fcc:
carbon occupies the **octahedral sites**

bcc:
carbon occupies the **octahedral sites**



[Leslie]

Figure II-1. Interstitial voids in iron. (a) Interstitial voids in the fcc structure, octahedral (1) and tetrahedral (2). (b) Interstitial voids in the bcc structure; octahedral (1) and tetrahedral (2). (From C.S. Barrett and T.B. Massalski, *Structure of Metals*, 3d ed., copyright 1966, used with the permission of McGraw-Hill Book Co., New York.)

6.2.3 마르텐사이트의 정방성 (Tetragonality)

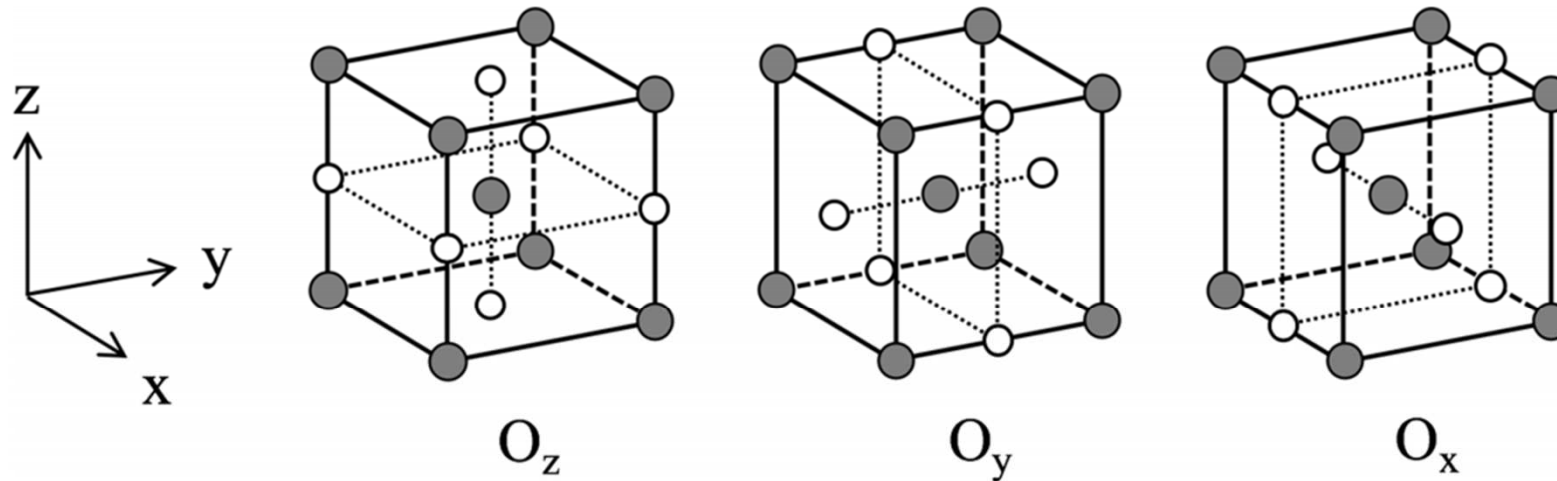


FIGURE 6.11 Types of octahedral sites in a bcc metal (open circles) designated according to the location of the nearest atoms (filled circles). Only a fraction of the sites become occupied by carbon atoms.

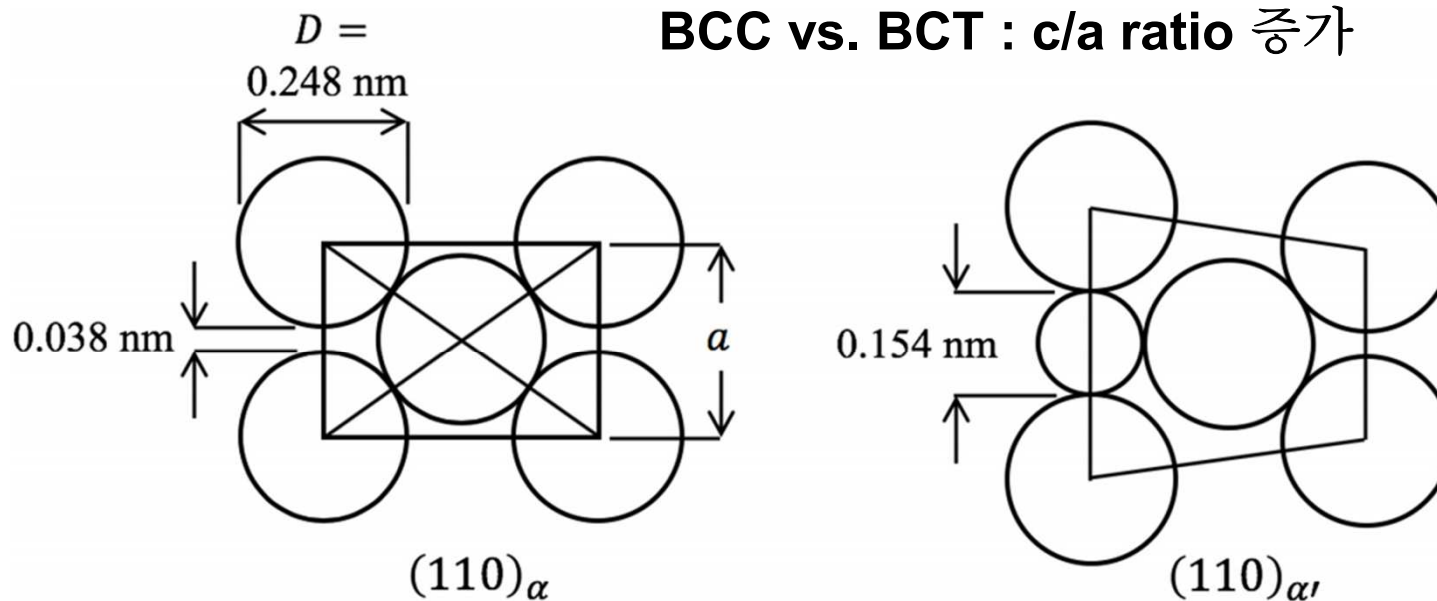


FIGURE 6.12 Hard sphere representation of bcc iron atoms as seen on a (110) plane and the distortion caused by the insertion of a carbon atom into an octahedral interstice.

Carbon in BCC α ferrite

- One consequence of the occupation of the octahedral site in ferrite is that the carbon atom has only two nearest neighbors.
- Each carbon atom therefore distorts the iron lattice in its vicinity.
- The distortion is a tetragonal distortion.
- If all the carbon atoms occupy the same type of site then the entire lattice becomes tetragonal, as in the martensitic structure.
- Switching of the carbon atom between adjacent sites leads to strong internal friction peaks at characteristic temperatures and frequencies.

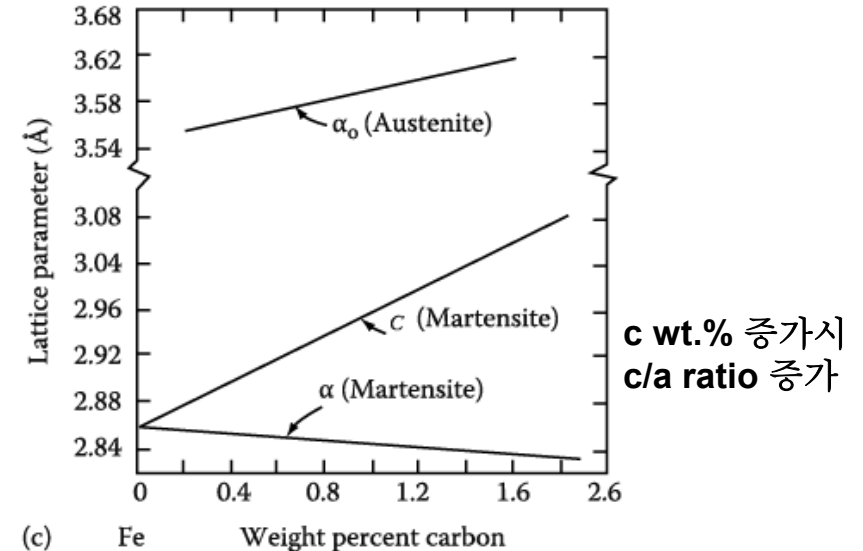
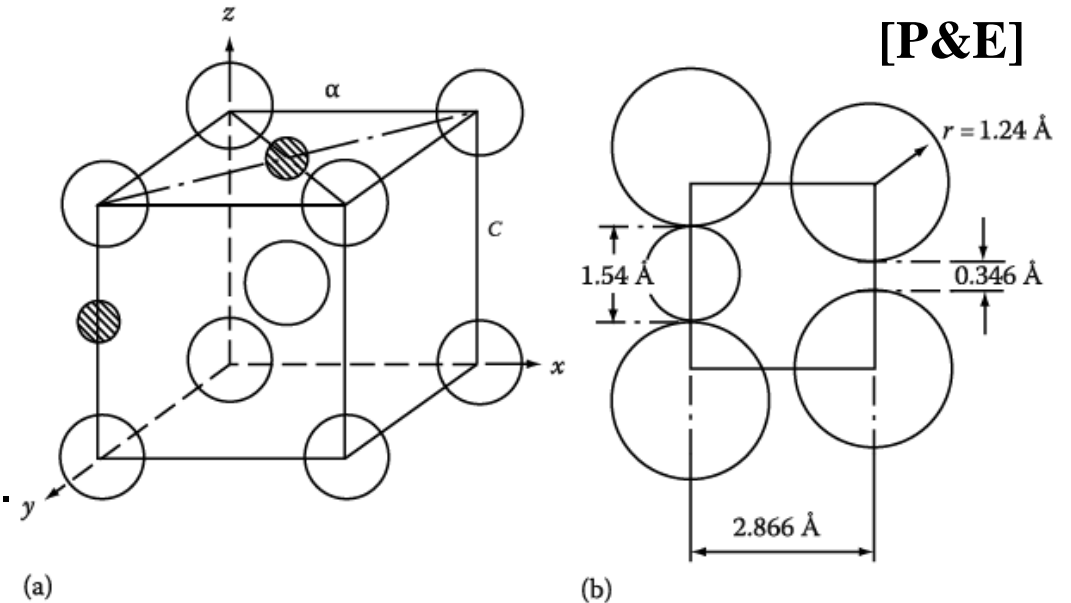


Fig. 6.5 Illustrating (a) possible sites for interstitial atoms in bcc lattice, and (b) the large distortion necessary to accommodate a carbon atom (1.54 \AA diameter) compared with the space available (0.346 \AA). (c) Variation of a and c as a function of carbon content.

Why tetragonal Fe-C martensite?

- At this point, it is worth stopping to ask why a tetragonal martensite forms in iron. The answer has to do with the preferred site for carbon as an interstitial impurity in bcc Fe.
- Remember: Fe-C martensites are unusual for being so strong (& brittle). Most martensites are not significantly stronger than their parent phases.
- Interstitial sites:
 - fcc: octahedral sites radius= 0.052 nm
tetrahedral sites radius= 0.028 nm
 - bcc: octahedral sites radius= 0.019 nm
tetrahedral sites radius= 0.036 nm
- Carbon atom radius = 0.08 nm.
- Surprisingly, it occupies the octahedral site in the bcc Fe structure, despite the smaller size of this site (compared to the tetrahedral sites) presumably because of the low modulus in the <100> directions.

6.2.4 Epsilon (ϵ) Martensite

γ 의 SFE (적층결함 E) 낮은 합금강 $\rightarrow \epsilon$ (hcp)이 안정상

e.g. 스테인리스강/Co 합금: M_s 이하 ϵ M 생성

대부분 ϵ M 소성변형의 결과로 생성

\rightarrow Transformation induced plasticity (TRIP): 고강도 고연신

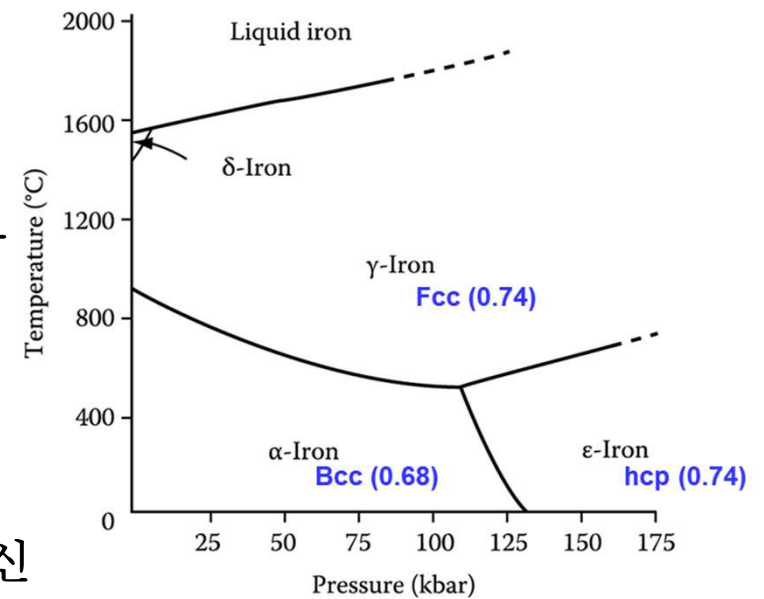
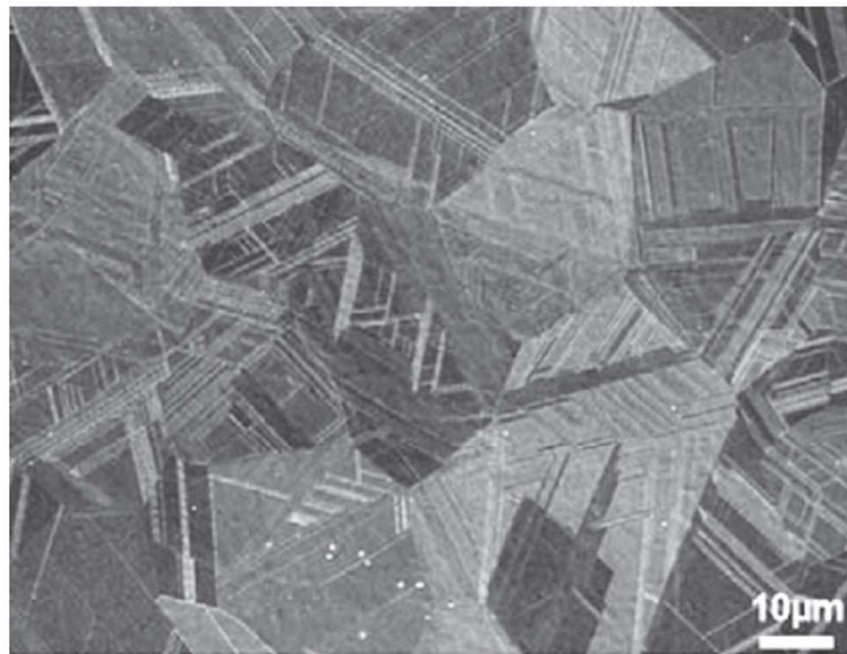
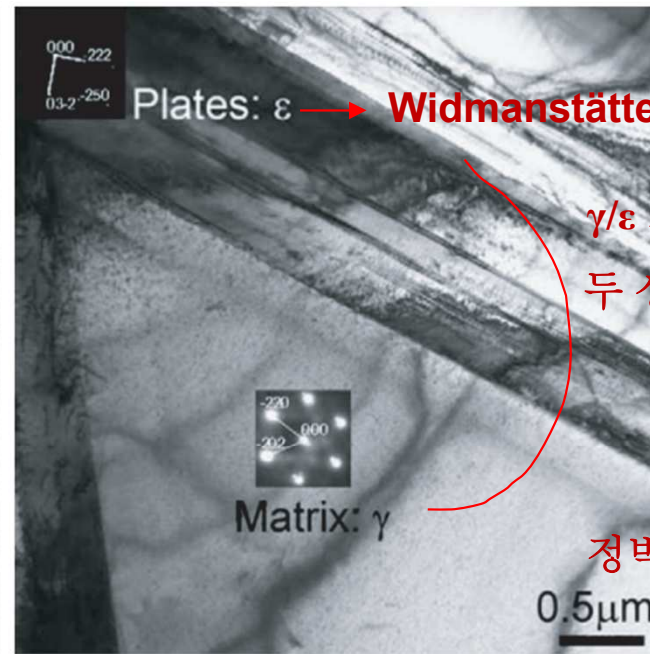


Fig. 1.5 Effect of pressure on the equilibrium phase diagram for pure iron



(a)



(b)

Plates: $\epsilon \rightarrow$ Widmanstätten 조직

γ/ϵ 계면은 완전정합

두 상에서 조밀방향이 서로 평행

$$\{0001\}_{\epsilon} \parallel \{111\}_{\gamma}$$

$$\langle 11\bar{2}0 \rangle_{\epsilon} \parallel \langle 110 \rangle_{\gamma}$$

정벽면은 불변면 변형을 함
(invariant plane strain)

FIGURE 6.16 Epsilon martensite in Fe-24Mn-0.02C alloy after air cooling austenite from 900°C. (a) Scanning electron micrograph showing ϵ -martensite plates in a Widmanstätten pattern in equiaxed austenite grains. (b) Higher magnification transmission electron microscope image showing cross-sections through the ϵ plates.

6.3 Mechanical Twinning in BCC Metals : 기계적 쌍정 vs M 변태

bcc 금속의 경우, 소성변형이 저온에서 일어나거나 또는 높은 변형속도로 변형될 때 **deformation twin**이 생성, 이 변형 쌍정은 **M** 변태와 유사성을 띤. 쌍정 변형의 구동력은 역학 **E** (화학 **E** 아님)이고 결정구조 동일, **glissile interface**의 이동에 의해 일어남

bcc 금속의
적층구조

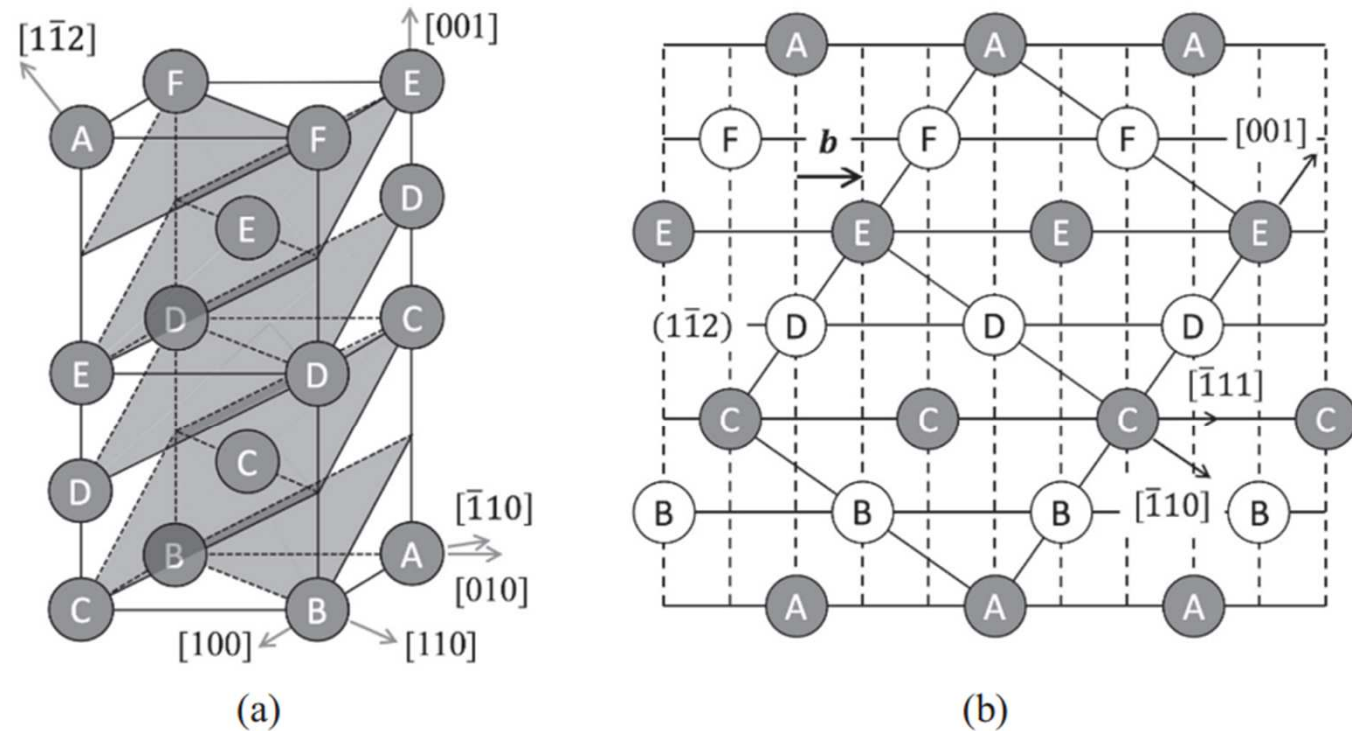


FIGURE 6.17 Stacking sequence in bcc lattice. (a) Two unit cells with shaded $(1\bar{1}2)$ planes. (b) The arrangement of the same lattice points on two (110) planes.

21

bcc 격자는 ABCDEFAB의 순서로 $(1\bar{1}2)$ 면이 적층, 벡터 b 는 $\frac{a}{6}[\bar{1}11]$ 의 크기와 방향 가짐

bcc 금속에서 전단변형에 의한 mechanical twinning: glide twin

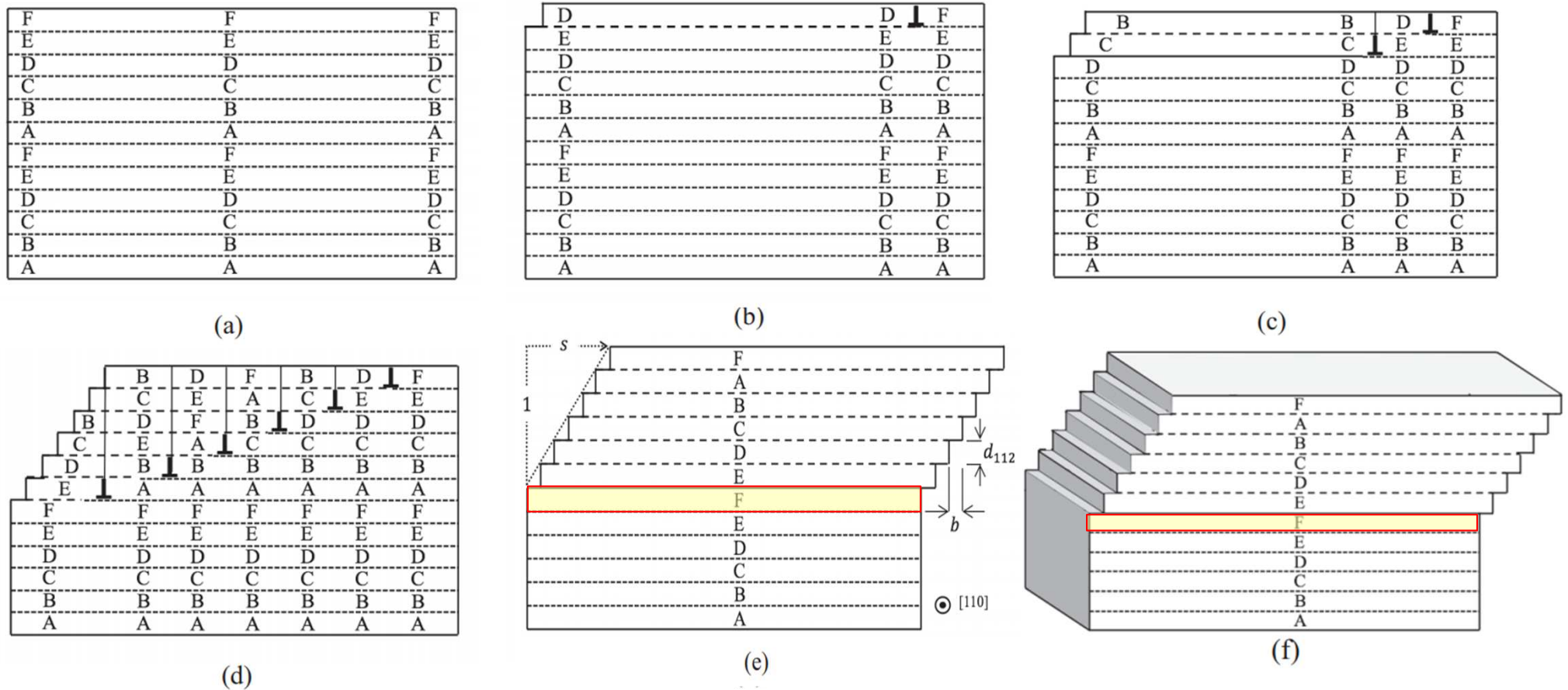


FIGURE 6.18 Twinning in a bcc crystal caused by the passage of an $\frac{a}{6}[\bar{1}11]$ partial dislocation over every $(1\bar{1}2)$ plane. (a) Bcc lattice represented as $(1\bar{1}2)$ layers of lattice points stacked in the sequence ABCDEF, etc. The direction $[110]$ is out of the plane of the figure. (b) A partial dislocation has passed through the lattice between the top two layers of atoms. In the area swept by the dislocation, lattice points in the top layer are shifted by the Burgers vector relative to their original positions, i.e., $F \rightarrow D$. (c) When a partial dislocation passes beneath the second layer, lattice points in that layer change from positions E to C and in the layer above from positions D to B. (d) As more partial dislocations pass between successive layers the following changes occur $A \rightarrow E$, $B \rightarrow F$, $C \rightarrow A$, $D \rightarrow B$, $E \rightarrow C$, $F \rightarrow D$. (e) All the partial dislocations have passed through the crystal leaving a twin in the top half, i.e., there is mirror symmetry in the stacking sequence relative to the middle F layer. The twinning shear $s = b/d_{112} = 0.71$. (f) Perspective view of (e).

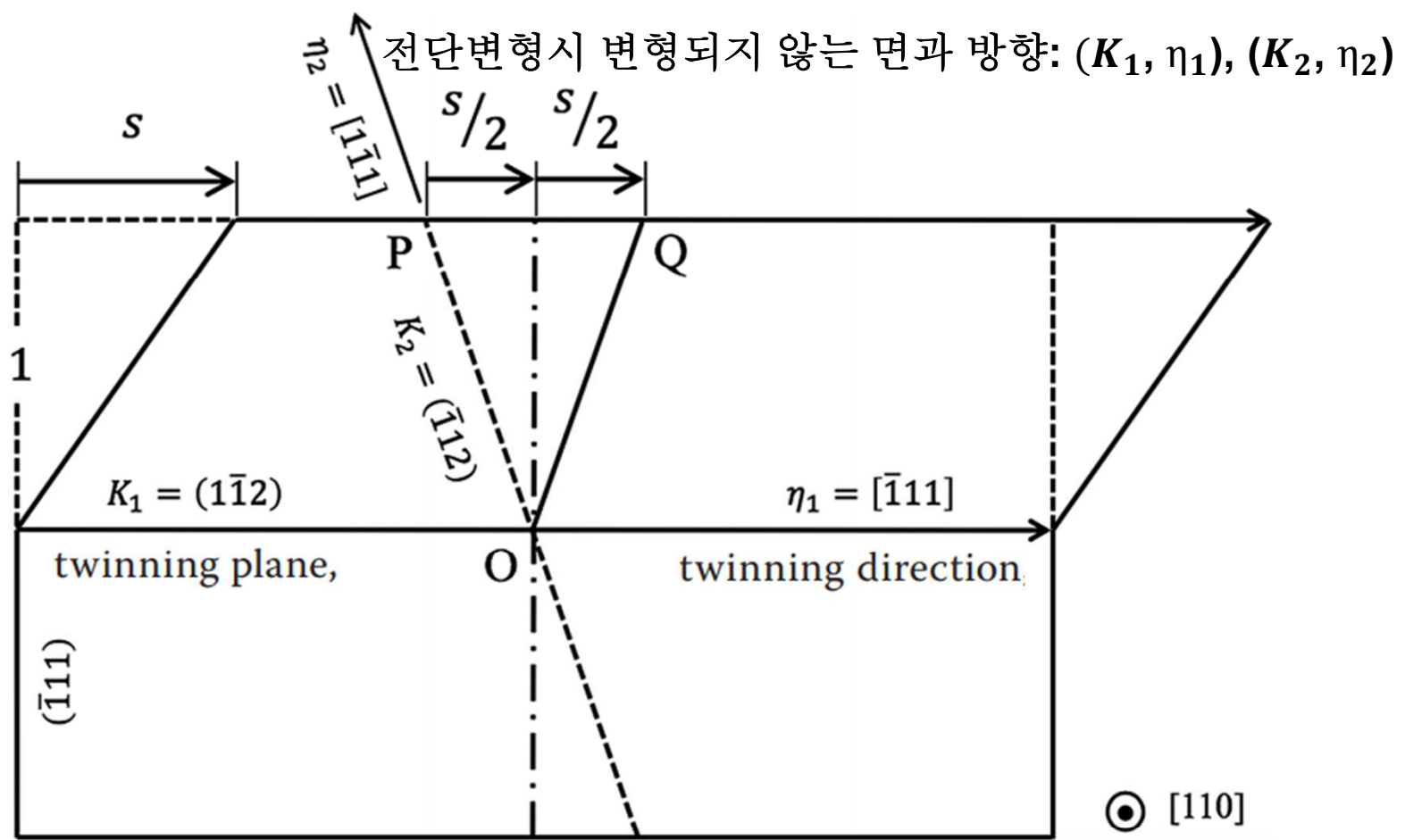


FIGURE 6.19 Glide twinning. Plane of the diagram (plane of shear) is (110) . The twinning plane, K_1 , is $(1\bar{1}2)$. The twinning direction, η_1 , is $[\bar{1}11]$. K_1 is invariant, i.e., undistorted and unrotated, and it is fully coherent. K_2 is undistorted, but rotated, so not invariant. Other planes are distorted by the glide twinning. $s = 0.71$.

- * 기계적 쌍정 vs M 변태 : 부분 전위로 이루어진 활주계면 포함/ 불변면 변형 발생함 유사, but
- (a) 쌍정은 외부에서 가한 전단응력에 의해 발행, M 변태 구동력은 두 상 사이 화학자유E 차이가 관여
- (b) 쌍정 생성시 결정구조 변화 없음, but M 변태시 결정구조 변화 발생

6.4 Athermal Nucleation and Growth: (a) FCC → HCP ($\gamma \rightarrow \epsilon$ 변태)

① 완전 전위가 두 개의 Shockley 부분 전위쌍으로 분해되고 그 사이에 적층 결함을 형성.

: $\gamma \rightarrow \epsilon$ 변태는 T_0 이하 냉각으로 적층결함 E가 음으로 될 때 부분전위 사이의 폭이 넓어지는 과정

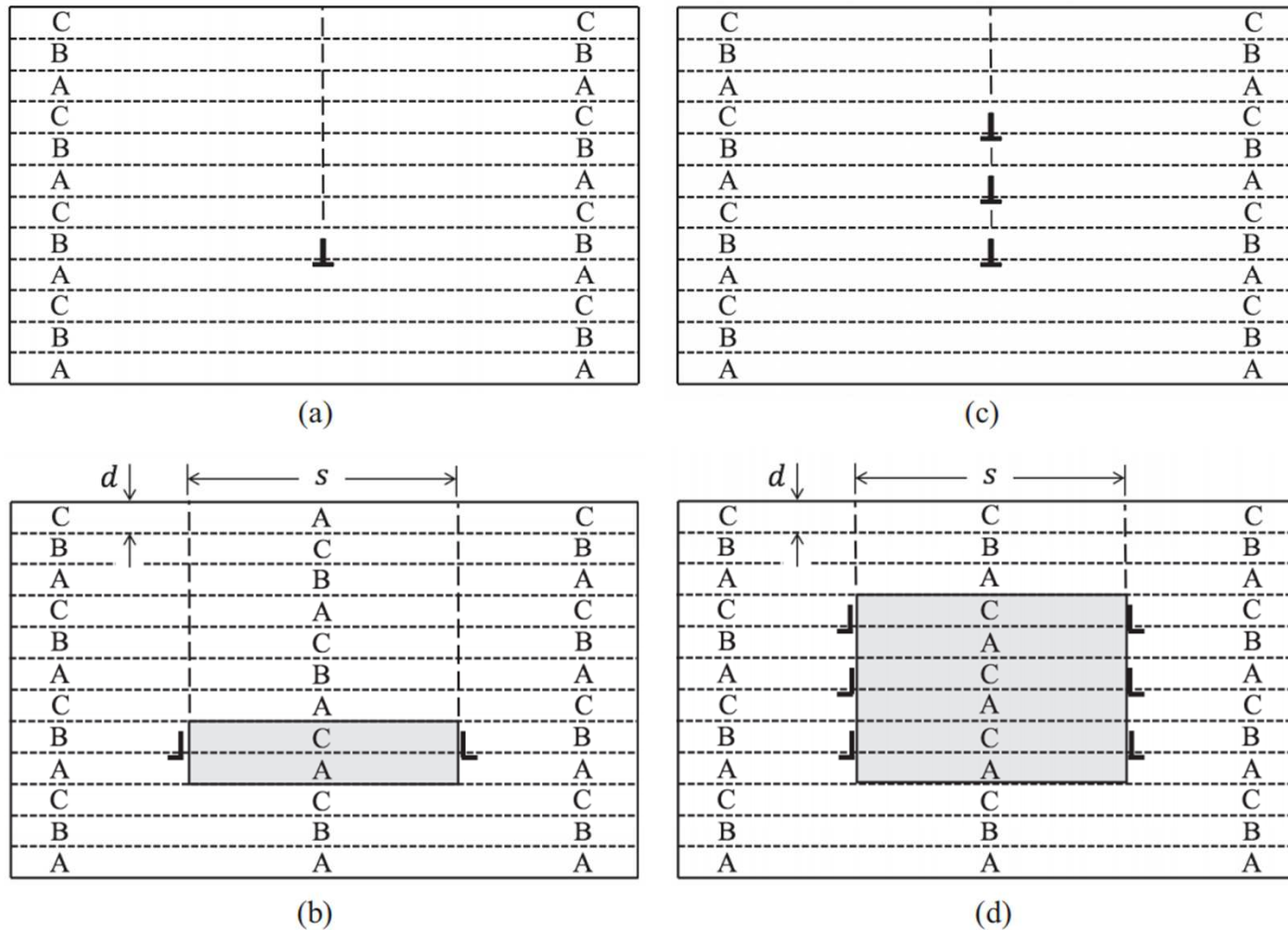


FIGURE 6.20 Schematic diagram showing single and composite intrinsic stacking faults in an fcc lattice. (a) and (c) Perfect dislocations. (b) and (d) Dislocations split into pairs of Shockley partial dislocations separated by stacking faults. In (b) $n = 1$, in (d) $n = 3$.

② 단위면적당 적층결함 $E = \gamma_{sf} = 2nd (\Delta G_{chem}^{\gamma \rightarrow \epsilon} + \Delta G_S) + 2\gamma_i$ (여기서, n = 배열된 전위 개수, d =면간거리)

a) $\gamma \rightarrow \epsilon$ 상변태: $\Delta G_{chem}^{\gamma \rightarrow \epsilon}$, b) 정합 탄성 E: ΔG_S , c) 양쪽의 γ/ϵ 정합 계면에너지: $2\gamma_i$ ($T \uparrow$ 시 일부 감소)

T'_0 아래 온도에서 $(\Delta G_{chem}^{\gamma \rightarrow \epsilon} + \Delta G_S) < 0$ (안정화 시작), 과냉이 커지면 $2\gamma_i$ 와 합산해 음수가 됨

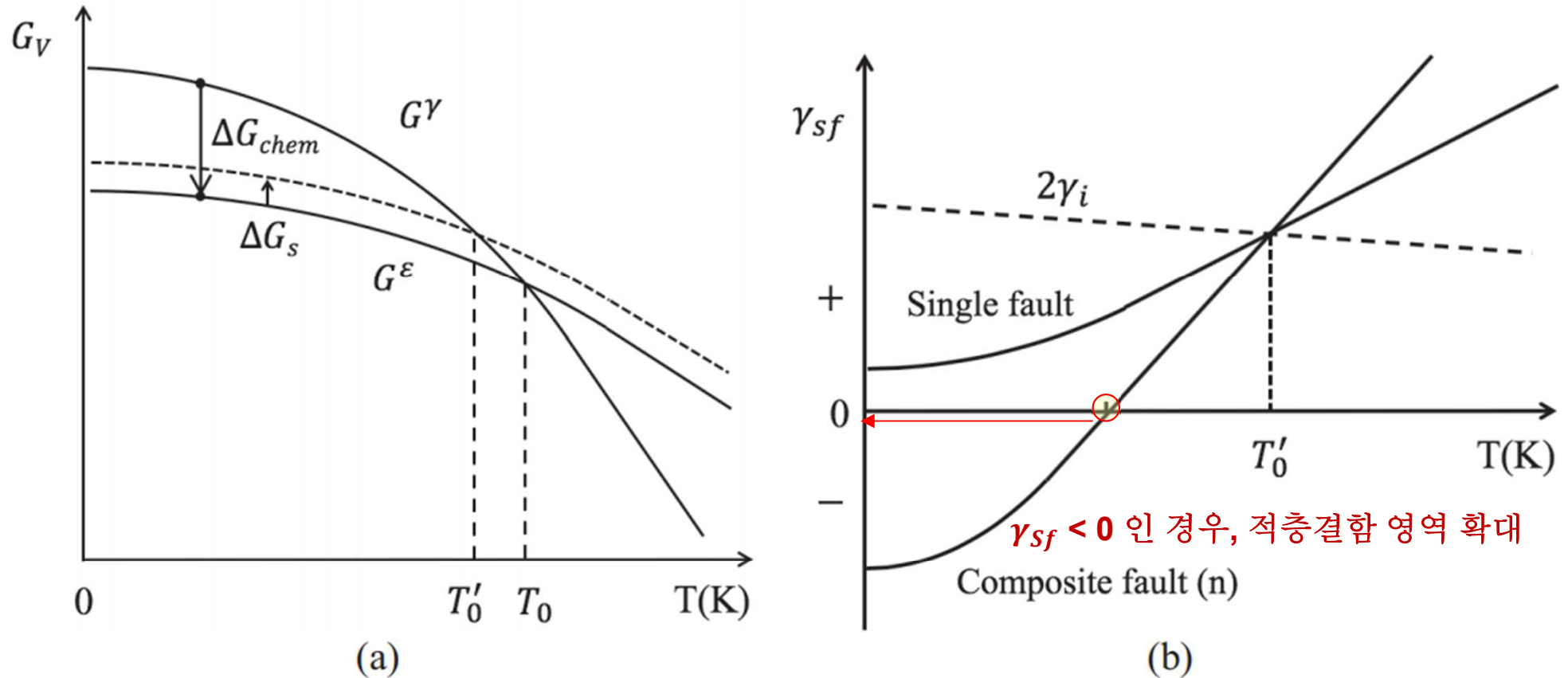


FIGURE 6.21 (a) Schematic variation of the free energy of the fcc γ and hcp ϵ phases vs. absolute temperature. (b) Energy of a single and a composite stacking fault vs. absolute temperature. Composite fault comprises n pairs of partial dislocations.

③ 부분 전위와 적층결함이 계의 에너지에 미치는 영향

ΔG 는 적층결함 평형간격 $s_{eq}(= k\mu b_p^2/\gamma_{sf})$ 에서 최소

$s_{eq}(= k\mu b_p^2/\gamma_{sf})$ 는 γ_{sf} 감소할수록 증가

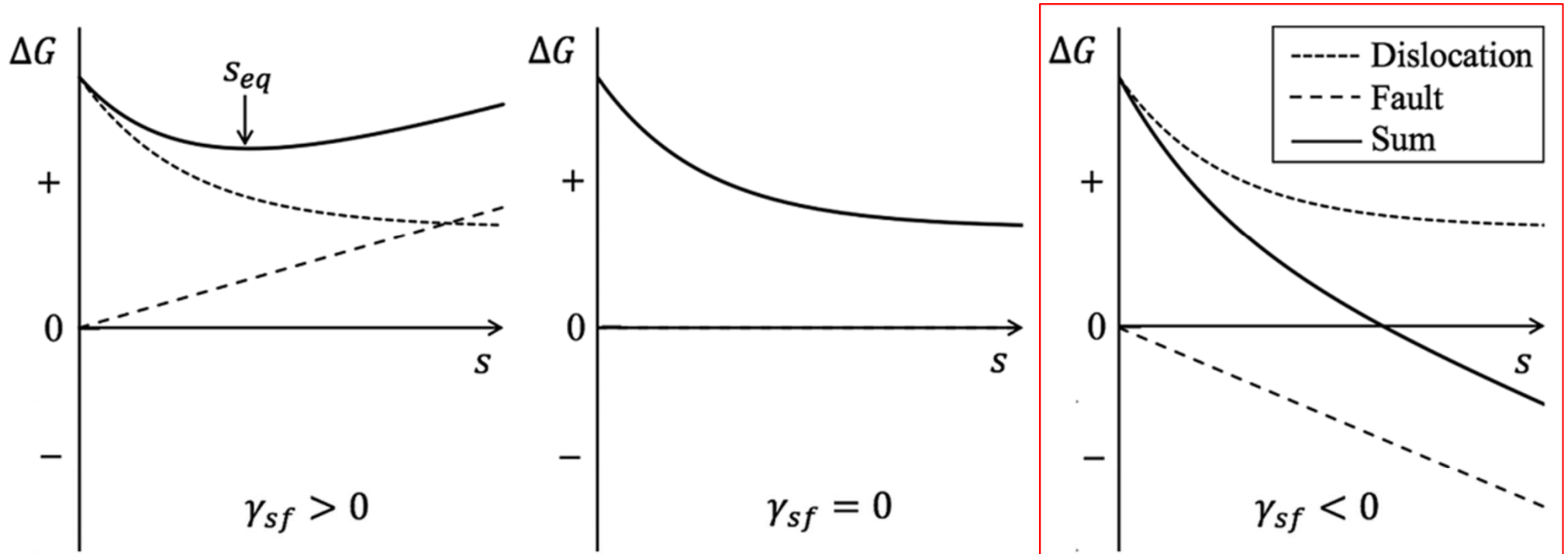


FIGURE 6.22 Schematic diagrams showing the contributions of the partial dislocations and stacking faults in Figure 6.20 to the energy of the system. $\Delta G = 0$ corresponds to the system without dislocations and faults.

부분전위 사이 거리 s
 (적층결함 간격) 증가하면
 계의 에너지도 안정화

전위 주위의 탄성응력장의 상호작용과 적층결함 E 에 의한 전위 사이 작용하는 힘 $F = -d(\Delta G)/ds$ (기울기) 26

④ ϵ Martensite가 핵생성 될 조건 : $-\gamma_{sf} > nF_r$

$\gamma_{sf} < 0 \rightarrow s$ 가 증가할수록 계의 ΔG 가 낮아져도, 전위이동의 저항력 (nF_r)을 극복해야 핵생성 가능

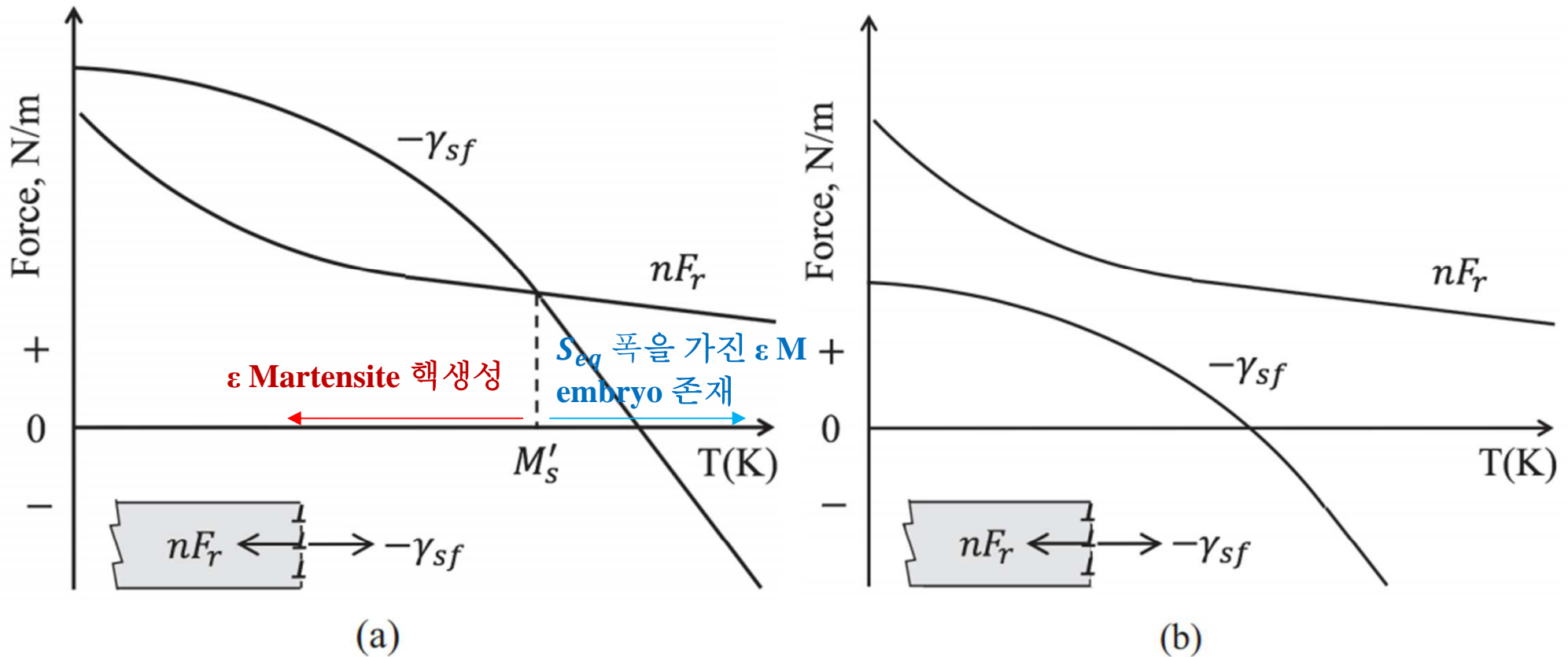


FIGURE 6.23 Forces acting on the edge of a composite fault when the fault energy is negative. $-\gamma_{sf}$ is the positive pulling force and nF_r is the resistance exerted by the atomic matrix. (a) Athermal nucleation is possible when $-\gamma_{sf} > nF_r$, i.e., below M'_s . (b) Athermal nucleation impossible.

nF_r = 격자내 원자들에 의한 전위이동에 대한 저항력 / $-\gamma_{sf}$ = Positive pulling force, S 넓어지도록 당기는 힘.

⑤ ϵ Martensite의 pole mechanism에 의한 Thickening

- : 부분 전위가 풀전위를 만나 풀전위 주위 부분전위가 나선모양으로 돌면서 두께 증가
- : 10원자층 (~2 nm)의 수백 배 두께 (수 백 nm) 성장 가능

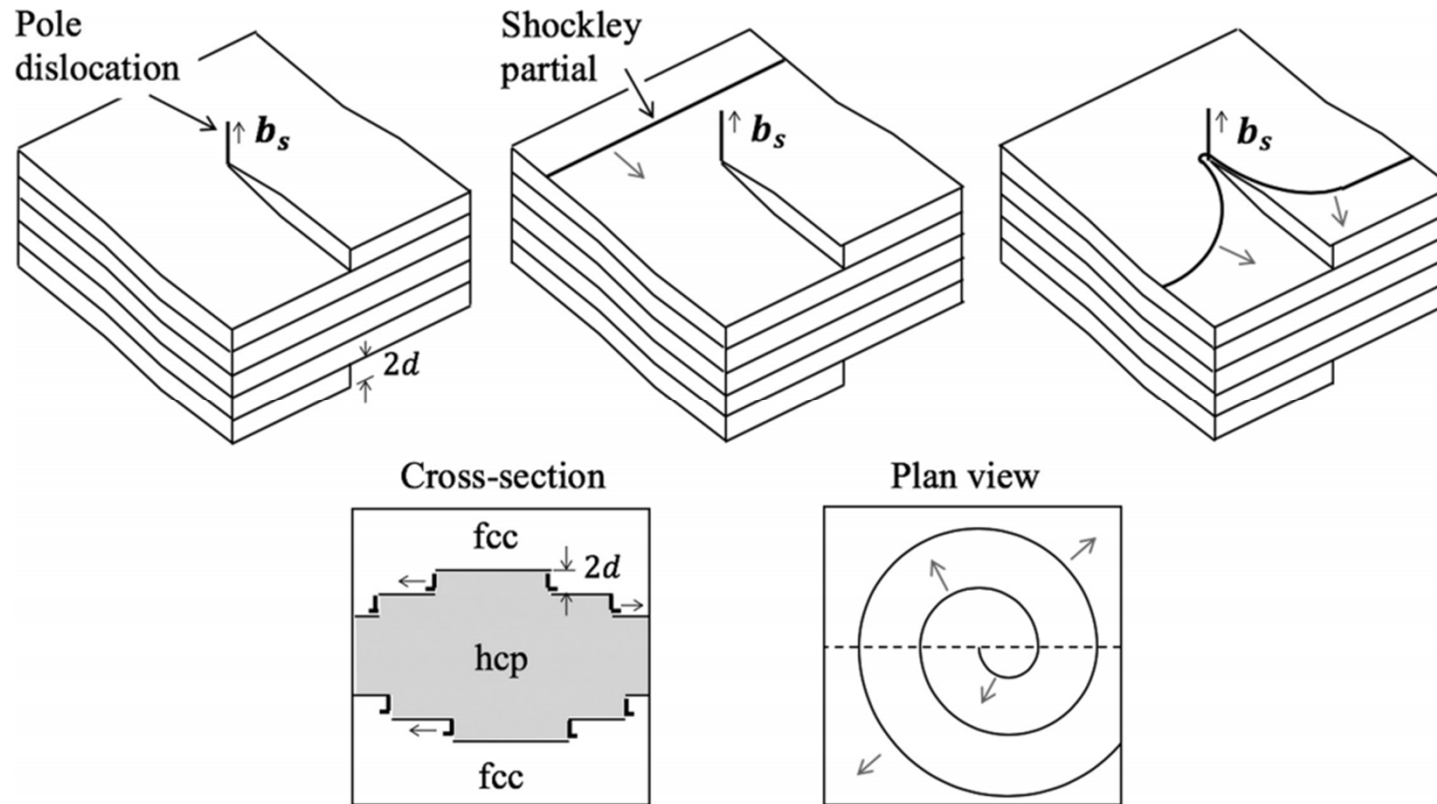


FIGURE 6.24 Thickening of ϵ -martensite via a pole mechanism. Schematic diagram showing only the screw component of the $\frac{a}{2}[112]_{\text{fcc}}$ pole dislocation normal to the $(111)_{\text{fcc}}$ planes, i.e., $b_s = \frac{2}{3}a[111]_{\text{fcc}}$. b_s is equal to two close-packed lattice spacings ($2d_{111}$). As the expanding Shockley partial transformation dislocations in Figure 6.20d encounter and bend around the pole dislocation, they are forced onto the next-but-one glide planes. All but the uppermost and lowermost dislocations in the transformation front cancel each other on meeting behind the pole, but the outermost dislocations begin to spiral around the pole causing “new” partial dislocations to expand across the fcc/hcp interface thereby thickening the ϵ -martensite plate.

⑥ ϵ Martensite 변태시 변형에너지로의 소모 줄이는 방법: 형상 변화 최소화!

: 3가지 다른 Partial D의 Burgers vector 이용한 변형을 통해 Widmanstätten 조직 M 생성

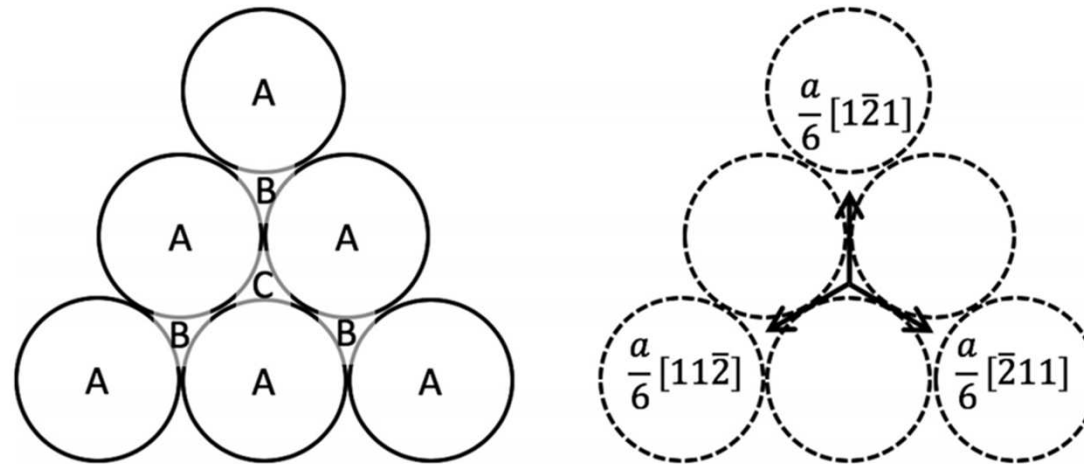


FIGURE 6.25 Three possible Burgers vectors of Shockley partial dislocations that can shift atoms from C-positions to B-positions in a $(111)_{fcc}$ plane.

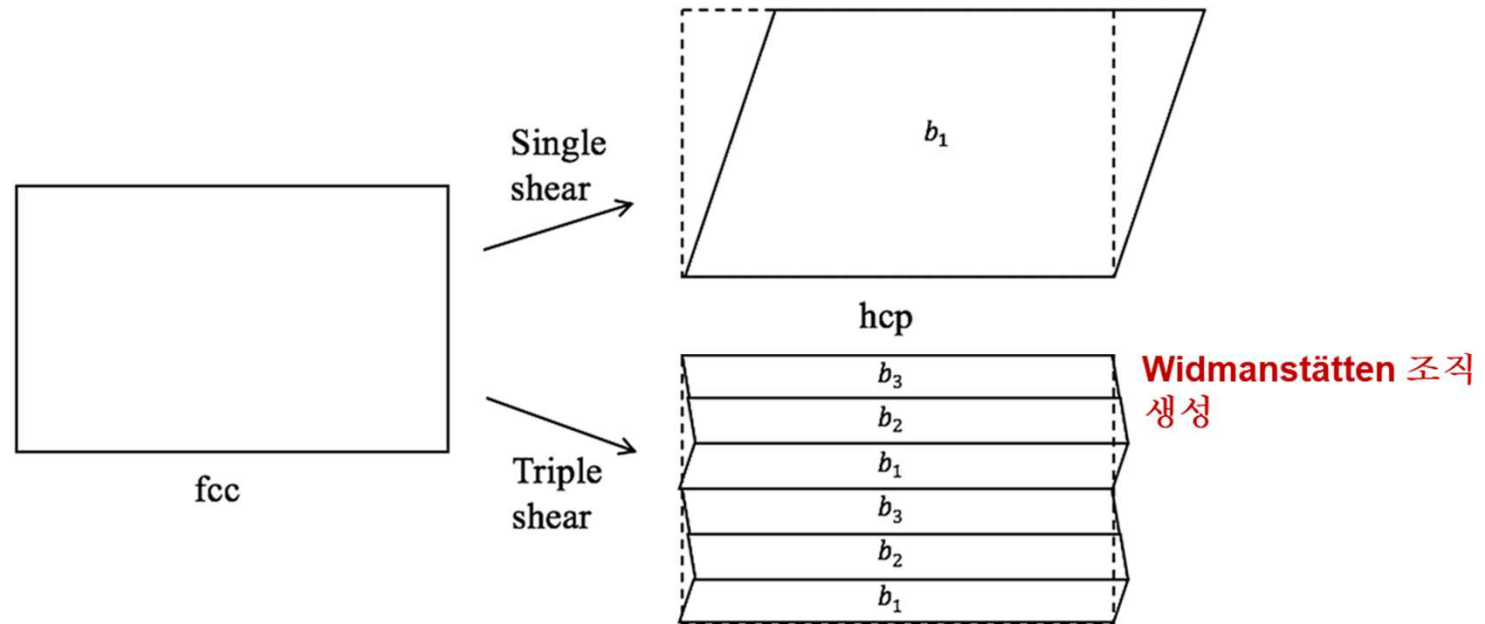


FIGURE 6.26 Strain energy reduction in the fcc \rightarrow hcp transformation by transforming adjacent regions using Shockley partial dislocations with all three possible Burgers vectors.

⑦ 자발촉매 기구에 의한 ϵ Martensite 변태 핵생성 및 성장

: a) 성장하던 판이 입계 등과 충돌하면 그 자리에서 다른 판을 핵생성 시킬 수 있음

b) 온도 M_s 이하로 낮추면 구동력이 약해 성장하지 못했던 embryo 들이 핵으로 성장

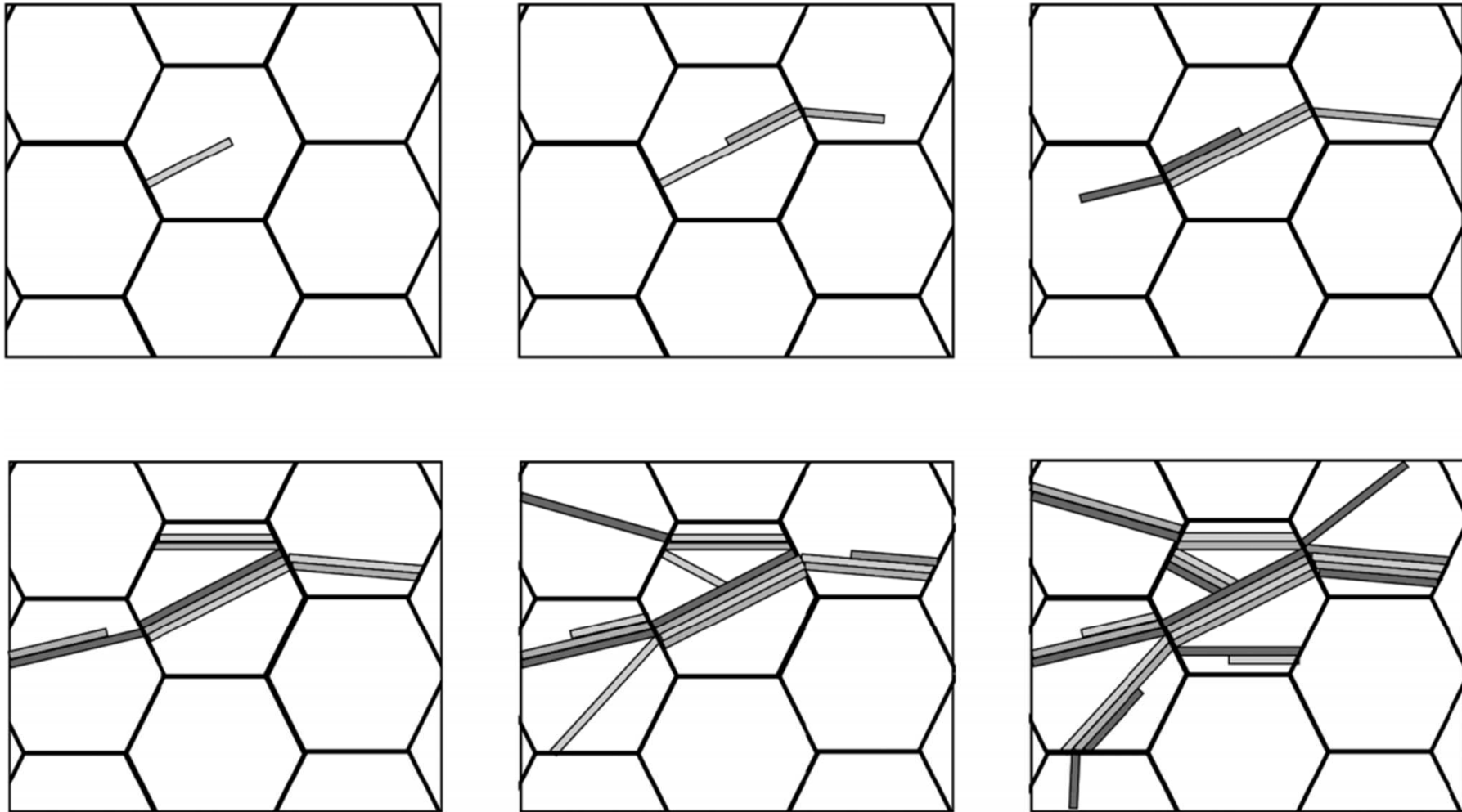


FIGURE 6.27 Series of schematic pictures illustrating autocatalytic nucleation of ϵ -martensite plates at austenite grain boundaries during cooling below M_s . Three shades of grey to show the different possible shears.

6.5 Athermal Nucleation and Growth : (b) FCC → BCC (or BCT) M 변태

: 최인접 원자수가 12 → 8 개로 변화

6.5.1 Atomic movement producing the FCC → BCC/BCT Transformation

- $\gamma \rightarrow \alpha'$:
- (1) Habit plane of M: not distorted by transformation
 - (2) A homogeneous shear (s) parallel to the habit plane
 - (3) ~4% expansion_dilatation normal to the habit plain (lens)

Possible atomic model for martensitic transformation:
the Bain Model: fcc → bct transformation

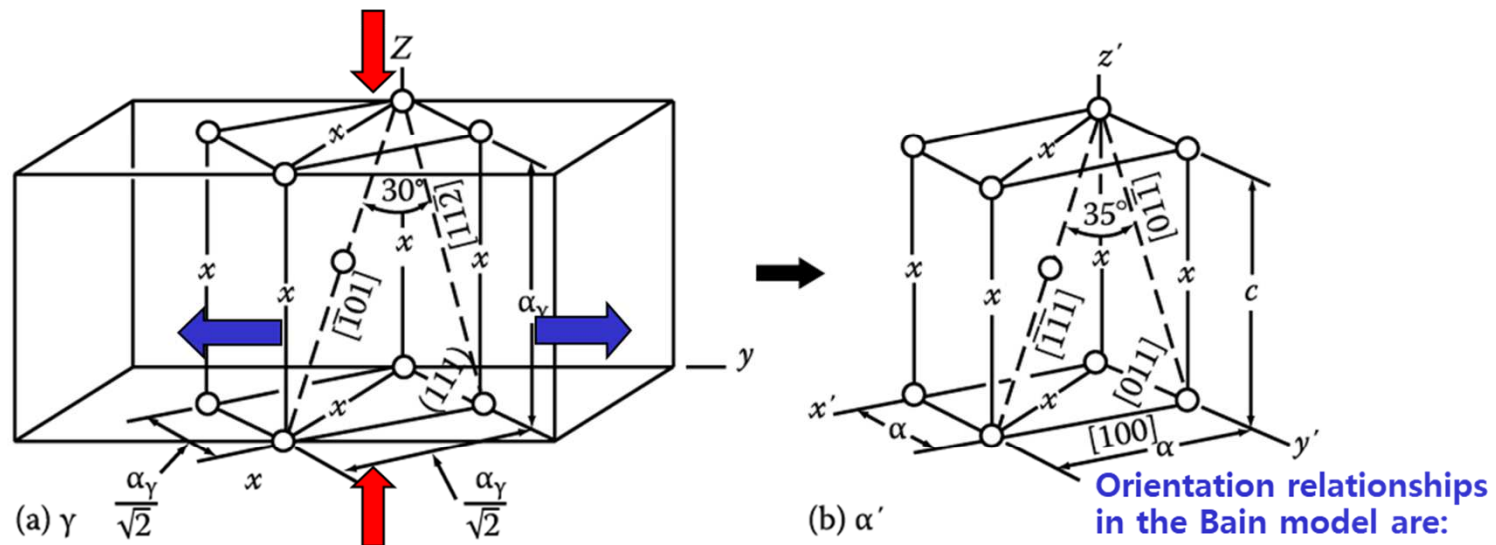


Figure. **Bain correspondence for the $\gamma \rightarrow \alpha'$ transformation.**
 Possible interstitial sites for carbon are shown by crosses.

$(111)_\gamma \rightarrow (011)_{\alpha'}$
 $[\bar{1}01]_\gamma \rightarrow [1\bar{1}1]_{\alpha'}$
 $[1\bar{1}0]_\gamma \rightarrow [100]_{\alpha'}$
 $[112]_\gamma \rightarrow [01\bar{1}]_{\alpha'}$

Bain model을 통한 변형시 γ 와 α' 간 방위관계: $(001)_{bcc} \parallel (001)_{fcc}$ and $[010]_{bcc} \parallel [110]_{fcc}$
FCC \rightarrow BCC

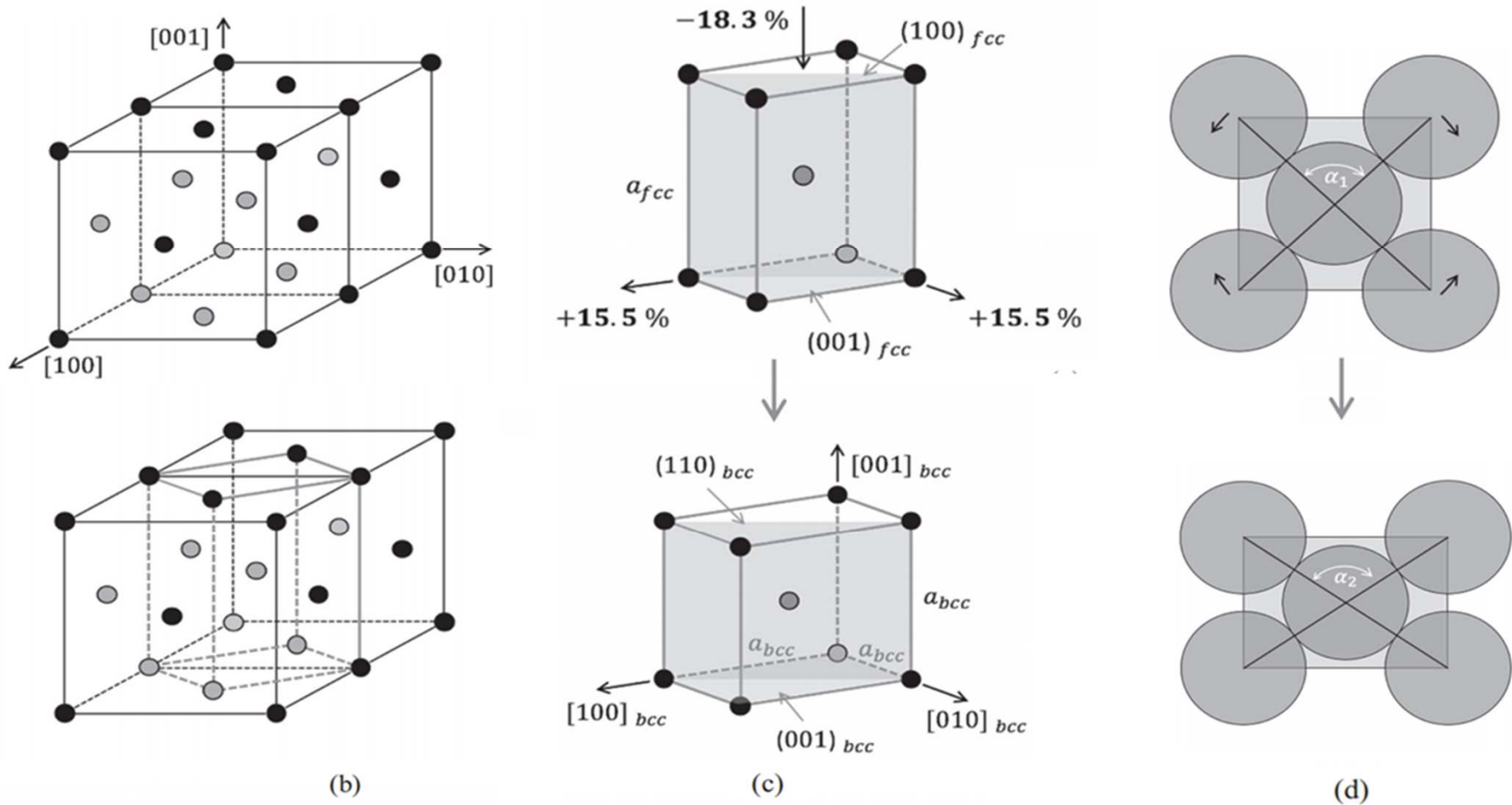


FIGURE 6.28 Bain lattice distortion (or strain) and orientation relationship for a hard sphere atomic model with constant atom diameter. (a) Fcc lattice points forming two unit cells. (b) A bct unit cell in the fcc structure. (c) A compression of 18.3 % along the $[001]_{fcc}$ direction combined with an expansion of all directions in the $(001)_{fcc}$ plane by 15.5 % changes the fcc crystal structure into the bcc structure. The resultant orientation relationship is $(001)_{bcc} \parallel (001)_{fcc}$ and $[010]_{bcc} \parallel [110]_{fcc}$. (d) Fcc and bcc atoms as hard spheres rolling over each other in the transformation as seen on $(100)_{fcc} / (110)_{bcc}$ planes $\alpha_1 = 90^\circ$ and $\alpha_2 = 109.5^\circ$.

* 실험적으로 관찰된 γ 와 α' 간 방위관계: K-S 또는 N-W 방위 관계와 가까움

(a) FCC \rightarrow BCC
K-S 방위관계

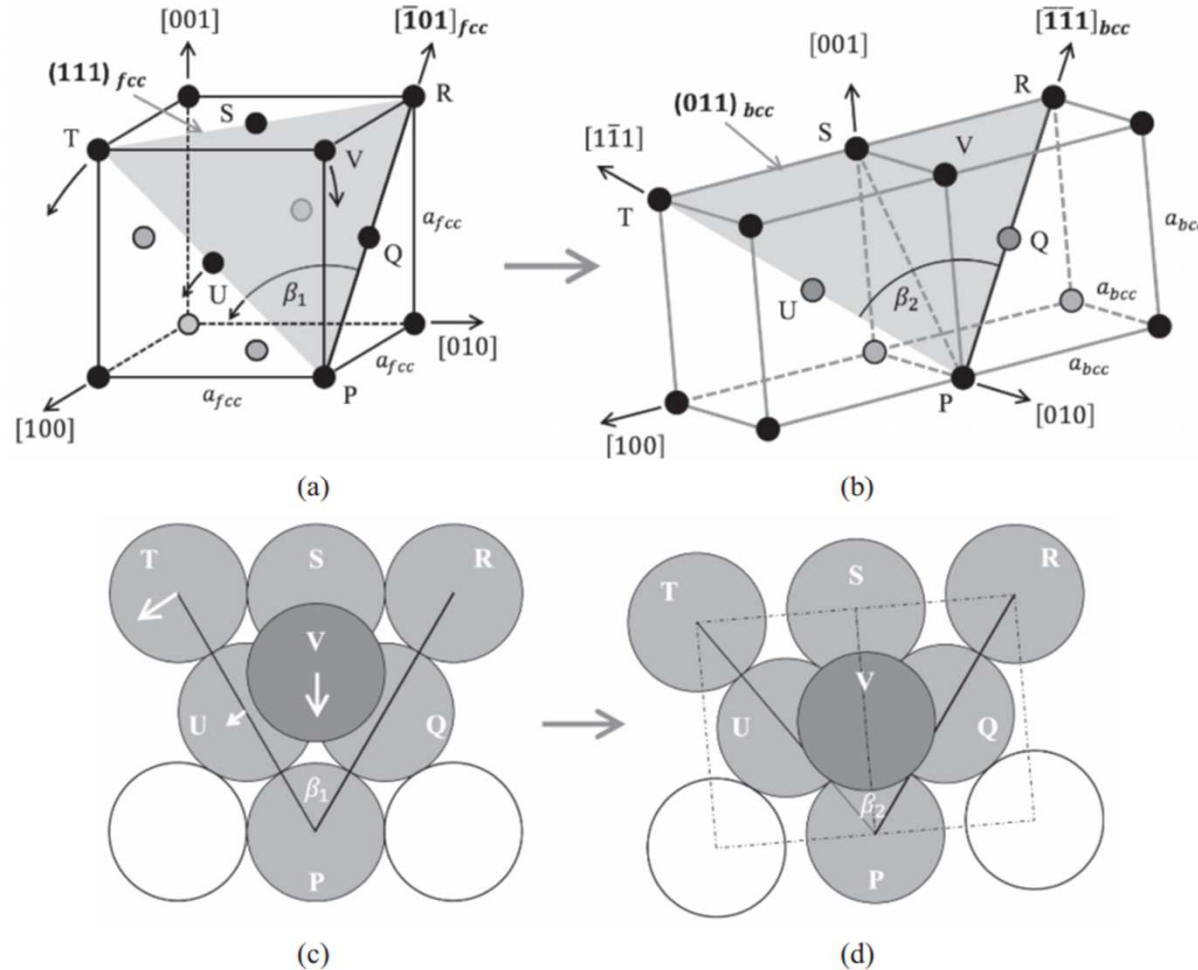


FIGURE 6.29 The Kurdjumov–Sachs (K–S) lattice distortion and orientation relationship for a hard sphere atomic model with constant atom diameter. (a) Fcc lattice with the (111) plane shaded. $\beta_1 = 60^\circ$. Arrows indicate some of the atomic paths during the distortion. (b) Positions of lattice points after the K–S distortion in which the (111) close-packed plane remains unrotated and the PQR close-packed direction remains unrotated and undistorted. $\beta_2 = 70.5^\circ$. (c) Atoms on the (111) close-packed plane shaded in (a) plus atom V that lies in the next $(111)_{fcc} / (110)_{bcc}$ close-packed plane. (d) The final positions of the atoms in (c) showing how atom V moves into its bcc position and the atoms in the fcc close-packed plane become atoms in a bcc close-packed plane by atoms T-S-R and U-Q losing contact. The final orientation relationship is $(011)_{bcc} \parallel (111)_{fcc}$ and $[\bar{1}\bar{1}1]_{bcc} \parallel [\bar{1}01]_{fcc}$.

(b) FCC → BCC
N-W 방위관계

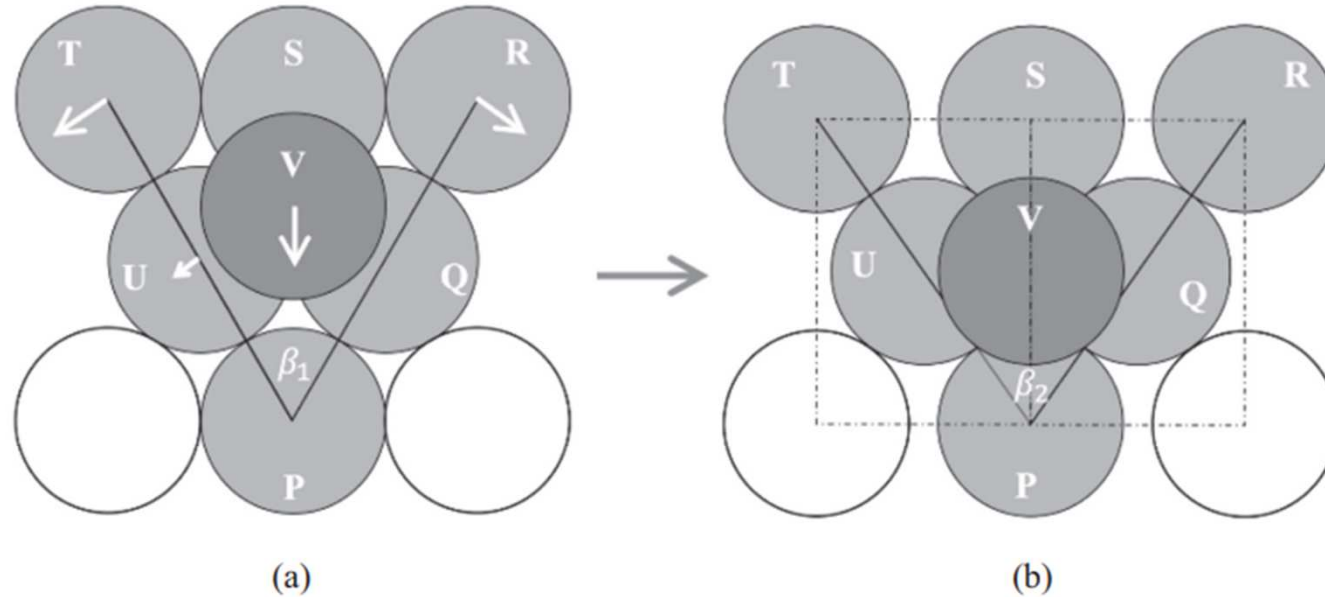


FIGURE 6.30 The Nishiyama (N) lattice distortion and N–W orientation relationship for a hard sphere atomic model with constant atom diameter. Atoms are the same as in Figure 6.29, but now the direction PS remains unrotated during the distortion. This direction is $[\bar{1}\bar{1}2]_{fcc} \parallel [0\bar{1}1]_{bcc}$. Therefore, the resultant orientation relationship is $(110)_{bcc} \parallel (111)_{fcc}$ and $[\bar{1}\bar{1}2]_{fcc} \parallel [0\bar{1}1]_{bcc}$, which is the N–W orientation relationship.

[참고] 위 모델은 모두 **Hard sphere** 모델로 예측해서 원자크기가 같은 것으로 가정했으나, **bcc** 철 원자 지름은 **fcc** 철 원자에 비해 약 **1%** 적다.

* **FCC → BCT Martensite**

: 침입형 원소 (C or N)가 3개의 부격자 중 하나의 부격자에만 위치하는 규칙화 발생시 일어남.

e.g. 고탄소강

탄소원자 M 변태 일어나기전 γ fcc의 8면체 자리에 위치 → bcc 구조로 원자 재배열시 bcc 격자의 한 부격자가 됨. 아래는 Bain 변형의 경우, 이러한 변화를 도식화 함.

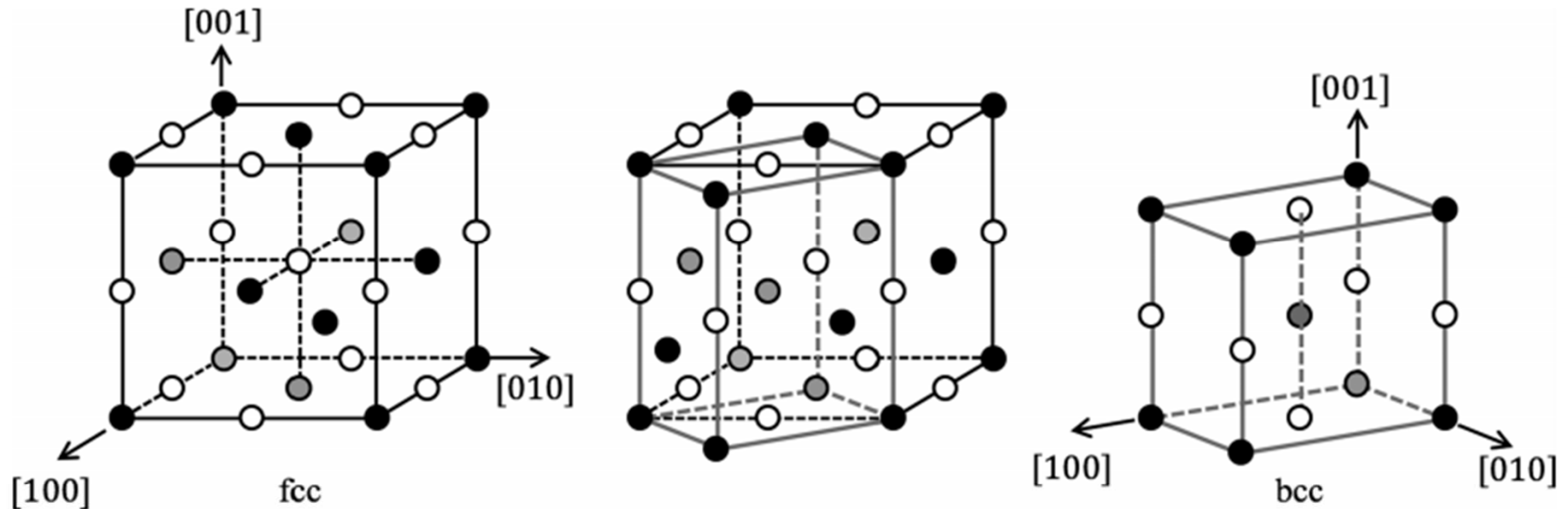


FIGURE 6.31 Octahedral sites in the fcc lattice (open circles) lie midway along the edges and at the center of the unit cell. They are all transformed into O_z octahedral sites in the bcc lattice by compression of the fcc unit cell along the z -axis $[001]$. Similarly, compression along x $[001]$ or y $[001]$ only creates O_x or O_y octahedral sites. Compare with Figure 6.11.

* 이전 내용은 **fcc** 구조를 이루는 원자가 아무런 제약을 받지 않은 상태에서 서로 이동하여 **bcc** 격자 구성하는 방법 고려 → 실제의 경우는 구속된 γ 의 변형으로 변형에너지의 영향을 상쇄할만한 추가적인 구조적 변화 필요

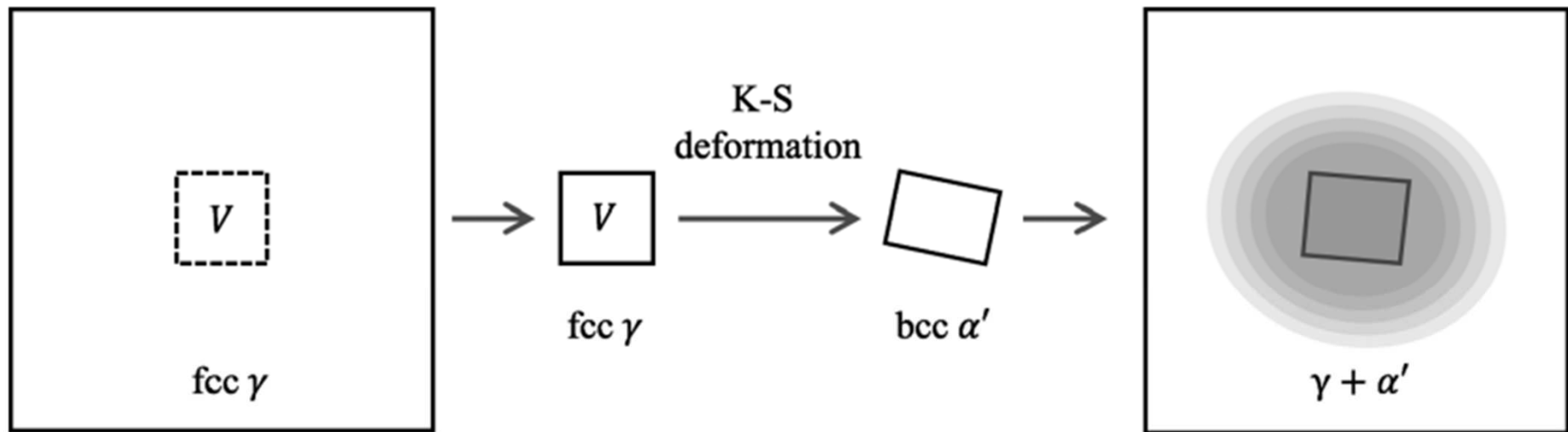


FIGURE 6.32 The source of the strain energy that results if a small volume of fcc austenite is transformed into bcc martensite, e.g., by one of the lattice distortions shown in Figures 6.28–6.30. Strain field shaded.

- (a) **K-S** 변형 또는 서로 다른 유형의 **Bain** 변형이 같이 일어나 변태가 일어난 부분이 작은 쌍정으로 이루어짐
- (b) 변태가 일어난 부분에서 주기적으로 슬립이 일어나 변태가 일어난 부분이 기지와 더 잘 맞도록 함

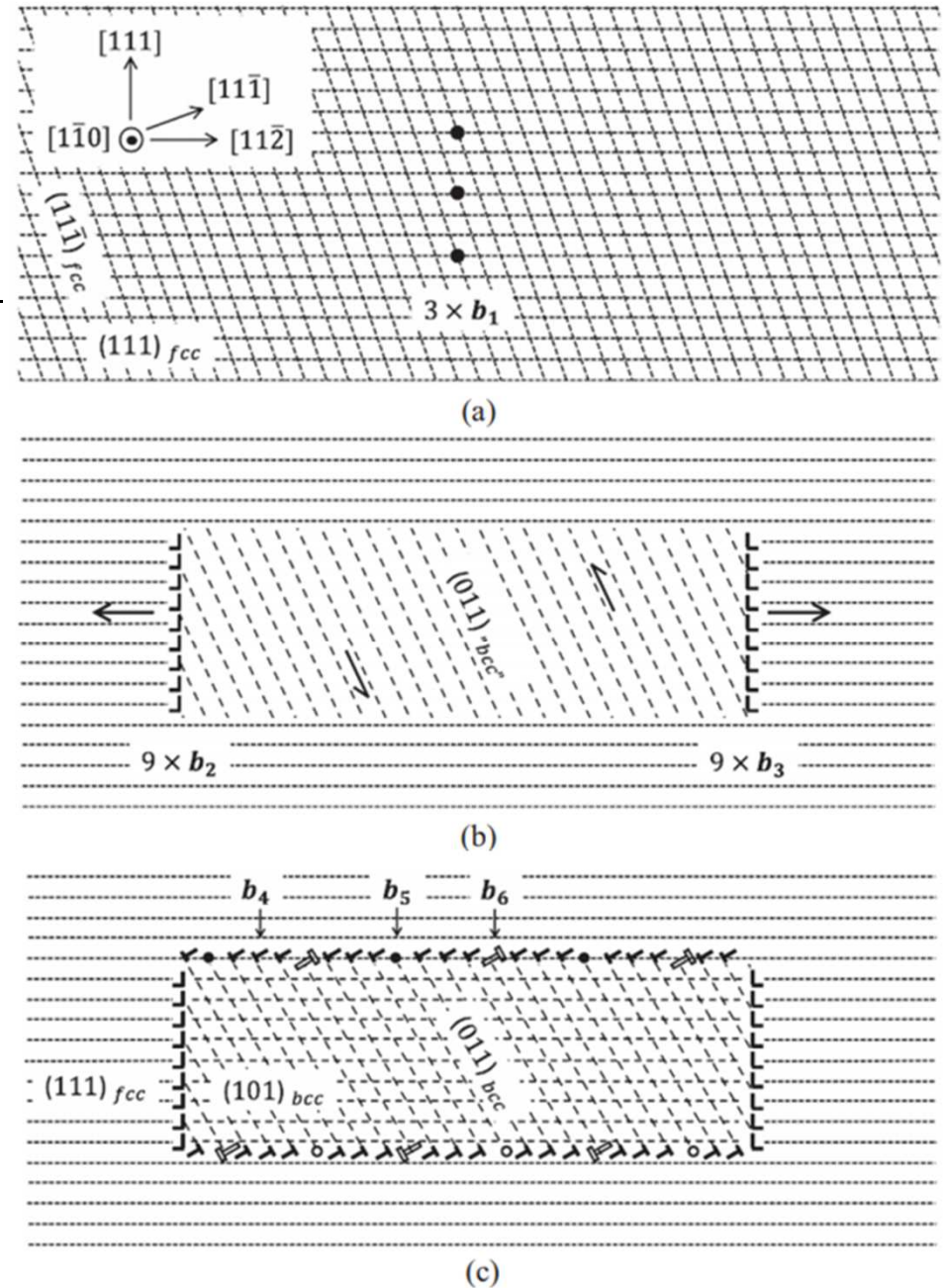
6.5.2 Nucleation and Early Growth of α' Martensite

Figure 6.33 Formation of a partially coherent bcc embryo in an fcc lattice by the dissociation of an array of screw dislocations

① 핵생성 단계에서 **bcc M embryo**는 나선전위 주위 변형장 도움을 받아 총 변형 E 감소, 성장시는 해당사항 없음.

② γ/ε 계면과 달리 γ/α' 계면은 불변면이 아니기 때문에 계면에 상당량의 계면 E 걸림 \rightarrow 원활한 성장을 위해 계면 E 상쇄가 필요

③ 낮은 온도에서 일어나는 M 변태의 경우, M 변형 E를 최소로 하기 위해, 즉 구동력을 최대로 하기 위해 불변면을 정벽면으로 선택함.



④ Bain 변형의 3가지 variants로 이루어진 여러 구역의 균집체를 가정하면, 서로 다른 이형의 Bain 변형에 의해 야기된 응력장은 부분적으로 서로 상쇄되어 총 변형 E를 줄임

a) Just above M_s , M embryo 형성

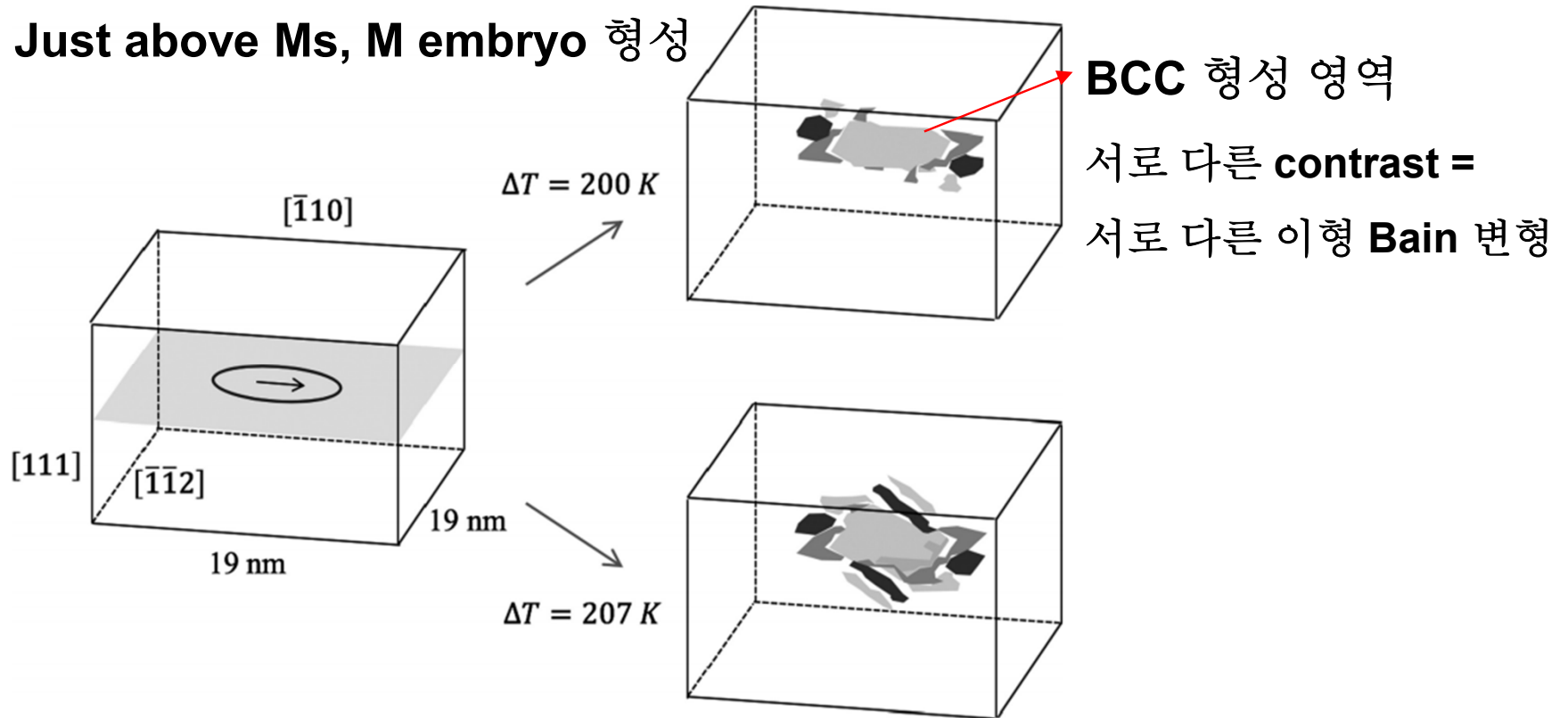
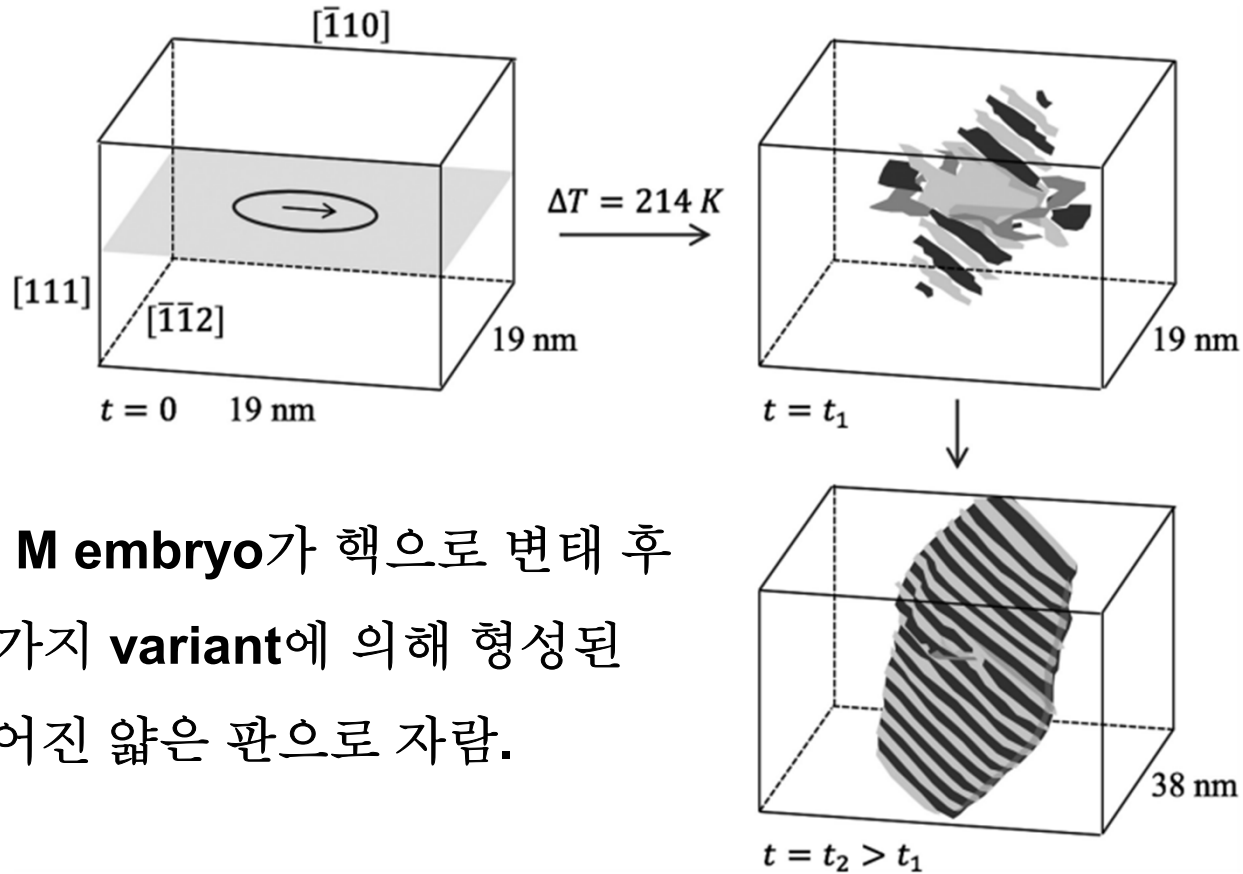


FIGURE 6.34 Phase field microelasticity model of martensite embryo formation in Fe-31 wt.% Ni alloy just above M_s . Only the middle $19 \times 19 \times 13$ nm of the total $\approx 77 \times 77 \times 77$ nm³ modelled volume is shown. Initiating defect is a dislocation loop with a diameter of 8 nm and a Burgers vector $\frac{a}{2}[\bar{1}10]$ lying in the middle of the volume on a (111) plane. The drawings on the right show the stable embryos predicted to develop around the dislocation at the undercoolings $\Delta T = 200$ and 207 K, i.e., the temperatures 205 K (-68°C) and 198 K (-75°C). Within the shaded regions, the atomic configuration is bcc or close to bcc. Each of the three shades of gray represents one of the three Bain strain variants. (Drawings based on data and figures in W. Zhang, Y.M. Jin, A.G. Khachatryan, *Acta Materialia*, 55:565–574 (2006).)

④ **Bain** 변형의 3가지 **variants**로 이루어진 여러 구역의 균집체를 가정하면, 서로 다른 이형의 **Bain** 변형에 의해 야기된 응력장은 부분적으로 서로 상쇄되어 총 변형 **E**를 줄임



b) 과냉 증가시 **M embryo**가 핵으로 변태 후 **Bain** 변형의 2가지 **variant**에 의해 형성된 쌍정으로 이루어진 얇은 판으로 자람.

FIGURE 6.35 As Figure 6.34, but $\Delta T = 214\text{ K}$, i.e., the temperature is 191 K ($-82\text{ }^\circ\text{C}$). The drawings on the right are at two times $t_1 < t_2$. Now, the embryo becomes unstable with respect to growth and develops into a nucleus expanding into a thin twinned plate, where the twins are formed from two variants of the Bain strain with a spacing of $\sim 3\text{ nm}$. Note that the volume of the box at t_2 is eight times that at t_1 . (Drawings based on data and figures in W. Zhang, Y.M. Jin, A.G. Khachaturyan, *Acta Materialia*, 55:565–574 (2006).)

* $\gamma \rightarrow \alpha'$ M 변태가 $\gamma \rightarrow \epsilon \rightarrow \alpha'$ 단계를 거치면서 일어날 수도 있음.

6.5.3 Growth of Athermal α' Martensite During Cooling

6.5.3. Growth of Plate and Lath Martensite

M 변태시 불변면을 정벽면으로 하여 평행한 형상을 가지는 경우, 변형 **E**를 최소화 함

→ M 변태는 γ 의 불변면 변형을 통해 일어남

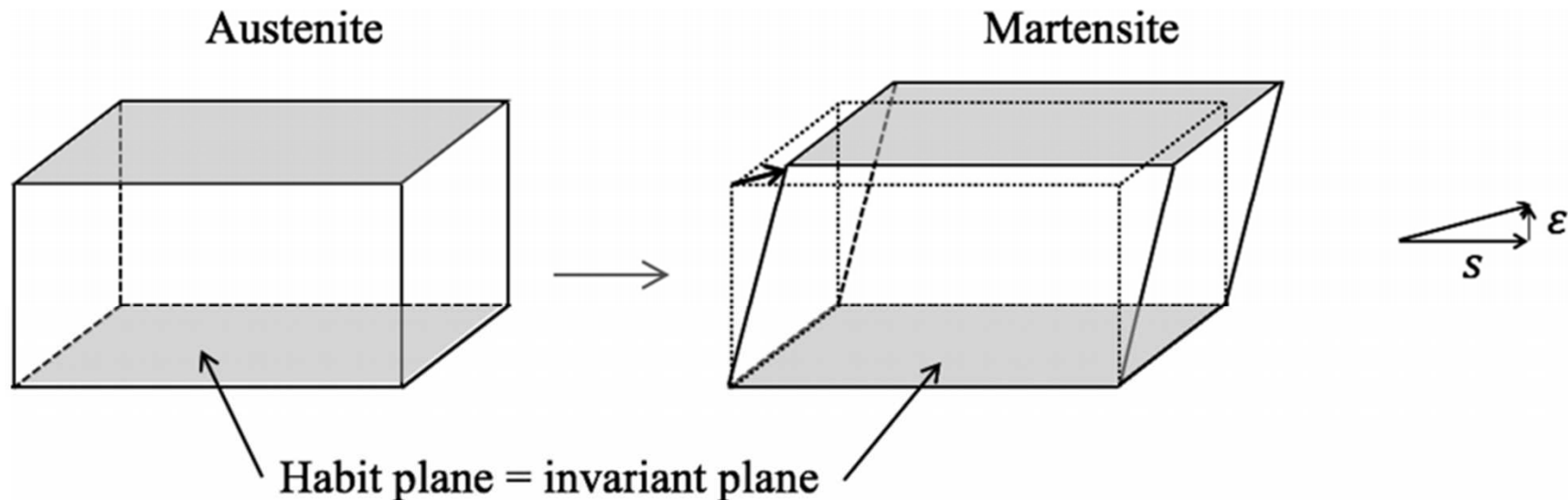


FIGURE 6.36 An invariant-plane strain can comprise a shear, s , parallel to the invariant plane and an expansion or contraction, ϵ , normal to the plane.

→ 위와 같은 불변면 변형이 얇은 타원회전체에서 일어난다고 가정하면,

변형시 변형 **E**가 동일 부피에서 c/a 가 작을수록 감소하는 것을 알 수 있음

즉, M 변태시 변형 **E** 최소화를 위해 정벽면이 불변면인 얇은 M 판 형태로 변태가 발생

* 판상 **M** 변태로 인한 전단변형, 변형 영역 및 표면 기복

: 철계 **M**의 경우 $s \approx 0.2-0.3$ (Lath m의 경우 약간 더 큼), $\epsilon \approx 0.002-0.004$

→ **M** 변태시 부피팽창과 같은 크기

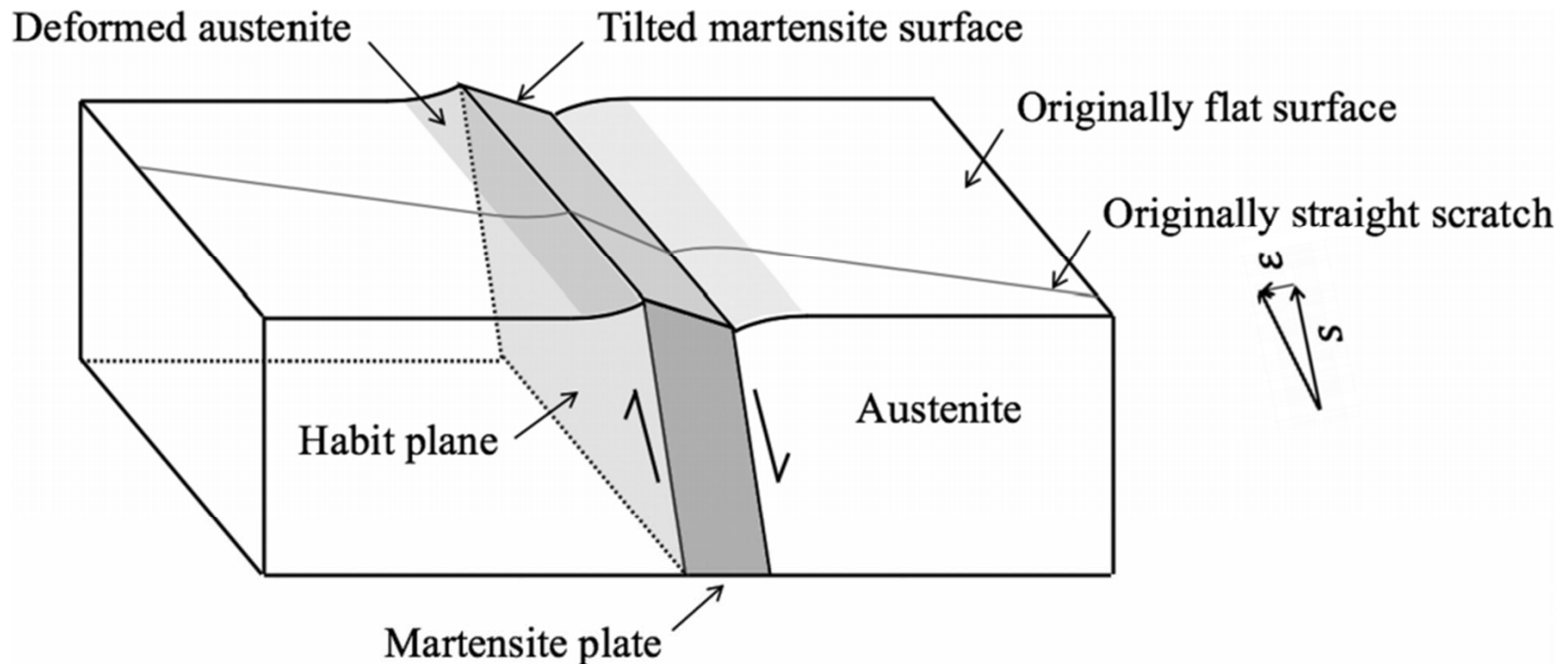


FIGURE 6.37 Surface tilt together with the shear and deformation zones associated with growth of a martensite plate.

* Figure 6.37의 정벽면 원자스케일 분석 결과: 계면은 **Terrace + step** 구조

→ 계면 정합성 증가 & 계면 E 감소

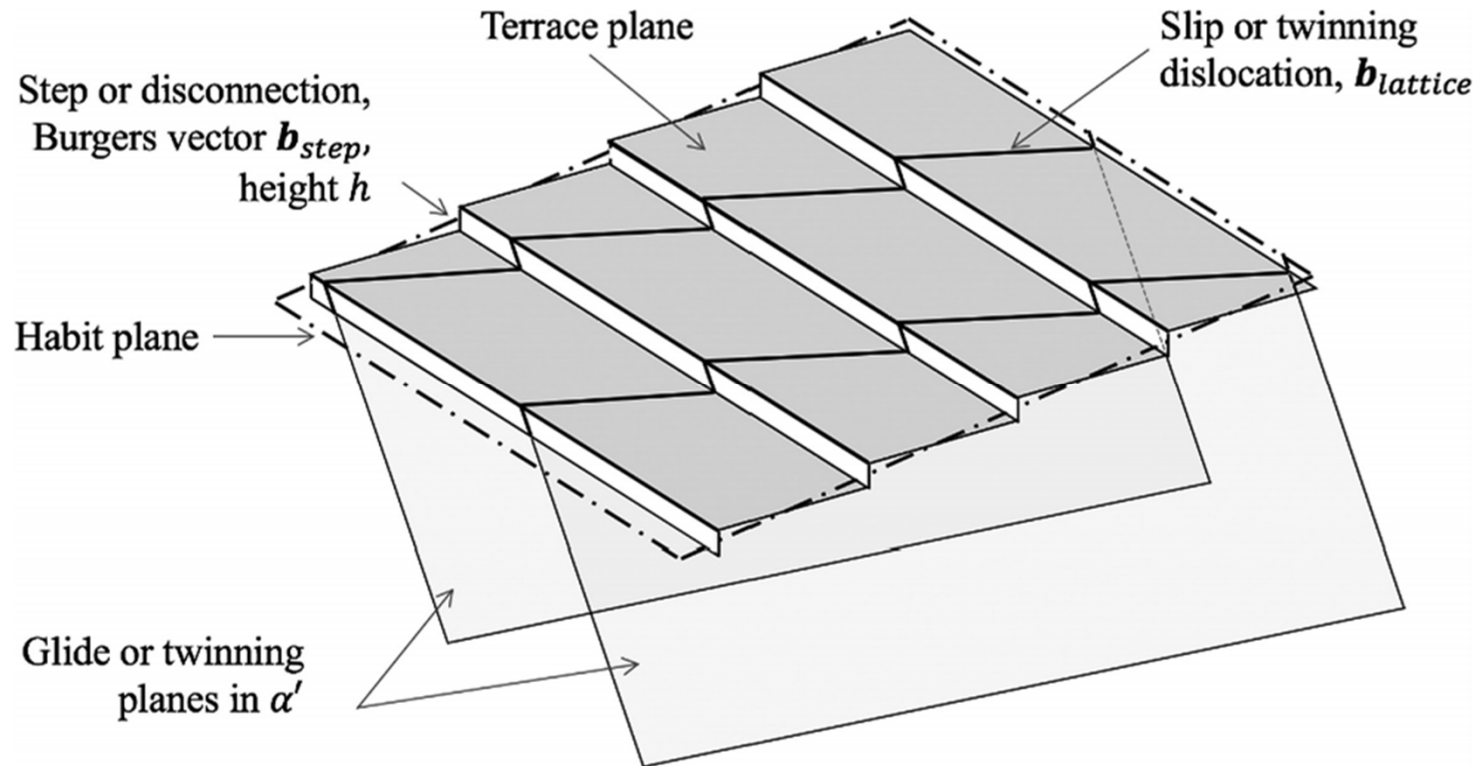


FIGURE 6.38 Schematic illustration showing topological features of the glissile interface between the upper parent phase (γ) and the lower martensite (α'). Terrace planes are parallel to the close-packed $\{111\}_\gamma / \{110\}_{\alpha'}$ planes that have an orientation relationship in the vicinity of the N-W/K-S relationships. The interface is reticulated by disconnections and dislocations. The disconnections are characterized by their step height h and Burgers vector content \mathbf{b}_{step} . Typically, h corresponds to one or two interplanar spacings of the close-packed planes. The slip or twinning dislocations have line and Burgers vectors that are parallel to glide planes in α' . A slip dislocation could have a Burgers vector $\frac{a_{\text{bcc}}}{2} \langle 111 \rangle$ lying on $\{110\}_{\text{bcc}}$. A twinning dislocation is $\frac{a_{\text{bcc}}}{6} \langle 111 \rangle$ lying on $\{112\}_{\text{bcc}}$. The deviation of the habit plane from the $\{111\}_\gamma$ terrace plane is determined by the spacing of the disconnections and their direction relative to the close-packed $\langle 110 \rangle_\gamma$ directions. (The figure is based on the topological model of X. Ma and R.C. Pond, *Journal of Nuclear Materials* **361**:313–321 (2007).)

* 실제 테라스의 폭은 둘레의 위치에 따라 다름 (쌍정으로 이루어진 중앙의 미드립은 표시하지 않음)

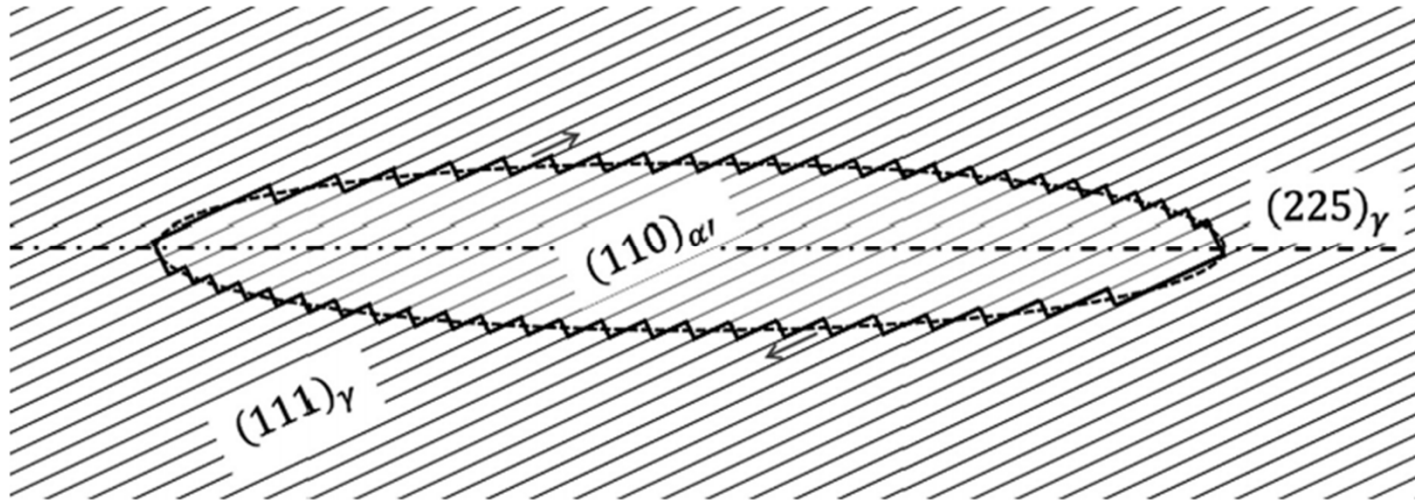


FIGURE 6.39 Schematic two-dimensional cross-section through $\{225\}_{\gamma}$ lenticular plate martensite viewed along $[1\bar{1}0]_{\gamma}$ and showing the parallel $(111)_{\gamma}$ and $(110)_{\alpha'}$ planes. Twinned mid-rib not shown. Terrace width varies around the perimeter.

* 쌍정으로 구성된 M 형성으로 인해 불변면인 $\{225\}_\gamma$ 정벽면이 생기는 과정 도식

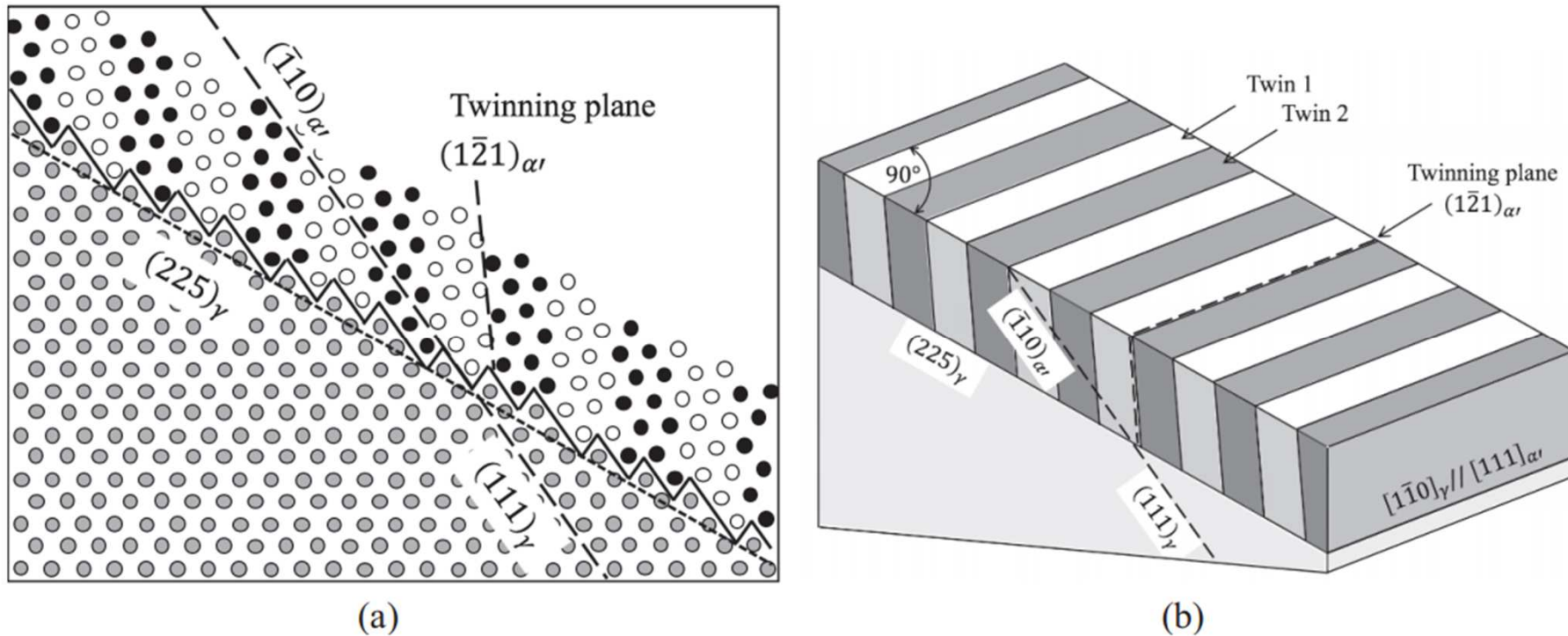


FIGURE 6.40 Schematic illustration of finely twinned α' thin plate martensite with a $(225)_\gamma$ habit plane and $(111)_\gamma \parallel (\bar{1}\bar{1}0)_{\alpha'}$. Light gray atoms are in austenite, black and white atoms are in the bcc martensite twins. Atom diameters are the same in both phases. (a) Atom positions projected along the common $[1\bar{1}0]_\gamma \parallel [111]_{\alpha'}$ directions showing a cross-section through the $(111)_\gamma \parallel (\bar{1}\bar{1}0)_{\alpha'}$ terrace planes and step heights equal to the close-packed plane spacing. Atom positions as given in by A.P. Baur, C. Cayron and R.E. Logé.³⁵ (b) Perspective view.

* 얇은 판상 M의 성장을 위해서는 쌍정에 평행한 가장자리에서 새로운 쌍정의 형성 필요

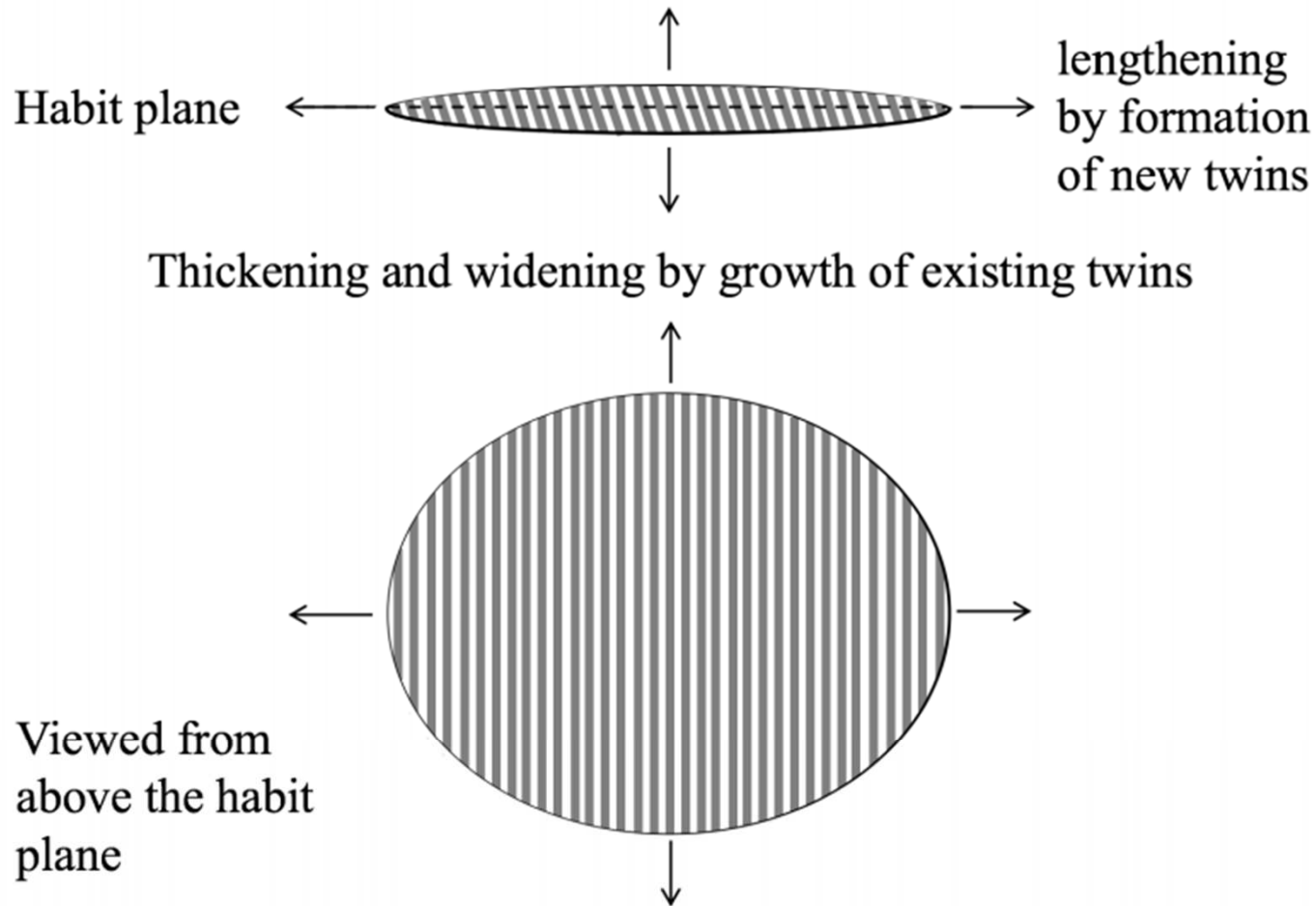


FIGURE 6.41 The growth of thin plate martensite only requires the formation of new twins at the edges parallel to the twins. Here, a plate is shown in elevation and plan view. Thickening and broadening occurs by the extension of existing twins.

* 냉각 중 혼합 M (=Lenticular plate M)의 형성

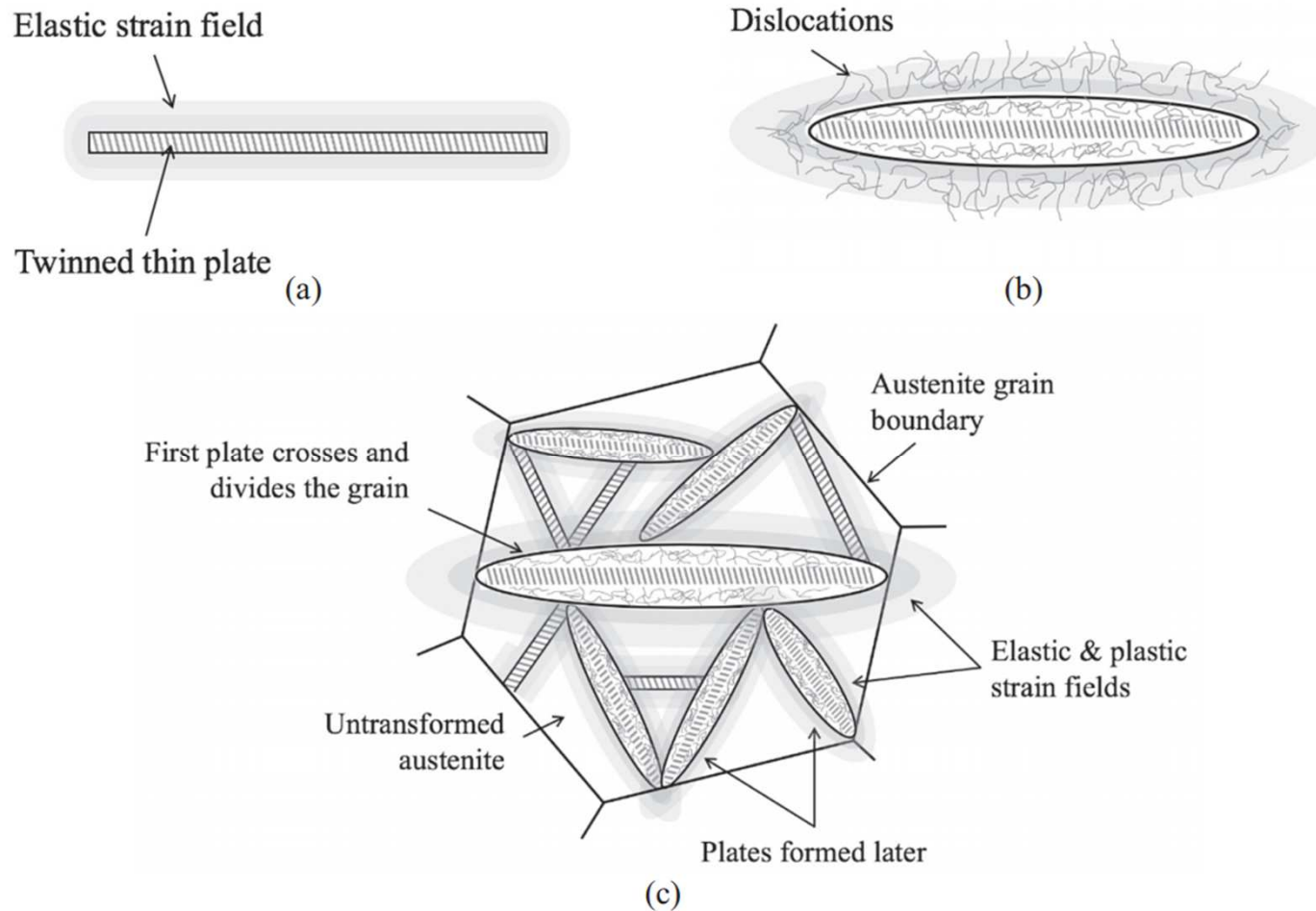
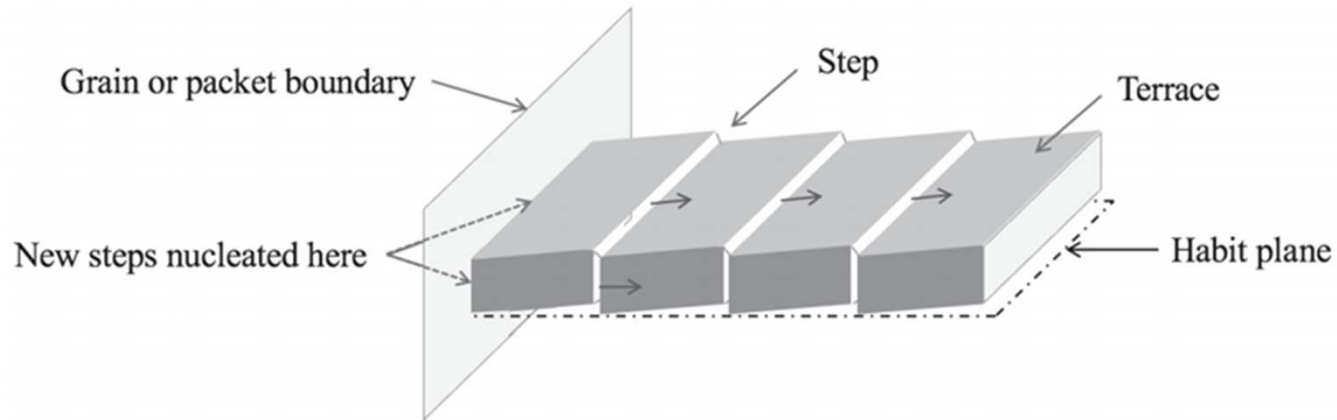
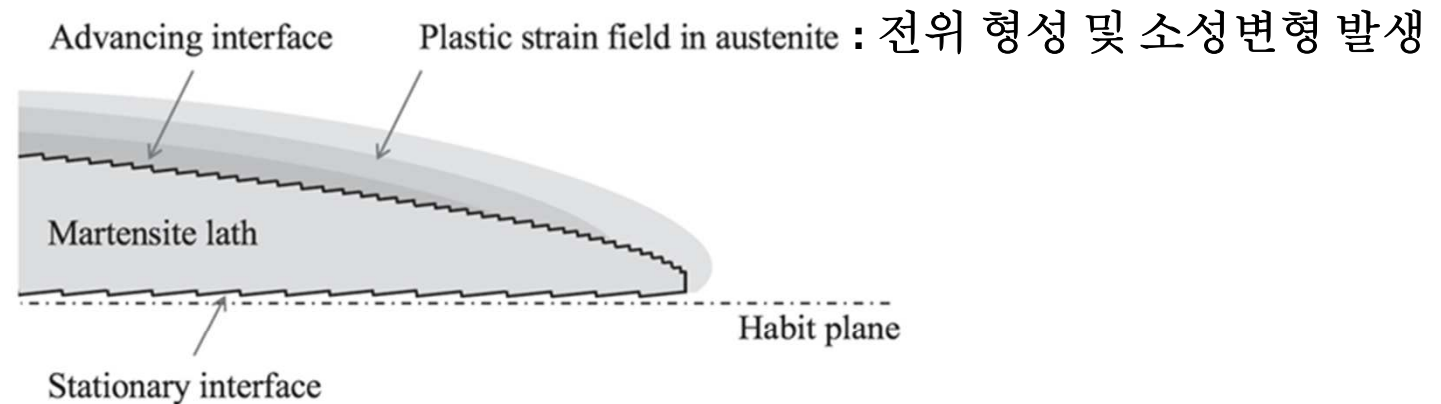


FIGURE 6.42 Formation of lenticular plate martensite during cooling. (a) Twinned plate nucleates and grows behind a glissile interface containing twinning dislocations. Growth creates elastic strains and stresses. (b) Plate thickens by the advance of a glissile interface containing slip dislocations rather than twinning dislocations. Transformation strain leads to elastic stresses and plastic deformation of both phases. (c) During cooling, more plates are nucleated and lengthen as thin twinned plate and possibly thicken. Plates are arrested at grain boundaries and other plates. Zig-zag patterns of plates are often seen.

* **Lath m**의 두께 증가와 폭 확장 기구 : 두께 증가를 위해 **step**이 테라스를 가로질러 이동 / 비슷한 방법으로 폭도 증가



(a)



(b)

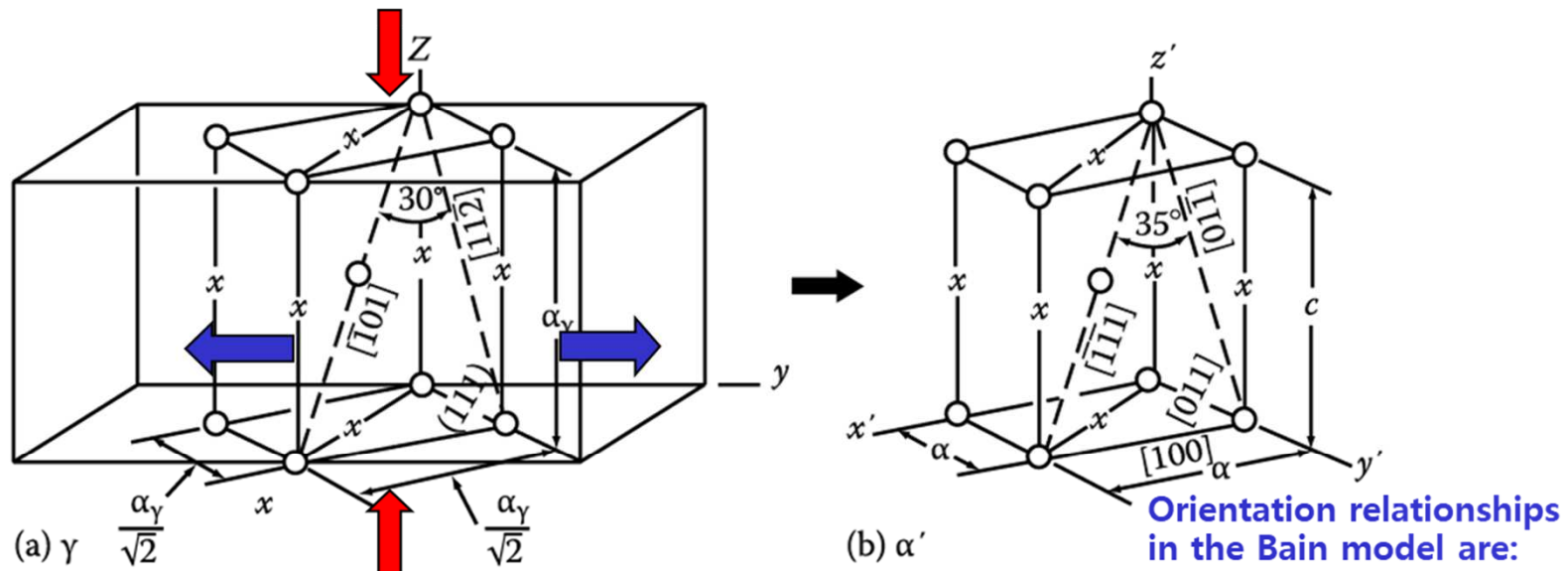
FIGURE 6.43 Possible mechanism for the thickening and broadening of a lath. (a) Schematic perspective view of lath growth. Thickening requires motion of steps across the terraces and the formation of new steps, e.g., at the intersection of the lath with a grain boundary or other interface. Such a mechanism leads to thickening in one direction. Broadening probably occurs in a similar fashion. (b) Lower magnification schematic cross-section through a growing lath. The transformation shape strain leads to the formation of dislocations, i.e., plastic strain, in the surrounding austenite and the lath. Darker shades of gray denote increasing plastic strain.

Q: Phenomenological Theory of Martensite crystallography

6.9. Martensite crystallography (Orientation btw M & γ)

Possible atomic model for martensitic transformation:
the Bain Model: fcc \rightarrow bct transformation

- For the case of **FCC Fe transforming to BCT ferrite** (Fe-C martensite), there is a basic model known as the **Bain model**.
- The essential point of the Bain model is that it accounts for the structural transformation with a *minimum of atomic motion*.
- Start with two FCC unit cells: contract by 18.3% in the z direction, and expand by 15.5% along the x and y directions.



$$\begin{aligned} (111)_\gamma &\rightarrow (011)_{\alpha'} \\ [\bar{1}01]_\gamma &\rightarrow [\bar{1}11]_{\alpha'} \\ [1\bar{1}0]_\gamma &\rightarrow [100]_{\alpha'} \\ [112]_\gamma &\rightarrow [011]_{\alpha'} \end{aligned}$$

Figure. **Bain correspondence for the $\gamma \rightarrow \alpha'$ transformation.**
 Possible interstitial sites for carbon are shown by crosses.

Crystallography, contd.

- Although the Bain model explains several basic aspects of martensite formation, additional features must be added for complete explanations (not discussed here).
- **The missing component of the transformation strain is an additional shear that changes the character of the strain so that an invariant plane exists.** This is explained in fig. 6.8.

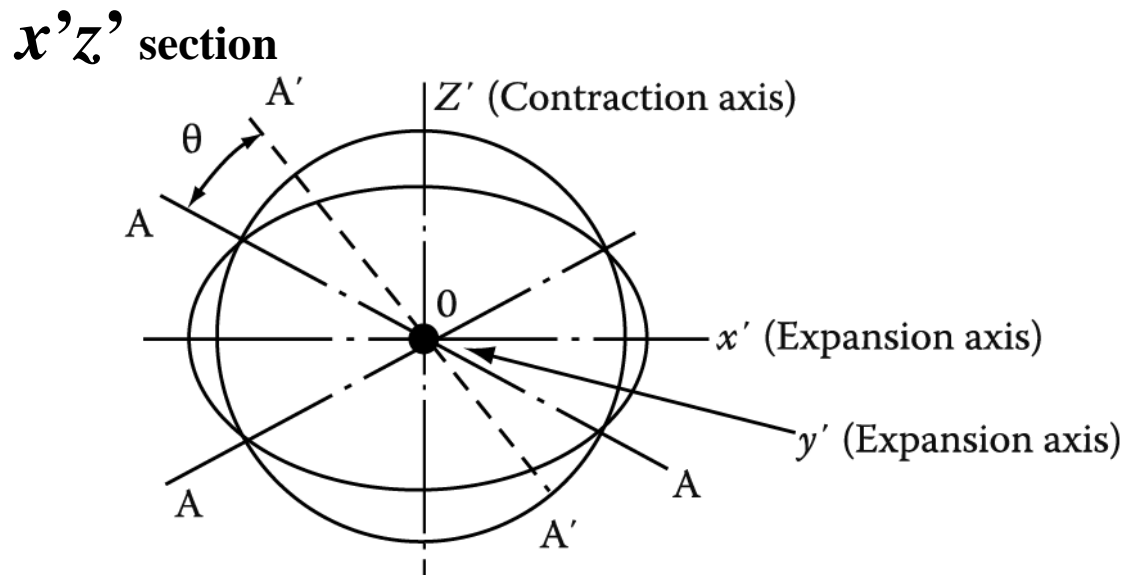


Fig. Bain deformation is here simulated by the pure deformation in compressing a sphere elastically to the shape of an oblate ellipsoid. **As in the bain deformation, this transformation involves two expansion axes and one contraction axis.**

Bain deformation = Pure deformation

In this plane, the only vectors that are not shortened or elongated by the Bain distortion are OA or $O'A'$.

However, the vector OY' (perpendicular to the diagram) must be undistorted.

This is clearly not true and therefore **the Bain transformation does not fulfill the requirements of bringing about a transformation with an undistorted plane.** * 변형되지 않는 평면 설명 못함

Hence, the key to the crystallographic theory of martensitic transformations is to postulate an additional distortion which reduces the extension of y' to zero (in fact a slight rotation, θ , of the AO plane should also be made as shown in the figure).

→ The second deformation can be in the form of dislocation slip or twinning.

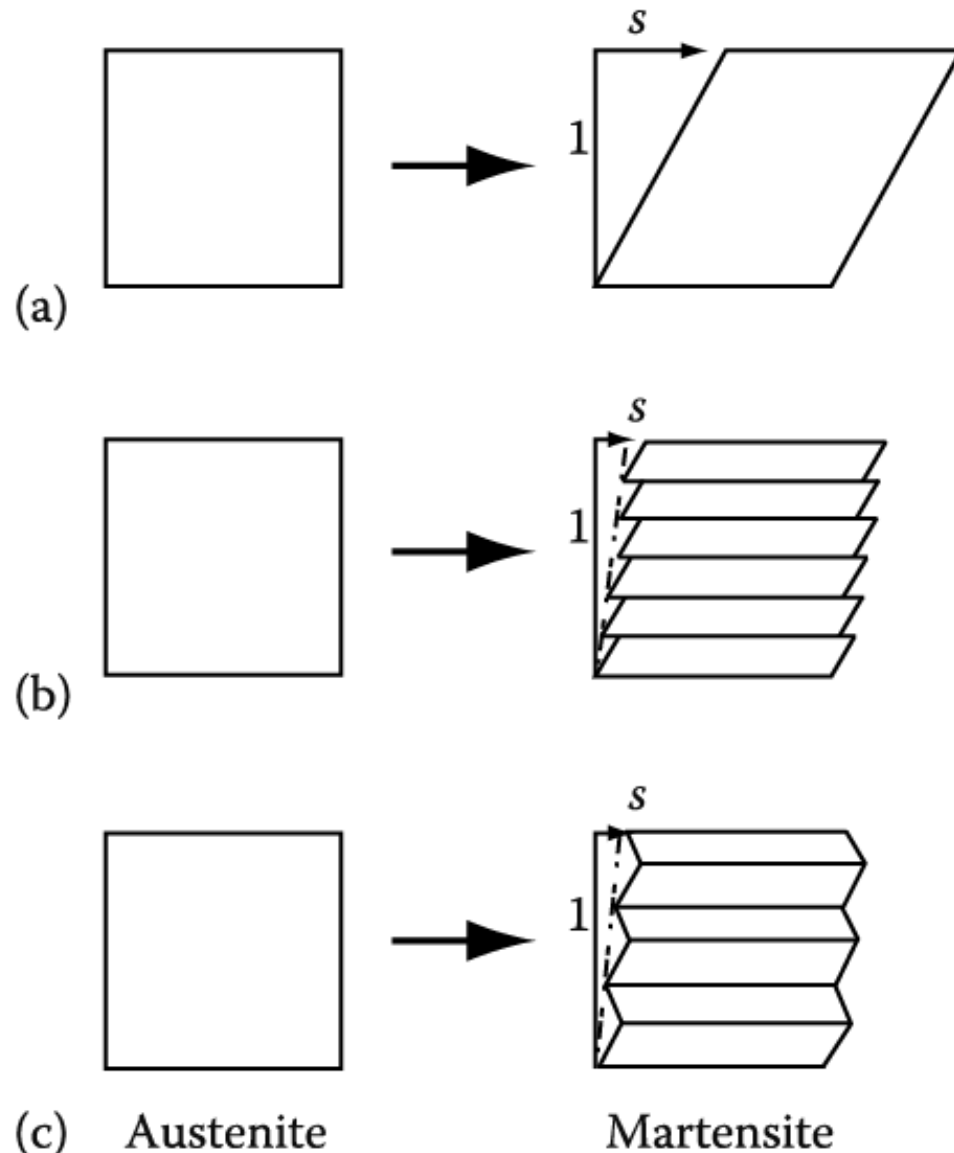
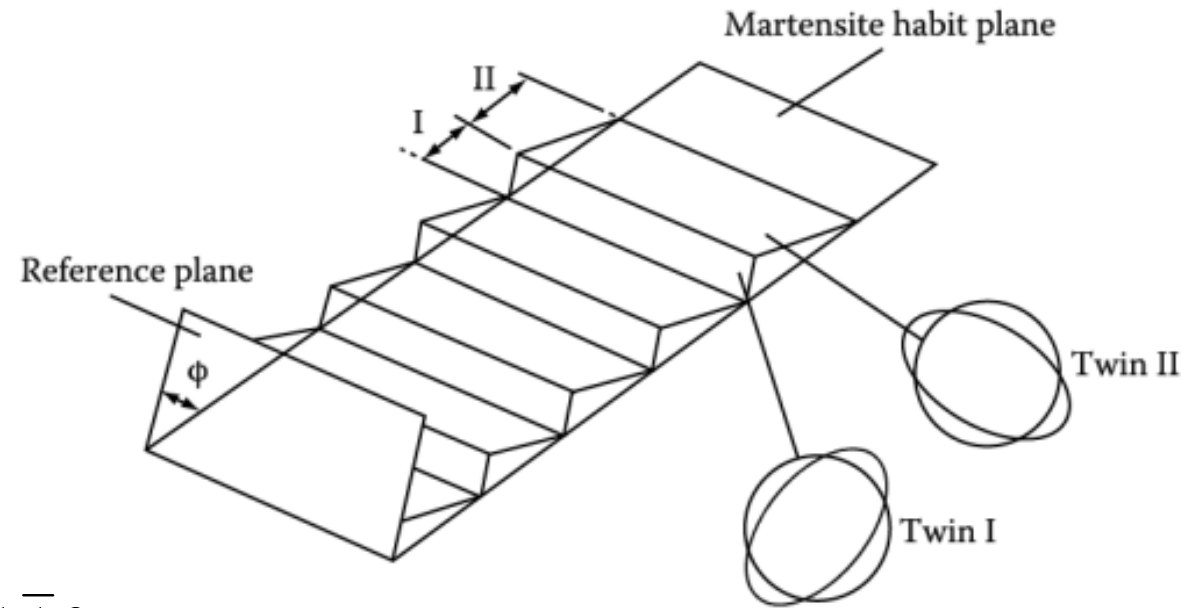
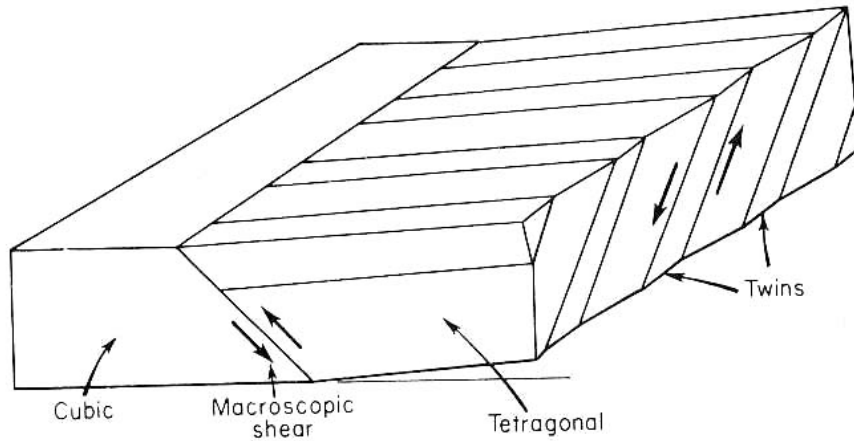
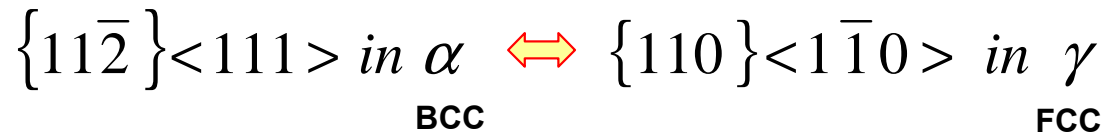


Figure. 6.9 Schematic illustration of **how dislocation glide or twinning of the martensite** can compensate for a pure lattice deformation such as a Bain deformation and thereby reduce the strain of the surrounding austenite. The transformation shear (s) is defined. Note how S can be reduced by slip or twinning.

Applying the twinning analogy to the Bain model, the physical requirements of the theory are satisfied.



Slip or Twinning on



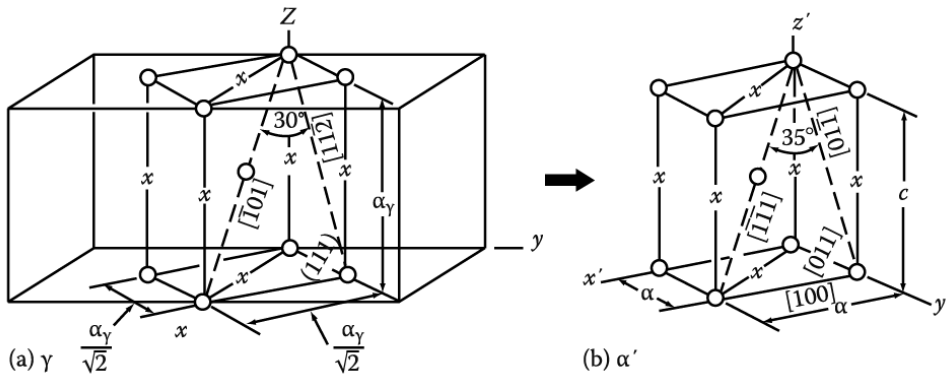
Twins in Martensite

may be self-accommodating and reduce energy by having alternate regions of the austenite undergo the Bain strain along different axes.

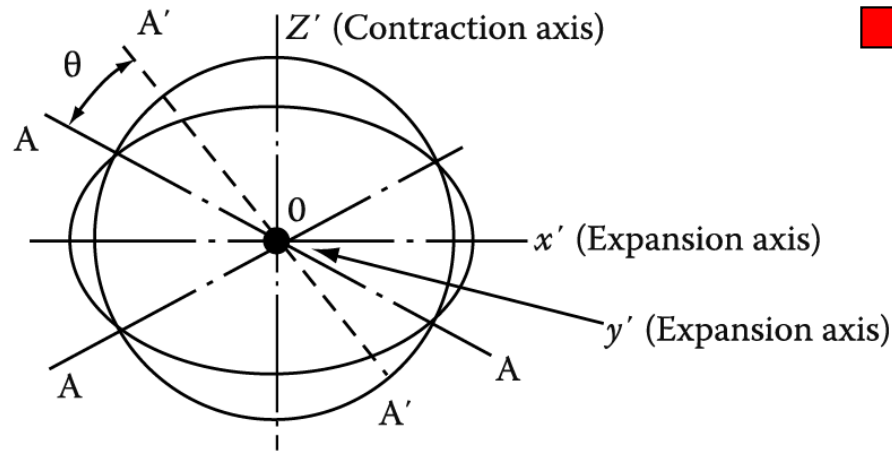
- On the basis, the habit plane of the M plate can be defined as a plane in the austenite which undergoes not net (macroscopic) distortion (=average distortion over many twins is zero)
- Local strain E by twins at the edge of the plate, but if the plate is very thin (a few atomic spacings) this strain can be relatively small.

6.9 Martensite crystallography (Orientation btw M & γ)

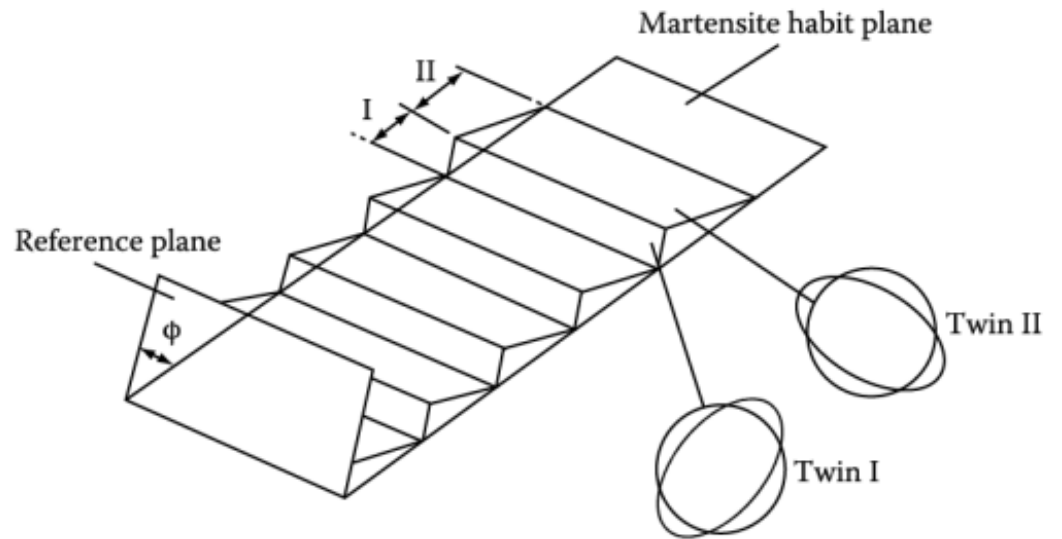
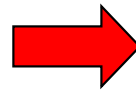
- $\gamma \rightarrow \alpha'$:
- (1) Habit plane of M: not distorted by transformation
 - (2) A homogeneous shear (s) parallel to the habit plane
 - (3) ~4% expansion_dilatation normal to the habit plain (lens)



Applying the twinning analogy to the Bain model,



Bain Model for martensite



Twins in Martensite

may be self-accommodating and reduce energy by having alternate regions of the austenite undergo the Bain strain along different axes.

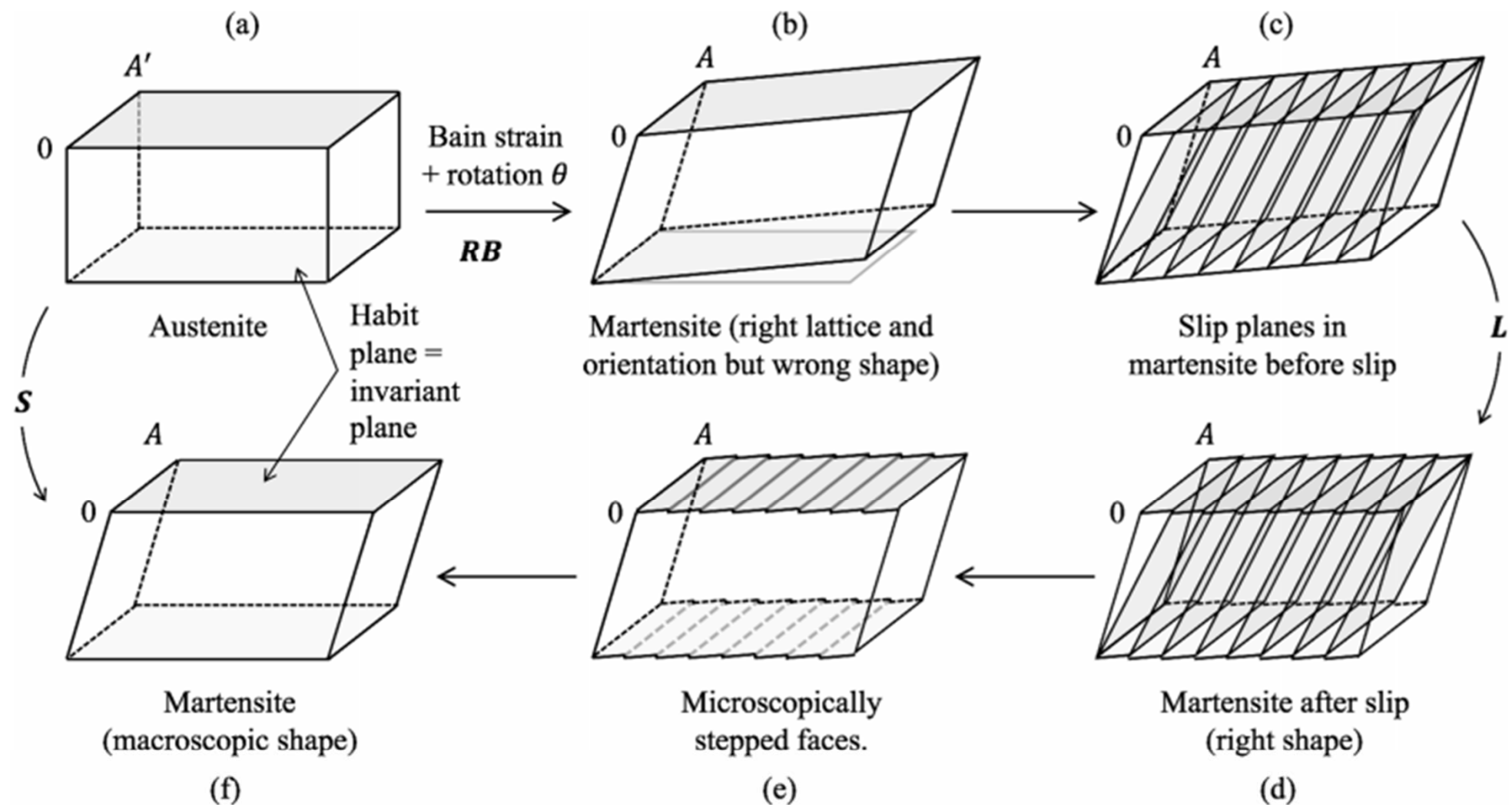


FIGURE 6.82 Generation of an invariant-plane strain by combining the invariant-line strain with slip on planes containing the invariant line. B is the deformation matrix representing the Bain strain, R is the rotation matrix, S is the shape strain, L is the lattice-invariant strain. (e) and (f) are just drawn to illustrate the microscopic and macroscopic features of (d).

2023 Fall

“Phase Transformation *in* Materials”

12.06.2023

Eun Soo Park

Office: 33-313

Telephone: 880-7221

Email: espark@snu.ac.kr

Office hours: by an appointment

6.2 Ferrous Martensite Morphologies and Crystallography

bcc 혹은 bct M 3가지 대표 형상 : lath / lenticular plate (렌즈형 판상) / thin plate

*(a) Lath M : 결정립 – Packet – block - Sub-block – Lath 구조

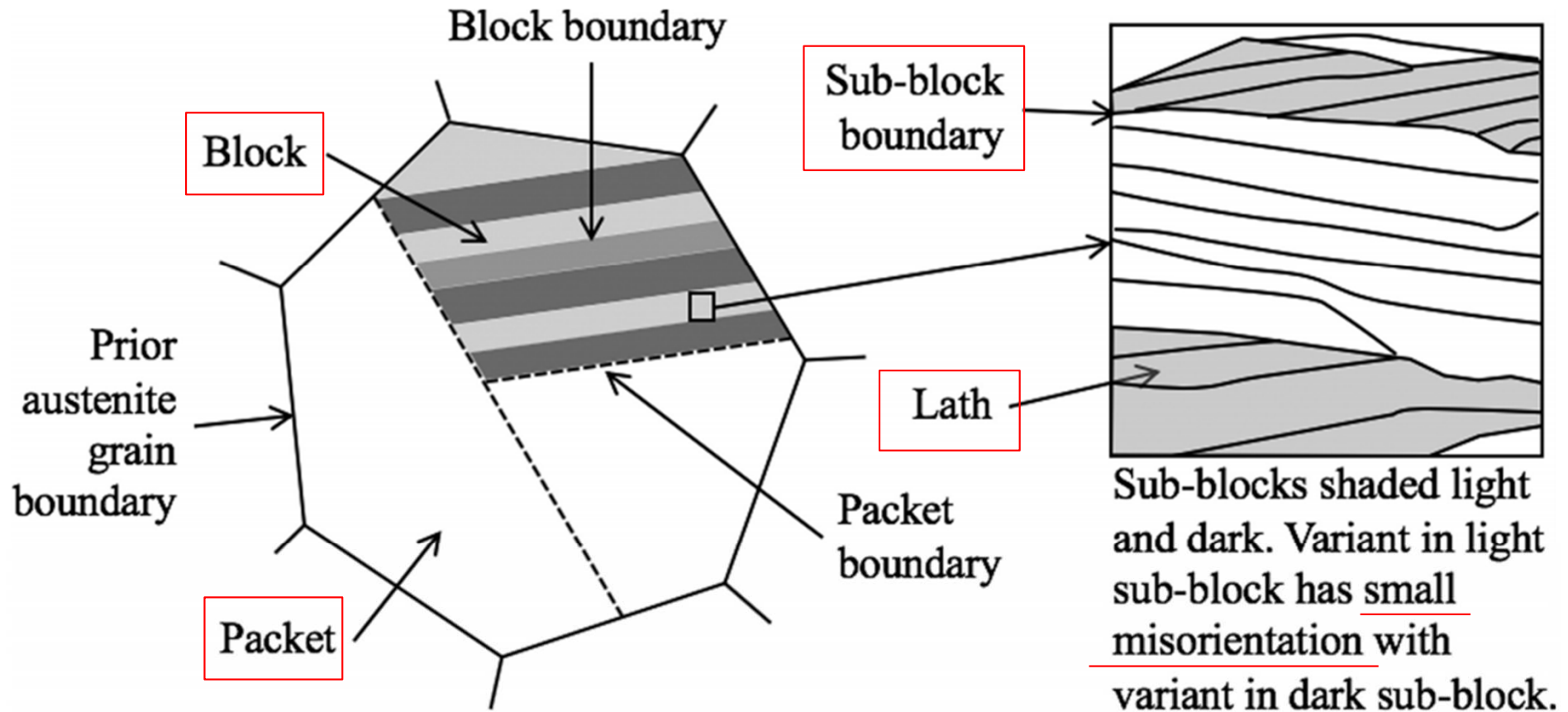


FIGURE 6.4 Schematic representation of lath martensite morphology in low-carbon alloys and steels.

6.2.2 Plate Martensite : Thin plate and Lenticular plate martensite

(c) Thin plate M : 상온 이하 낮은 온도의 M_s 를 가지는 경우, 쌍정으로 이루어진 얇은 판상 형성 $\{259\}_\gamma$ 또는 $\{3\ 10\ 15\}_\gamma$ *habit plane*에 평행하게 배열

M과 γ 의 방위관계는 **K - S**와 **N - W** 관계의 중간에 해당하는 **G - T** 방위관계

M에 접한 γ 는 탄성변형만 받고 있음, 이 탄성변형장의 깊이는 **M** 두께의 **10** 배

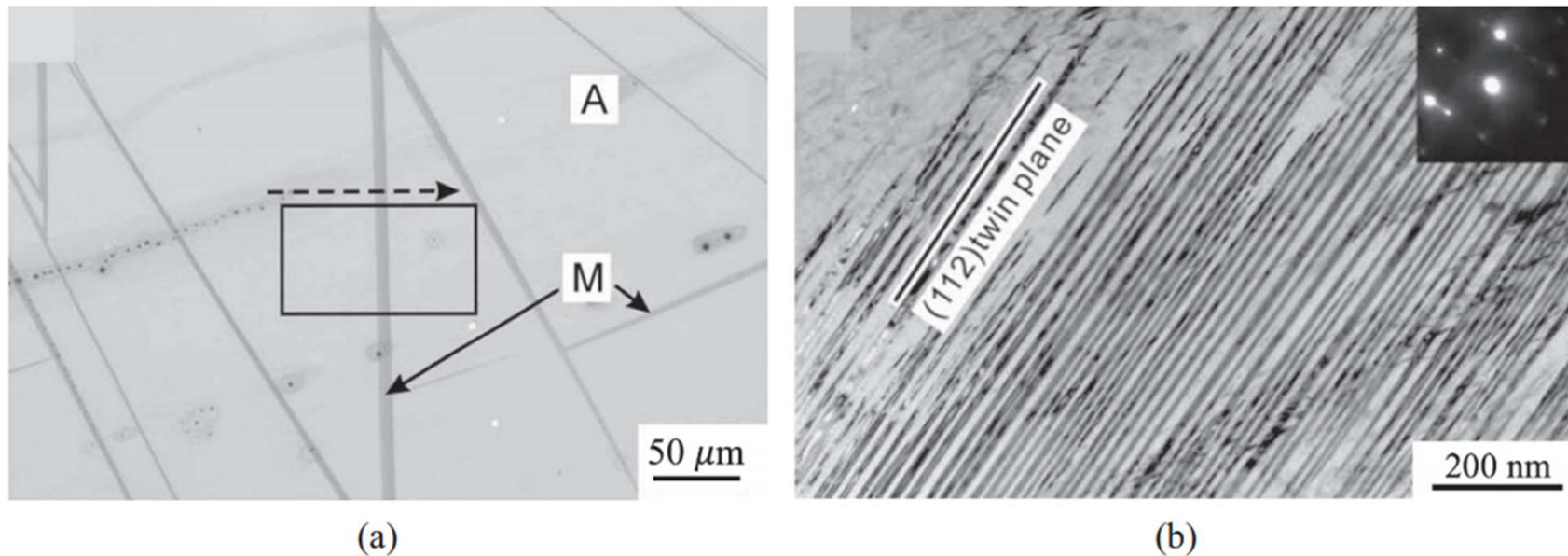


FIGURE 6.8 (a) Thin plate martensite formed by cooling an Fe-30Ni-0.4C alloy (wt.%) to just below its M_s temperature (77 K, -196°C). Scanning electron microscope image. Boxed area used for strain measurements. (Reprinted from *Acta Materialia*, Vol. 57, G. Miyamoto, A. Shibata, T. Maki, T. Furuhashi, Precise measurement of strain accommodation in austenite matrix surrounding martensite in ferrous alloys by electron backscatter diffraction analysis, 1120–1131 (2009),¹¹ with permission from Elsevier.) (b) Transmission electron microscopy image of a thin foil specimen showing fine twins as seen in thin plate martensite and the midrib of lenticular martensite. Twin thickness ~ 10 nm and spacing ~ 20 nm. (Reprinted from *Acta Materialia*, Vol. 57, A. Shibata, S. Morito, T. Furuhashi, T. Maki, Substructures of lenticular martensites with different martensite start temperatures in ferrous alloys, 483–492 (2009), with permission from Elsevier.)

(b) Lenticular plate martensite : $M_{s_thin\ plate\ M} < M_{s_LPM} < M_{s_lath\ M}$

초기엔 쌍정으로 이루어진 얇은 판상 M으로 자라다 변태 잠열에 의한 온도 증가로 렌즈모양으로 두꺼워짐.

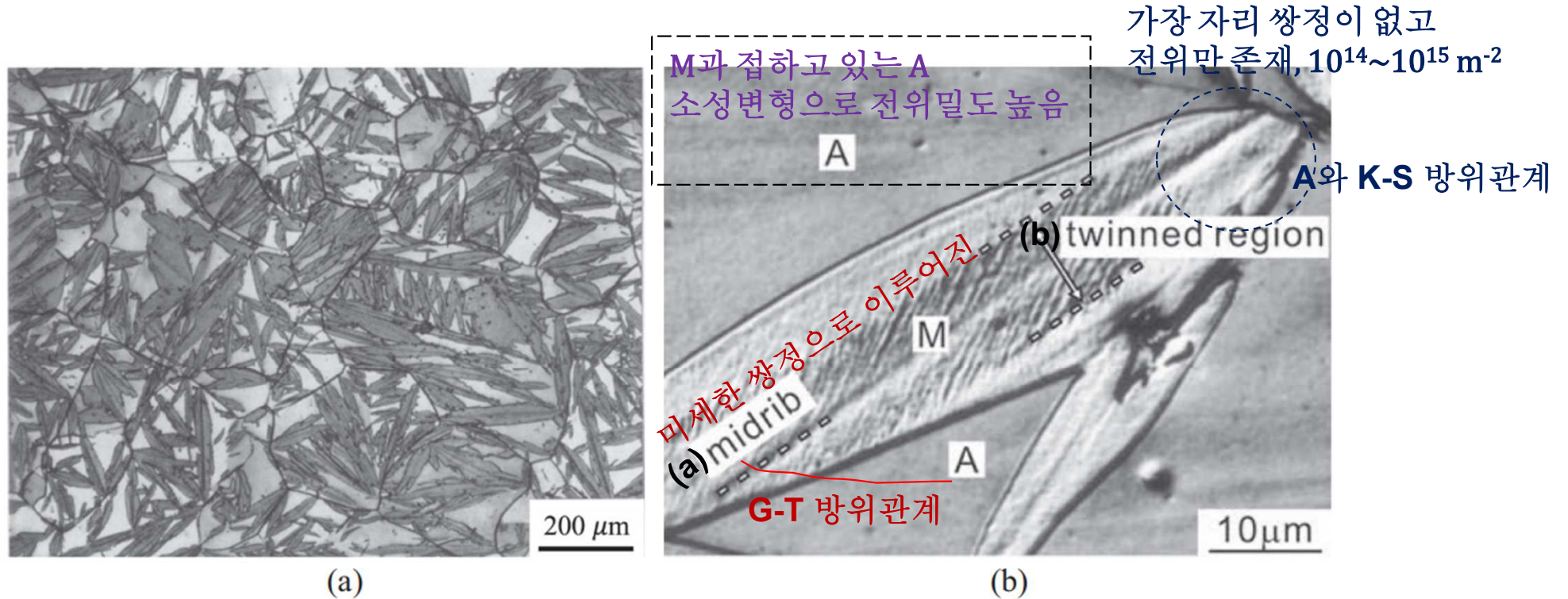


FIGURE 6.9 Examples of lenticular plate martensite. Specimens fully austenitic at room temperature, cooled to below M_s and reheated back to room temperature. Light optical micrographs after polishing and etching. (a) Typical zig-zig pattern. Fe-32.3Ni cooled to 202 K (-71°C) for 150 mins. (Reprinted by permission from Springer Nature Customer Service Centre GmbH: Springer, *Metallurgical and Materials Transactions A*, **23A**:2987–2998, Distributed-activation kinetics of heterogeneous martensitic nucleation, M. Lin, G.B. Olson and M. Cohen (1992).) (b) Detail of the internal structure of a lenticular plate in Fe-33Ni (M_s 171 K, -102°C). A = austenite, M = martensite. (Reprinted from *Acta Materialia*, Vol. 57, A. Shibata, S. Morito, T. Furuhashi, T. Maki, Substructures of lenticular martensites with different martensite start temperatures in ferrous alloys, 483–492 (2009), with permission from Elsevier.)

Q. Crystallography: Why tetragonal Fe-C martensite?

Why tetragonal Fe-C martensite?

- At this point, it is worth stopping to ask why a tetragonal martensite forms in iron. The answer has to do with the preferred site for carbon as an interstitial impurity in bcc Fe.
- Remember: Fe-C martensites are unusual for being so strong (& brittle). Most martensites are not significantly stronger than their parent phases.
- Interstitial sites:
 - fcc: octahedral sites radius= 0.052 nm
tetrahedral sites radius= 0.028 nm
 - bcc: octahedral sites radius= 0.019 nm
tetrahedral sites radius= 0.036 nm
- Carbon atom radius = 0.08 nm.
- Surprisingly, it occupies the octahedral site in the bcc Fe structure, despite the smaller size of this site (compared to the tetrahedral sites) presumably because of the low modulus in the <100> directions.

6.2.4 Epsilon (ϵ) Martensite

γ 의 SFE (적층결함 E) 낮은 합금강 $\rightarrow \epsilon$ (hcp)이 안정상

e.g. 스테인리스강/Co 합금: M_s 이하 ϵ M 생성

대부분 ϵ M 소성변형의 결과로 생성

\rightarrow Transformation induced plasticity (TRIP): 고강도 고연신

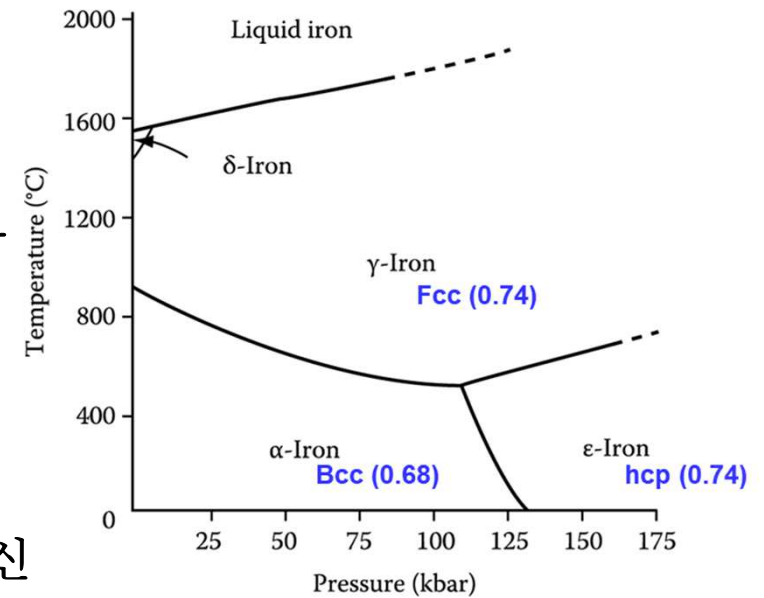
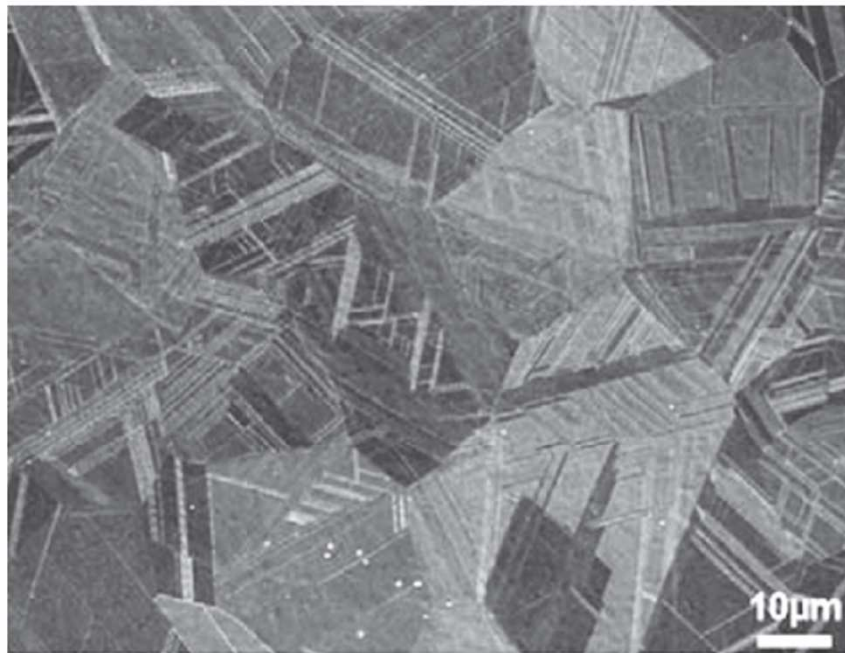
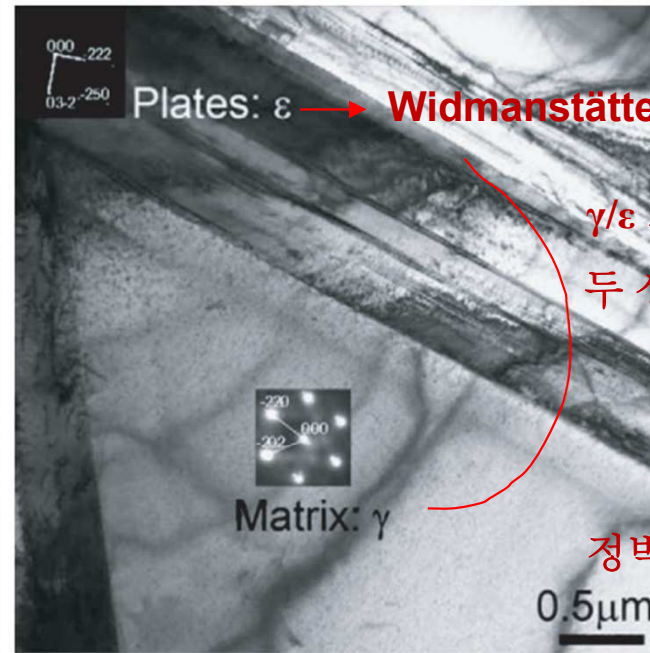


Fig. 1.5 Effect of pressure on the equilibrium phase diagram for pure iron



(a)



(b)

Plates: $\epsilon \rightarrow$ Widmanstätten 조직

γ/ϵ 계면은 완전정합

두 상에서 조밀방향이 서로 평행

$$\{0001\}_{\epsilon} \parallel \{111\}_{\gamma}$$

$$\langle 11\bar{2}0 \rangle_{\epsilon} \parallel \langle 110 \rangle_{\gamma}$$

정벽면은 불변면 변형을 함
(invariant plane strain)

FIGURE 6.16 Epsilon martensite in Fe-24Mn-0.02C alloy after air cooling austenite from 900°C. (a) Scanning electron micrograph showing ϵ -martensite plates in a Widmanstätten pattern in equiaxed austenite grains. (b) Higher magnification transmission electron microscope image showing cross-sections through the ϵ plates.

6.4 Athermal Nucleation and Growth: (a) FCC → HCP ($\gamma \rightarrow \epsilon$ 변태)

④ ϵ Martensite가 핵생성 될 조건 : $-\gamma_{sf} > nF_r$

$\gamma_{sf} < 0 \rightarrow s$ 가 증가할수록 계의 ΔG 가 낮아져도, 전위이동의 저항력 (nF_r)을 극복해야 핵생성 가능

단위면적당 적층결합 E = $\gamma_{sf} = 2nd (\Delta G_{chem}^{\gamma \rightarrow \epsilon} + \Delta G_S) + 2\gamma_i$ (여기서, n = 배열된 전위 개수, d =면간거리)

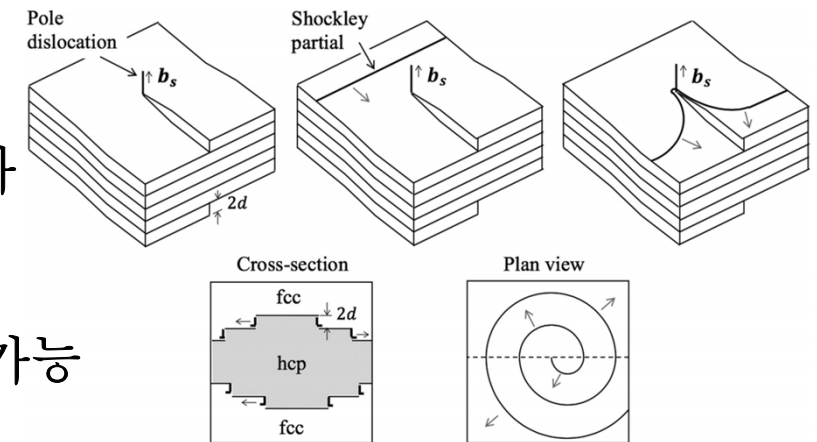
a) $\gamma \rightarrow \epsilon$ 상변태: $\Delta G_{chem}^{\gamma \rightarrow \epsilon}$, b) 정합 탄성 E : ΔG_S , c) 양쪽의 γ/ϵ 정합 계면에너지: $2\gamma_i$ ($T \uparrow$ 시 일부 감소)

nF_r = 격자내 원자들에 의한 전위이동에 대한 저항력 / $-\gamma_{sf}$ = Positive pulling force, S 넓어지도록 당기는 힘.

⑤ ϵ Martensite의 pole mechanism에 의한 Thickening

: 부분 전위가 풀전위를 만나 풀전위 주위 부분전위가 나선모양으로 돌면서 두께 증가

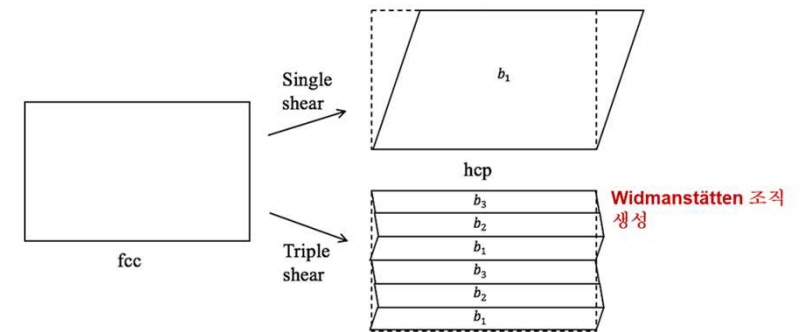
: 10원자층 (~2 nm)의 수백 배 두께 (수 백 nm) 성장 가능



⑥ ϵ Martensite 변태시 변형에너지로 소모 줄이는 방법: 형상 변화 최소화!

: 3가지 다른 Partial D의 Burgers vector 이용한 변형을 통해

Widmanstätten 조직 M생성



6.5 Athermal Nucleation and Growth : (b) FCC → BCC (or BCT) M 변태

: 최인접 원자수가 12 → 8 개로 변화

6.5.1 Atomic movement producing the FCC → BCC/BCT Transformation

- $\gamma \rightarrow \alpha'$:
- (1) Habit plane of M: not distorted by transformation
 - (2) A homogeneous shear (s) parallel to the habit plane
 - (3) ~4% expansion_dilatation normal to the habit plain (lens)

Possible atomic model for martensitic transformation:
the Bain Model: fcc → bct transformation

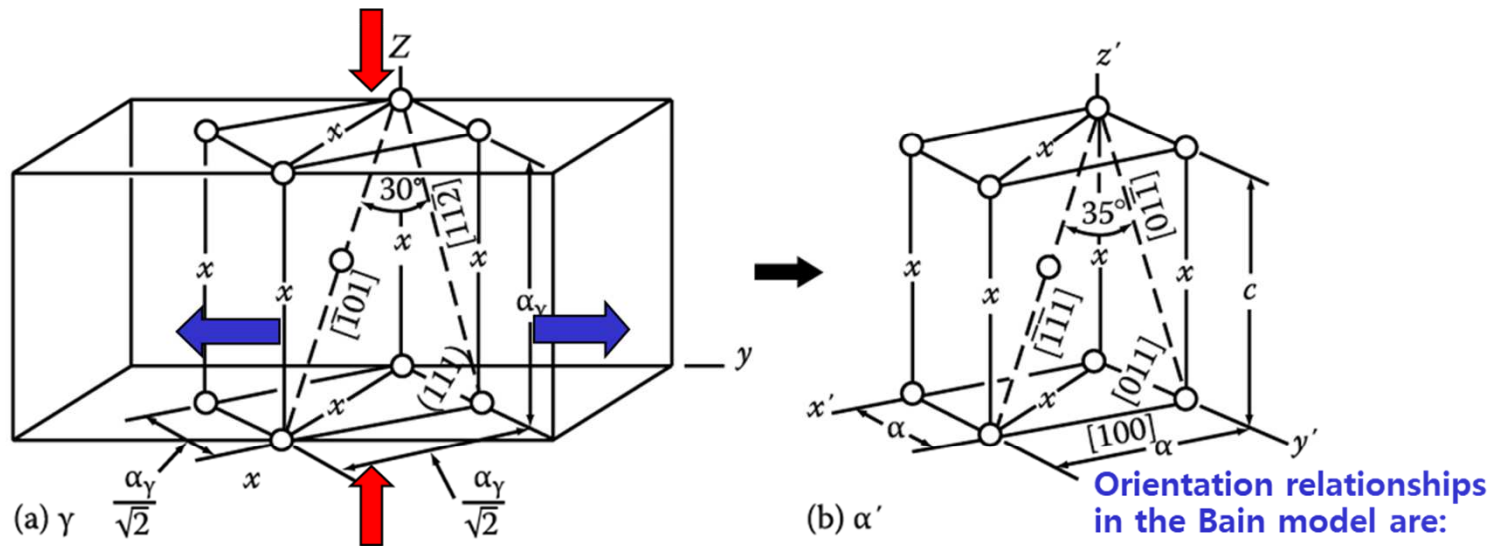


Figure. **Bain correspondence for the $\gamma \rightarrow \alpha'$ transformation.**
 Possible interstitial sites for carbon are shown by crosses.

$$\begin{aligned} (111)_\gamma &\rightarrow (011)_{\alpha'} \\ [\bar{1}01]_\gamma &\rightarrow [\bar{1}11]_{\alpha'} \\ [1\bar{1}0]_\gamma &\rightarrow [100]_{\alpha'} \\ [112]_\gamma &\rightarrow [011]_{\alpha'} \end{aligned}$$

Bain model을 통한 변형시 γ 와 α' 간 방위관계: $(001)_{bcc} \parallel (001)_{fcc}$ and $[010]_{bcc} \parallel [110]_{fcc}$
FCC \rightarrow BCC

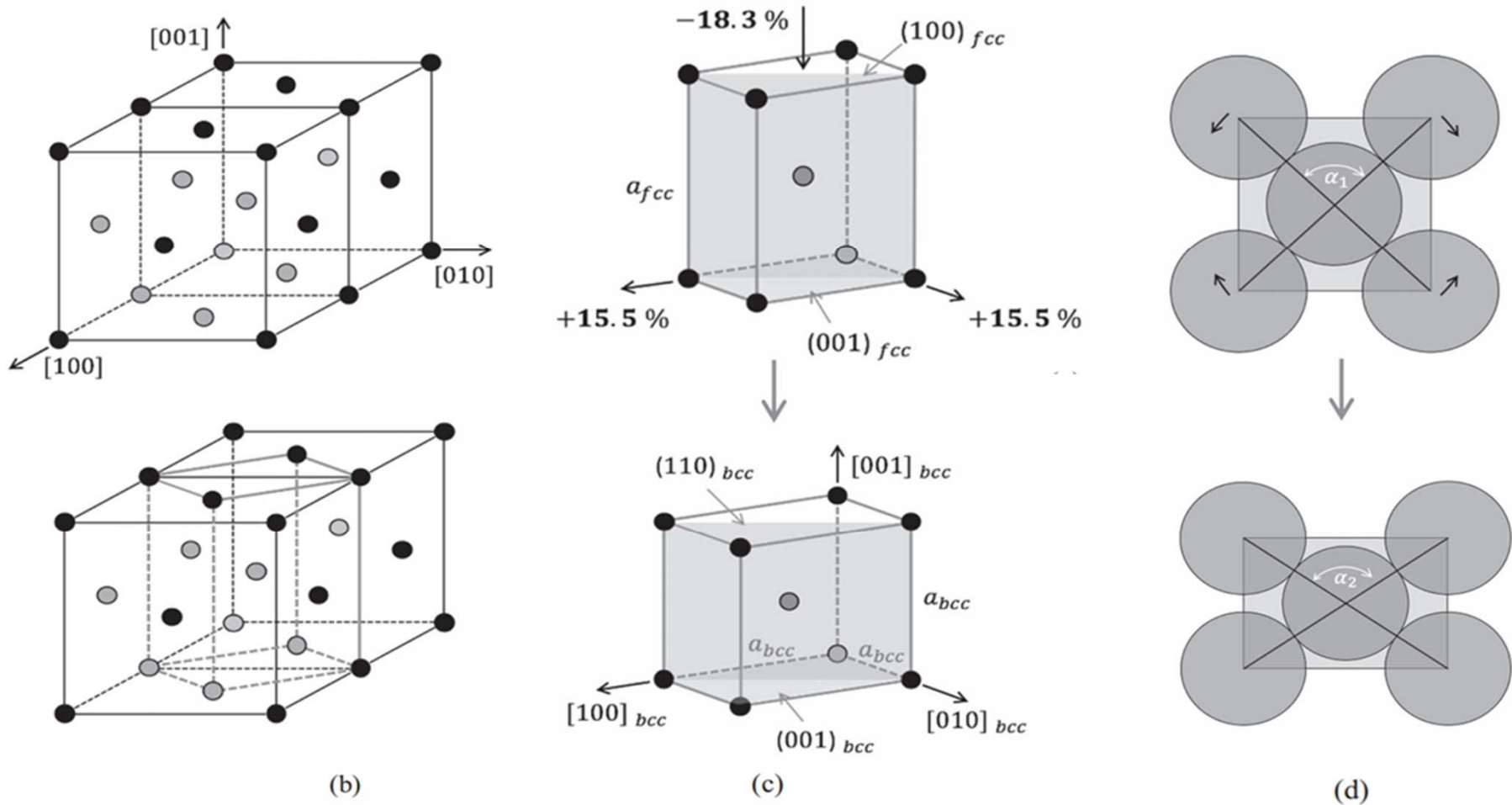


FIGURE 6.28 Bain lattice distortion (or strain) and orientation relationship for a hard sphere atomic model with constant atom diameter. (a) Fcc lattice points forming two unit cells. (b) A bct unit cell in the fcc structure. (c) A compression of 18.3 % along the $[001]_{fcc}$ direction combined with an expansion of all directions in the $(001)_{fcc}$ plane by 15.5 % changes the fcc crystal structure into the bcc structure. The resultant orientation relationship is $(001)_{bcc} \parallel (001)_{fcc}$ and $[010]_{bcc} \parallel [110]_{fcc}$. (d) Fcc and bcc atoms as hard spheres rolling over each other in the transformation as seen on $(100)_{fcc} / (110)_{bcc}$ planes $\alpha_1 = 90^\circ$ and $\alpha_2 = 109.5^\circ$.

* 실험적으로 관찰된 γ 와 α' 간 방위관계: K-S 또는 N-W 방위 관계와 가까움

(a) FCC \rightarrow BCC
K-S 방위관계

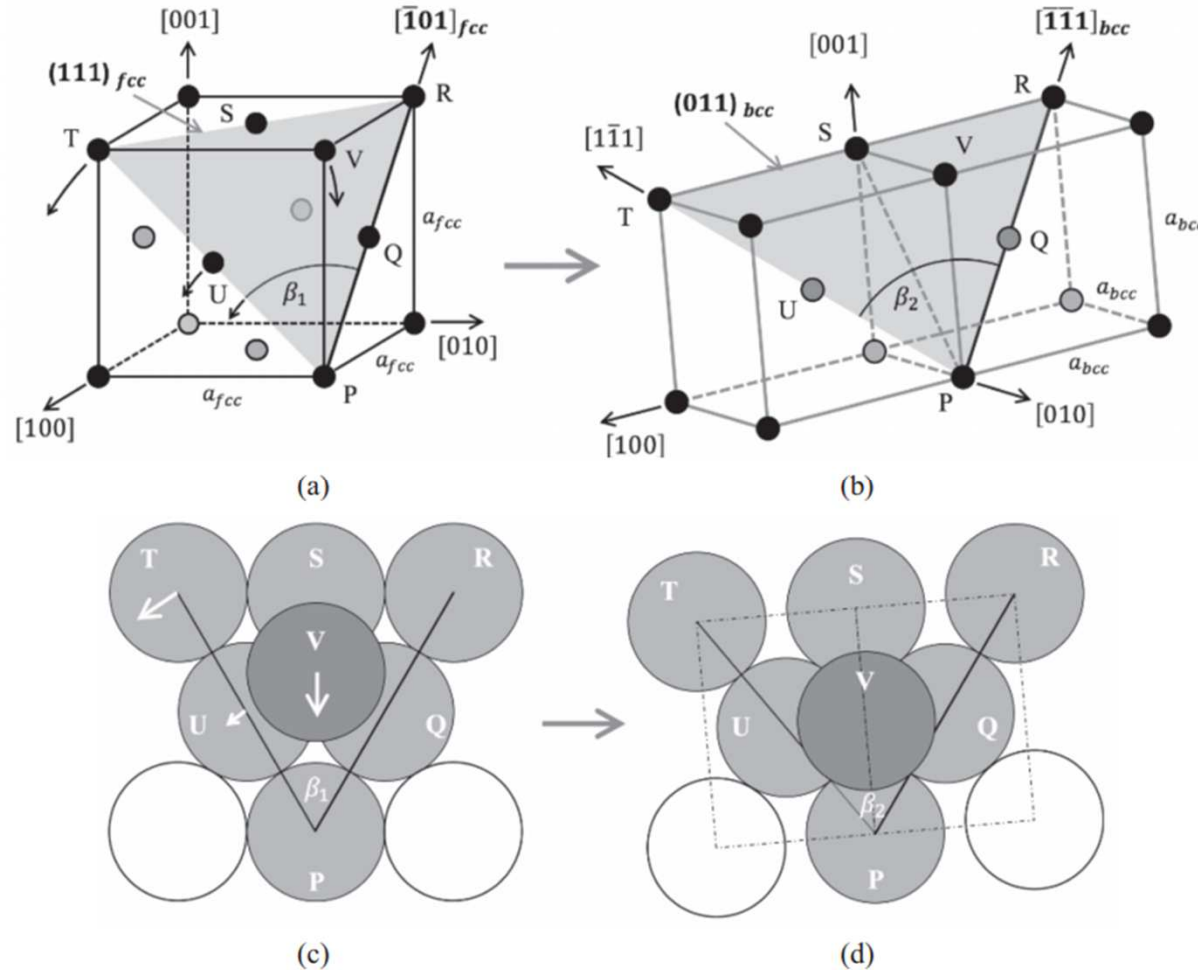


FIGURE 6.29 The Kurdjumov–Sachs (K–S) lattice distortion and orientation relationship for a hard sphere atomic model with constant atom diameter. (a) Fcc lattice with the (111) plane shaded. $\beta_1 = 60^\circ$. Arrows indicate some of the atomic paths during the distortion. (b) Positions of lattice points after the K–S distortion in which the (111) close-packed plane remains unrotated and the PQR close-packed direction remains unrotated and undistorted. $\beta_2 = 70.5^\circ$. (c) Atoms on the (111) close-packed plane shaded in (a) plus atom V that lies in the next $(111)_{fcc} / (110)_{bcc}$ close-packed plane. (d) The final positions of the atoms in (c) showing how atom V moves into its bcc position and the atoms in the fcc close-packed plane become atoms in a bcc close-packed plane by atoms T-S-R and U-Q losing contact. The final orientation relationship is $(011)_{bcc} \parallel (111)_{fcc}$ and $[\bar{1}\bar{1}1]_{bcc} \parallel [\bar{1}01]_{fcc}$.

(b) FCC → BCC
N-W 방위관계

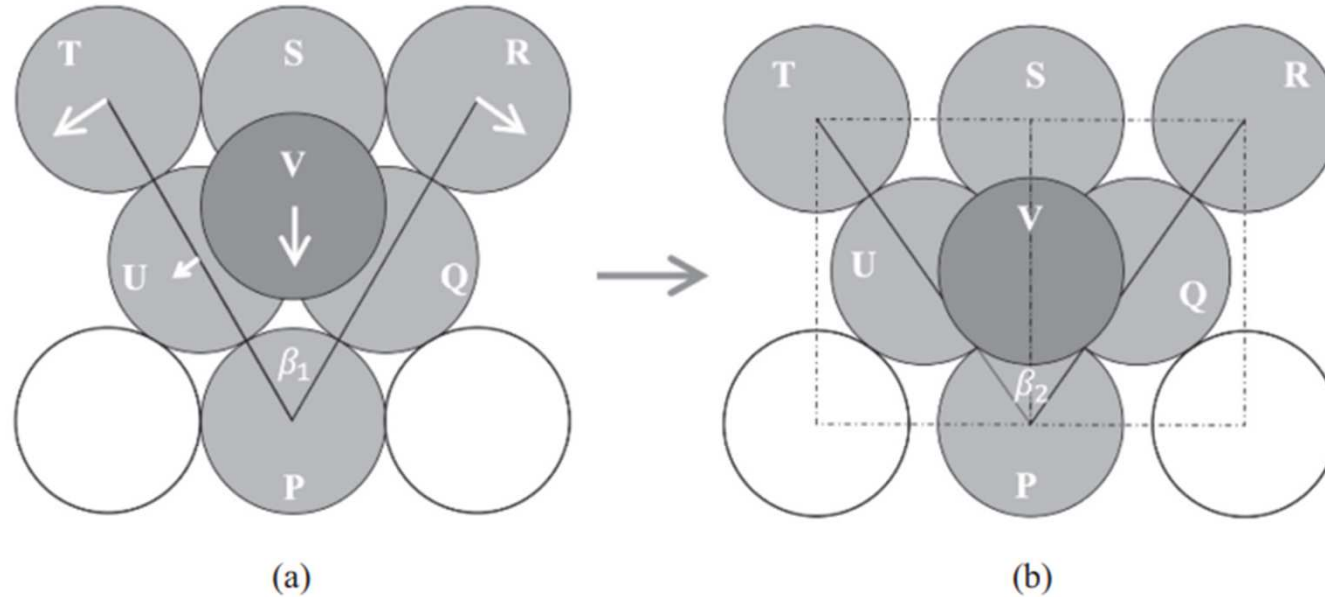


FIGURE 6.30 The Nishiyama (N) lattice distortion and N–W orientation relationship for a hard sphere atomic model with constant atom diameter. Atoms are the same as in Figure 6.29, but now the direction PS remains unrotated during the distortion. This direction is $[\bar{1}\bar{1}2]_{fcc} \parallel [0\bar{1}1]_{bcc}$. Therefore, the resultant orientation relationship is $(110)_{bcc} \parallel (111)_{fcc}$ and $[\bar{1}\bar{1}2]_{fcc} \parallel [0\bar{1}1]_{bcc}$, which is the N–W orientation relationship.

[참고] 위 모델은 모두 **Hard sphere** 모델로 예측해서 원자크기가 같은 것으로 가정했으나, **bcc** 철 원자 지름은 **fcc** 철 원자에 비해 약 **1%** 적다.

* **FCC → BCT Martensite**

: 침입형 원소 (C or N)가 3개의 부격자 중 하나의 부격자에만 위치하는 규칙화 발생시 일어남.

e.g. 고탄소강

탄소원자 M 변태 일어나기전 γ fcc의 8면체 자리에 위치 → bcc 구조로 원자 재배열시 bcc 격자의 하나의 부격자가 됨. 아래는 Bain 변형의 경우, 이러한 변화를 도식화 함.

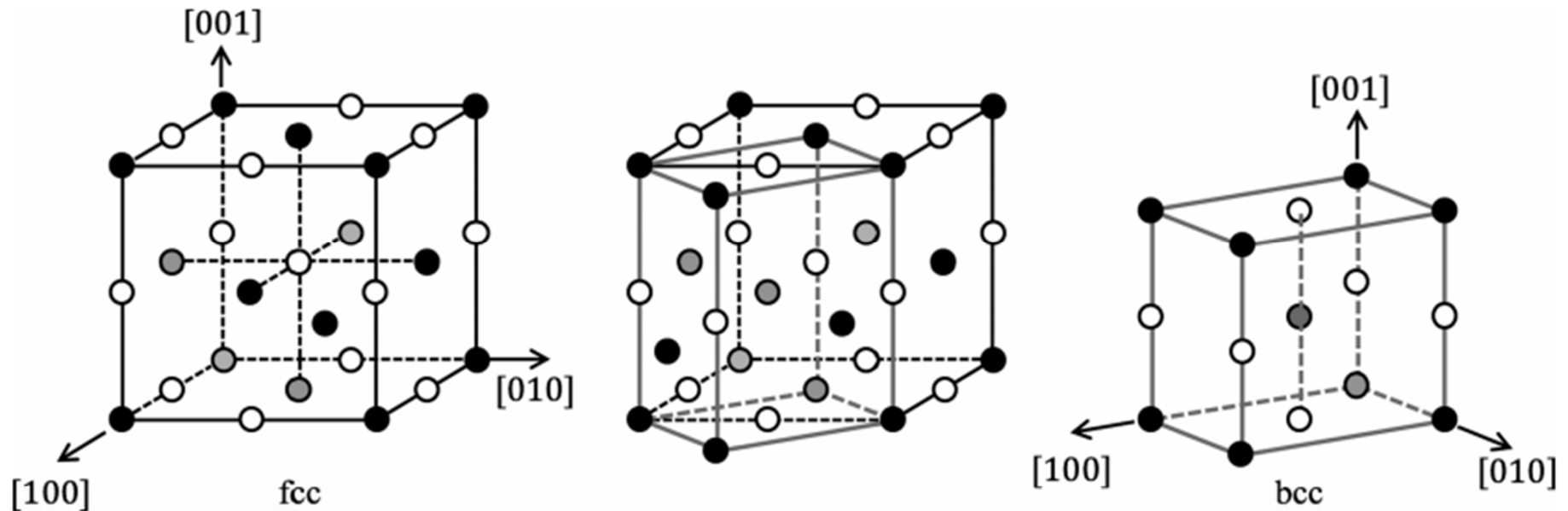


FIGURE 6.31 Octahedral sites in the fcc lattice (open circles) lie midway along the edges and at the center of the unit cell. They are all transformed into O_z octahedral sites in the bcc lattice by compression of the fcc unit cell along the z -axis $[001]$. Similarly, compression along x $[001]$ or y $[001]$ only creates O_x or O_y octahedral sites. Compare with Figure 6.11.

* 이전 내용은 **fcc** 구조를 이루는 원자가 아무런 제약을 받지 않은 상태에서 서로 이동하여 **bcc** 격자 구성하는 방법 고려 → 실제의 경우는 구속된 γ 의 변형으로 변형에너지의 영향을 상쇄할만한 추가적인 구조적 변화 필요

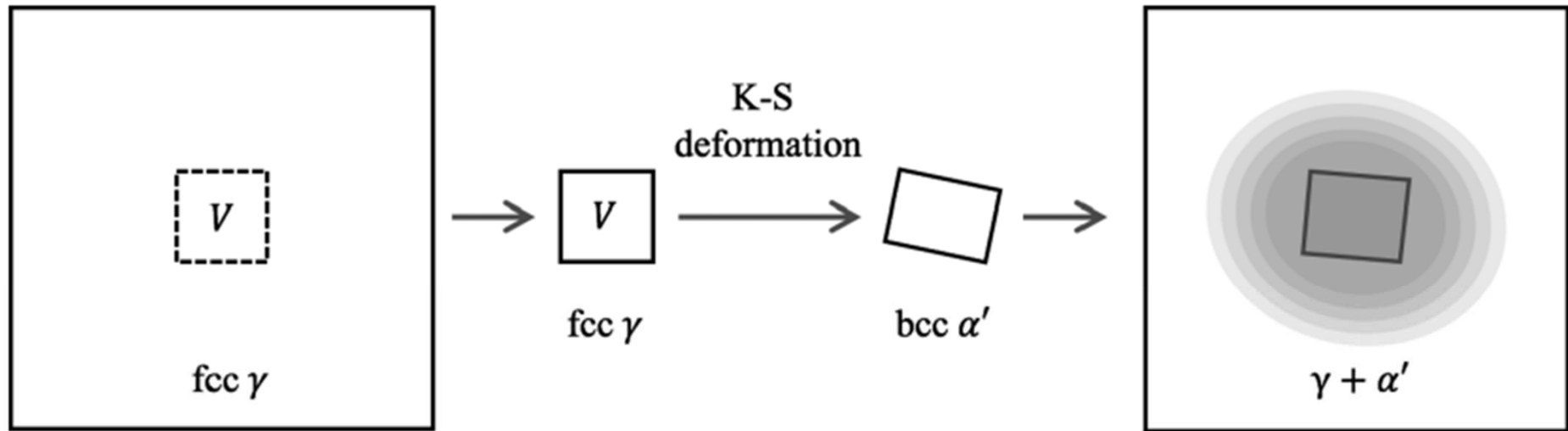


FIGURE 6.32 The source of the strain energy that results if a small volume of fcc austenite is transformed into bcc martensite, e.g., by one of the lattice distortions shown in Figures 6.28–6.30. Strain field shaded.

- (a) **K-S** 변형 또는 서로 다른 유형의 **Bain** 변형이 같이 일어나 변태가 일어난 부분이 작은 쌍정으로 이루어짐
- (b) 변태가 일어난 부분에서 주기적으로 슬립이 일어나 변태가 일어난 부분이 기지와 더 잘 맞도록 함

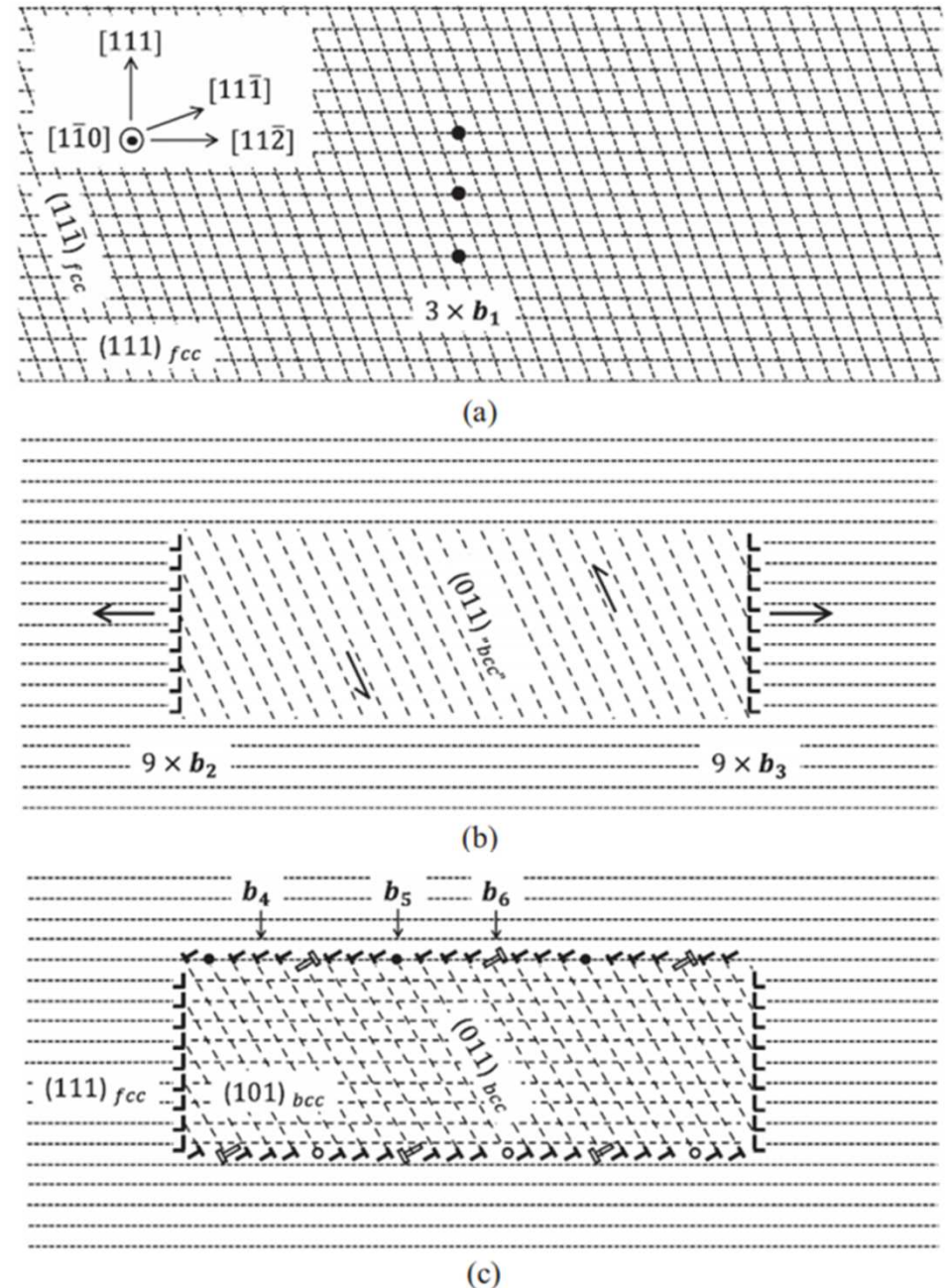
6.5.2 Nucleation and Early Growth of α' Martensite

Figure 6.33 Formation of a partially coherent bcc embryo in an fcc lattice by the dissociation of an array of screw dislocations

① 핵생성 단계에서 **bcc M embryo**는 나선전위 주위 변형장 도움을 받아 총 변형 E 감소, 성장시는 해당사항 없음.

② γ/ε 계면과 달리 γ/α' 계면은 불변면이 아니기 때문에 계면에 상당량의 계면 E 걸림 \rightarrow 원활한 성장을 위해 계면 E 상쇄가 필요

③ 낮은 온도에서 일어나는 M 변태의 경우, M 변형 E를 최소로 하기 위해, 즉 구동력을 최대로 하기 위해 불변면을 habit plane으로 선택함.



- ④ Bain 변형의 3가지 variants로 이루어진 여러 구역의 균집체를 가정하면, 서로 다른 이형의 Bain 변형에 의해 야기된 응력장은 부분적으로 서로 상쇄되어 총 변형 E를 줄임

a) Just above M_s , M embryo 형성

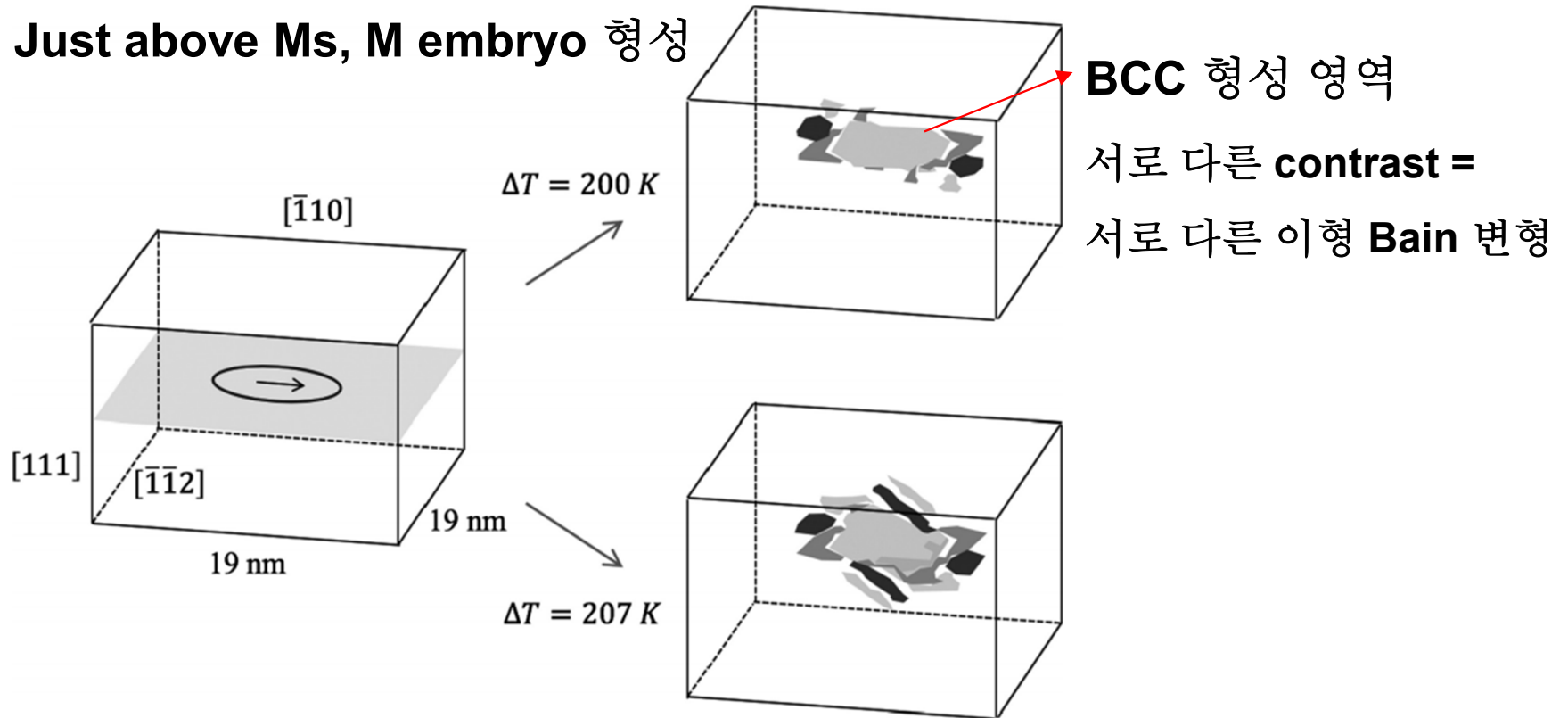
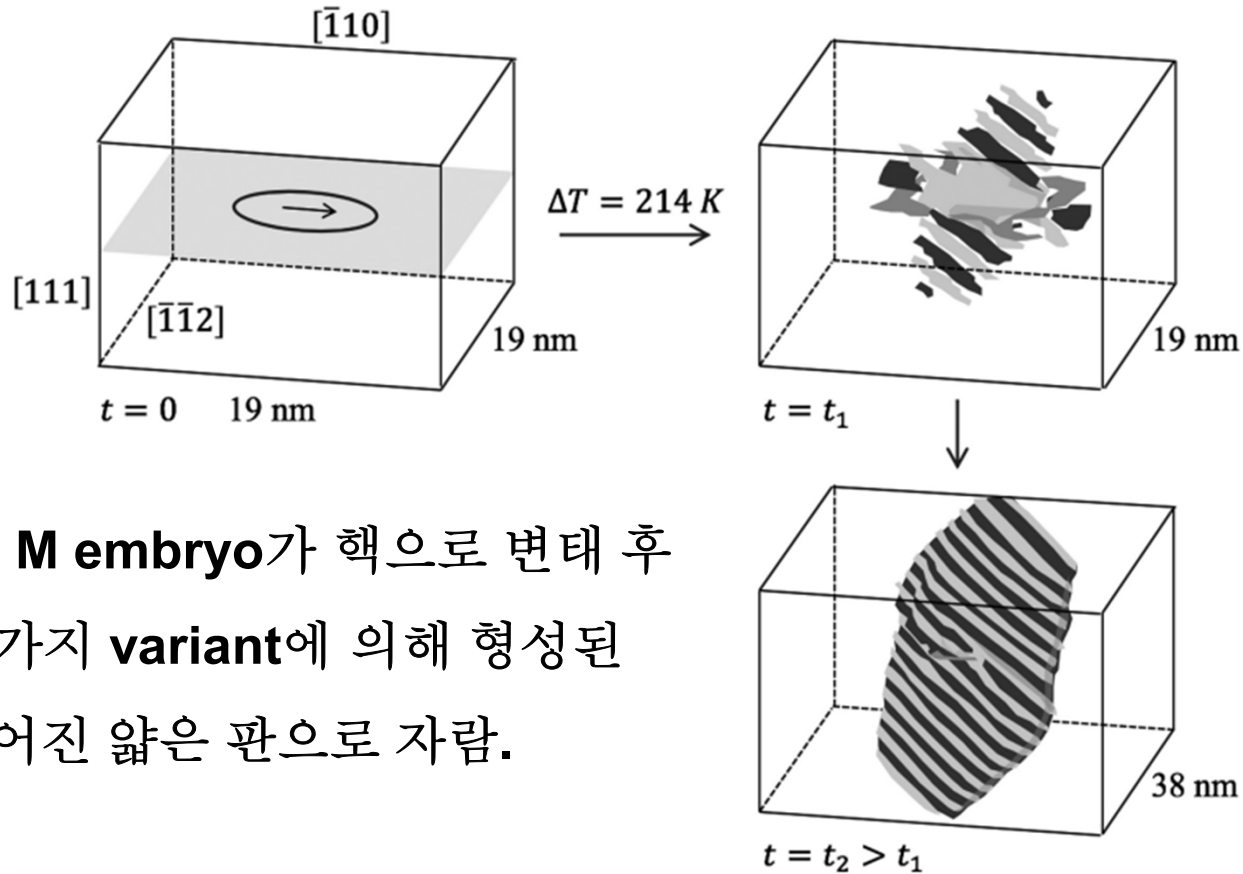


FIGURE 6.34 Phase field microelasticity model of martensite embryo formation in Fe-31 wt.% Ni alloy just above M_s . Only the middle $19 \times 19 \times 13$ nm of the total $\approx 77 \times 77 \times 77$ nm³ modelled volume is shown. Initiating defect is a dislocation loop with a diameter of 8 nm and a Burgers vector $\frac{a}{2}[\bar{1}10]$ lying in the middle of the volume on a (111) plane. The drawings on the right show the stable embryos predicted to develop around the dislocation at the undercoolings $\Delta T = 200$ and 207 K, i.e., the temperatures 205 K (-68°C) and 198 K (-75°C). Within the shaded regions, the atomic configuration is bcc or close to bcc. Each of the three shades of gray represents one of the three Bain strain variants. (Drawings based on data and figures in W. Zhang, Y.M. Jin, A.G. Khachaturyan, *Acta Materialia*, 55:565–574 (2006).)

④ **Bain** 변형의 3가지 **variants**로 이루어진 여러 구역의 균집체를 가정하면, 서로 다른 이형의 **Bain** 변형에 의해 야기된 응력장은 부분적으로 서로 상쇄되어 총 변형 **E**를 줄임



b) 과냉 증가시 **M embryo**가 핵으로 변태 후 **Bain** 변형의 2가지 **variant**에 의해 형성된 쌍정으로 이루어진 얇은 판으로 자람.

FIGURE 6.35 As Figure 6.34, but $\Delta T = 214\text{K}$, i.e., the temperature is 191K (-82°C). The drawings on the right are at two times $t_1 < t_2$. Now, the embryo becomes unstable with respect to growth and develops into a nucleus expanding into a thin twinned plate, where the twins are formed from two variants of the Bain strain with a spacing of $\sim 3\text{nm}$. Note that the volume of the box at t_2 is eight times that at t_1 . (Drawings based on data and figures in W. Zhang, Y.M. Jin, A.G. Khachaturyan, *Acta Materialia*, 55:565–574 (2006).)

* $\gamma \rightarrow \alpha'$ M 변태가 $\gamma \rightarrow \epsilon \rightarrow \alpha'$ 단계를 거치면서 일어날 수도 있음.

6.5.3 Growth of Athermal α' Martensite During Cooling

6.5.3. Growth of Plate and Lath Martensite

M 변태시 불변면을 정벽면으로 하여 평행한 형상을 가지는 경우, 변형 \mathbf{E} 를 최소화 함

→ M 변태는 γ 의 불변면 변형을 통해 일어남

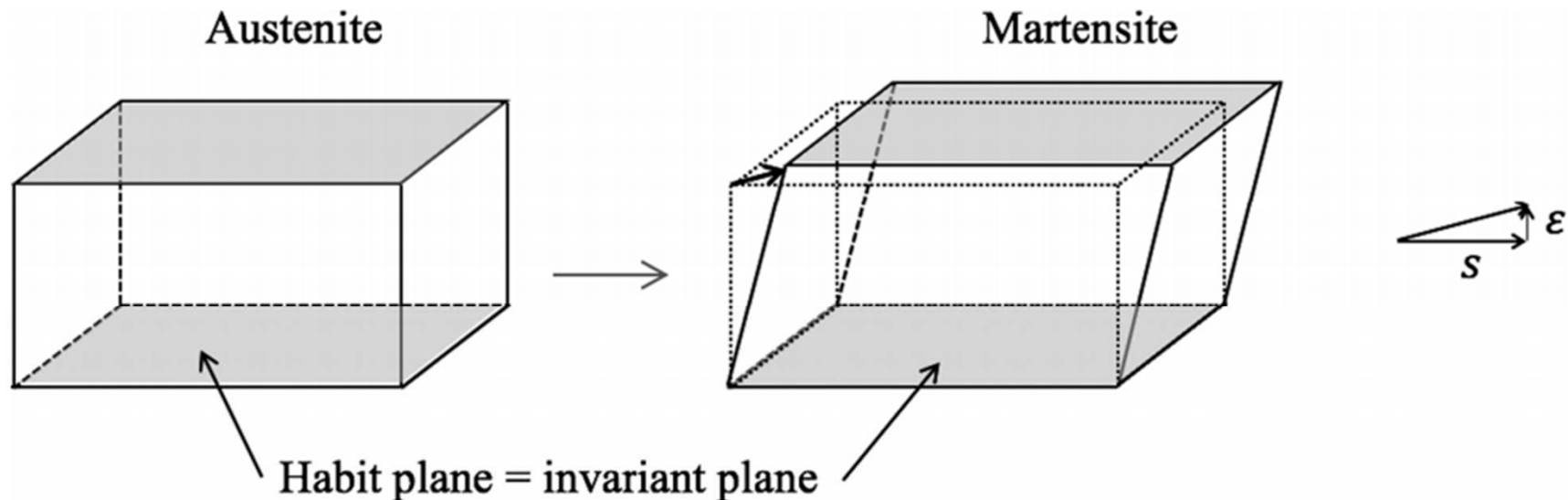


FIGURE 6.36 An invariant-plane strain can comprise a shear, s , parallel to the invariant plane and an expansion or contraction, ϵ , normal to the plane.

→ 위와 같은 불변면 변형이 얇은 타원회전체에서 일어난다고 가정하면,

변형시 변형 \mathbf{E} 가 동일 부피에서 c/a 가 작을수록 감소하는 것을 알 수 있음

즉, M 변태시 변형 \mathbf{E} 최소화를 위해 정벽면이 불변면인 얇은 M 판 형태로 변태가 발생

* 판상 **M** 변태로 인한 전단변형, 변형 영역 및 표면 기복

: 철계 **M**의 경우 $s \approx 0.2-0.3$ (Lath m의 경우 약간 더 큼), $\epsilon \approx 0.002-0.004$

→ **M** 변태시 부피팽창과 같은 크기

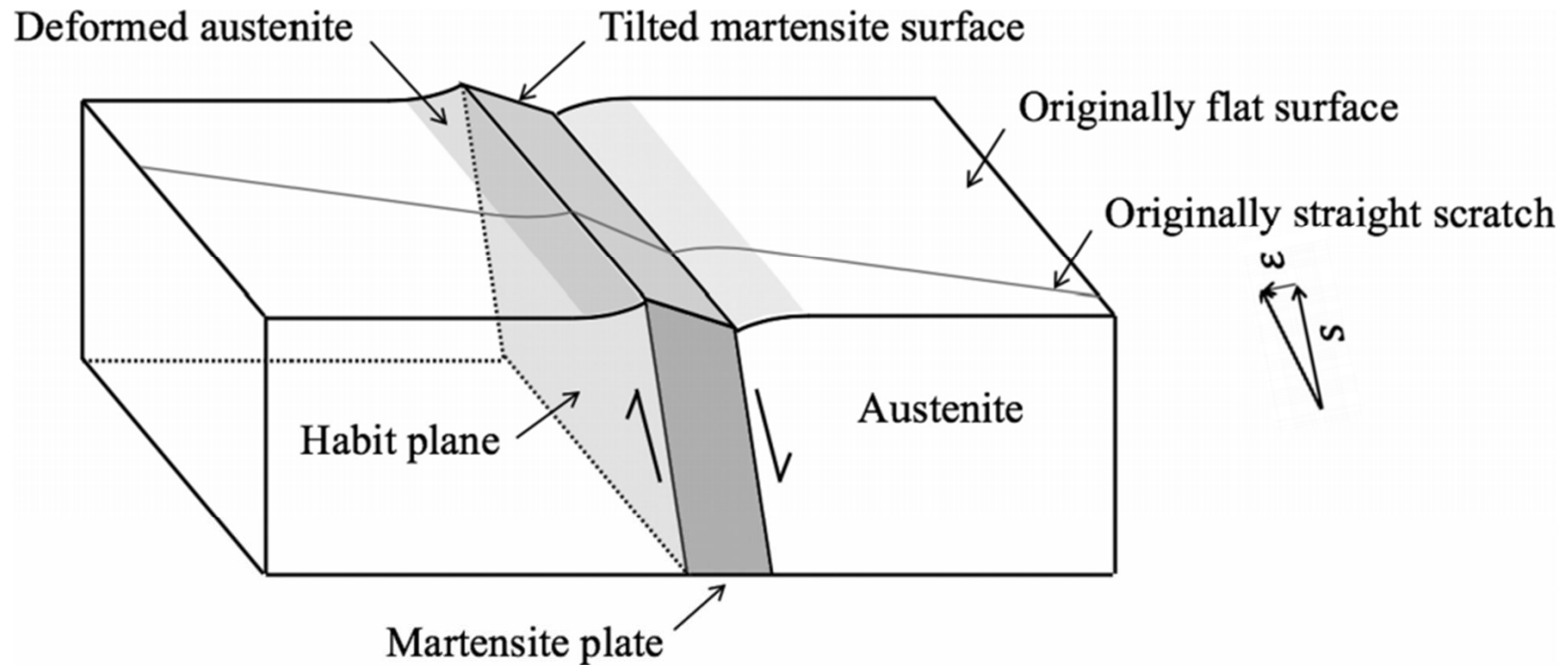


FIGURE 6.37 Surface tilt together with the shear and deformation zones associated with growth of a martensite plate.

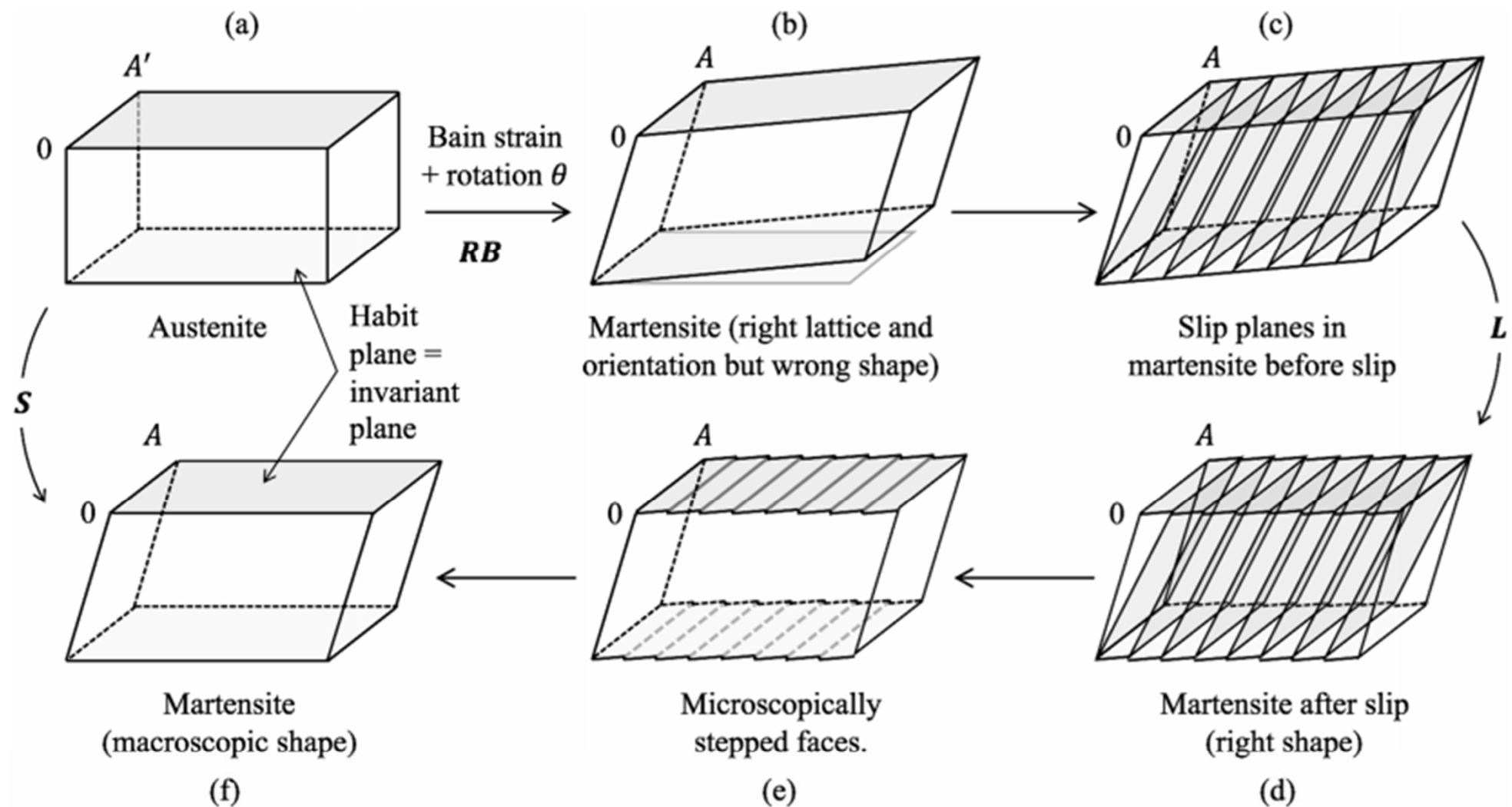


FIGURE 6.82 Generation of an invariant-plane strain by combining the invariant-line strain with slip on planes containing the invariant line. B is the deformation matrix representing the Bain strain, R is the rotation matrix, S is the shape strain, L is the lattice-invariant strain. (e) and (f) are just drawn to illustrate the microscopic and macroscopic features of (d).

* Figure 6.37의 정벽면 원자스케일 분석 결과: 계면은 **Terrace + step** 구조

→ 계면 정합성 증가 & 계면 E 감소

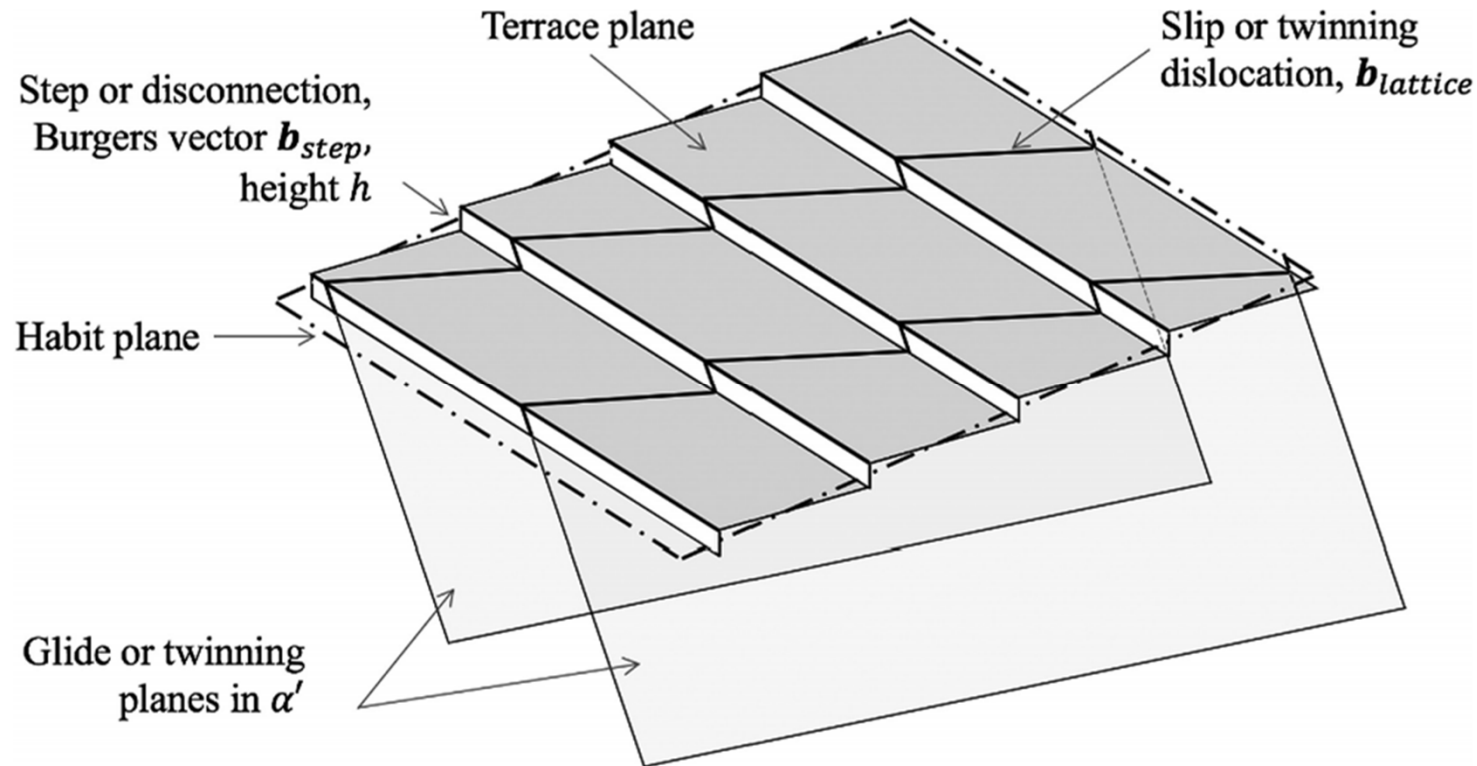


FIGURE 6.38 Schematic illustration showing topological features of the glissile interface between the upper parent phase (γ) and the lower martensite (α'). Terrace planes are parallel to the close-packed $\{111\}_\gamma / \{110\}_{\alpha'}$ planes that have an orientation relationship in the vicinity of the N-W/K-S relationships. The interface is reticulated by disconnections and dislocations. The disconnections are characterized by their step height h and Burgers vector content \mathbf{b}_{step} . Typically, h corresponds to one or two interplanar spacings of the close-packed planes. The slip or twinning dislocations have line and Burgers vectors that are parallel to glide planes in α' . A slip dislocation could have a Burgers vector $\frac{a_{\text{bcc}}}{2} \langle 111 \rangle$ lying on $\{110\}_{\text{bcc}}$. A twinning dislocation is $\frac{a_{\text{bcc}}}{6} \langle 111 \rangle$ lying on $\{112\}_{\text{bcc}}$. The deviation of the habit plane from the $\{111\}_\gamma$ terrace plane is determined by the spacing of the disconnections and their direction relative to the close-packed $\langle 110 \rangle_\gamma$ directions. (The figure is based on the topological model of X. Ma and R.C. Pond, *Journal of Nuclear Materials* **361**:313–321 (2007).)

* 실제 테라스의 폭은 둘레의 위치에 따라 다름 (쌍정으로 이루어진 중앙의 미드립은 표시하지 않음)

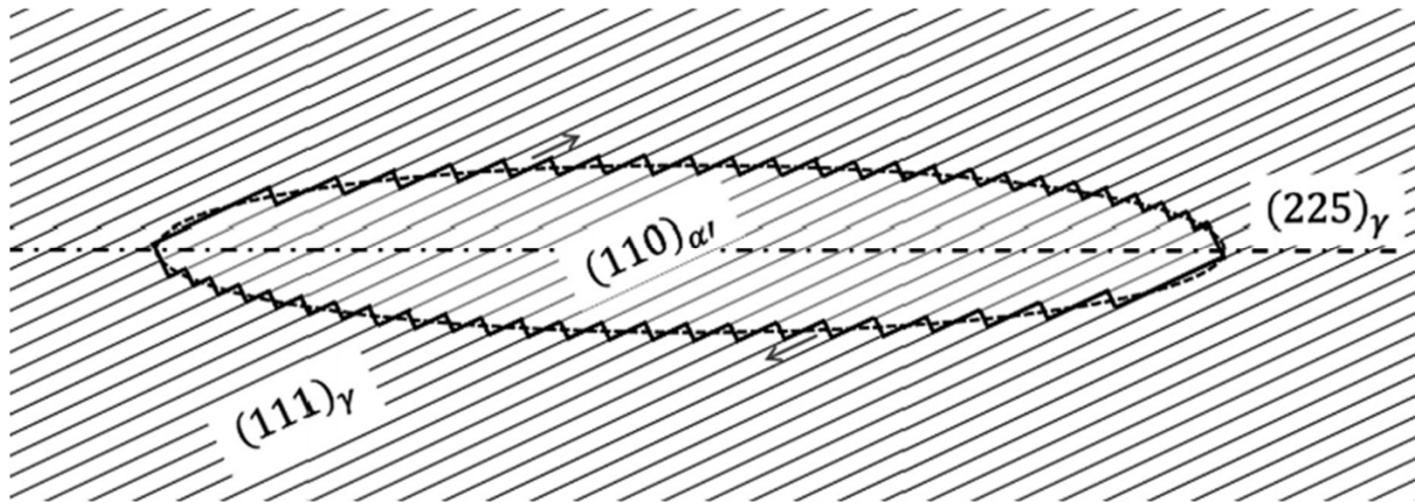


FIGURE 6.39 Schematic two-dimensional cross-section through $\{225\}_{\gamma}$ lenticular plate martensite viewed along $[1\bar{1}0]_{\gamma}$ and showing the parallel $(111)_{\gamma}$ and $(110)_{\alpha'}$ planes. Twinned mid-rib not shown. Terrace width varies around the perimeter.

* 쌍정으로 구성된 M 형성으로 인해 불변면인 $\{225\}_\gamma$ 정벽면이 생기는 과정 도식

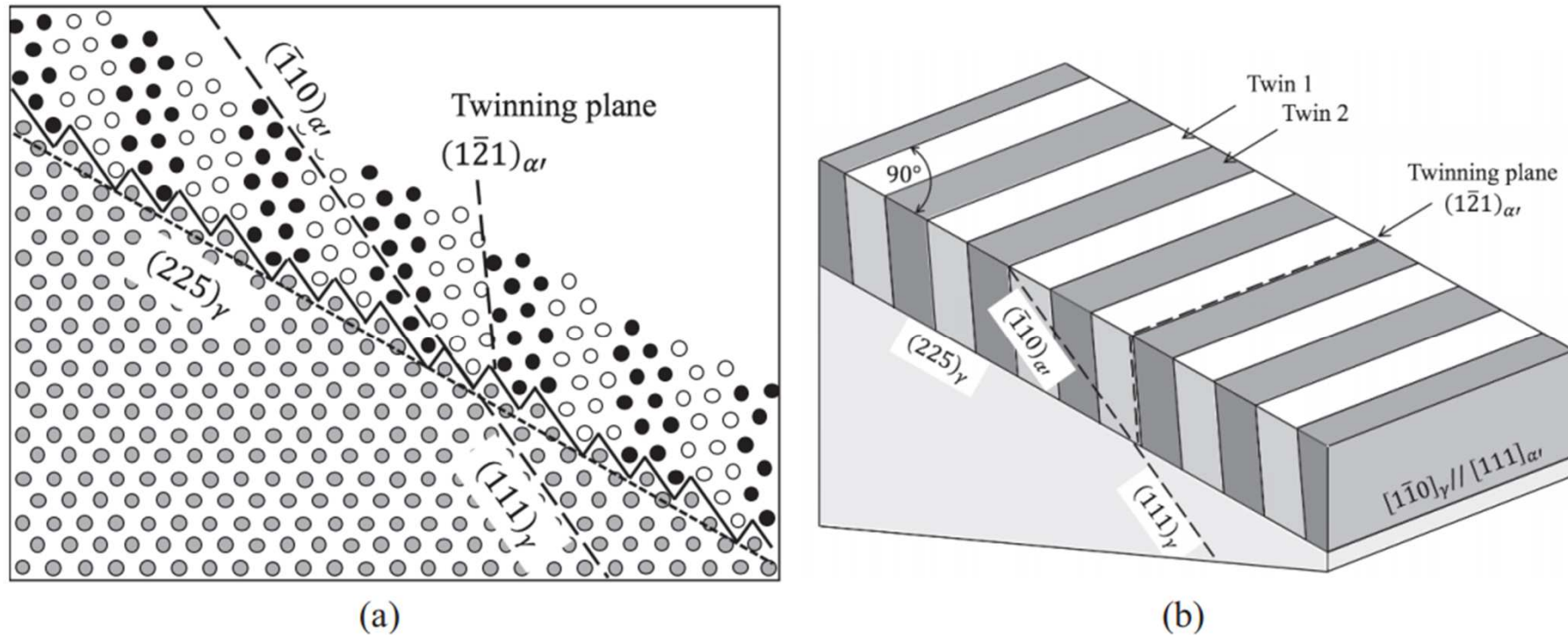


FIGURE 6.40 Schematic illustration of finely twinned α' thin plate martensite with a $(225)_\gamma$ habit plane and $(111)_\gamma \parallel (\bar{1}\bar{1}0)_{\alpha'}$. Light gray atoms are in austenite, black and white atoms are in the bcc martensite twins. Atom diameters are the same in both phases. (a) Atom positions projected along the common $[1\bar{1}0]_\gamma \parallel [111]_{\alpha'}$ directions showing a cross-section through the $(111)_\gamma \parallel (\bar{1}\bar{1}0)_{\alpha'}$ terrace planes and step heights equal to the close-packed plane spacing. Atom positions as given in by A.P. Baur, C. Cayron and R.E. Logé.³⁵ (b) Perspective view.

* 얇은 판상 M의 성장을 위해서는 쌍정에 평행한 가장자리에서 새로운 쌍정의 형성 필요

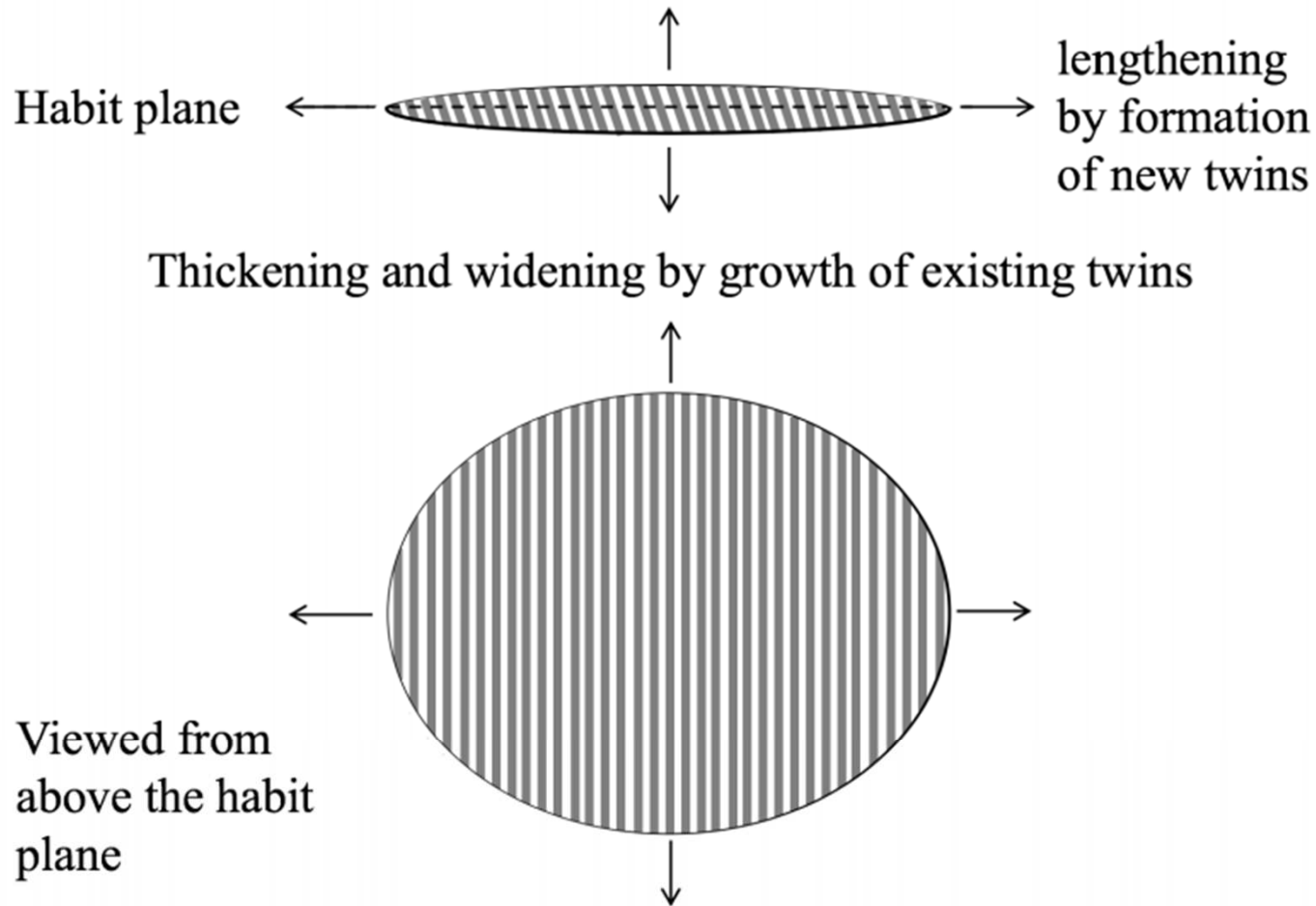


FIGURE 6.41 The growth of thin plate martensite only requires the formation of new twins at the edges parallel to the twins. Here, a plate is shown in elevation and plan view. Thickening and broadening occurs by the extension of existing twins.

* 냉각 중 혼합 M (=Lenticular plate M)의 형성

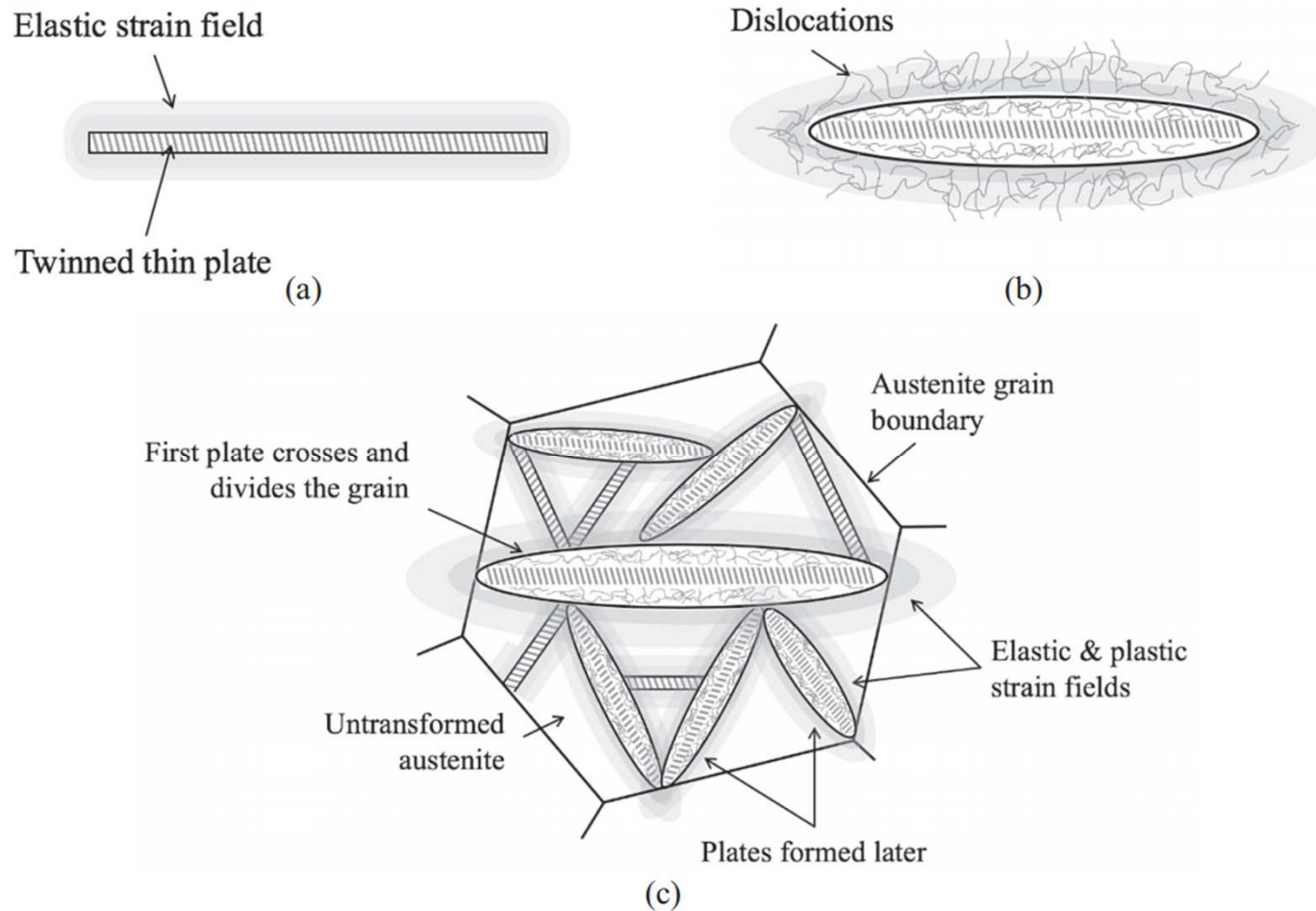


FIGURE 6.42 Formation of lenticular plate martensite during cooling. (a) Twinned plate nucleates and grows behind a glissile interface containing twinning dislocations. Growth creates elastic strains and stresses. (b) Plate thickens by the advance of a glissile interface containing slip dislocations rather than twinning dislocations. Transformation strain leads to elastic stresses and plastic deformation of both phases. (c) During cooling, more plates are nucleated and lengthen as thin twinned plate and possibly thicken. Plates are arrested at grain boundaries and other plates. Zig-zag patterns of plates are often seen.

* **Lath M**의 두께 증가와 폭 확장 기구 : 두께 증가를 위해 **step**이 테라스를 가로질러 이동 / 비슷한 방법으로 폭도 증가

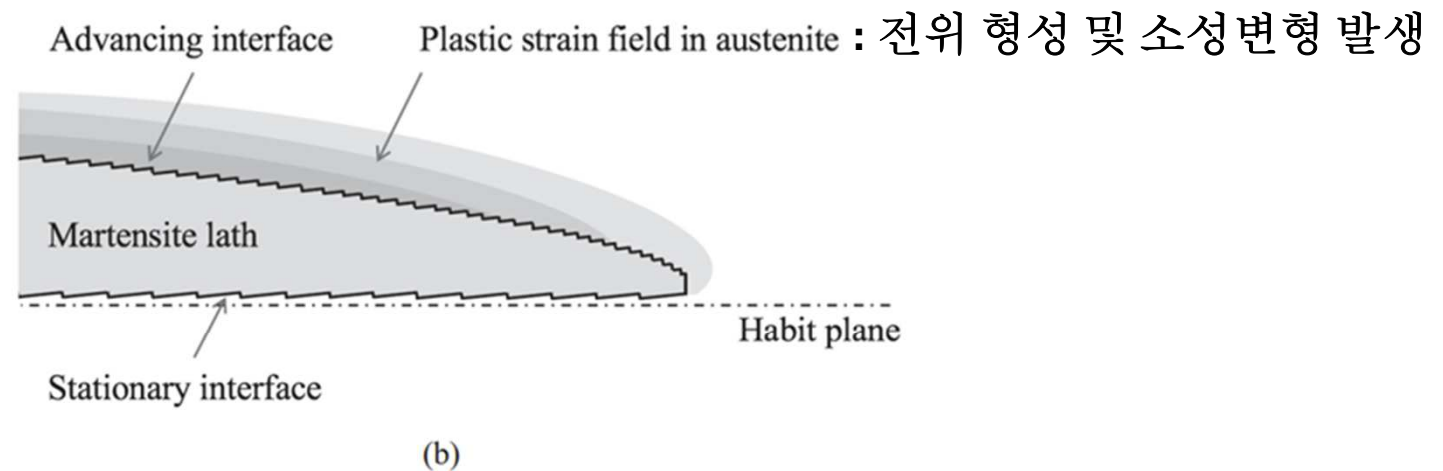
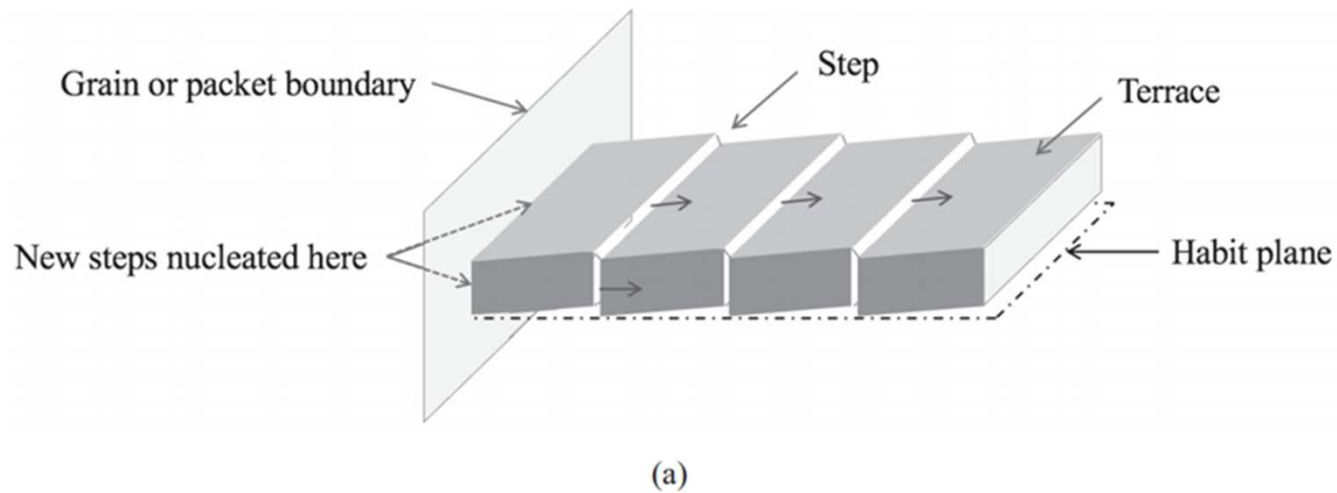


FIGURE 6.43 Possible mechanism for the thickening and broadening of a lath. (a) Schematic perspective view of lath growth. Thickening requires motion of steps across the terraces and the formation of new steps, e.g., at the intersection of the lath with a grain boundary or other interface. Such a mechanism leads to thickening in one direction. Broadening probably occurs in a similar fashion. (b) Lower magnification schematic cross-section through a growing lath. The transformation shape strain leads to the formation of dislocations, i.e., plastic strain, in the surrounding austenite and the lath. Darker shades of gray denote increasing plastic strain.

6.5.4 M start temperature (M_s , 마르텐사이트 시작온도)

* dilatometer (온도에 따른 길이변화 측정)를 이용한 $\gamma \rightarrow \alpha'$ 상변화 거동 측정

혹은 극저온에서 M_s 갖는 고합금계, M_s 온도에서 전기저항 급격히 감소 현상 이용 측정 가능

* 냉각 중 M 부피분율

① Koistinen-Marburger (K-M) 실험식

$$f_r = \exp\{-(T_{KM} - T)/\lambda\}$$

$$f_{\alpha'} = 1 - \exp\{-(T_{KM} - T)/\lambda\}$$

여기서, λ 는 강의 조성에 따라 변하는 상수 ~50-100 K, T_{KM} 은 dilatometer로 측정한 온도로 M_s 보다 약간 낮음
철강의 경우 λ 는 다음 실험식으로 예측 가능

$$\lambda = 100 / (2.24 - 1.07C - 0.07Mn - 0.005Ni - 0.012Cr - 0.01 Mo) \text{ K}$$

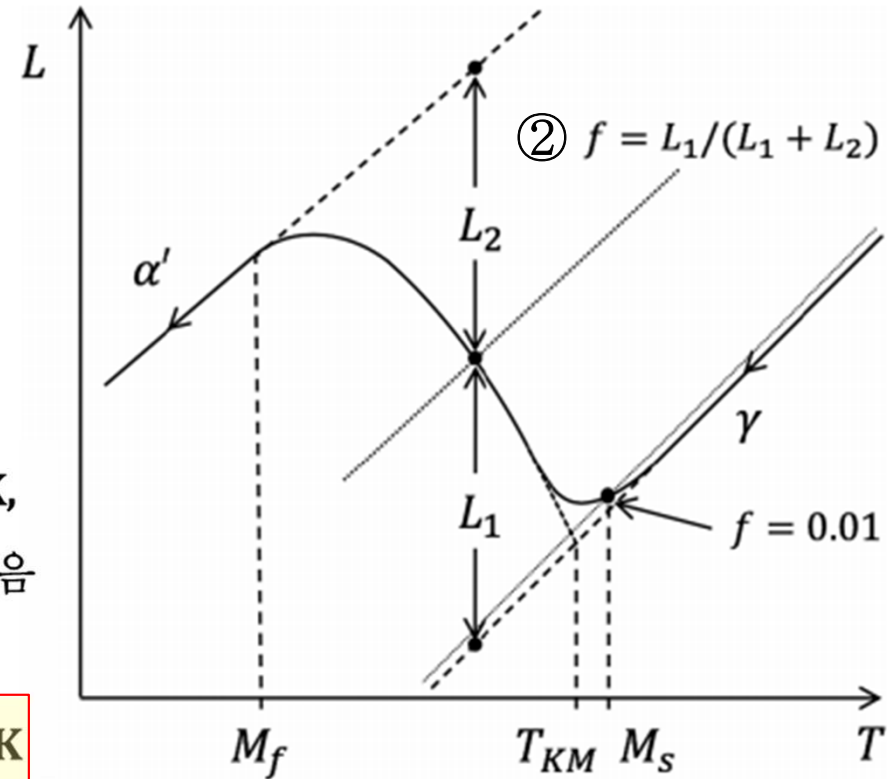


FIGURE 6.45 Determination of M_s , M_f and fraction transformed using dilatometry. Idealized schematic plot shows specimen dimension vs. temperature. The $\gamma \rightarrow \alpha'$ transformation causes a gradual expansion from the curve showing the contraction of γ , $L_\gamma(T)$, to that of α' , $L_{\alpha'}(T)$. An approximate volume fraction of martensite is given by $L_1 / (L_1 + L_2)$. M_s can be defined by the offset method as the point giving 1% martensite ($f = 0.01$). Note that the lines $L_{\alpha'}(T)$ and $L_\gamma(T)$ are not parallel nor exactly straight lines.

6.5.4.1 Lath M vs Plate M ① 형성에 냉각속도의 영향?

: 이론적으로 **Athermal M = M_s** 냉각속도에 무관 (통상 냉각속도 **0.01~100 K/s**)

실제의 경우, 빠른 냉각속도 조건에서 **Lath M** 억제되고 **Plate M** 형성

이러한 **M** 변태 완벽한 비열적 변태 아님/ 시간 영향/ **Lath** 생성속도 < **Plate** 생성속도

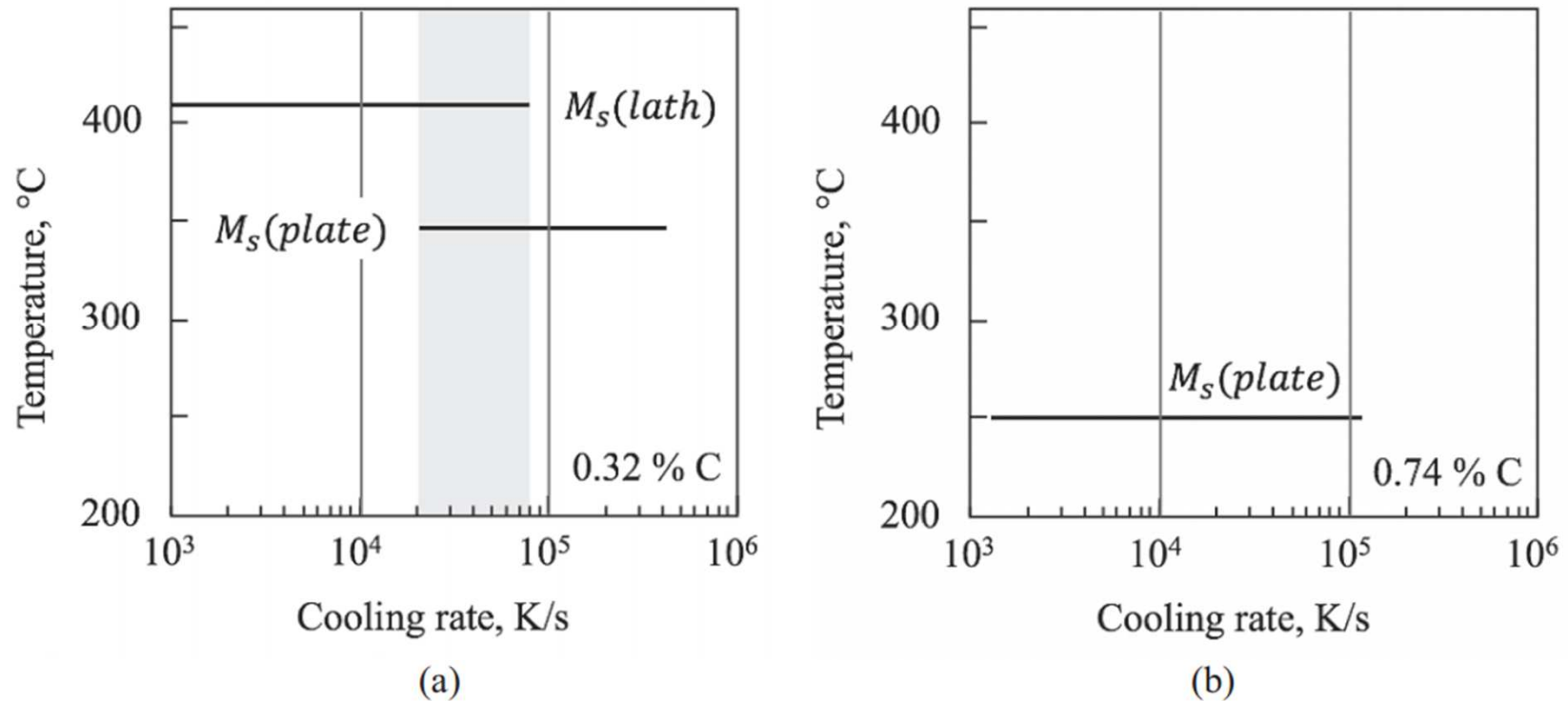


FIGURE 6.46 Some results of experiments showing that the M_s temperature is independent of the cooling rate and that the formation of lath martensite can be suppressed in favor of plate martensite at very high cooling rates. Note that there is no data for what happens beyond the cooling rate range covered by the horizontal M_s lines. (a) Fe – 0.32 wt.% C that is fully lath martensite at normal quenching rates. (b) Fe – 0.74 wt.% C that only forms plate martensite. (Data from D.A. Mirzayev, M.M. Shteynberg, T.N. Ponomareva and V.M. Schastlivtsev, *Phys. Met. Metall.*, 47:102 (1979).)

6.5.4.1 Lath M vs Plate M ② 형성에 조성의 영향

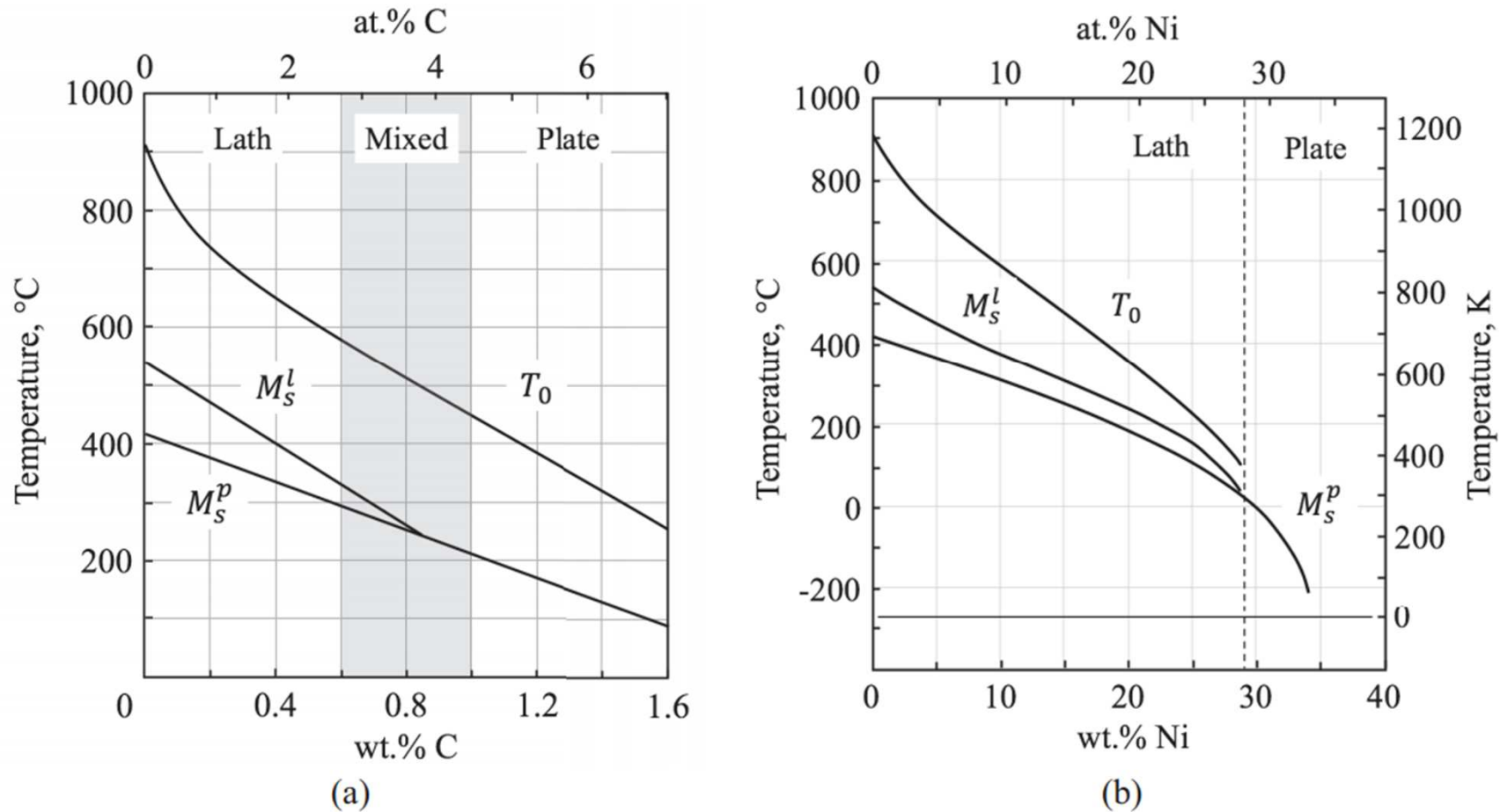


FIGURE 6.47 Martensite start temperatures for lath martensite (M_s^l) and plate martensite (M_s^p) (as given in J.-C. Zhao, *Mater. Sci. Technol.*, **8**:997 (1992). T_0 calculated using Thermo-Calc® 2019a and the database TCFE9. (Courtesy of Vahid Javaheri).) (a) Binary Fe–C alloys. For practical quenching rates, lath martensite predominates up to ~0.6 wt.% C and plate martensite beyond ~1.0 wt.% C. (b) Binary Fe–Ni alloys. Plate martensite predominates beyond ~29 wt.% Ni.

6.5.4.2 M_s 예측을 위한 경험식 (Empirical Formulae) : 합금계 별로 구성 가능

e.g. (a) 저 합금강

$$M_s (\text{°C}) = 550 - 350C - 40Mn - 35V - 20Cr - 17Ni - 10Cu - 10Mo - 8W + 15Co + 30Al$$

(원소기호는 원소의 wt.%)

: Co와 Al을 제외한 대부분의 합금과 원소는 M_s 를 낮추는 역할

(b) Ni 함량이 높은 Fe-Ni-C 합금

$$M_s (\text{°C}) = 641 - 23Ni - 225C$$

6.5.4.3 임계 구동력 (Critical Driving Force) - ΔG_{crit}

M_s 를 결정하는 방법의 개략도와 Lath M으로부터 Plate M으로의 천이

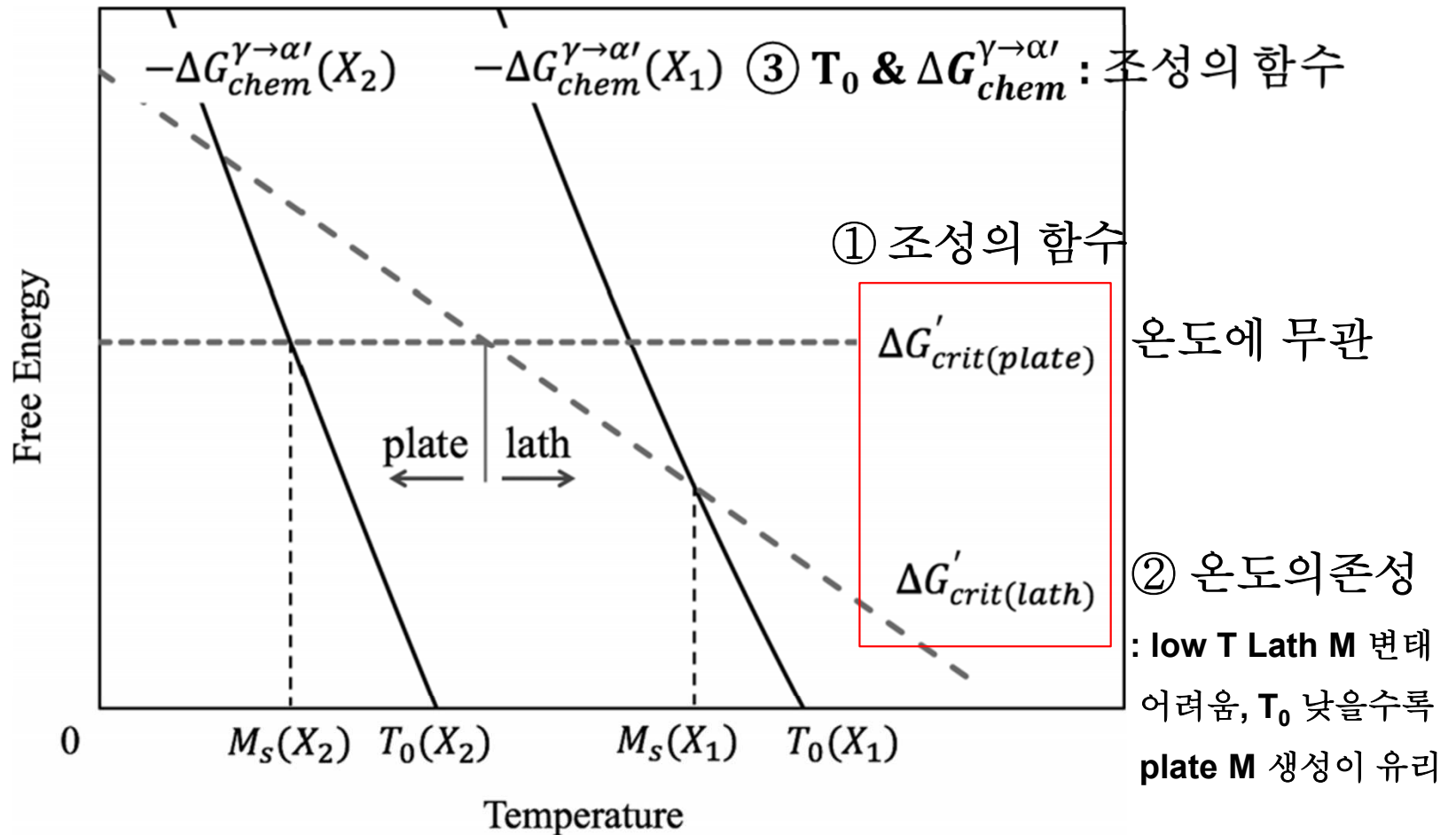


FIGURE 6.48 Schematic illustration of how Equations 6.24 and 6.25 determine the M_s temperature and the transition from lath to plate martensite. Alloy X_2 has a lower T_0 than alloy X_1 . The effect of chemical composition on the functions f_p and f_l and thereby the vertical positions of the lines $\Delta G'_{crit(plate)}$ and $\Delta G'_{crit(lath)}$ has been ignored for clarity.

변태 저항력

변태 구동력

$$\Delta G_{crit} = \Delta G'_{crit} + \Delta G_{s(gs)} + \Delta G_{disl} = - \Delta G_{chem}^{\gamma \rightarrow \alpha'} + \Delta G_{stress} + \Delta G_{mag}$$

화학 응력 외부자기장

작은 **GS** 경우
극복해야하는
추가 변형 **E**

전위가 있는 경우
 γ/α' 계면이
통과하는데 추가 **E**

6.5.4.4 결정립 크기가 M_s 에 미치는 영향 :

- ① 300 μm 이하 작은 결정립 갖는 경우 M_s 감소 ② 작은 결정립 경우 추가 **Strain E** 필요

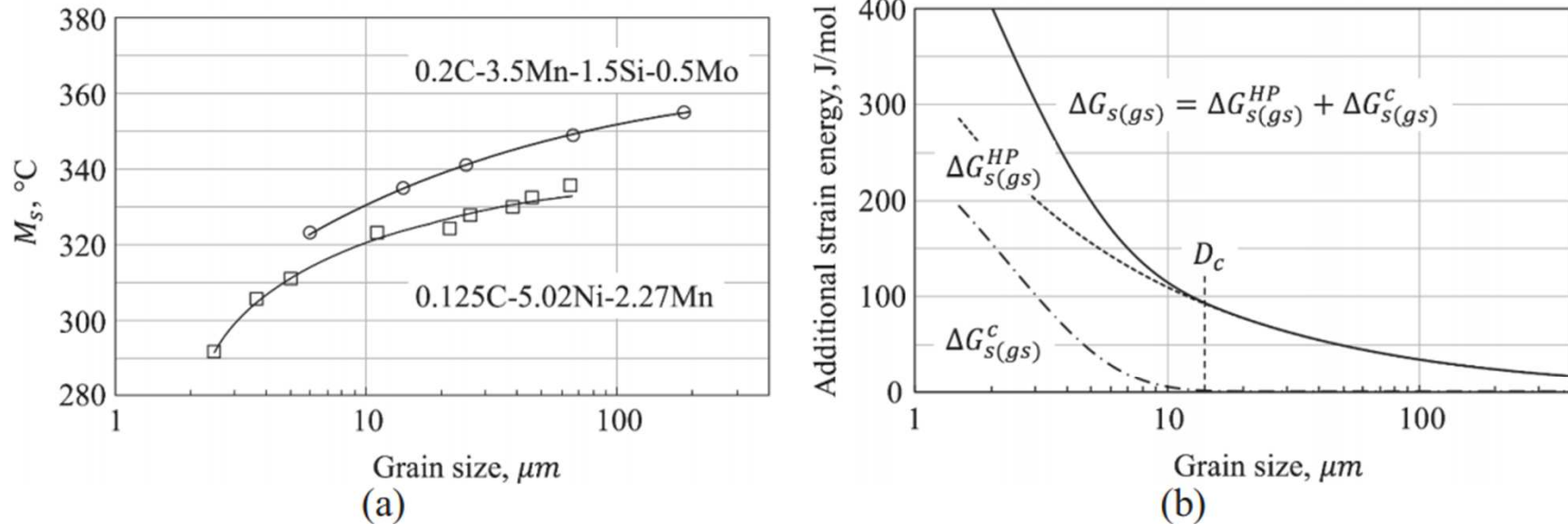


FIGURE 6.49 (a) The effect of austenite grain size on M_s as defined by the formation of a volume fraction of 1 % martensite. (Circles from C. Celada-Casero, J. Sietsma, M.J. Santofimia, *Materials and Design*, **167**:107625 (2019) cover the range 6–185 μm . Squares from H-S. Yang and H.K.D.H. Bhadeshia, *Scripta Materialia*, **60**:493–495 (2009) cover the range 2.5–65 μm . Error bars have been omitted.) (b) The additional strain energy to be overcome by a higher chemical free energy release.

a) 결정립 미세화 M 변태시 소성변형의 저항 증가: $\Delta G_{s(gs)}^{HP} \approx 350/\sqrt{D_\gamma}$ J/mol

b) 결정립 (패킷 크기) 미세화 c/a 가 증가하여 추가 변형 E 발생: $\Delta G_{s(gs)}^C \approx 370 \exp(-\frac{6D_\gamma}{D_c})$ J/mol

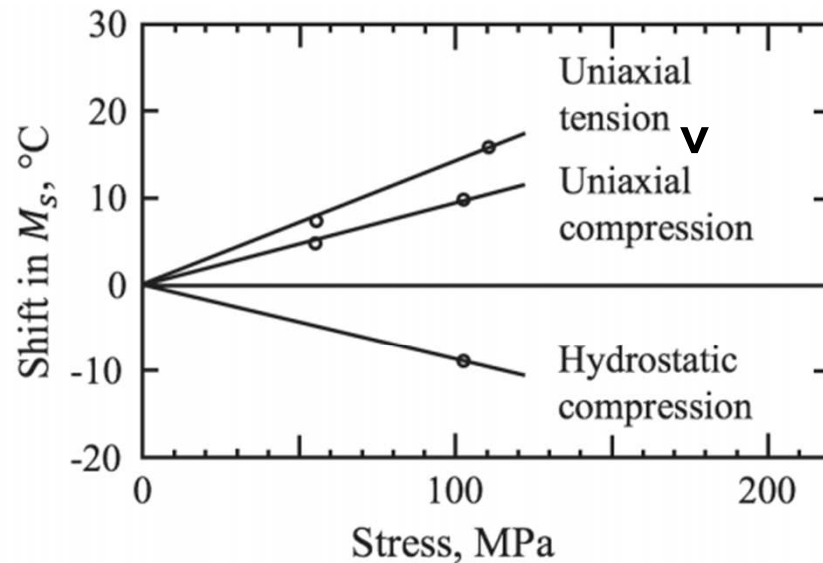
여기서, $D_\gamma = \gamma$ 의 결정립 크기, $D_c =$ 패킷과 결정립 크기 간 관계 상수 e.g. 저탄소강 $\sim 14 \mu\text{m}$

6.5.4.5 탄성응력이 M_s 에 미치는 영향 : $\Delta G_{stress} =$ 응력에 의한 변태 구동력 $(+)$ 면 $M_s \uparrow$

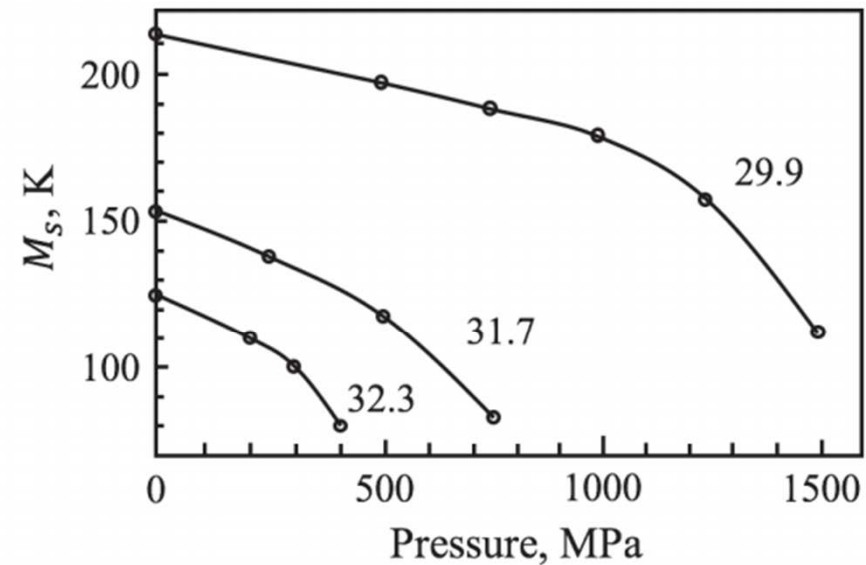
① 일축인장 or 압축 인가시 ΔG_{stress} 증가 $\rightarrow M_s$ 증가 ② 정수압 인가시 $\Delta G_{stress} = P \cdot \epsilon$

일축인장시 ΔG_{stress} 일축압축 보다 큼

정수압 인장시 P 양수, 정수압 압축시 P 음수
변태시 부피증가하면 정수압 압축인가 $M_s \downarrow$



(a)



(b)

FIGURE 6.50 The effect of applied stress on M_s . (a) Lines for uniaxial stresses apply to Fe–20Ni–0.5C alloy. Line for hydrostatic compression applies to Fe–30Ni alloy (weight percentages). (Based on data in J.R. Patel and M. Cohen, *Acta Metallurgica*, 1:531–538 (1953).) Initial slopes are approximately 14°C/100 MPa and 10°C/100 MPa for uniaxial tension and compression respectively, and –9°C/100 MPa for hydrostatic compression. (b) Effect of hydrostatic compression on Fe–Ni alloys. Numbers refer to nickel contents in at.%. (Data points from K. Kakeshita and T. Saburi, *Philosophical Magazine B*, 80:171–181 (2000).)

6.5.4.6 소성변형이 M_s 에 미치는 영향 : 소성변형 $\rightarrow \gamma$ 내 전위밀도 증가

(a) 더 강력한 새로운 핵생성 자리를 제공하여 M_s 증가

(b) 부분정합을 이루는 활주 계면의 이동에 대한 저항이 증가로 더 큰 구동력 필요 M_s 감소

(a)와 (b)의 경쟁 ...소성변형으로 γ 의 전위밀도가 얼마나 영향 받았는지 중요

6.5.4.7 외부자기장이 M_s 에 미치는 영향 :

자기장 인가시 상자성 γ 와 강자성 bcc/bct M 자유E 차이 증가

$\gamma \rightarrow \alpha'$ 변태구동력이 $-\Delta G_{chem}^{\gamma \rightarrow \alpha'}$ 에서 $-\Delta G_{chem}^{\gamma \rightarrow \alpha'} + \Delta G_{mag}$ 으로 증가

= 약 2.5 K/Tesla 비율로 M_s 증가

$$\Delta G_{crit} = \overbrace{\Delta G'_{crit} + \Delta G_{s(gs)} + \Delta G_{disl}}^{\text{변태 저항력}} = \overbrace{-\Delta G_{chem}^{\gamma \rightarrow \alpha'} + \Delta G_{stress} + \Delta G_{mag}}^{\text{변태 구동력}}$$

화학
응력
외부자기장

작은 **GS** 경우
극복해야하는
추가 변형 **E**

전위가 있는 경우
 γ/α' 계면이
통과하는데 추가 **E**

결정립 미세화 or γ 소성변형으로 전위밀도 증가 : $\Delta G_{crit} \uparrow \rightarrow M_s \downarrow$

6.5.5 변형 유기 비열적 α' M (Strain-induced athermal α' M)

: 소성변형으로 인한 비열적 M의 핵생성 및 성장을 위한 새로운 자리 생성 거동

변형시 변형 유기 M 변태 일어나는 경우(TRIP) : 가공경화속도 (S-S 커브 기울기) 증가
 추가가공경화를 통한 네킹지연 총연신율 증가

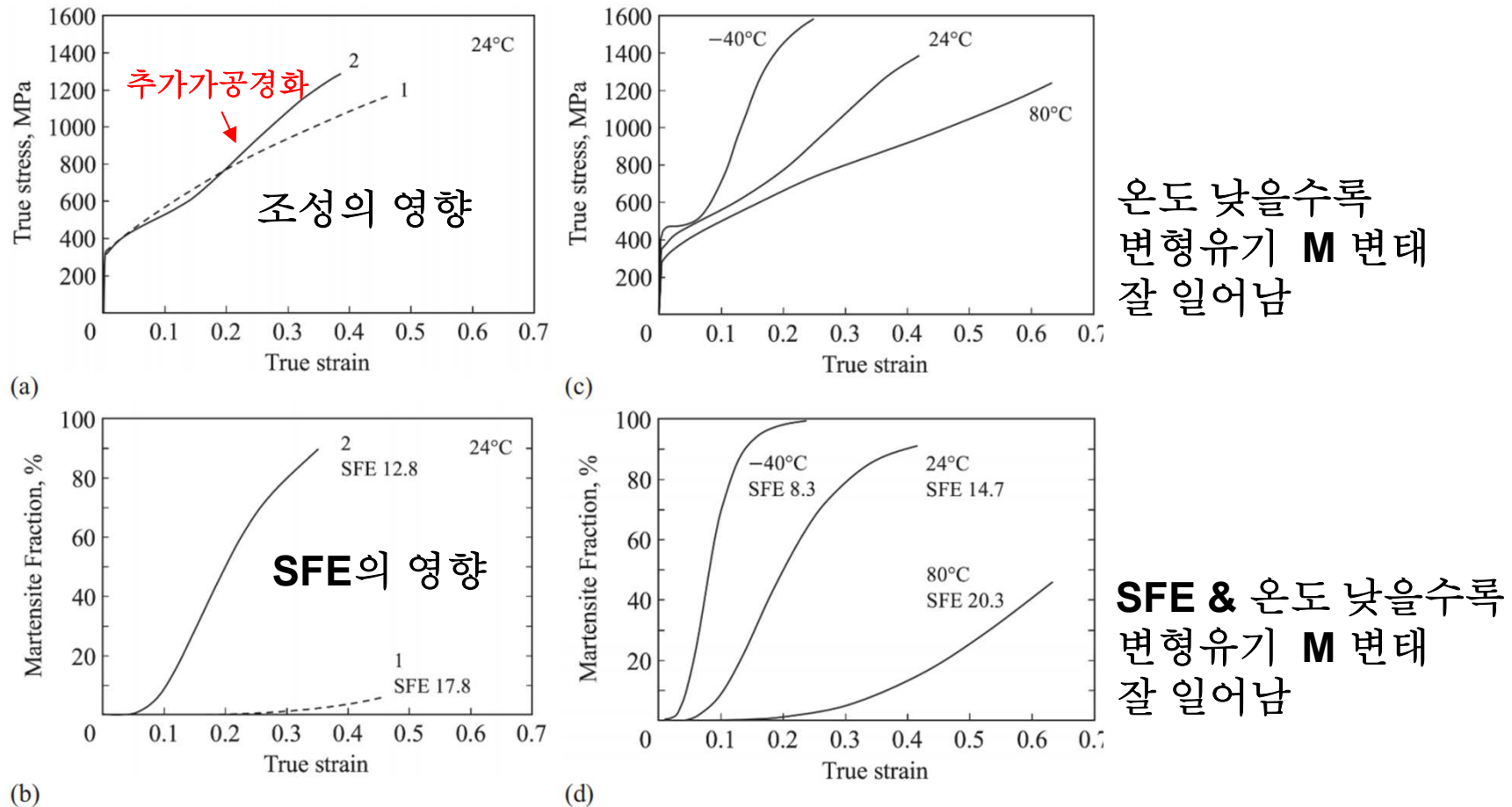


FIGURE 6.51 The effect of strain-induced α' -martensite on the stress–strain diagrams of meta-stable austenitic stainless steels. In (a) and (b) the testing temperature is 24°C; steel 1 has the composition (wt.%) 0.04C–18Cr–8Ni (AISI 304) grain size 5.9 μm , M_{d30} -16°C ; and steel 2 has the composition 0.02C–18Cr–7Ni–0.094N (AISI 301LN), grain size 11.6 μm , M_{d30} 37°C . In (c) and (d) the steel composition is 0.02C–17Cr–7Ni–0.145N (AISI 301LN), grain size 14.8 μm , M_{d30} 23°C . SFE is stacking fault energy in mJ/m^2 .

SFE는 **fcc** 결정에서 **Shockley** 부분전위 사이의 평형 간격 결정: **SFE** ↓ → 전위간격 ↑
(백금 $300 \text{ mJ/m}^2 \leftrightarrow 10 \text{ mJ/m}^2$ 일부 **stainless steel** 이나 구리 합금)

① 큰 **SFE** 갖는 합금 → 소성변형시 두 부분전위 사이 간격 좁음 → 전위의 **cross slip** 용이
→ **cellular structure** (망상구조)의 하부조직 같은 전위조직 생성/ 변형량 ↑ → **cell** 크기 ↓

큰 **SFE** 합금 → 변형 후 **D cell** 형성

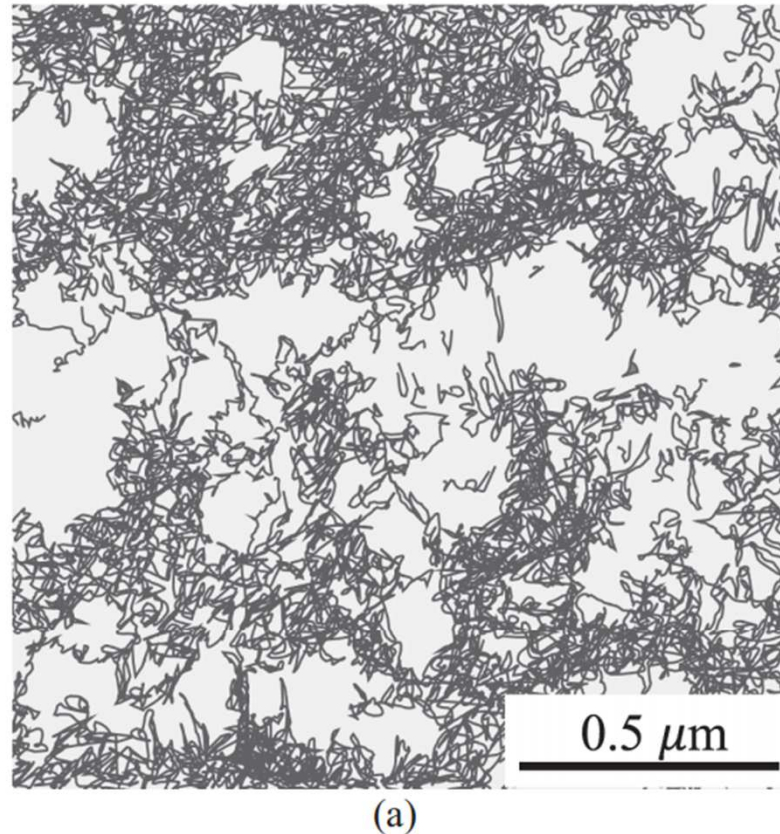
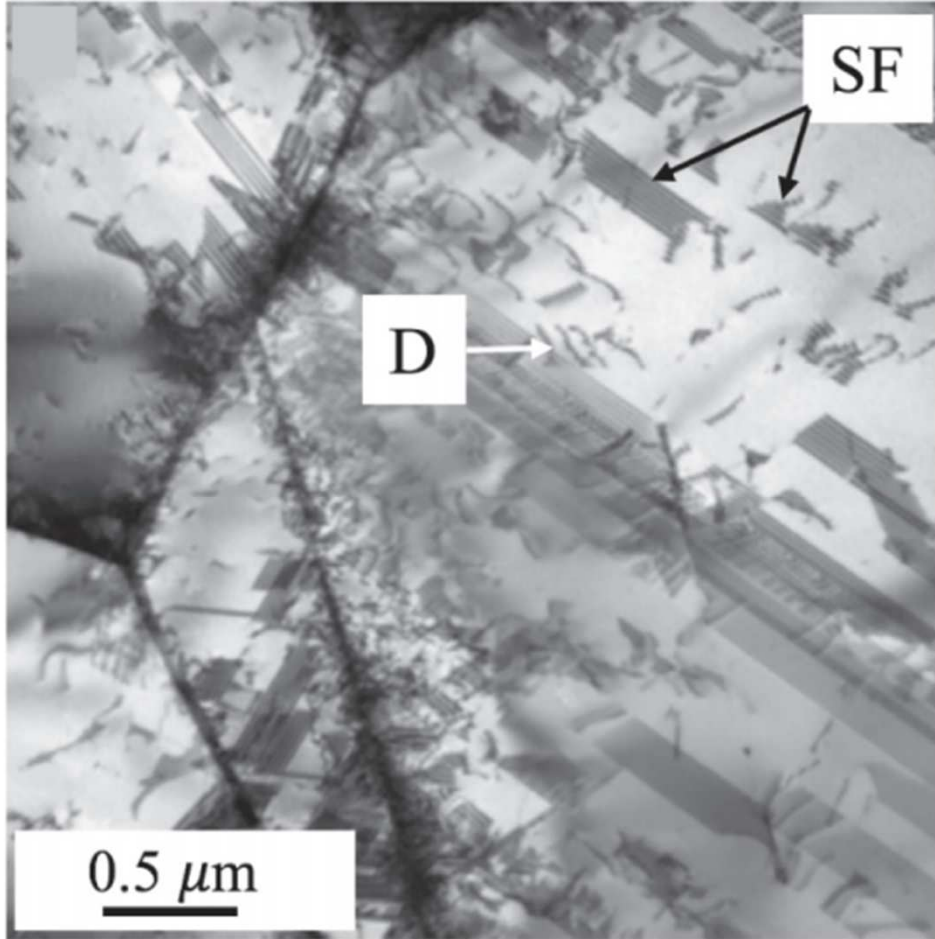


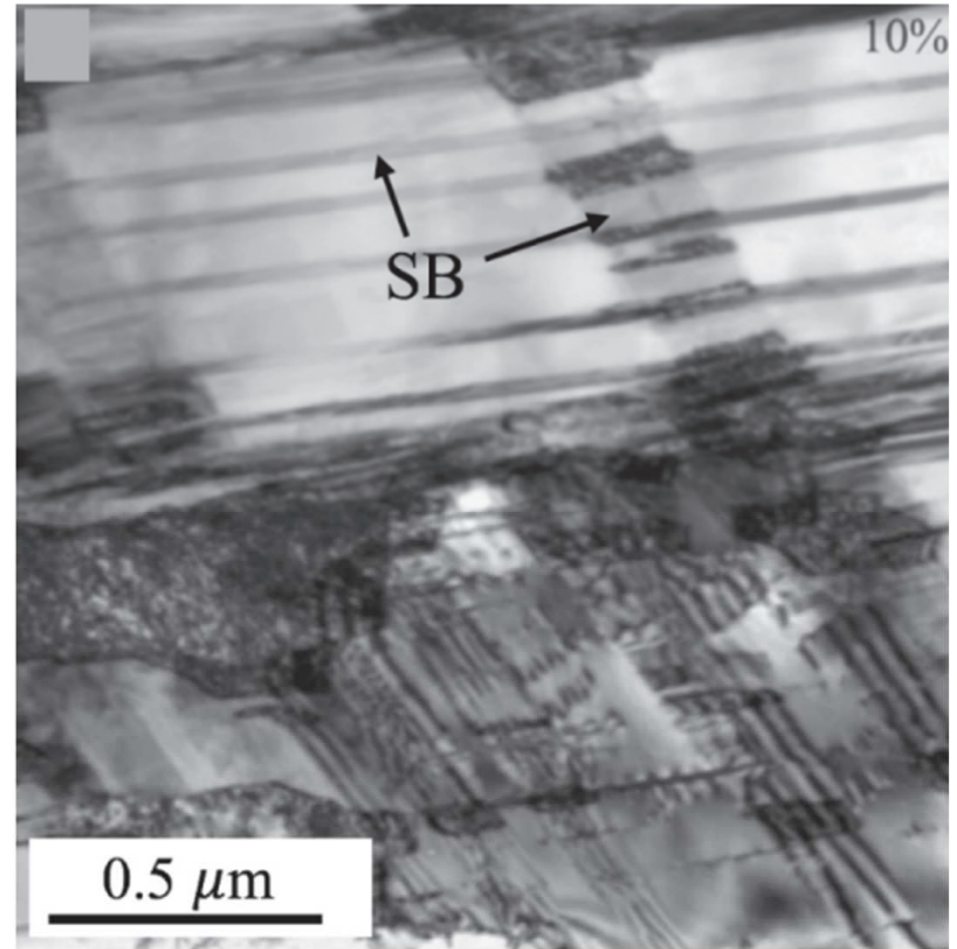
FIGURE 6.52 Dislocation and stacking fault structures in metastable austenitic stainless steels after tensile straining at room temperature. (a) Sketch of dislocation cells in an Fe–Cr–Ni steel with a relatively high stacking fault energy after elongating to $\epsilon \approx 0.2$. (b) Wide stacking faults (SF) and dislocations (D) with narrow stacking faults in an Fe–15Cr–9Mn–1Ni–2Cu–0.1N–0.1C steel strained to $\epsilon = 0.02$. (c) Shear bands (SB) in the same steel after straining to $\epsilon = 0.1$

② 낮은 **SFE** → 변형 후 부분전위 간격 증가 → **SF**
 영역 ↑ & 전단띠에 형성 → 변형 전단띠에 집중



(b)

③ 전단띠 교차 → 결정립 방위로 인해
 하나 이상의 slip 시스템 작동 때문



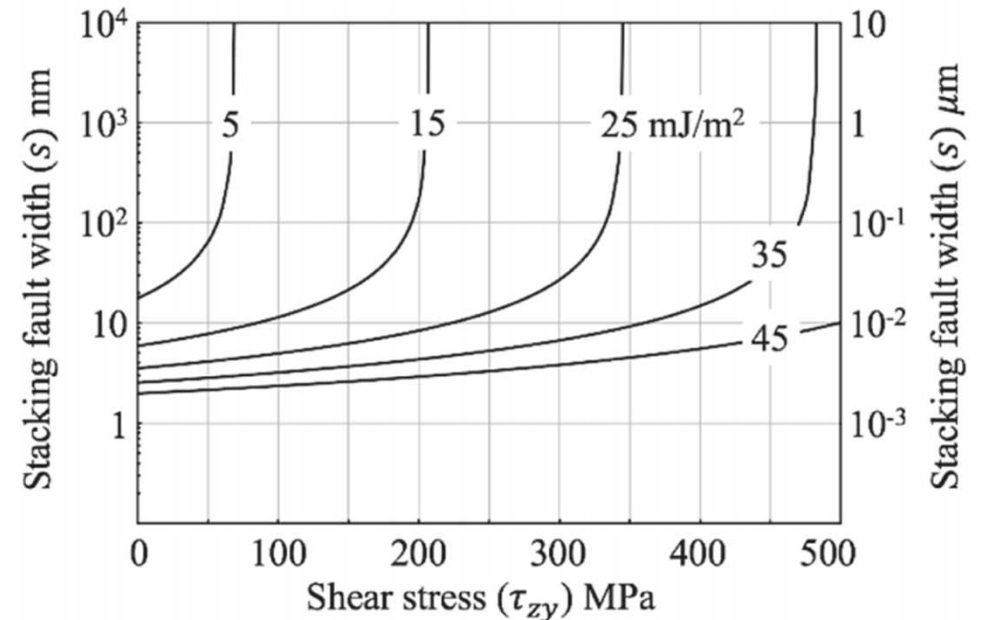
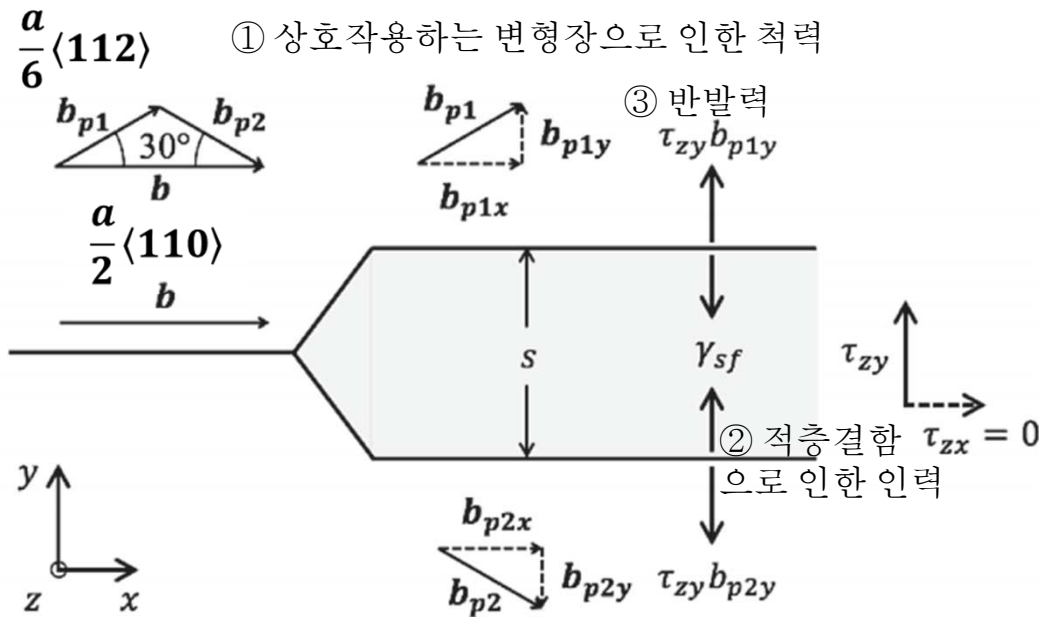
(c)

FIGURE 6.52 Dislocation and stacking fault structures in metastable austenitic stainless steels after tensile straining at room temperature. (a) Sketch of dislocation cells in an Fe–Cr–Ni steel with a relatively high stacking fault energy after elongating to $\epsilon \approx 0.2$. (b) Wide stacking faults (SF) and dislocations (D) with narrow stacking faults in an Fe–15Cr–9Mn–1Ni–2Cu–0.1N–0.1C steel strained to $\epsilon = 0.02$. (c) Shear bands (SB) in the same steel after straining to $\epsilon = 0.1$

(a) 분해된 나선전위사이 적층결함 폭(s)에 미치는 힘 (b) τ_{zy} 가 나선전위사이 적층결함 폭 s 에 미치는 힘

- τ_{zy} 가 증가함에 따라 s는 힘의 균형을 유지하기 위해 증가
- 이론적으로는 간격이 무한히 넓어지는 임계전단응력 존재
- 척력은 간격에 따라 $1/s$ 로 감소, 간격이 넓어지면 무시가능
- 임계전단응력은 $\tau_{zy}^{crit}(s \rightarrow \infty) = 2\gamma_{sf}/b_p$ ($\tau_{zy}^{crit} b_{p1y} = \tau_{zy}^{crit} b_{p2y}$)

- γ_{sf} 가 $\sim 5-15 \text{ mJ/m}^2$ 으로 작은 경우, 인가한 응력은 변형초기에 s에 큰 영향을 미침
- γ_{sf} 가 큰 경우, 그 영향이 크지 않음

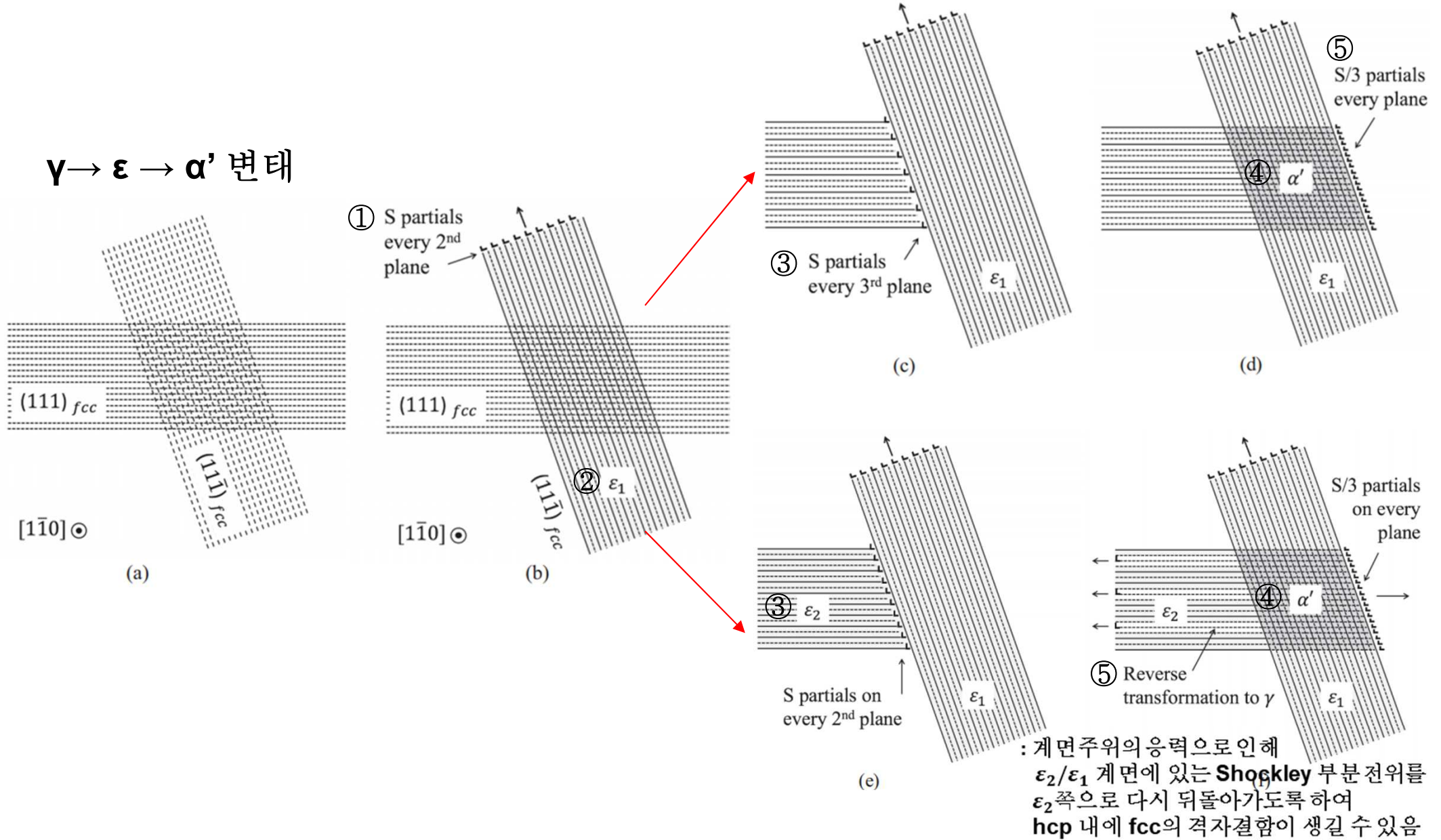


(a)

(b)

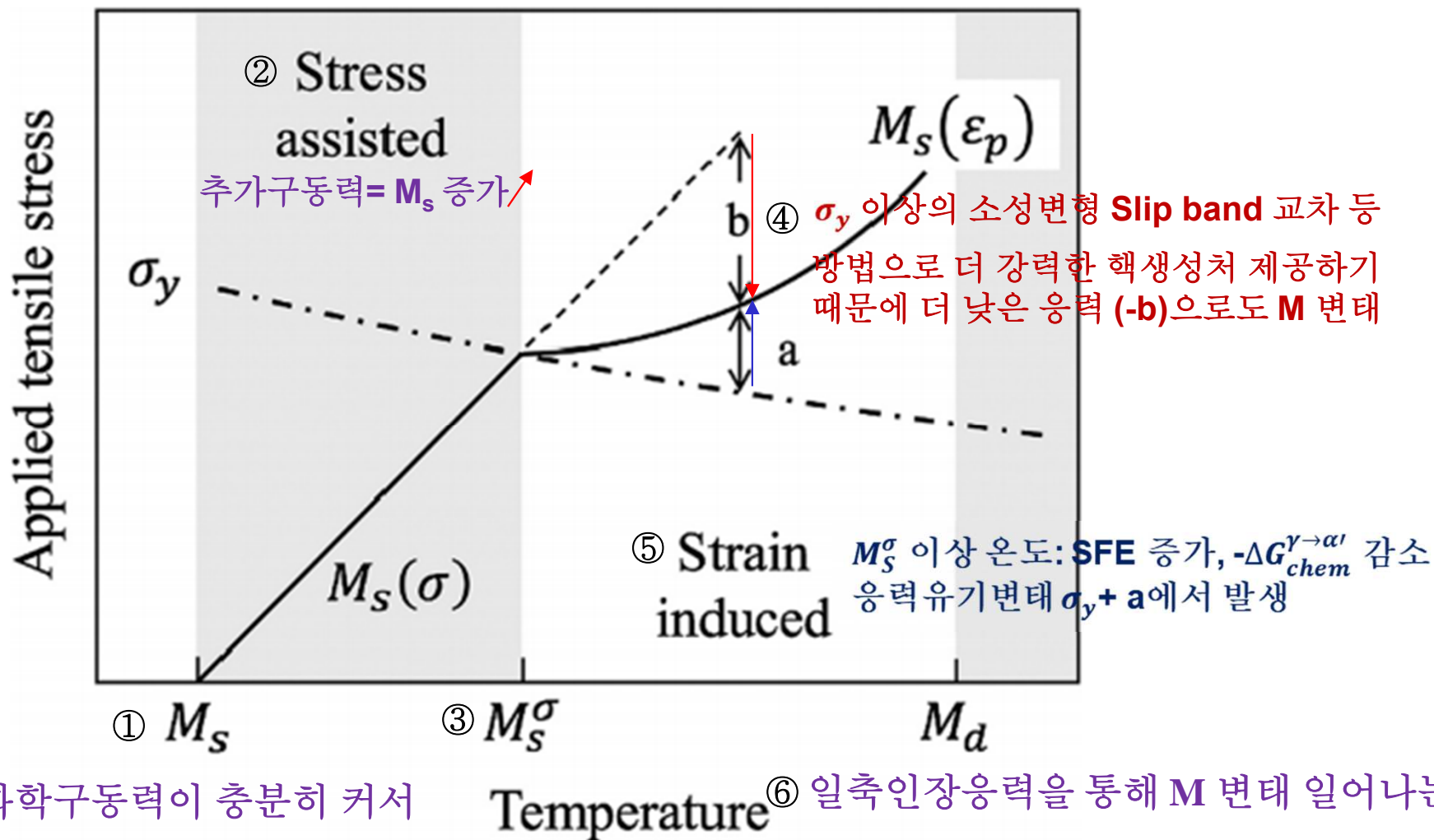
FIGURE 6.53 (a) Forces that affect the width of the stacking fault of a dissociated dislocation. (b) The effect of a shear stress on the slip plane normal to the total Burgers vector (τ_{zx}) on the width of the stacking fault between the partial dislocations of a screw dislocation. Stacking fault energies 5, 15, 25, 35, 45 mJ/m². $\nu = 0.28$, $\mu = 65.6 \text{ GPa}$, $b_p = 0.145 \text{ nm}$. (Calculations based on formula given in T.S. Byun, *Acta Materialia*, **51**:3063–3071 (2003).)

Figure 6.54 α' M가 두개의 hcp ϵ M 전단띠의 교차부에서 형성될 때 특징을 보여주는 도식



* SFE가 비교적 크고 ϵ 상이 γ 에 비해 안정하지 않은 경우, ϵ M 형성 없이 적층결합이나 쌍정이 뭉쳐있는 전단띠의 교차에 의해서 변형유기 M변태 발생 가능 ($\gamma \rightarrow \alpha'$ 변태)

Figure 6.55 SFE가 낮은 철강에서 온도와 인장응력에 따른 응력유기 M변태와 변형유기 M변태 거동



① M_s ③ M_s^σ ⑥ 일축인장응력을 통해 M 변태 일어나는 경계/
 $\gamma \rightarrow \alpha'$ 화학구동력이 충분히 커서 γ 안정성 평가 지표, 낮을수록 γ 안정
 외부응력 없이도 M 변태 (γ 내 embryo 성장)

SFE;

45 mJ/m² 이상 전위기반 소성 / 20-45 mJ/m² 기계적 Twin (TWIP) / 20 mJ/m² 미만 M 변태 (TRIP)

6.6 Thermally Activated Martensite (=Isothermal Martensite)

: 온도가 일정하게 유지된 상태에서 M 형성

$\gamma_{sf} < 0 \rightarrow s$ 가 증가할수록 계의 ΔG 가 낮아져도, 전위이동의 저항력 (nF_r)을 극복해야 핵생성 가능

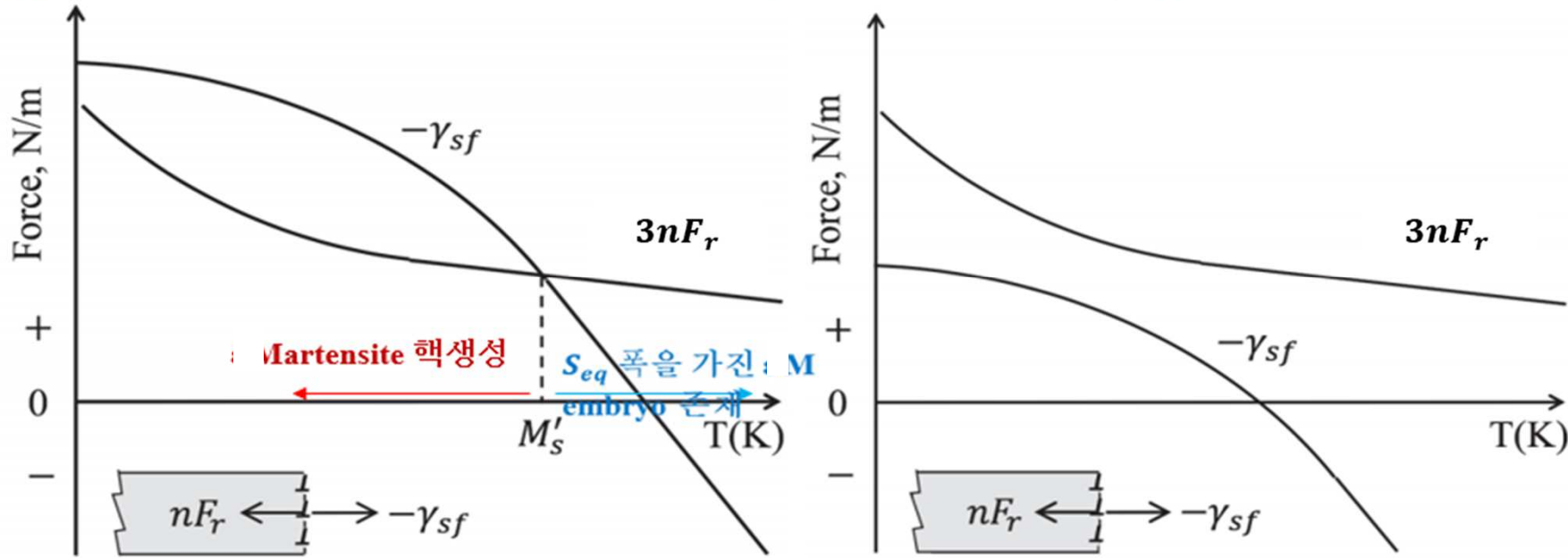


Figure 6.23 (a) (b)

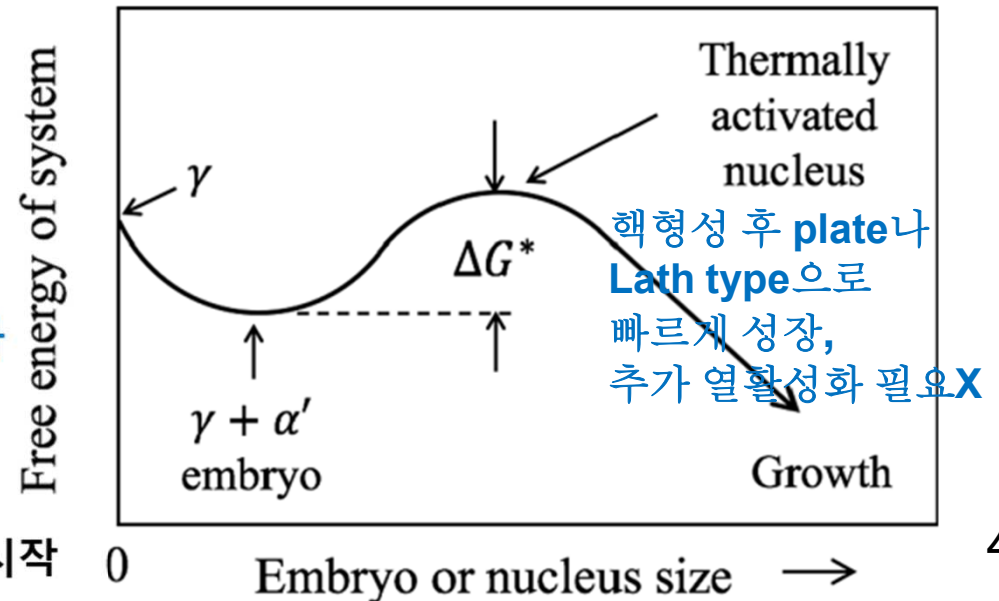
비열적 M 핵생성 조건 ($\gamma \rightarrow \alpha'$): M'_S 이하

(a) M'_S 이상 및 (b) 합금 :

$\gamma + \alpha'$ embryo 존재 \rightarrow 특정온도에서 등온 유지

\rightarrow embryo 경계의 전위 열E에 의한 진동 (열활성화

$\Delta G^* =$ 모자라는 E 보완) 에 의해 성장 $\rightarrow \alpha'$ M 변태



온도가 M'_S 에 근접함에 따라 $\Delta G^* \rightarrow 0$; 비열적 M 시작

$$\text{핵생성 속도} \propto \exp\left(-\frac{\Delta G^*}{RT}\right)$$

열활성화 M 변태가능

최고 온도

M_{si}

Temperature

M_s

비열적 M 변태
개시온도

0 $\Delta G^* \rightarrow$

M_{si}

M_s

$t_{1\%}$

0 Time \rightarrow

(a)

(a) $M_s >$ 상온

(b) M_s 극저온
혹은 일어나지 않는 경우

Temperature

M_{si}

0 $\Delta G^* \rightarrow$

극저온에서 ΔG^* 증가 이유: 규명 X

M_{si}

$t_{1\%}$

0 Time \rightarrow

(b)

FIGURE 6.57 Schematic plots of the variation of activation energy ΔG^* vs. temperature and corresponding TTT diagrams for the start of the transformation to thermally activated martensite. M_{si} is the highest temperature at which thermal activation is possible. (a) M_s above room temperature. (b) Very low M_s or no athermal transformation at any temperature.

M_s > 상온인 강에서 열활성 마르텐사이트 예:

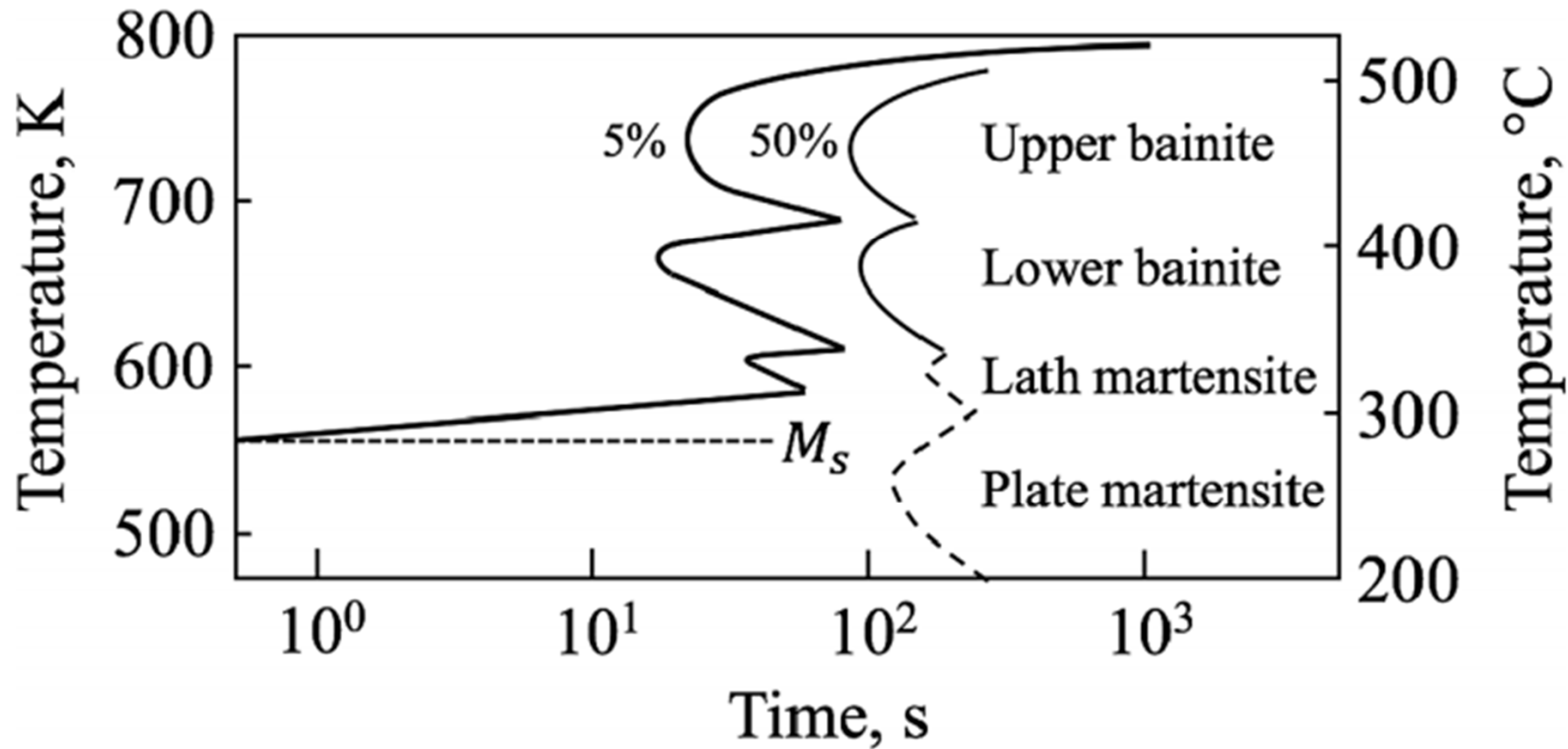


FIGURE 6.58 TTT diagram for a steel with the composition (wt.%) 0.42C-0.8Cr-0.3Mo-1.5Ni. M_s temperature for athermal transformation to plate martensite during rapid continuous cooling is shown with a dashed line. (Based on data in J-C. Zhao, M.R. Notis, *Materials Science and Engineering: R: Reports*, 15:135-207 (1995).)

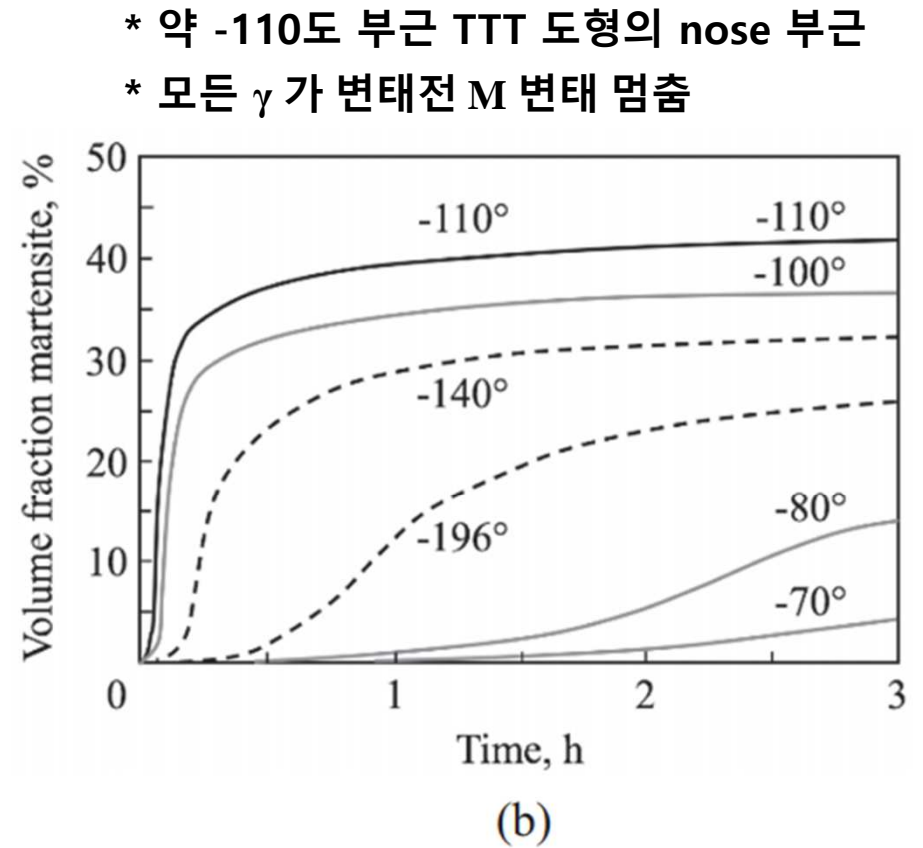
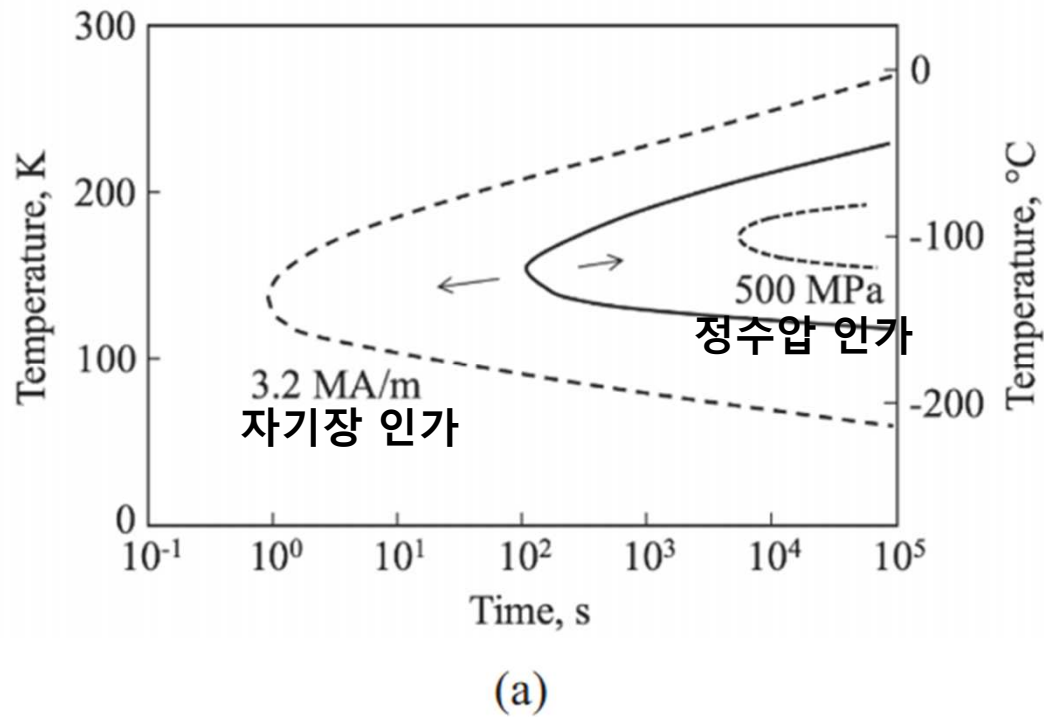


FIGURE 6.59 (a) TTT diagram showing time for 1% transformation isothermally to martensite in an alloy with the composition (at.%) Fe-24Ni-4Mn ($M_s < 4.2 K$). Full line: no applied pressure or magnetic field. Dashed lines show how the transformation is accelerated by the application of a magnetic field and retarded by an applied hydrostatic pressure. (Data from T. Kakeshita, T. Saburi and K. Shimizu, *Philosophical Magazine B*, **80**:171-181 (2000).) (b) Volume fraction martensite formed with the aid of thermal activation at various temperatures above M_s as a function of time. Fe-23.2Ni-2.8Mn alloy, temperatures in $^{\circ}C$, gray lines for high temperatures, dashed lines for low temperatures. (Data from G. Ghosh and V. Raghavan, *Materials Science and Engineering*, **79**:223-231 (1986).)

열활성 마르텐사이트: $-\Delta G_{chem}^{\gamma \rightarrow \alpha'} + \Delta G_{stress} + \Delta G_{mag} < \Delta G_{crit}$

$\therefore M_S$ 이상 온도에서 부족한 구동력: $\Delta G_{miss} = \Delta G_{crit} - \{-\Delta G_{chem}^{\gamma \rightarrow \alpha'} + \Delta G_{stress} + \Delta G_{mag}\}$

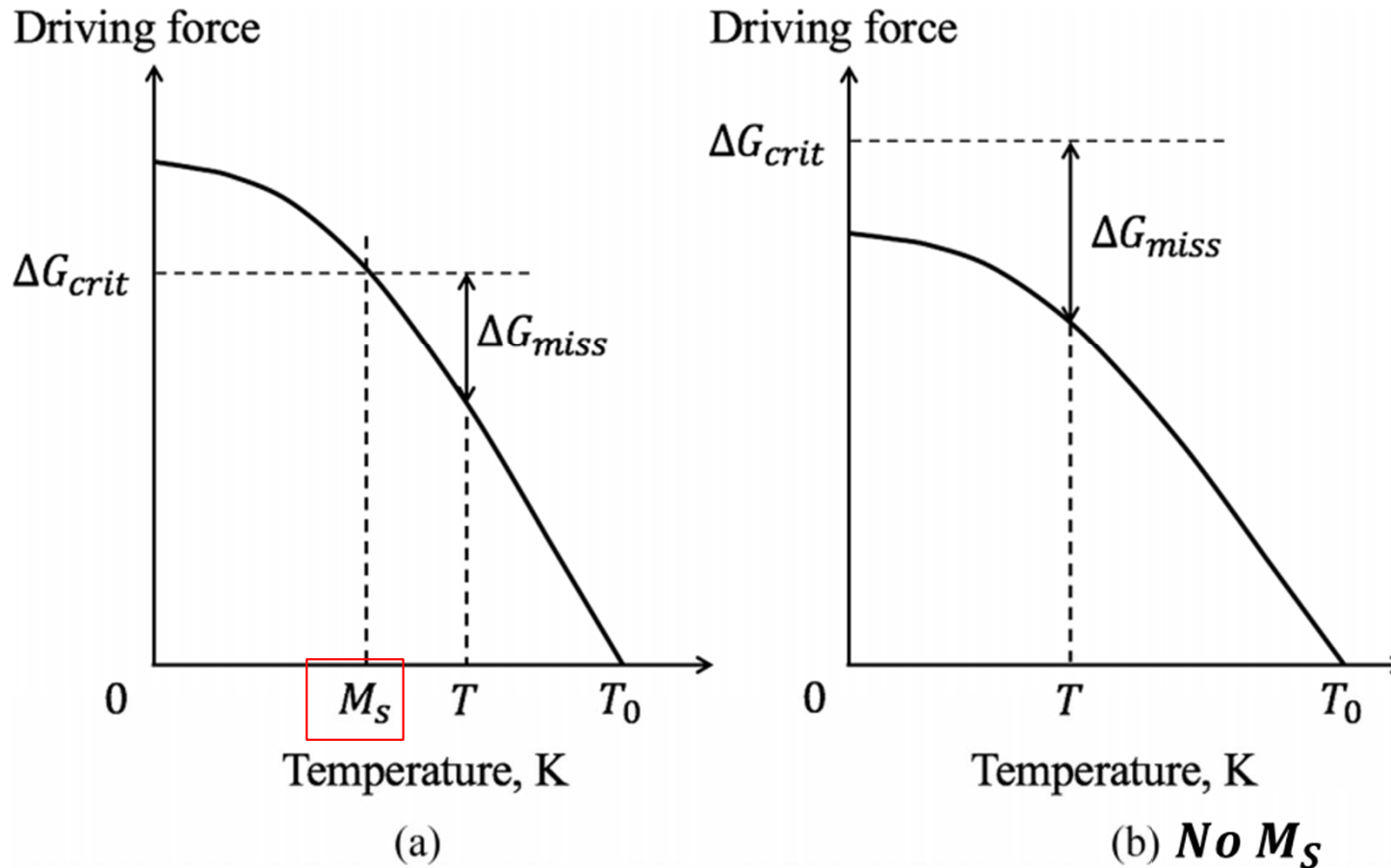


FIGURE 6.60 Free energy conditions for martensite formation with the aid of thermal activation. (a) A system where the driving force exceeds ΔG_{crit} at some temperature such that athermal martensite can form at M_S . (b) A system where ΔG_{crit} is never reached.

증거: $\gamma(+\alpha')$ 의 탄성계수 낮아짐 (softening)

* Martensite 변태

T_0 이하의 온도 ($T_0 - M_s$ 사이)에서 γ 내 준안정 α' embryo 존재

$$\underline{\text{구동력} < M_s} < \underline{\text{구동력} + \text{열진동}} < M_{Si}$$

$$\Delta G_{crit} = \Delta G'_{crit} + \Delta G_{s(gs)} + \Delta G_{disl}$$

$$= -\Delta G_{chem}^{\gamma \rightarrow \alpha'} + \Delta G_{stress} + \Delta G_{mag}$$

⇒ **Athermal Martensite 변태**

$$\Delta G_{miss} = \Delta G_{crit} - \{ -\Delta G_{chem}^{\gamma \rightarrow \alpha'} + \Delta G_{stress} + \Delta G_{mag} \}$$

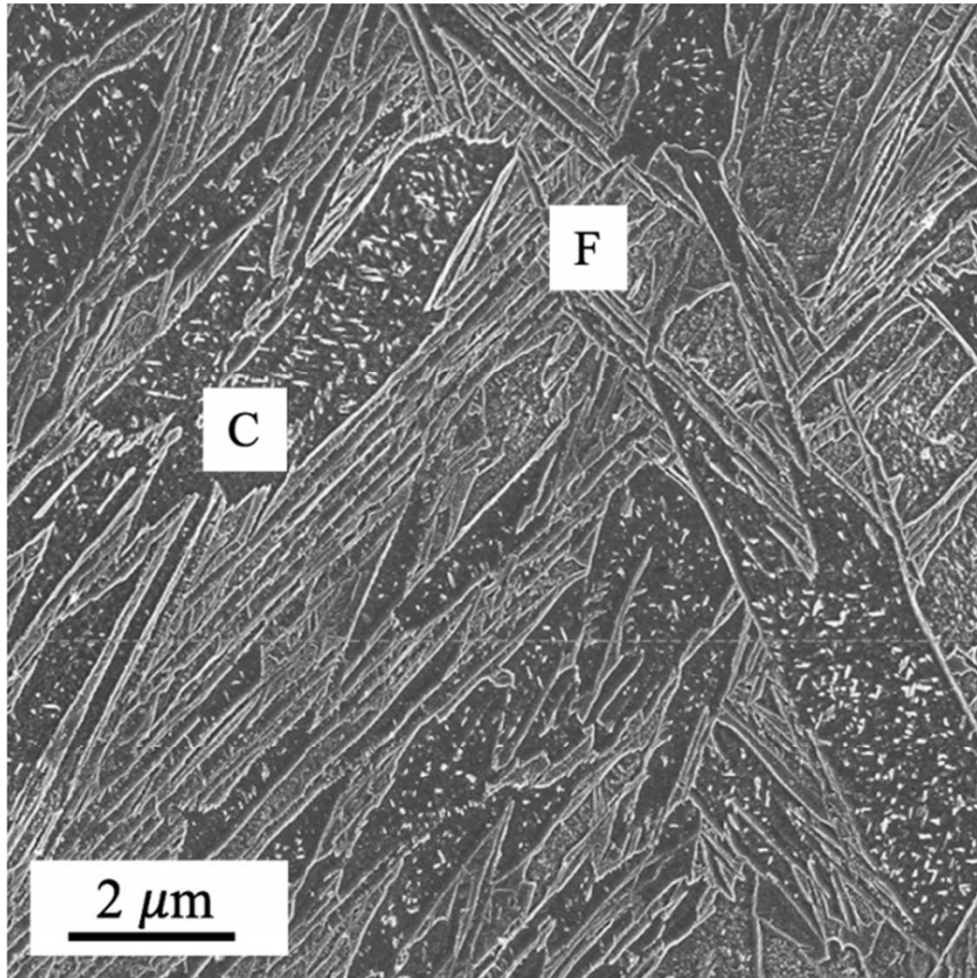
ΔG_{miss} 를 등온유지시 열진동으로 극복

Thermal Martensite 변태

6.7 Carbon diffusion phenomena in Ferrous Martensite

6.7.1 오토템퍼링 (Auto-tempering)

: γ /Lath M 계면 확산없이 빠르게 진행, but bct 또는 bcc 조직내 carbon 확산도
빨라 냉각 중 편석 혹은 석출 발생



Lath M 내 전위주위에 탄소농도국부적 증가
: 전위 주위에 Cottrell 분위기 형성

(Coarse & Fine) Bimodal Lath 분포
Ms 바로 아래 vs 낮은 온도 형성 Lath
1~5 μm vs 50~500 nm

M 분율 증가시 잔류 γ 내 전위 농도 증가
활주계면의 이동에 대한 저항 증가

a) 조대 Lath 내 Fe_3C 석출물
(γ 내 높은 C 과포화 & bcc M 내 낮은 C 고용도
→ Si 또는 Al 첨가를 통해 형성 억제)
혹은 b) 철탄화물 e.g. η 상
혹은 c) 농축된 탄소편석

퀀칭 후 Lath는 탄소 농도가 높은 γ film으로
분리 → Lath 경계 밝게 보이는 이유

FIGURE 6.61 Autotempered lath martensite in a steel with the composition (wt.%) Fe-0.13C-1.7Mn-0.7Si-0.3Cr quenched at 120°C/s to room temperature showing a mixture of coarse (C) and fine (F) laths. $M_s = 435$ °C. (Courtesy of S. R. Babu.)

퀵칭 후 Lath는 탄소 농도가 높은 γ film으로 분리 \rightarrow Lath 경계 밝게 보이는 이유

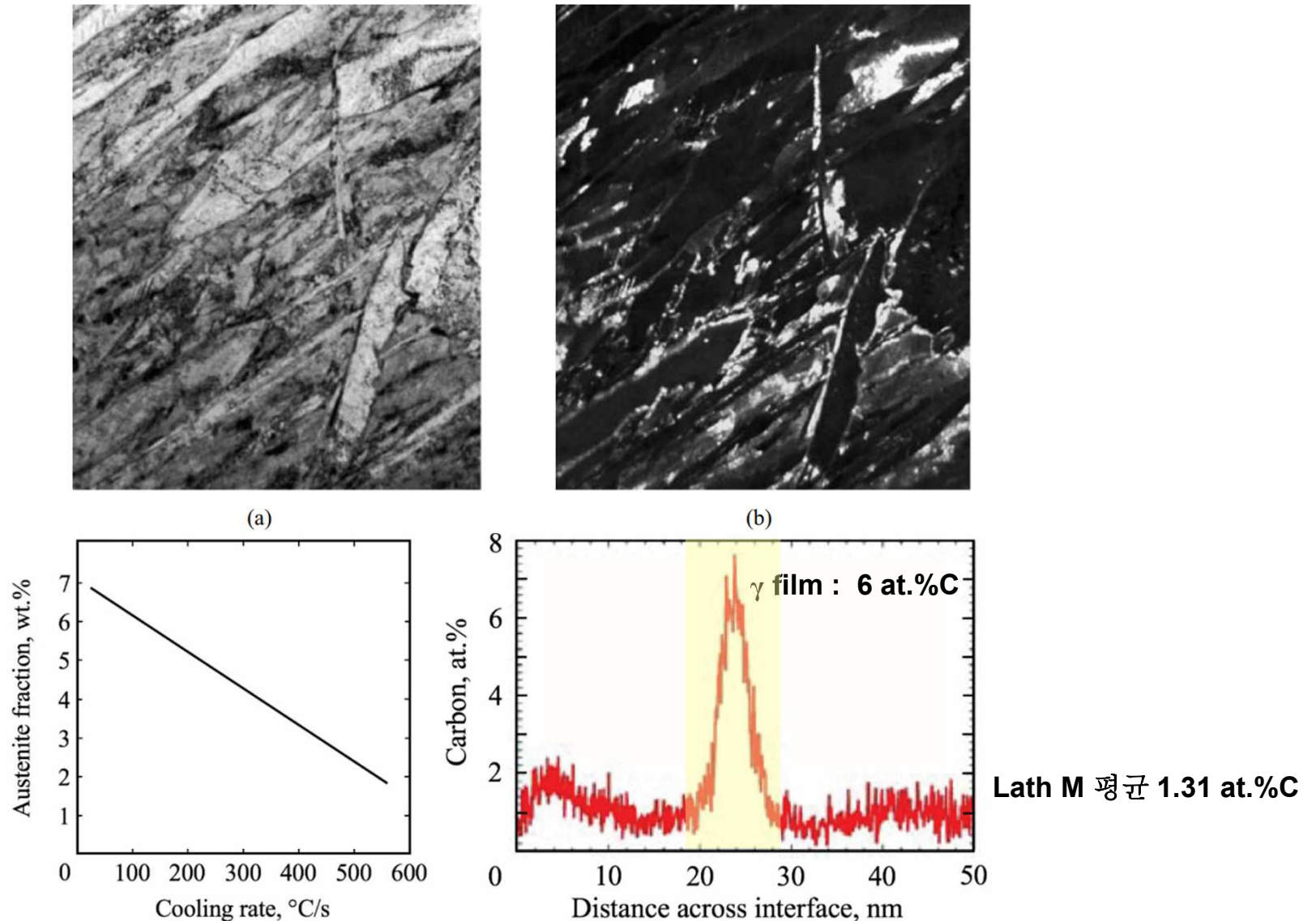
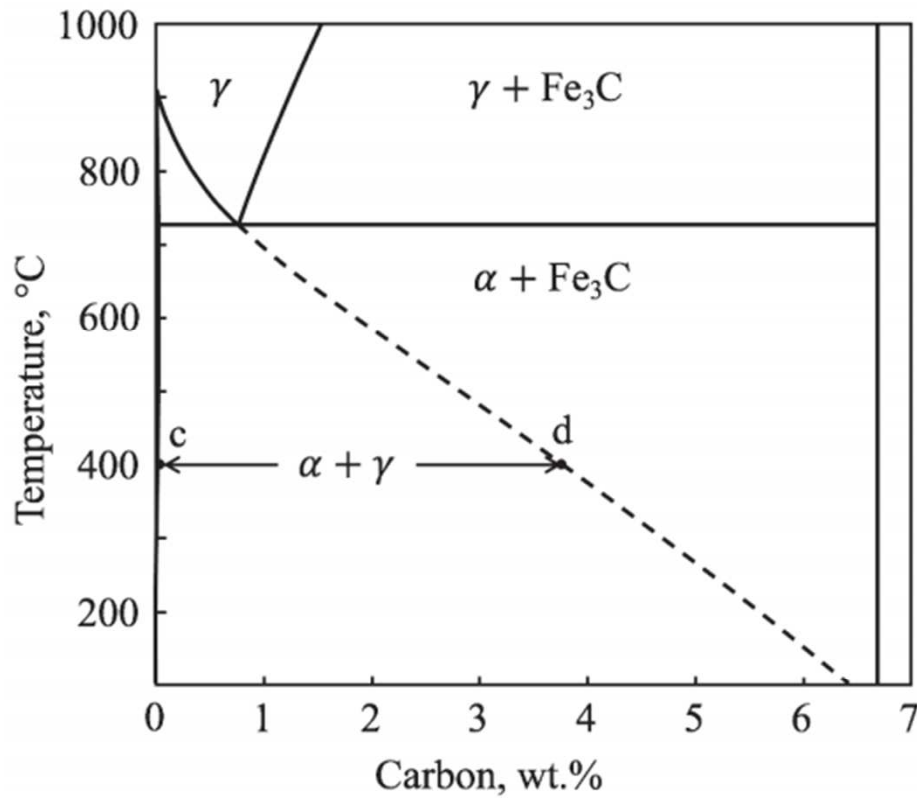
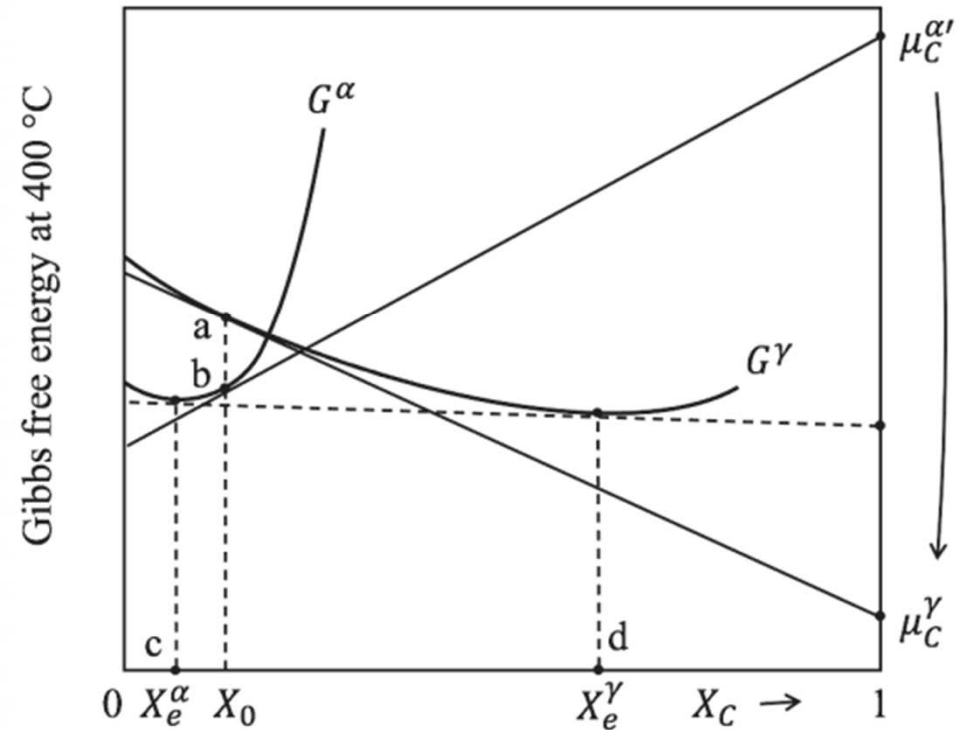


FIGURE 6.62 (a) Bright-field transmission electron microscope image of laths in an as-quenched medium-carbon engineering steel containing (wt.%) 0.29C–1.65Si and a total of ~3 wt.% manganese, nickel, chromium, molybdenum, copper, aluminum, titanium, and vanadium. Cooling rate 55°C/s. (b) Dark-field image of corresponding area showing austenite films (light contrast) surrounding the laths. (c) The effect of cooling rate on the volume fraction of as-quenched retained austenite at 22°C. Cooling rate range 560°C/s–25°C/s obtained with a Jominy specimen sectioned at 0.125–12.125 mm from the quenched end. (d) Atom probe tomography measurement of carbon concentration across an interlath austenite film after cooling at 560°C/s.



(a)



(b)

FIGURE 6.64 (a) Fe–C equilibrium phase diagram calculated using Thermo-Calc™ software (version 2019b/TCFE9). The dashed line (extrapolated A₃ temperature) shows the concentration of carbon in fcc austenite in equilibrium with bcc ferrite in the absence of cementite (Fe₃C). The concentration of carbon in bcc ferrite in equilibrium with austenite is extremely small, irresolvable on the scale of the diagram. (b) Grossly distorted schematic free energy diagram for ferrite and austenite at 400°C. Points a and b show the free energy of alloy X_0 before and after the $\gamma \rightarrow \alpha$ transformation. The intersection of the tangents to these points with the 100% carbon vertical gives the chemical potential of carbon in γ and α . The real location of points c and d in this schematic diagram are shown in (a).

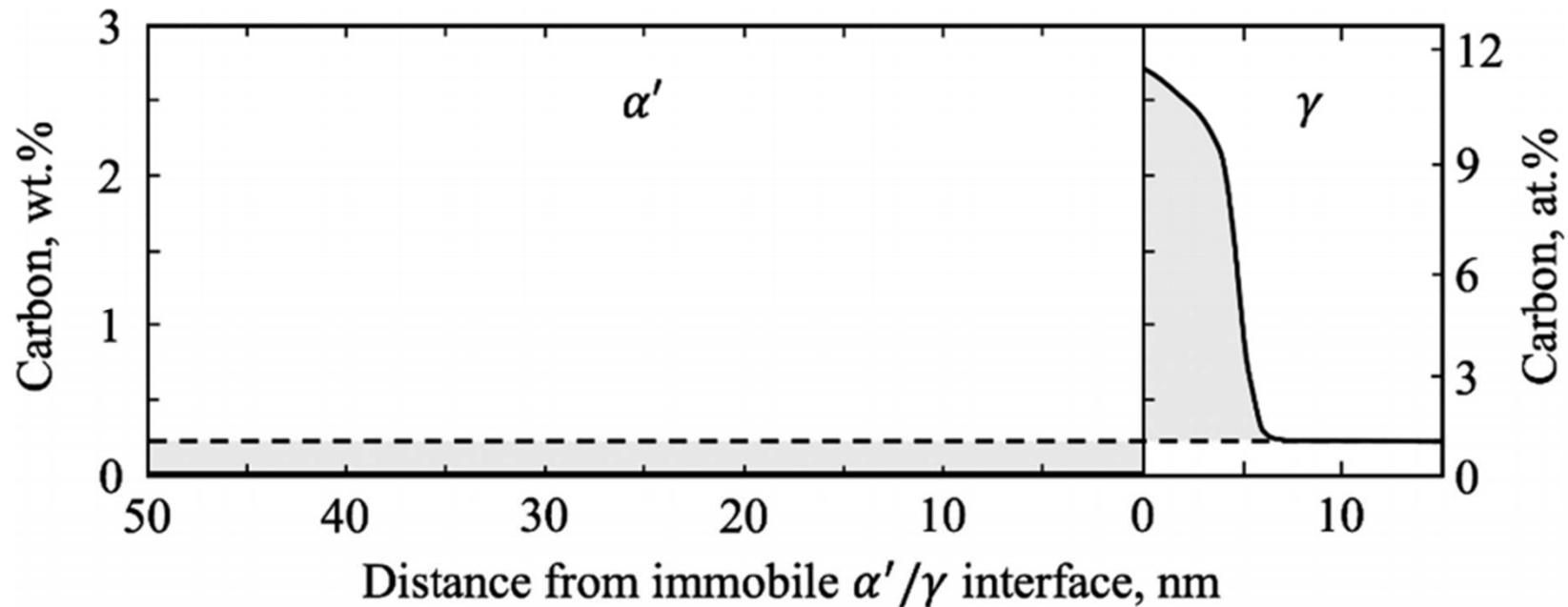


FIGURE 6.65 One-dimensional model of carbon diffusion out of a 100 nm thick ferrite lath formed at 290°C during cooling at 120°C/s. Original carbon content (0.23 wt.%) given by the dashed line. The conservation of carbon requires the shaded areas to be equal. It is assumed that austenite exists on both sides of the lath, giving mirror symmetry about the middle of the lath. Carbon trapping at dislocations and possible carbide precipitation is ignored. (Based on data in S.R. Babu, M. Jaskari, A. Jarvenpää, T.P. Davis, J. Kömi, D. Porter, *Metals*, **10**:850 (2020).)

6.7.2 Quenched and Partitioned Steel (Q&P Steel)

: M_S 와 M_f 사이 온도에서 급냉정지온도 (quenched stop temperature, OST)로 급냉 후 이 온도에서 등온유지하거나 더 높은 온도에서 등온 유지 → γ 내 C contents ↑
(M내 전위에 편석된 양으로 예측치보단 적음) → γ 안정화 → 이후 냉각시 잔류 γ 분율 증가 → M의 우수한 강도와 γ 연신의 조화 → 잔류 γ TRIP 거동 유발을 통해 추가 연성 확보 가능

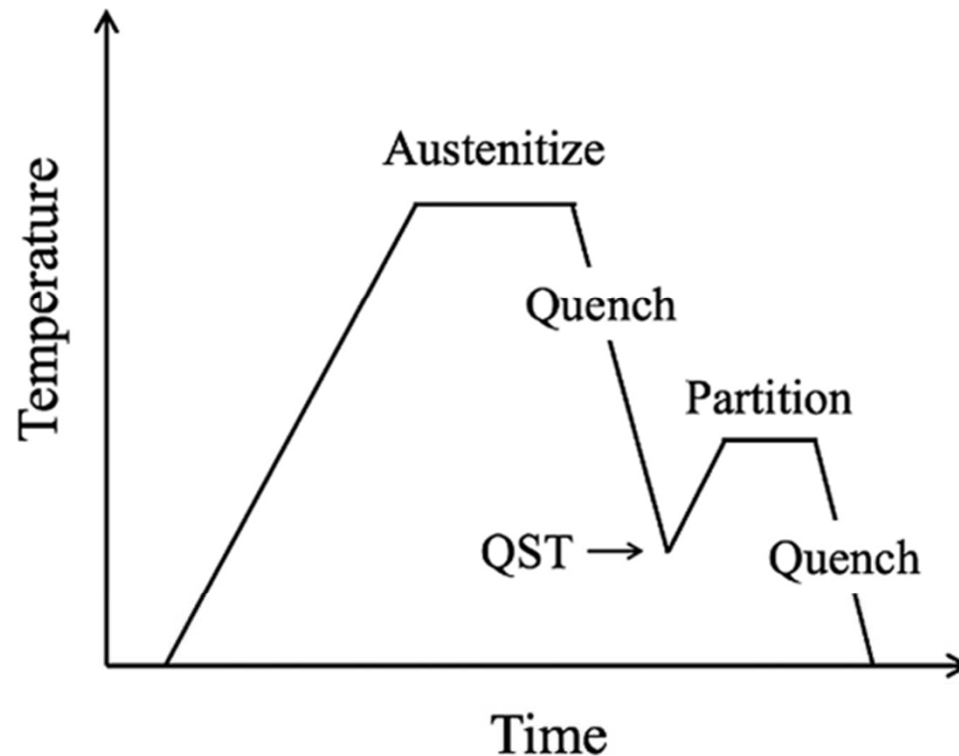


FIGURE 6.66 Schematic heat treatment cycle that can be used to make Q&P steels. QST = quench stop temperature.

6.7.3 Lath M의 Tempering

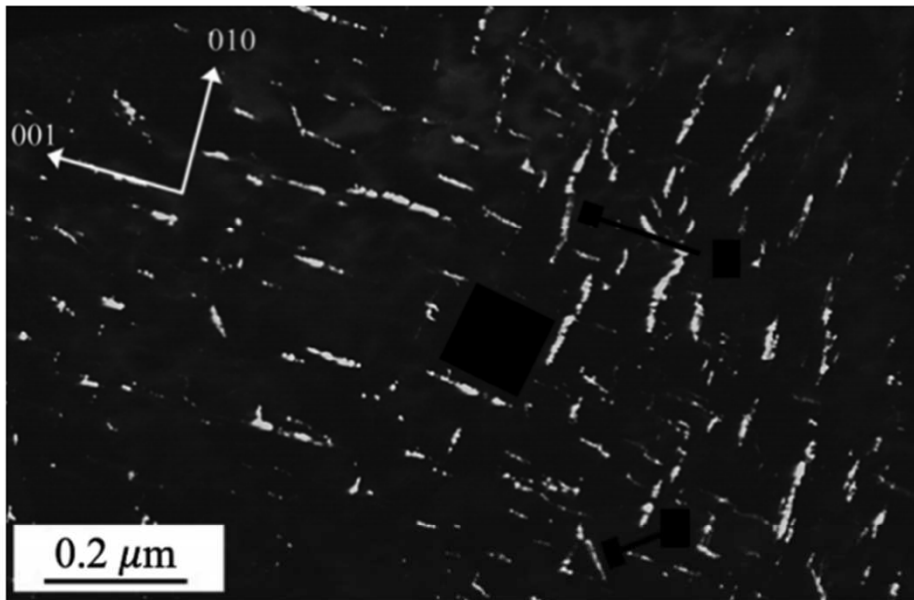
: 퀴칭 후 형성된 Lath M (전위로 편석된 탄소+높은 밀도 고경각 및 저경각 입계) = 높은 경도와 인장강도, but 특히 0.3 wt.%C 이상인 공업용 강의 경우, 낮은 인장연성 및 인성

→ 150°C-700°C 내 Tempering 열처리로 (경도와 강도는 감소) 연성과 인성 증가

6.7.3.1 탄소강과 저합금강의 Tempering

① Tempering시 탄소는 전위, Lath 경계, 잔류 γ 로의 편석 지속

② 약 0.1-0.2C(wt.%) 이상 탄소를 포함하는 강의 경우, 약 350°C Tempering시 3개의 천이상 $\epsilon - M_2C$, $\eta - M_2C$, $\chi - M_5C_2$ 가 더 안정한 시멘타이트 (Fe_3C), $\theta - M_3C$ 보다 빠르게 석출

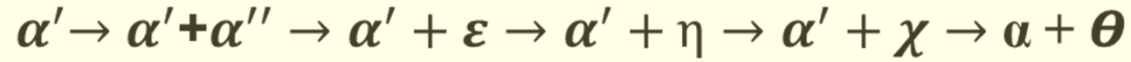


ϵ, η 석출물의 구별 어려움

ϵ, η 석출물이 기지 M과 정합관계 유지하며 석출

FIGURE 6.70 ϵ/η precipitates in a steel containing (wt.%) 0.4C-0.7Mn-0.3Si-1.7Ni-0.9Cr-0.2Mo (known as AISI 4340) after austenitizing, quenching and tempering 1 hour at 200°C. M_s 278°C. Dark field transmission electron micrograph from the middle of a large lath. The precipitates are roughly equiaxed with a diameter of ~5 nm and grouped with a spacing of ~10 nm into rod shapes ~100 nm long, mainly aligned parallel to $\langle 100 \rangle_{\alpha'}$.

* AI에서 천이상 석출과 유사하게, 아래와 같은 천이상 석출 순서 나타냄



C과포화된
bcc 또는 bct

초기단계
탄소 농축영역

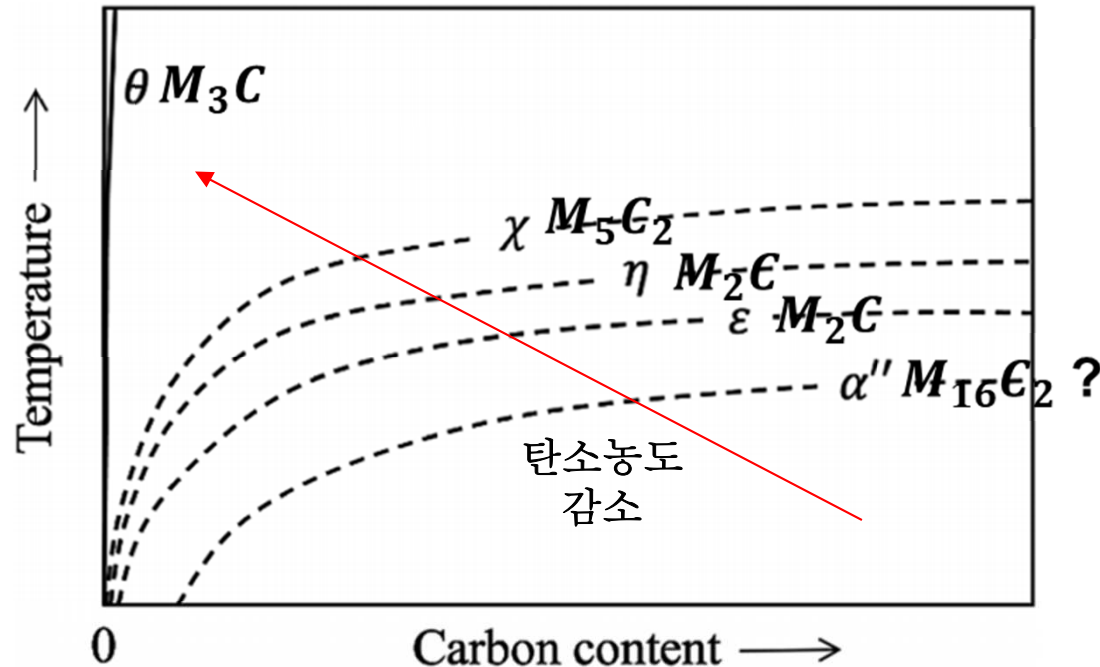


FIGURE 6.71 Schematic diagram showing relative positions of the solvi for α'' , ε , η , χ and cementite (θ) in a pseudo-binary M–C phase diagram, where M = Fe+Mn+Si+Cr+Ni+Mo, for example, and paraequilibrium conditions exist, i.e. the ratios of substitutional alloying elements in the carbides is the same as that in the martensite matrix.

* **AISI 4340** 천이탄화물의 석출 순서에 대한 온도의 영향 ($M_s \sim 280^\circ\text{C}$)

845°C γ 단일상 만든 후 오일 퀴칭을 통해 **Lath M** 형성시 **autotempering**에 의해 수십 nm 길이의 η -탄화물, 전위나 계면으로의 탄소편석 및 잔류 γ 포함

200 °C 이하, 1 hr 열처리: η -탄화물 부피증가, 잔류 γ 부피일정

250 °C , 1 hr 열처리: η -탄화물 부피증가, 잔류 $\gamma \rightarrow \alpha + \text{Fe}_3\text{C}$ (θ) 로 분해 감소

300 °C 이상, 1 hr 열처리: η -탄화물 Fe_3C (θ)로 대체, 모든 잔류 $\gamma \rightarrow \alpha + \text{Fe}_3\text{C}$ 로 분해 (이때, θ 의 핵생성처는 η/α' 계면, 판상 (폭 $\sim 100\text{-}200$ nm, 두께 ~ 15 nm) \rightarrow 고온 조대화)

: **Tempering T** 증가시 **M** 항복강도/경도감소, 충격/파괴인성 증가

but 200-400 °C 잔류 γ 분해, γ film이 Fe_3C film으로 대체 취성 증가 \rightarrow **temper embrittlement**

공업용 철강 200 °C 이하 **tempering**, M 기반 고강도 구조용강 400 °C 이상 고온 **tempering**

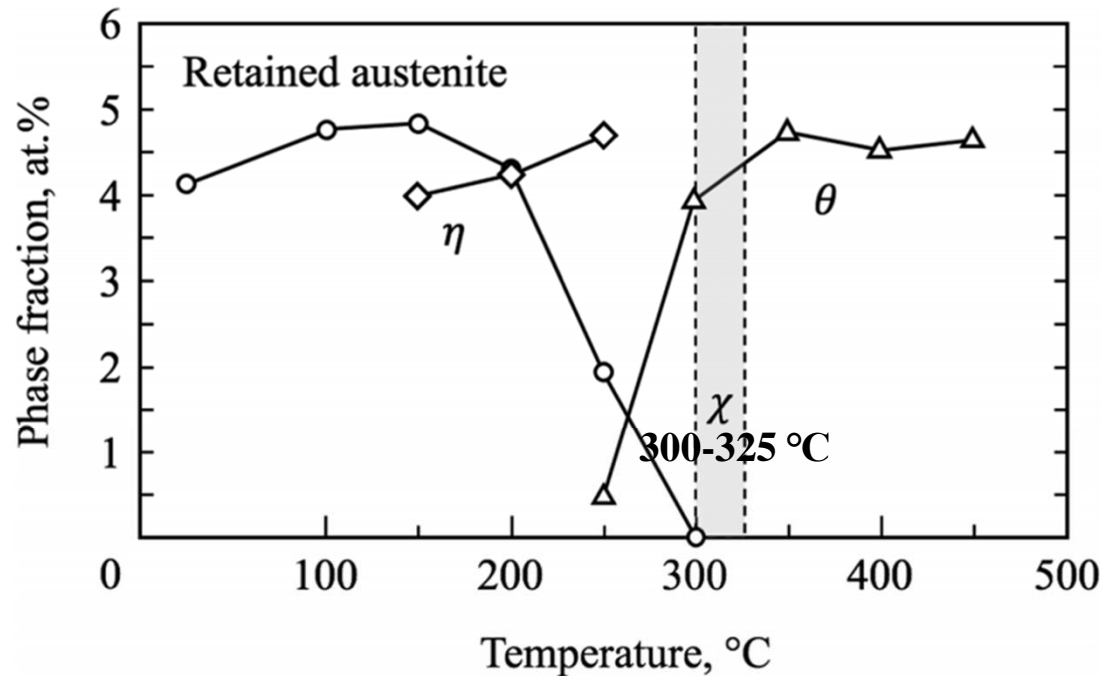


FIGURE 6.72 Phase fractions after tempering a steel containing 0.42 wt.% carbon and ~4 wt.% Mn+Si+Ni+Cr+Mo (AISI 4340) for 1 hour at various temperatures. High-energy X-ray diffraction shows that a small, indeterminate fraction of Hägg carbide (χ) is present after tempering in the range 300°C – 325°C .

- * 400-700 °C tempering : Fe_3C 석출물 형상이 계면 E 줄이기 위해 구형의 회전타원체화
- * 400 °C 이상 tempering: Lath의 전위밀도가 recovery 과정을 거치면서 감소
- * 600-700 °C tempering : M Lath 조직 재결정과 유사한 과정으로 등축정 페라이트로 대체

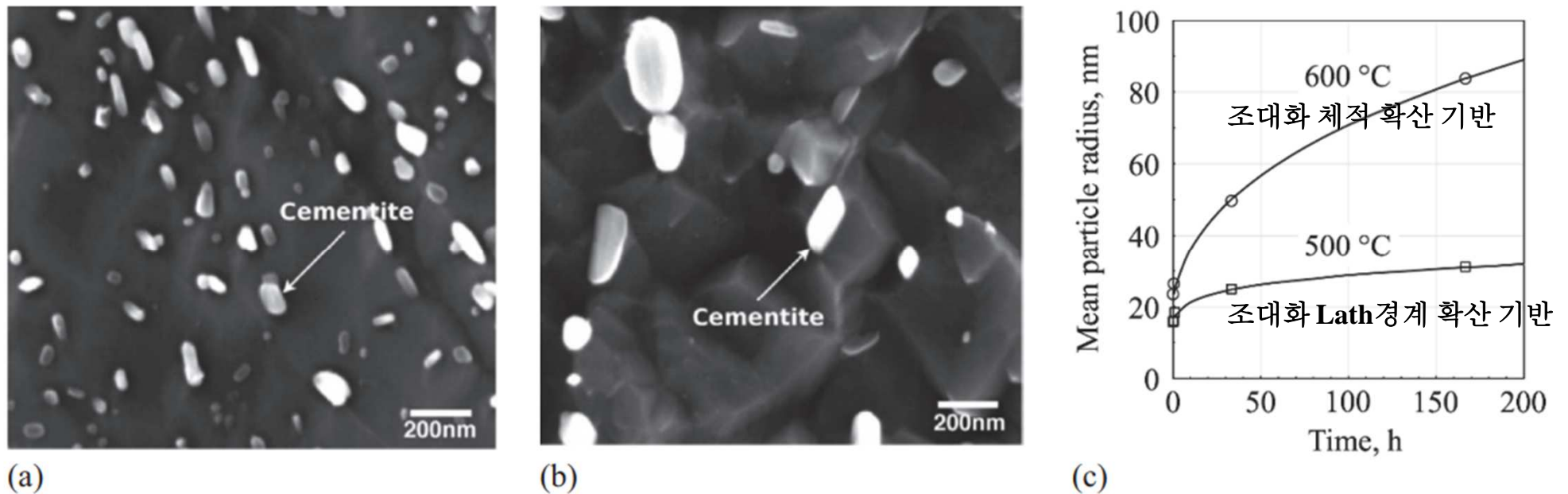


FIGURE 6.73 Cementite precipitates in tempered martensite, scanning electron microscope images after picral etching. Alloy composition (wt.%) Fe-0.1C-2Mn. (a) 0.5 h at 600°C. (b) 33.33 h at 600°C. (c) Variation of mean equivalent circle radius with holding time. ((a) and (b) reprinted from *Acta Materialia*, Vol. 159, Y.X. Wu, W.W. Sun, M.J. Styles, A. Arlazarov and C.R. Hutchinson, Cementite coarsening during tempering of Fe-C-Mn martensite, 209-224 (2018), with permission from Elsevier.)

6.7.3.2 2차 경화 (Secondary Hardening)

- Cr, Mo, V, W 등과 같은 탄화물 형성원소를 상당히 포함하는 강의 경우,

$\alpha + \text{Fe}_3\text{C}$ 로 존재하는 것보다 $\alpha + M_xC_y$ 로 존재하는 것이 안정

500-600 °C 열처리시 비교적 조대한 Fe_3C 가 미세한 M_xC_y 로 바뀌어 경도 증가 → 2차 경화

- $\text{Fe}_3\text{C} \rightarrow M_xC_y$ 변태가 일어나는 방법 :

직접변태 (in-situ transformation) vs 별도의 핵생성/성장

시멘타이트/페라이트 경계면 핵생성 후
시멘타이트 없어질 때까지 성장

전위, Lath 경계, Prior γ 경계에서 합금 탄화물
불균일 핵생성 후 시멘타이트 소비하면서 성장

Table 6.3 M tempering시 석출되는 합금 탄화물

Carbide	Crystal Structure	Shape	Orientation Relationship	Temperature of Formation
VC-V ₄ C ₃	Cubic	Plates	$(100)_c \parallel (100)_\alpha$ $[011]_c \parallel [011]_\alpha$	~550°C
Mo ₂ C	hcp	—	$(0001)_c \parallel (011)_\alpha$ $[11\bar{2}0]_c \parallel [100]_\alpha$	~550°C
W ₂ C	hcp	needles	as Mo ₂ C	~600°C
Cr ₇ C ₃	Hexagonal	spheres	—	~550°C
Cr ₂₃ C ₆ (M ₂₃ C ₆)	Cubic	plates	$(100)_c \parallel (100)_\alpha$ $[010]_c \parallel [010]_\alpha$	~700°C
M ₆ C (M = Fe, Mo, W)	Cubic	—	—	~700°C

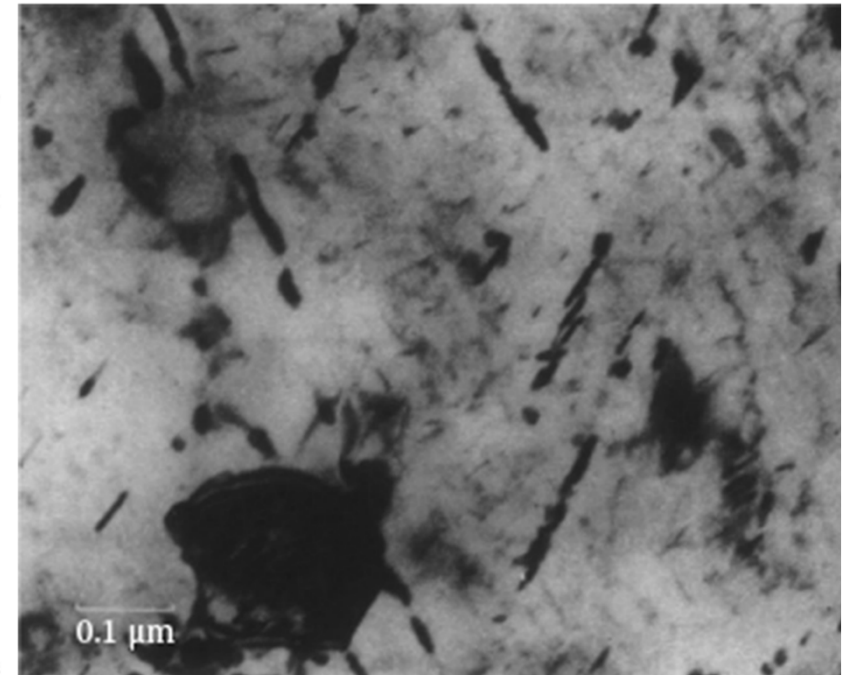


Figure 6.74 W₂C needles laying along the sites of former Fe₃C precipitates in Fe-6.3W-0.23C quenched and tempered 20 h at 600°C 56

* 일반적으로 VC, NbC, TiC, TaC 및 HfC의 경우 미세한 석출 분산/복잡한 결정구조 및 형성엔탈피가 낮은 M₇C나 M₆C 탄화물 조대분산

6.7.3.3 Maraging Steels

매우 적은 탄소 (<0.03 wt.%) 포함하는 고합금 강

M_s 는 약 150 °C, 공랭시 비교적 경도 낮은 Lath M 변태 (기지)

대표조성: Fe-18Ni-9Co-5Mo-0.7Ti-0.1 Al

후속 열처리 (400-500 °C) 통한 높은 부피분율의 미세한 금속간 화합물 (e.g. Ni_3Mo , Ni_3Ti 및 Fe_2Mo)을 통해 최대 2500 MPa의 인장강도 얻음.
낮은 탄소 함량으로 탄화물 석출 없음.

기존 γ (fcc, disordered solid solution) \rightarrow M (bcc or hcp)

6.8. Athermal Nucleation and Growth: Ordered Alloys

γ (B2, D0₃, 또는 L1₂ 같은 Ordered Alloy) \rightarrow M (Cubic system보다 대칭성이 낮은 단사정 monoclinic, 사방정 orthorhombic 또는 면심정방정 face-centered tetragonal) 경우

6.8.1. Thermoelastic Martensite

규칙합금: **Thermoelastic M: AuCd, AgCd, CuZn, CuZnGa, CuZnAl, CuNiAl, NiAl, TiNi, TiNiCu, TiNiFe, FePt**
 작은 열이력(50K이하) / γ 의 자유E 낮추어 M_s 저온부 이동

미세 쌍정 \rightarrow 판상 M : 변태시 전단변형 \rightarrow 부피변화 없이 탄성 변형만 \rightarrow 계면 정합 변형 수용 용이

온도 변화에 따라 탄성적으로 반응

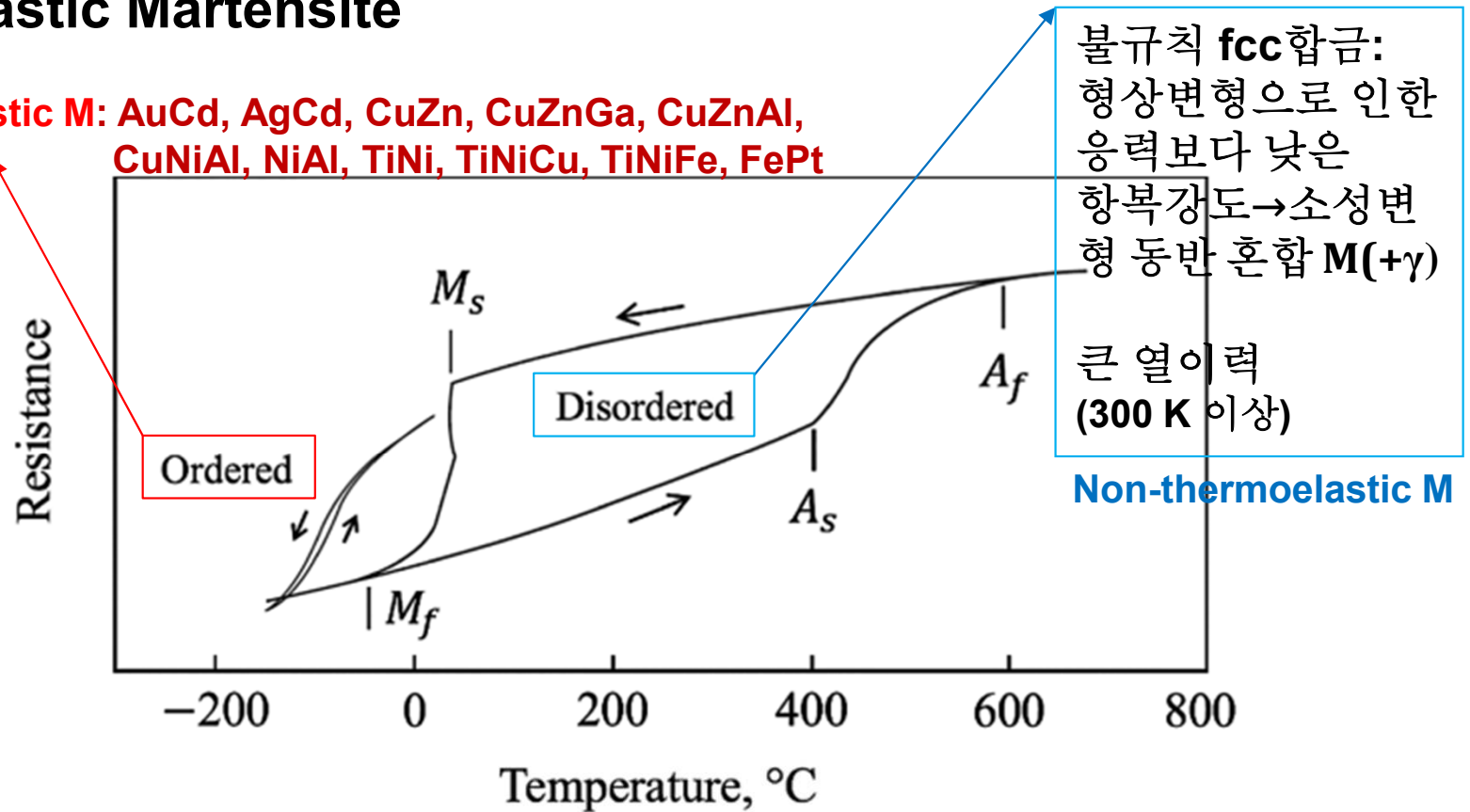


FIGURE 6.76 Martensite transformation hysteresis in an Fe–25 at.% Pt alloy revealed by the variation of electrical resistivity. Large thermal hysteresis loop for disordered Fe₃Pt. Small loop for L1₂ ordered Fe₃Pt. (Hysteresis loop positions from D. Dunne, Chapter 4 in *Phase Transformations in Steels*, Vol. 2, Ed. E. Pereloma and D.V. Edmonds, Woodhead Publishing, 2012.)

6.8.2. Superelasticity (SE) and Shape Memory

대표조성: NiTiX 합금 (입방정 B2 → 단사정 monoclinic B19' or 사방정 Orthorhombic B19)
얇은 판상 M

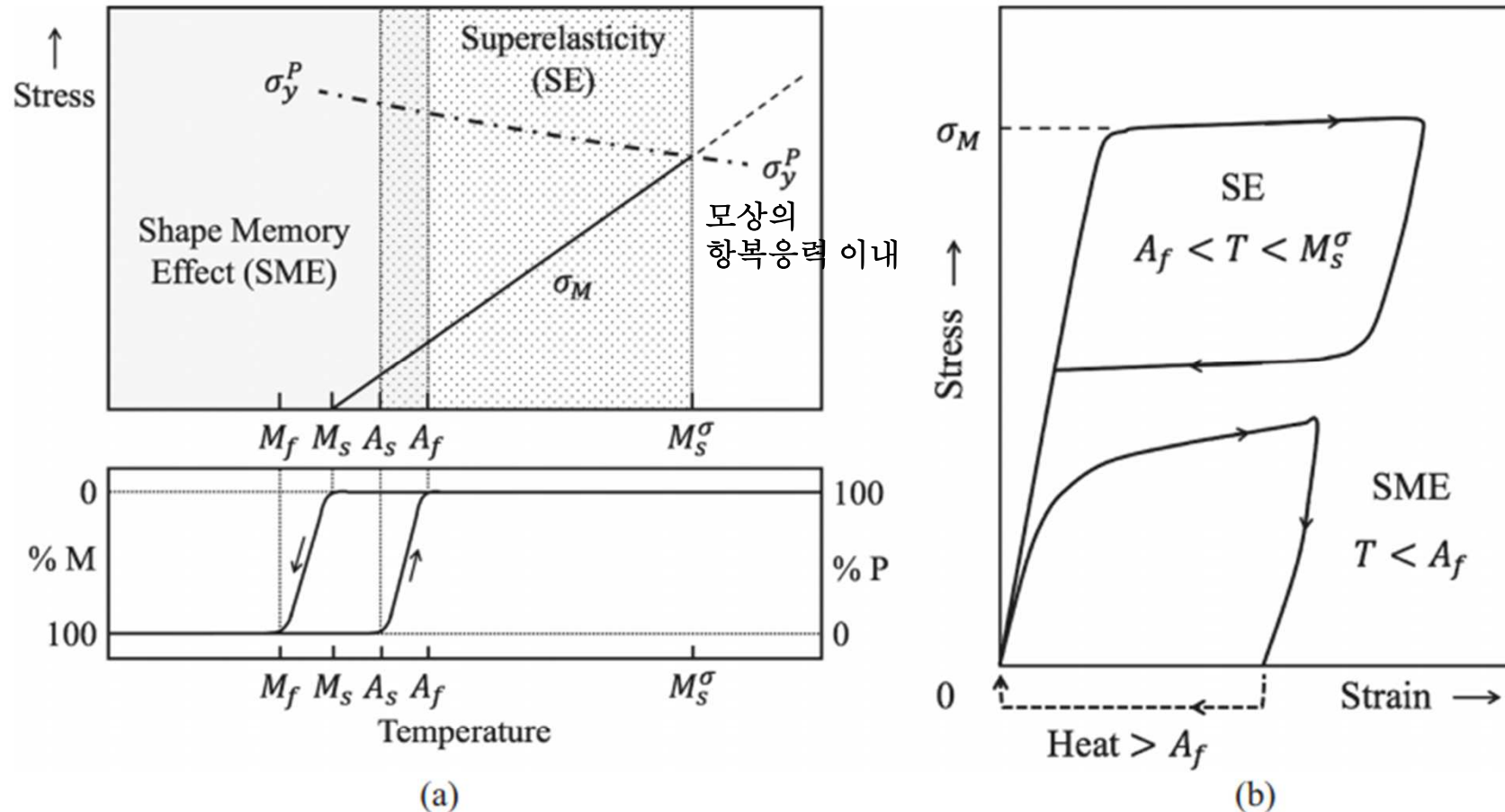
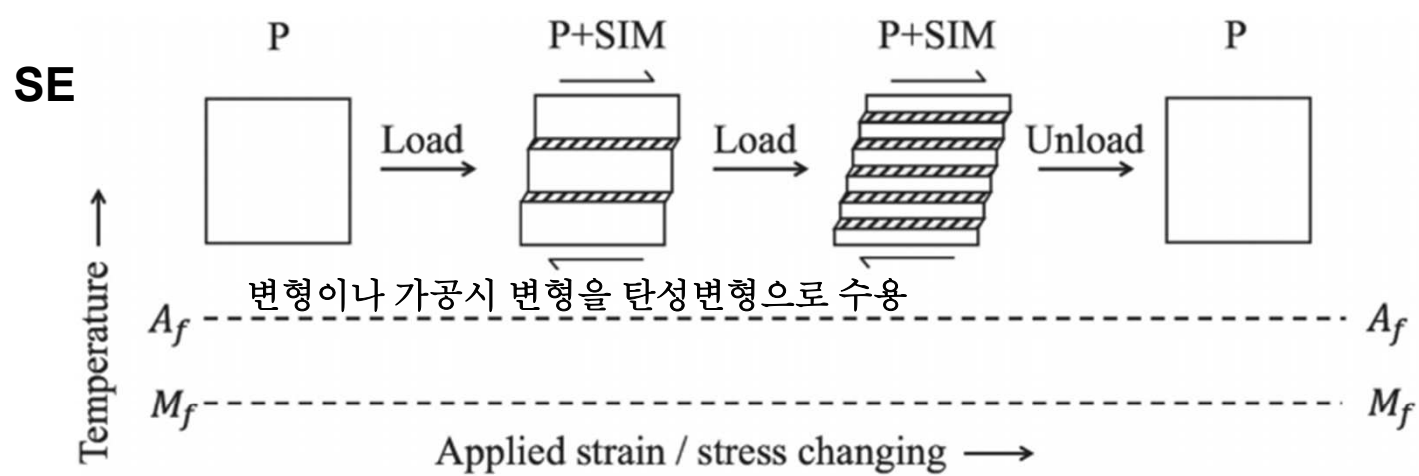
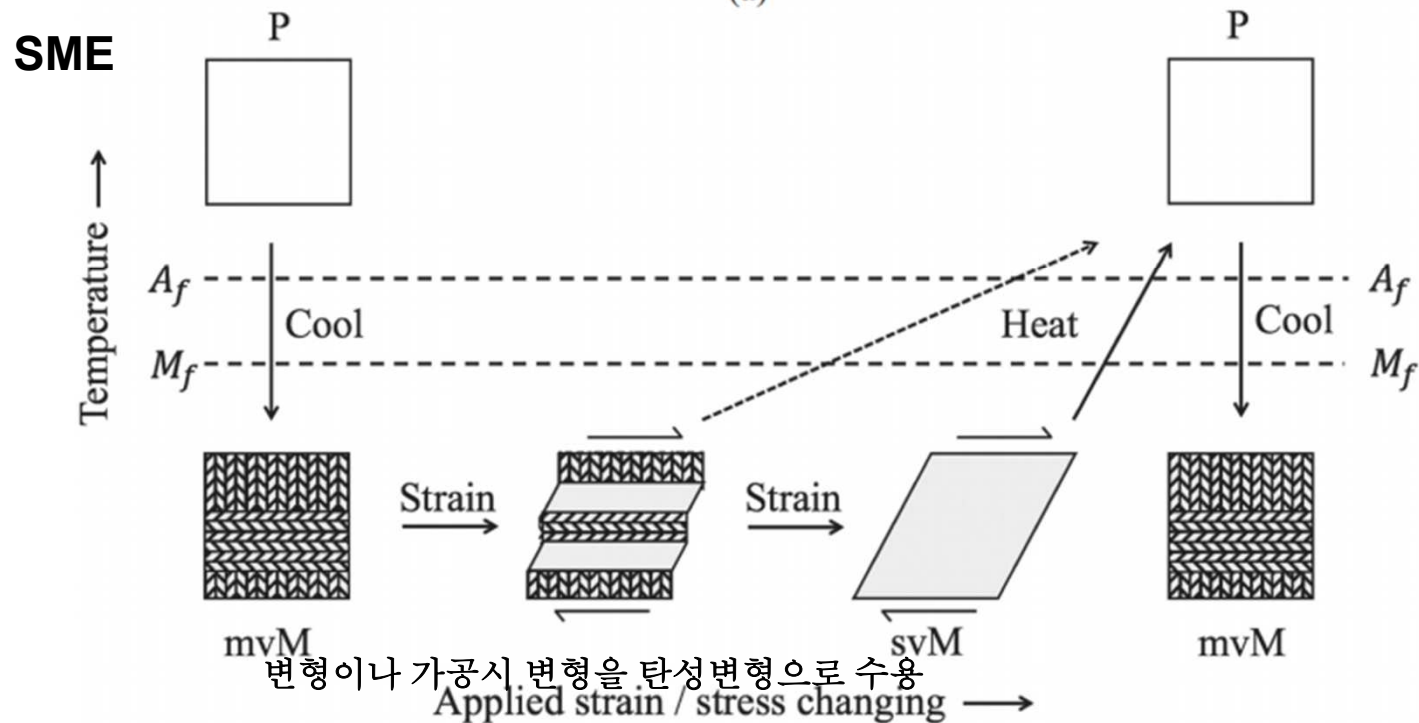


FIGURE 6.77 Schematic diagrams showing superelasticity (SE) and the shape memory effect (SME). (a) Stress – temperature diagram showing the yield stress of the parent phase (P), the stress to induce martensite above M_s , and the temperature ranges for SE and SME. Lower plot shows the definitions of the martensite and austenite start and finish temperatures. (b) Schematic tensile stress – strain curves for material in the SE and SME temperature regimes. Note stress scale differs from that in (a).

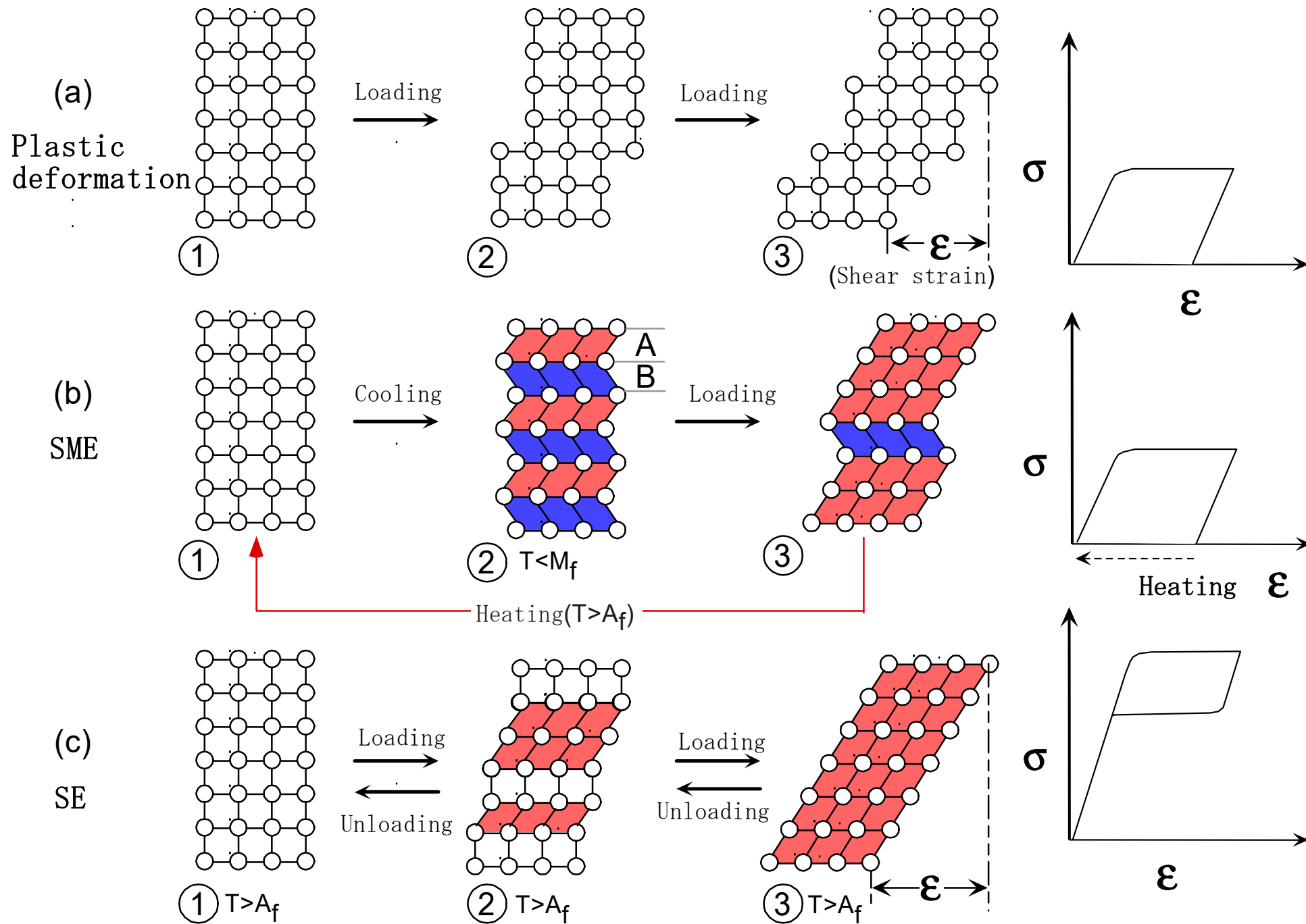


(a)



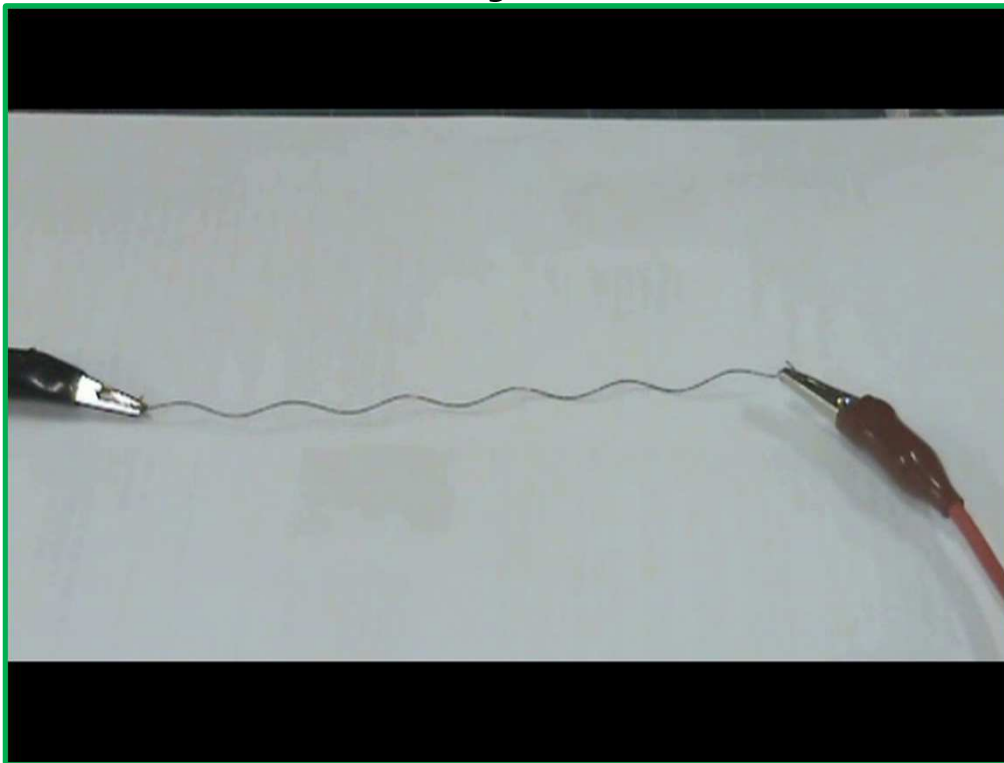
(b)

FIGURE 6.78 (a) Schematic illustration of the superelasticity phenomenon for a single crystal deformed in shear. Isothermal loading and unloading above A_f . The final single-variant stage of deformation is not shown. (b) Schematic illustration of the shape memory effect for a single crystal deformed by shearing below M_f . Original martensite shape is regained by heating to above A_f . In the absence of an applied stress, the shape is also retained on subsequent cooling. Abbreviations: mvM = multivariant martensite, svM = single-variant martensite.



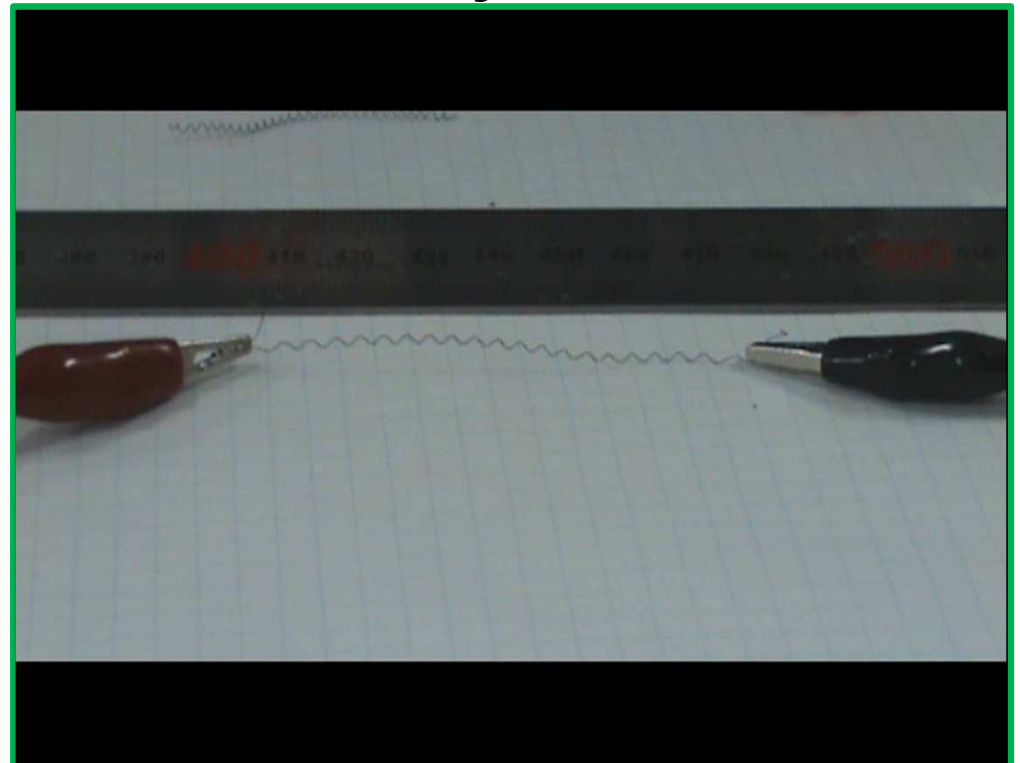
* One-way / Two-way shape memory effect

▼ One-way SME



- ↳ A_f 이상의 고온 형상만을 기억
 - 저온($< M_f$)에서 소성변형 후 A_f 이상의 고온으로 가열
 - 기억된 고온 형상으로 회복

▼ Two-way SME



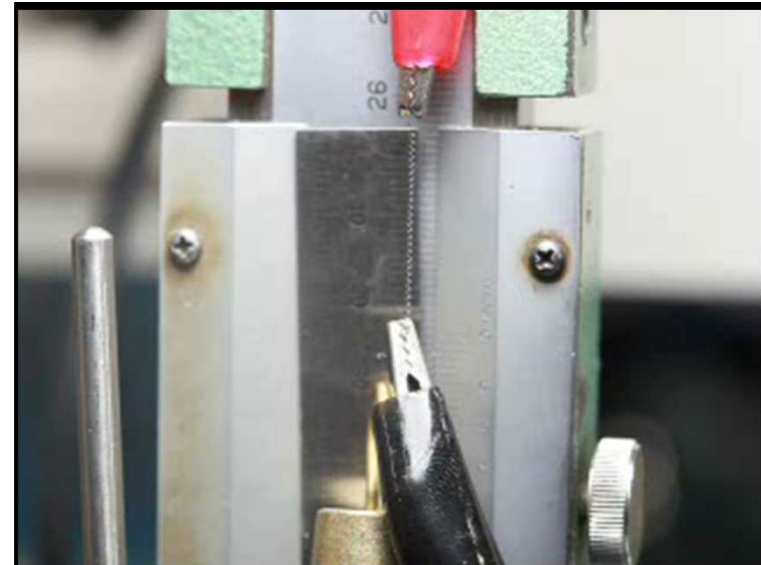
- ↳ 고온($> A_f$) 형상과 저온($< M_f$) 형상을 모두 기억
 - 반복적인 변형으로 인한 형상기억합금 내 전위 밀도의 상승 & 특정방향 응력장의 형성
 - 저온에서 반복소성변형 방향으로 회복

* SMA Actuator

▶ 액츄에이터(Actuator) : 전기 에너지, 열에너지 등의 에너지를 운동에너지로 전환하여 기계장치를 움직이도록 하는 구동소자

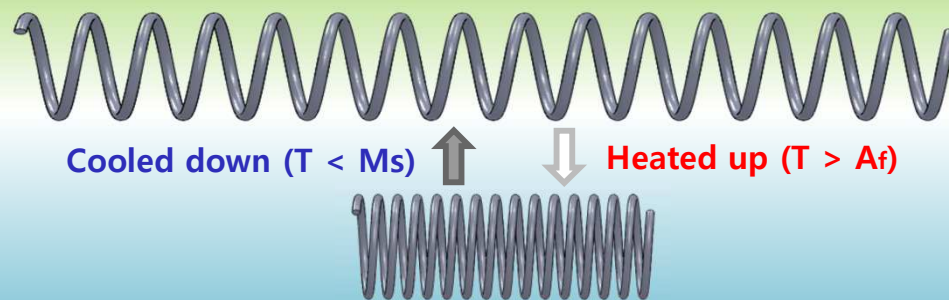


▲ 기존의 매크로 스케일 액츄에이터 (모터-기어 방식)



▲ SMA 스프링 액츄에이터

SMA Spring Actuator

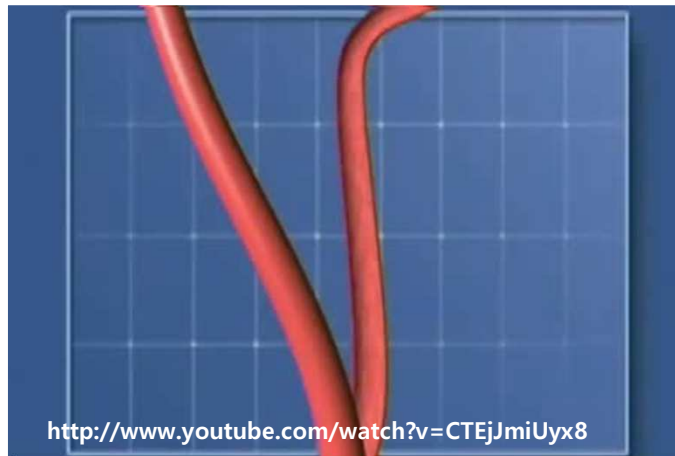
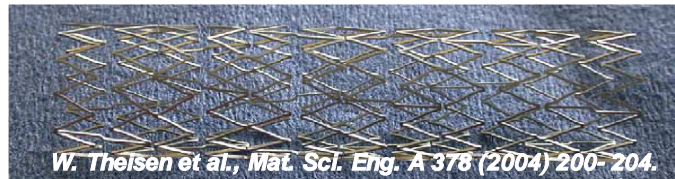
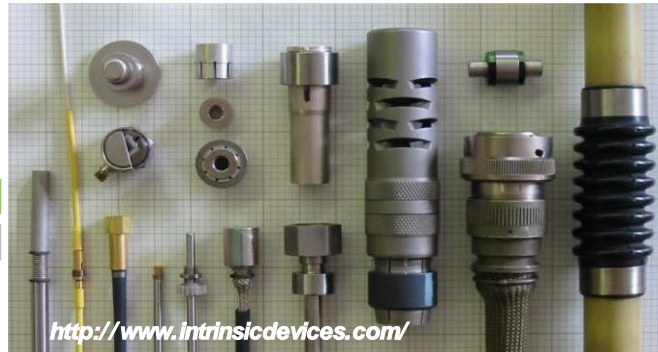


재료의 수축과 신장을 통하여 기계적인 동작을 가능하게 함.

1. 단위 체적당 출력이 높음
2. 모터 구동에 비해 매우 단순한 구조
3. 온도에 의한 제어가 용이
4. 소형화가 쉬움.

* Application of SMAs

▼ 산업 부문: 부품소재 (파이프 이음, 스위치소자나 온도제어용 장치 등)

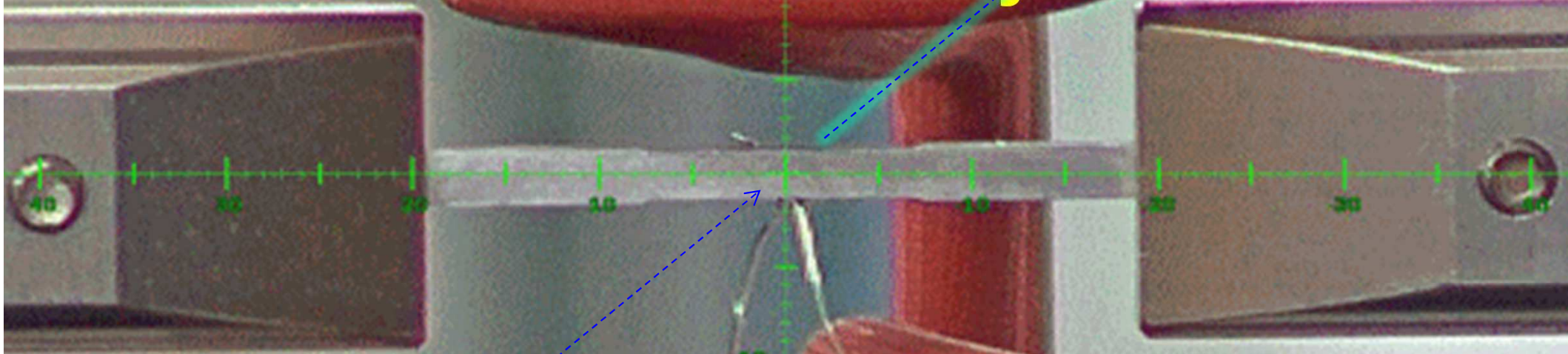
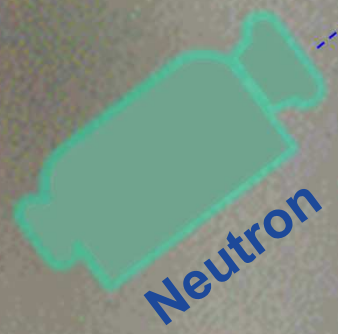
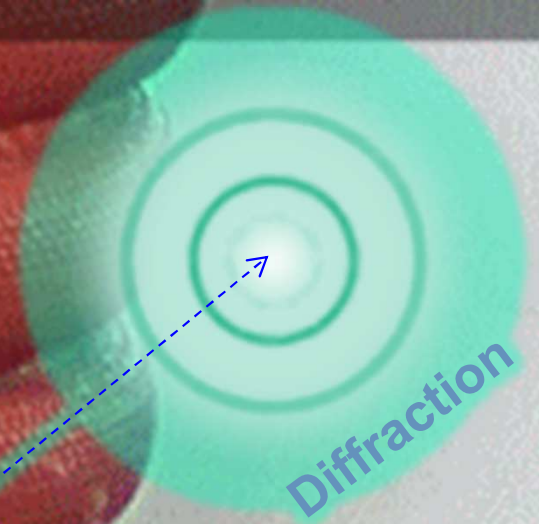


▲ 생체의료 부문: 첨단의료재료
(stent, 치열교정용 강선 등)



▲ 심해저/우주항공 부문: 극지재료
(잠수함, 태양전지판 등)

Healable Alloys



Materials design for reuse

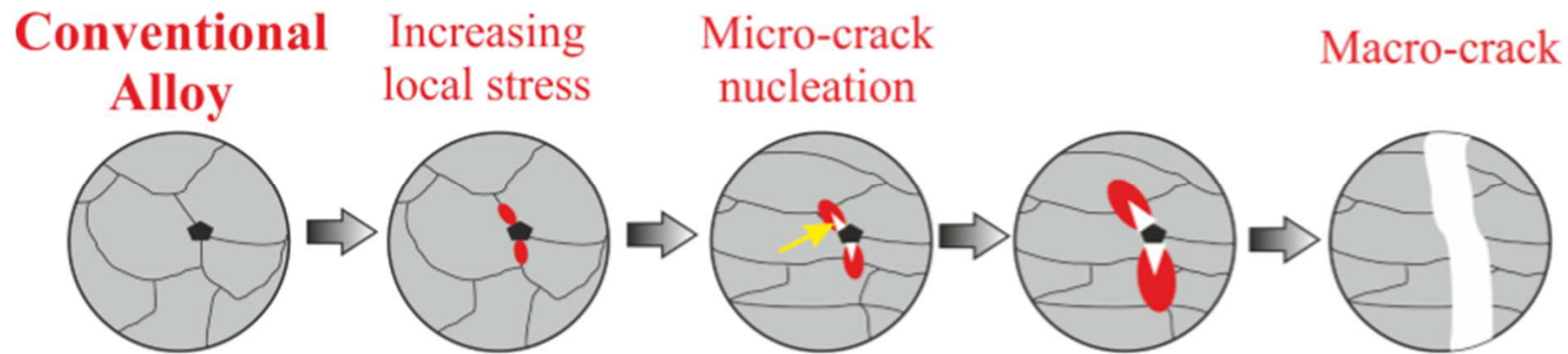
Damage process is incremental, and often local → repair opportunity

Two damage repair options possible:

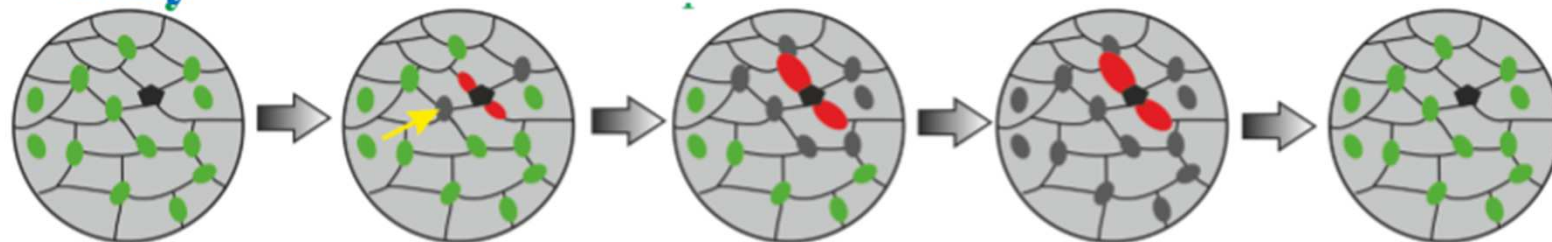
- The metal autonomously repair damage → *Self-healing*
- Damage is repaired by an external treatment → *Resetting*

Self-healing metals vs Resettable alloys

- self-healing: “*autonomic closure of micro-cracks*”
- resetting: “*non-autonomic retrieval of crack-arresting ability*”



Resettable Alloy



Resetting: before critical level
treatment of “damage” & feasible

: revert to the original
microsturcture

Different failure mechanisms require different resetting strategies



서울대학교
SEOUL NATIONAL UNIVERSITY



한국연구재단

준정적 가역상변화 기반 무한수명 특성복귀합금 개발

2018년 선정 도전형 소재기술개발 프로그램

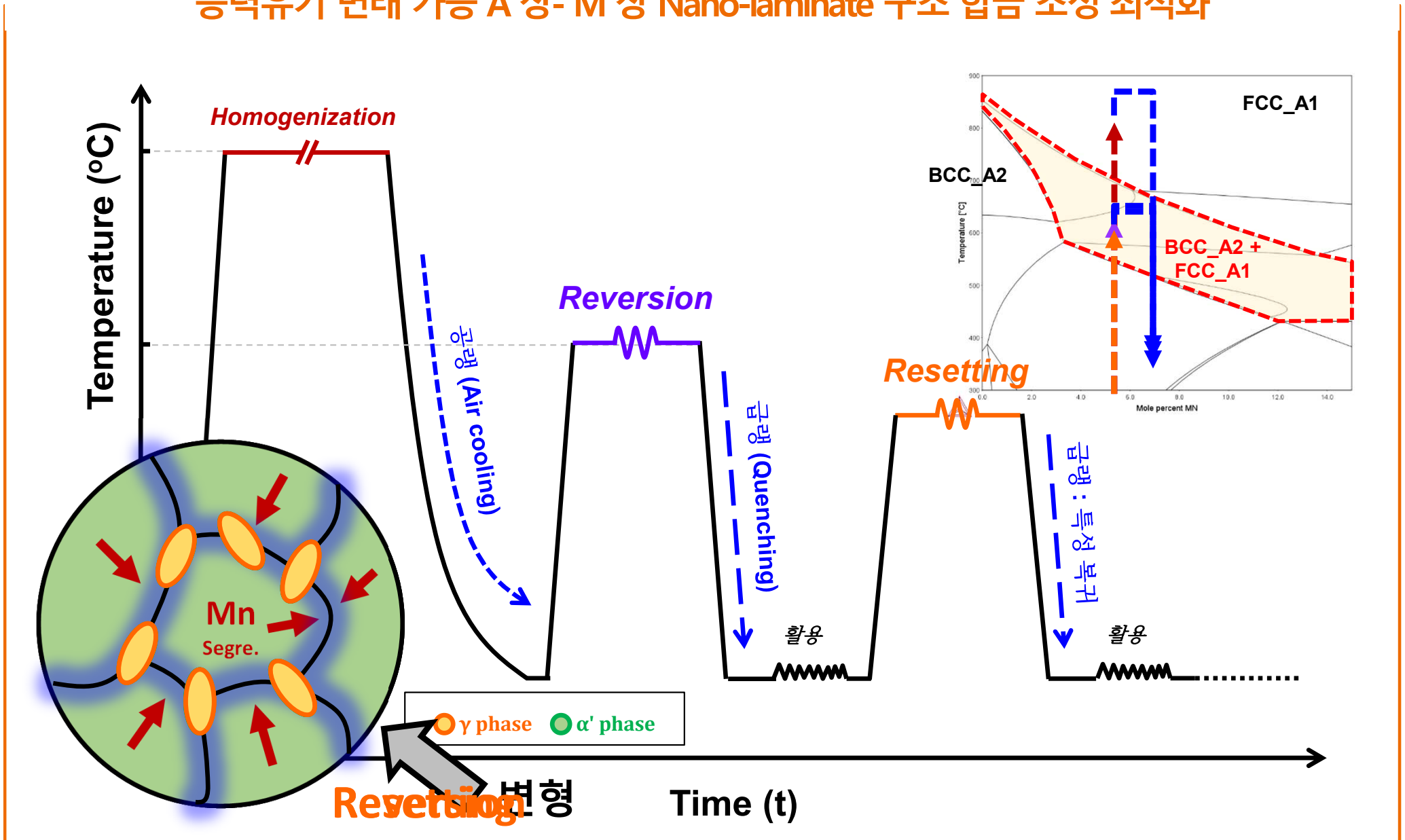
2018 년 - 2022 년

박 은 수

서울대학교 재료공학부

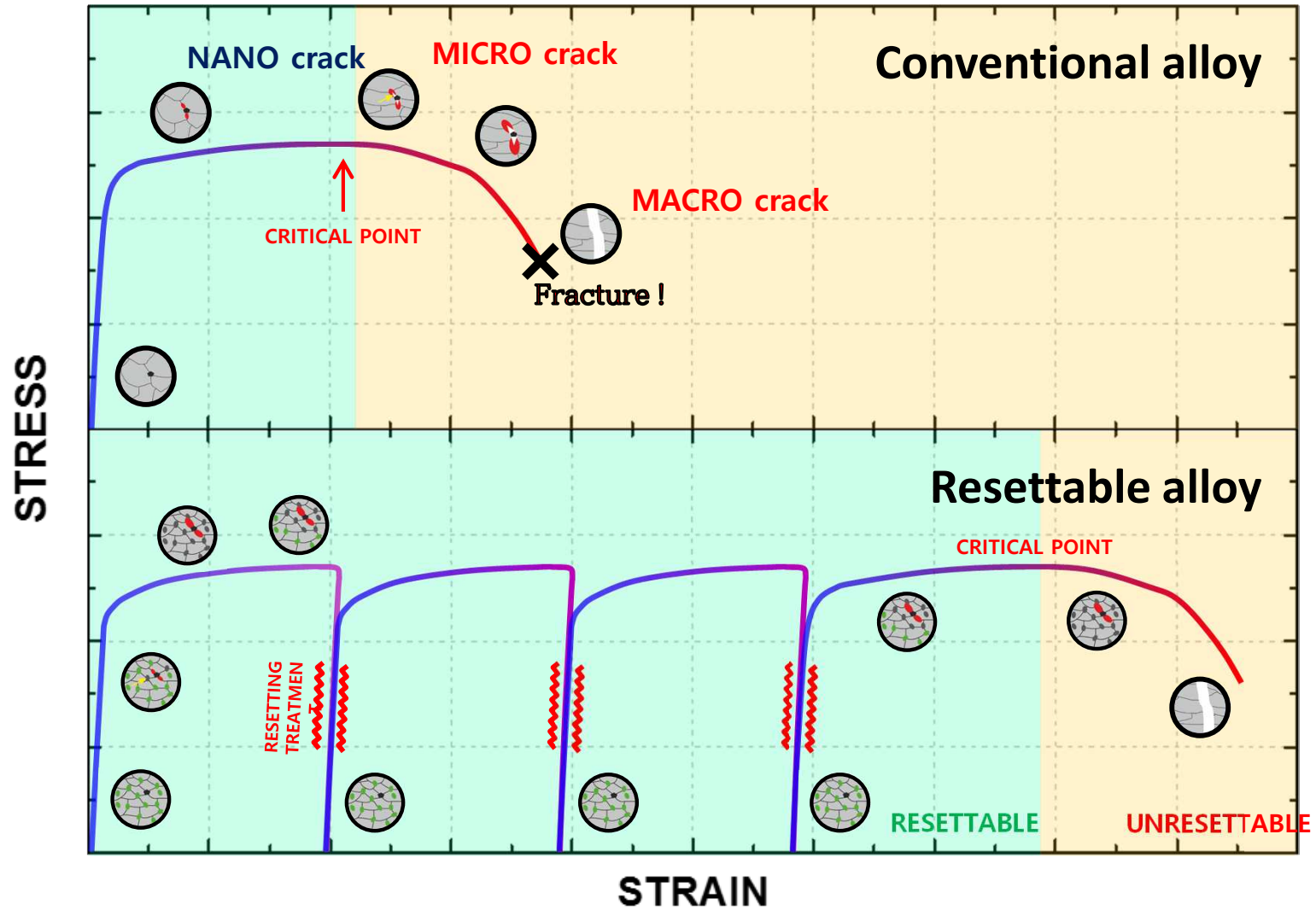
New challenges : *Resettable alloys!*

응력유기 변태 가능 A 상- M 상 Nano-laminate 구조 합금 조성 최적화

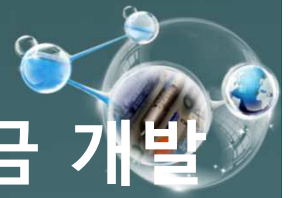


Resetting treatment 를 통해 초기 미세구조로 회복 가능한 Resettable alloy! 69

New challenges : *Resettable alloys!*



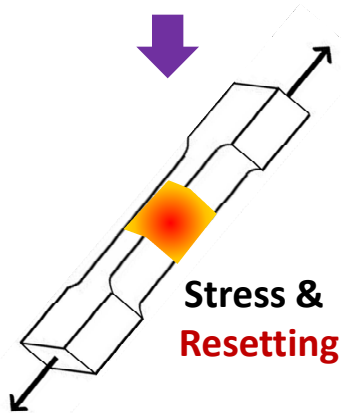
Resetting treatment 를 통해 초기 미세구조로 회복 가능한 Resettable alloy! 70



(3) 실험결과 I : 준정적 가역 상변화 가능 특성복귀 합금 개발

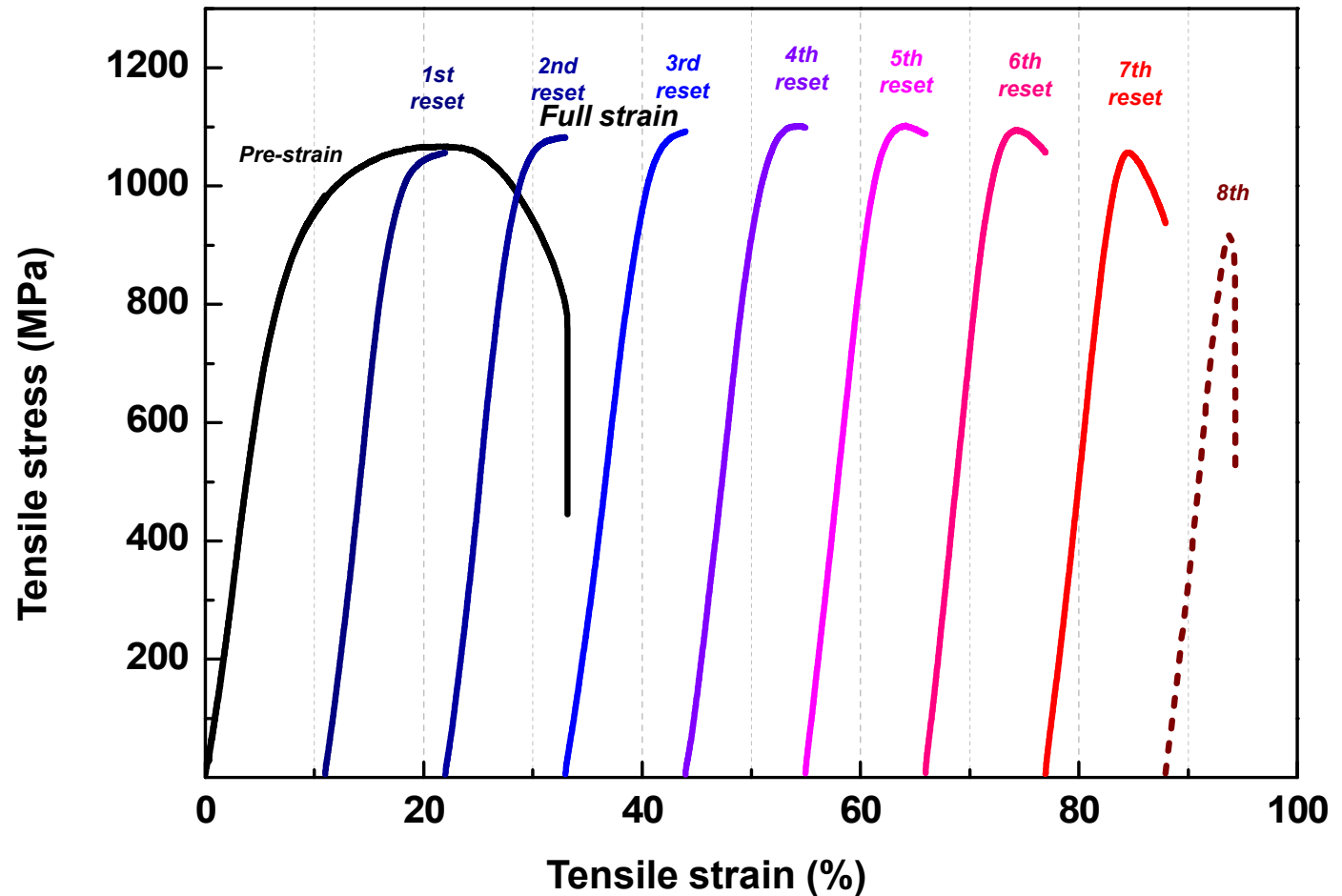
c. (조성)-(결합)-(Resetting 공정) 최적화 기반 변형 Informatics 구축

Air cooling
After homogenization
at 980 °C for 8h
and Reversion
at 550 °C for 20 hour



(1) Pre-strain (12%)
by tensile test
for crack formation

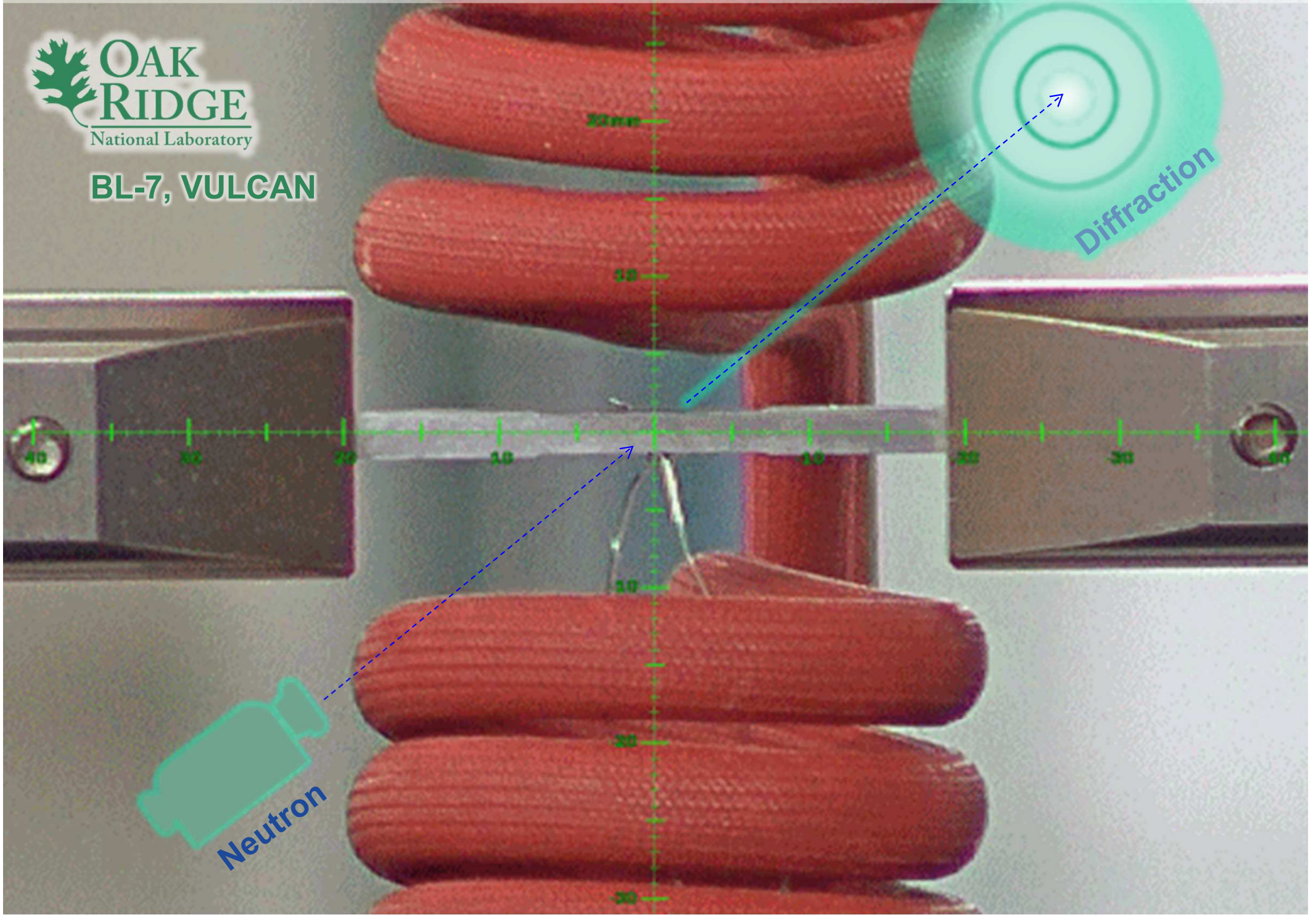
(2) Reset Annealing
at 550 °C for 2h

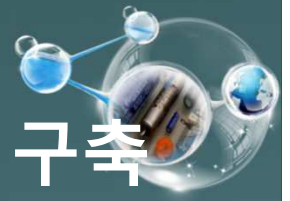


- Resetting Process를 통해, 300% 이상의 연신율 회복
- 리셋 공정 통해 특성 향상 가능 특성 복귀 합금 성공적 개발!



BL-7, VULCAN

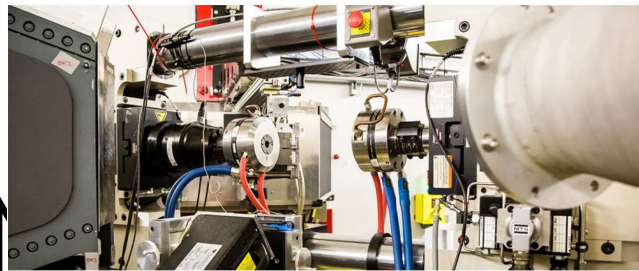




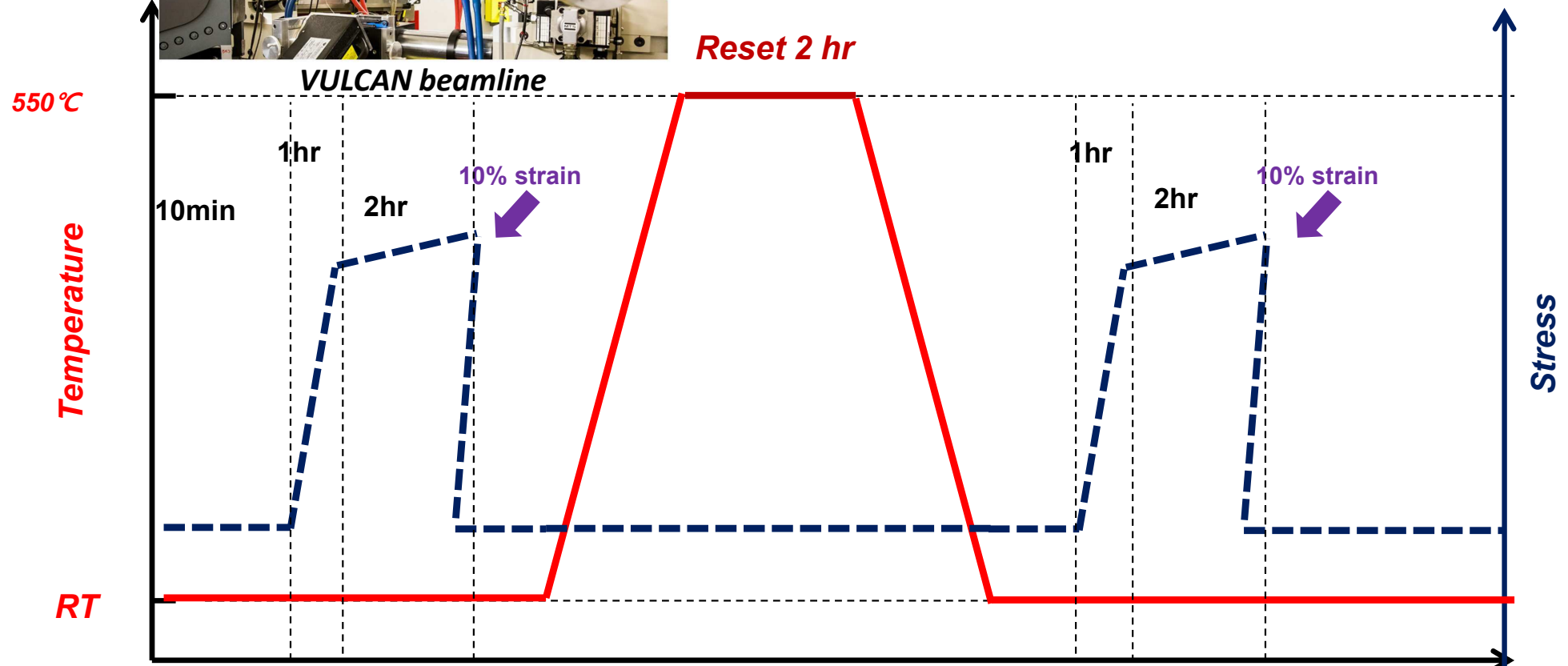
(3) 실험결과 II : 리셋 공정 최적화 변형 Informatics 구축

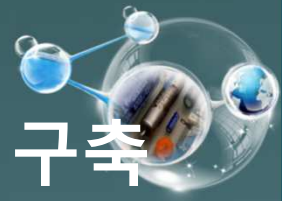
결합 정량화 Smart Monitoring 기반 Deformation Informatics 구축

② 비파괴 검사 통한 사용환경 중 변형 Smart Monitoring 기술 개발



: (손상)-(회복)-(손상) cycle 시의 A 상분율
정량 분석을 통한 손상 정량화



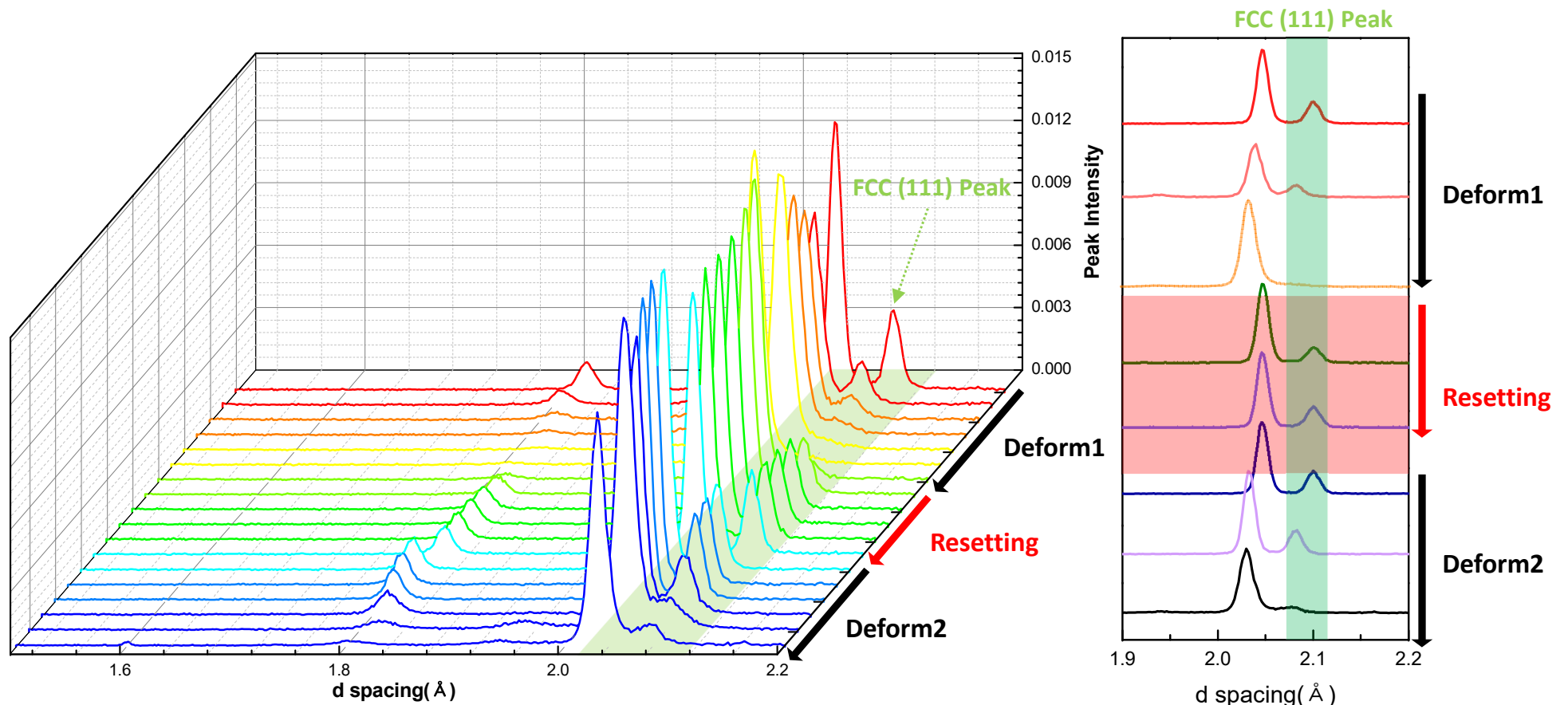


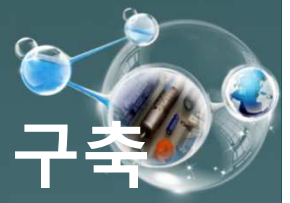
(3) 실험결과 II : 리셋 공정 최적화 변형 Informatics 구축

결합 정량화 Smart Monitoring 기반 Deformation Informatics 구축

② 비파괴 검사 통한 사용환경 중 변형 Smart Monitoring 기술 개발

: (손상)-(회복)-(손상) cycle 시의 A 상분을 정량 분석을 통한 손상 정량화

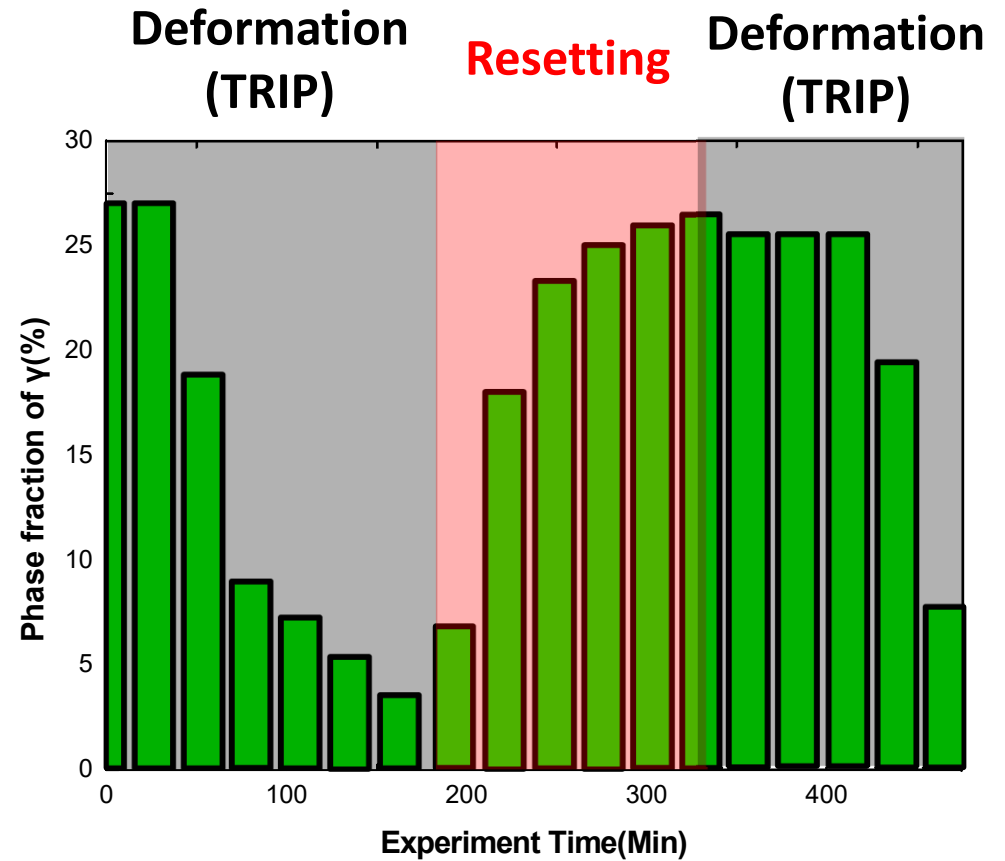
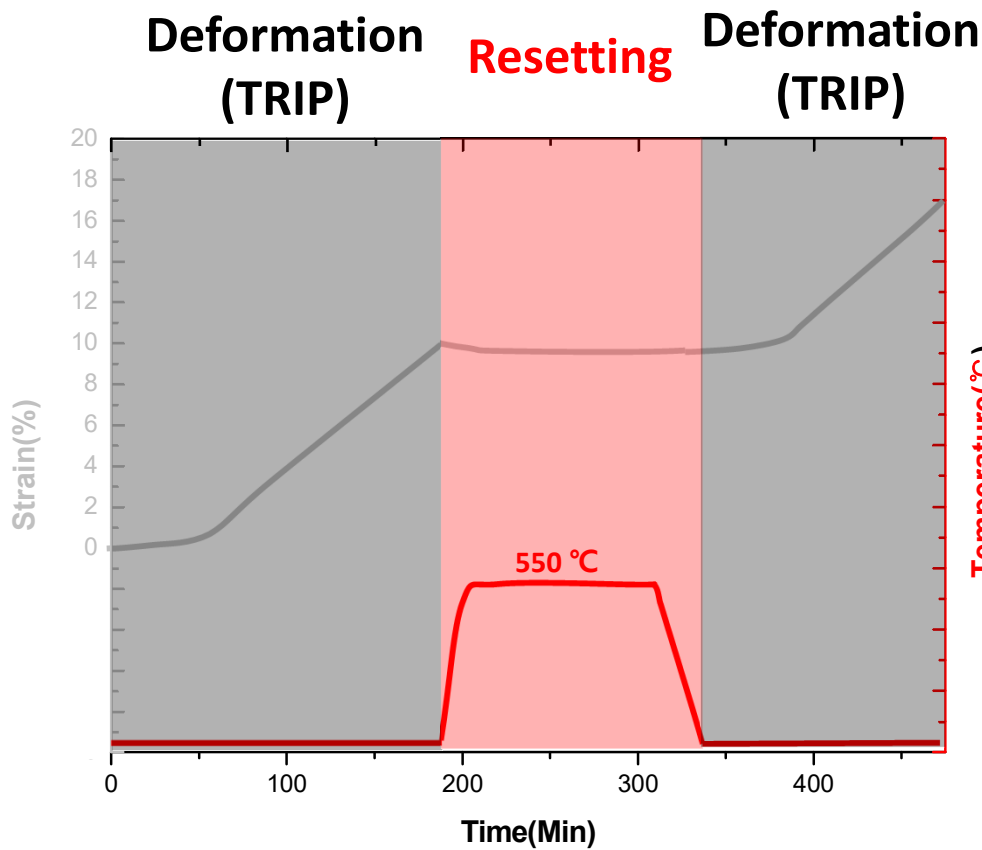




(3) 실험결과 II : 리셋 공정 최적화 변형 Informatics 구축

결합 정량화 Smart Monitoring 기반 Deformation Informatics 구축

② 비파괴 검사 통한 사용환경 중 변형 Smart Monitoring 기술 개발



▶ (손상) - (회복) 에 따른 상분율 정량 변화 분석을 통한 Deformation Informatics 구축!



서울대학교
SEOUL NATIONAL UNIVERSITY

지능형 자가변환 기반 자가치유 센테니얼 합금 개발

연구책임자: **박은수** (서울대학교 재료공학부)

참여연구원: 고원석 (울산대학교 첨단소재공학부)
한흥남 (서울대학교 재료공학부)
김원태 (청주대학교 레이저광정보학과)

서진유 (KIST, 고온에너지재료연구센터)
김영운 (서울대학교 재료공학부)
심기동 (KAIST, 기계공학과)

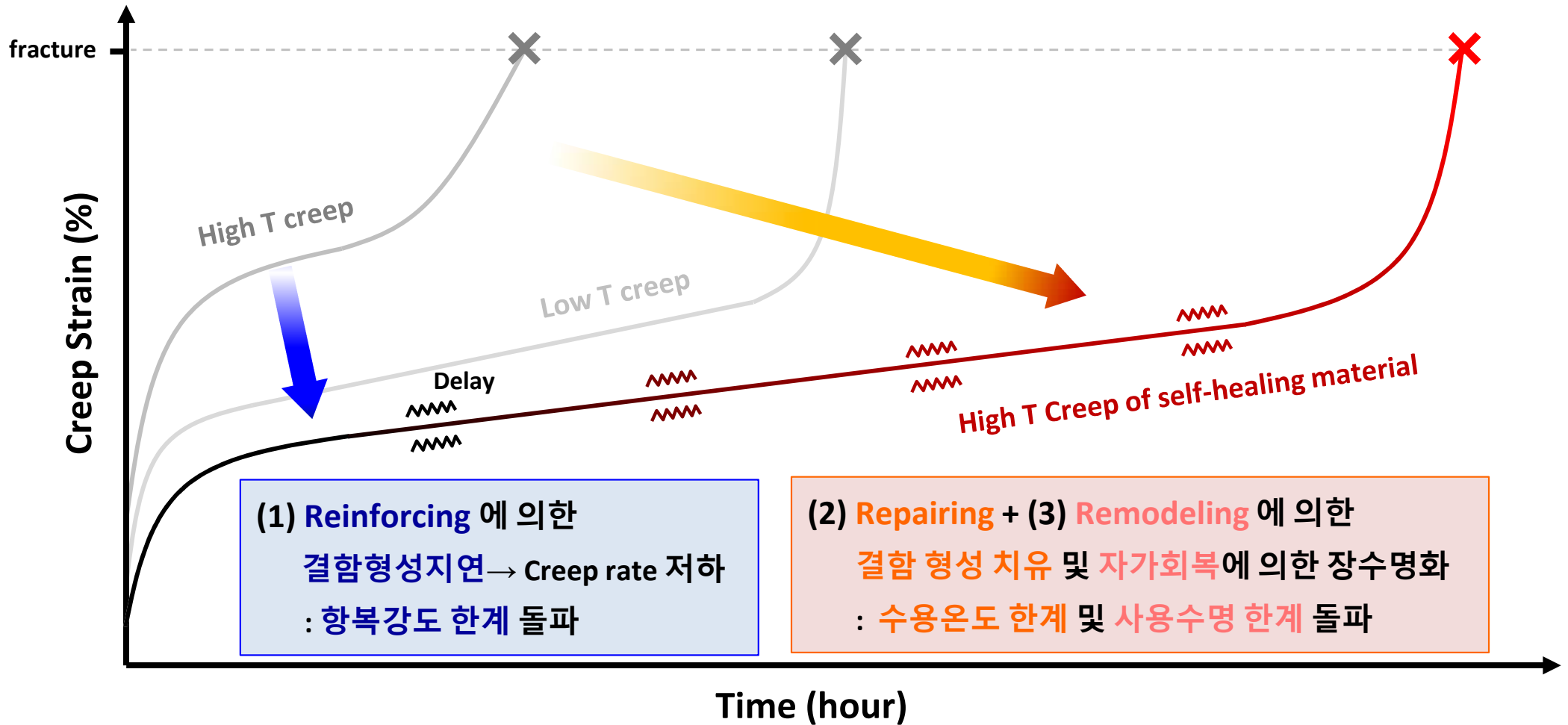
김도향 (연세대학교 신소재공학부)
이동우 (성균관대학교 기계공학부)

박형기 (한국생산기술연구원)
이제인 (부산대학교 재료공학부)



New Challenges ! = 지능형 자가치유 센테니얼 합금

Creep def. of Centennial alloy (high T or high σ)

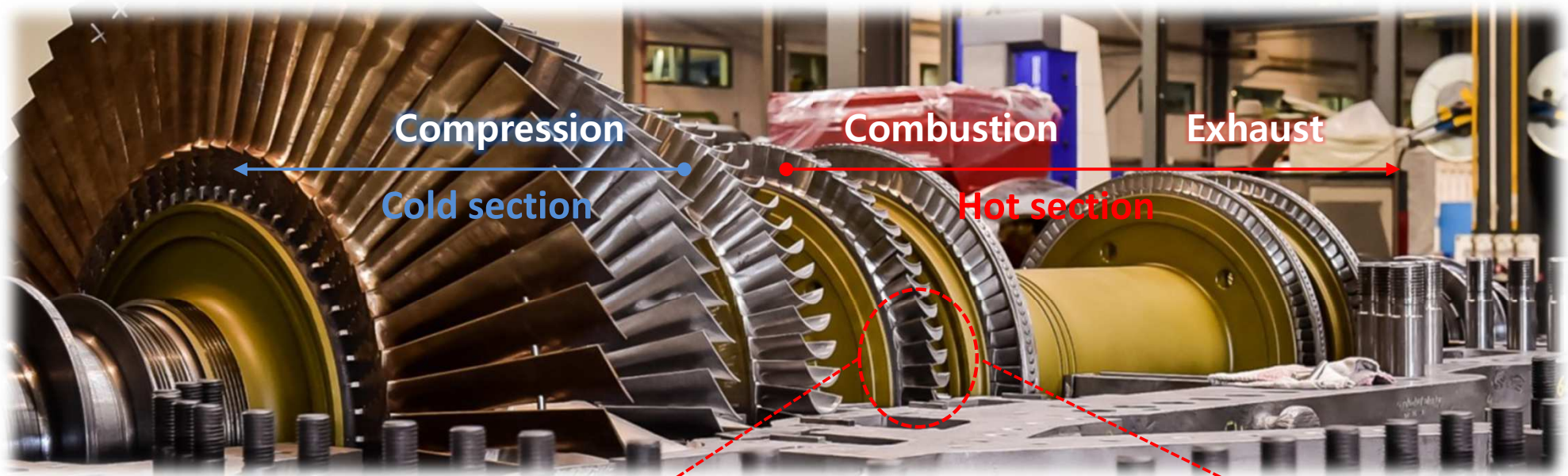


(항복강도 · 수용온도 · 사용수명) 한계 돌파 센테니얼 합금

맞춤형 구조제어 직접디지털제조 공정기술 개발



Target 부품 : 가스복합화력발전용 H-class (TIT 1500°C) gas turbine * Siemens SGT6-8000 H



- 고효율 균일냉각
Complex cooling channel
- 고온 크리프 특성 향상
자가치유 + 미세구조 제어
- 고온 강도 향상
Precipitate control



High efficiency blade for H-class gas turbine



3D 프린팅 기반의 초고효율 블레이드 부품개발

❖ 발전부품 3D 프린팅 현재 국내 기술수준: 인코넬 이용 E/F-class (TIT 1300°C 이하) vane 개발 진행 중

6.10 Case studies Skip

*** Homework 8 : Summary of sections 6.10**

within 5 pages PPT until 18th December (before exam)

*** Homework 9 : Exercises 6 (pages 495-498)**

until 18th December (before exam)

Contents in Phase Transformation

Background
to understand
phase
transformation

(Ch1) Thermodynamics and Phase Diagrams

(Ch2) Diffusion: Kinetics

(Ch3) Crystal Interface and Microstructure

Representative
Phase
transformation

(Ch4) Solidification: Liquid \rightarrow Solid

(Ch5) Diffusional Transformations in Solid: Solid \rightarrow Solid

(Ch6) Diffusionless Transformations: Solid \rightarrow Solid

Microstructure-Properties Relationships

Alloy design &
Processing

Performance

“Phase Transformation”

Microstructure
down to atomic scale

Properties

“Tailor-made Materials Design”

On-line (& Off-line) Office hours

12월 13일 수요일 9시-11시 <https://zoom.us/j/95938581413>

PTM 기말고사 (2023.12.18. 오전 8시30분-11시) 계산기 지참 요망

한 학기 동안 재료 상변태 강좌 수강하느라 고생하셨습니다.

이 강좌를 통해 “재료”을 다스리는데 필수적인 스킬인 “재료 상변태”에 대한 이해도가 한층 높아졌기를 바랍니다!! **ES**